UC Santa Barbara

UC Santa Barbara Electronic Theses and Dissertations

Title

Understanding Atomic-Scale Compositions, Structures, and Properties of Semi-Crystalline Inorganic Nanomaterials

Permalink

https://escholarship.org/uc/item/2vr591c0

Author

Berkson, Zachariah

Publication Date

2018

Peer reviewed|Thesis/dissertation

eScholarship.org Powered by the California Digital Library
University of California

UNIVERSITY OF CALIFORNIA

Santa Barbara

Understanding Atomic-Scale Compositions, Structures, and Properties of Semi-Crystalline Inorganic Nanomaterials

A dissertation submitted in partial satisfaction of the

requirements for the degree Doctor of Philosophy

in Chemical Engineering

by

Zachariah J. Berkson

Committee in charge:

Professor Bradley F. Chmelka, Co-Chair

Professor Jacob N. Israelachvili, Co-Chair, in memoriam

Professor Michael J. Gordon

Professor Horia Metiu

December 2018

The dissertation of Zachariah J. Berkson is approved.

_____
Horia Metiu

_____
Michael J. Gordon

_____
Bradley F. Chmelka, Committee Co-Chair

_____
Jacob N. Israelachvili, Committee Co-Chair

October 2018

Understanding Atomic-Scale Compositions, Structures, and Properties of Semi-Crystalline Inorganic Nanomaterials

Copyright © 2018

by

Zachariah J. Berkson

ACKNOWLEDGEMENTS

Completion of this dissertation would not have been possible without substantial support from many people, to whom I am greatly indebted. First and foremost are my PhD advisors, Brad Chmelka and Jacob Israelachvili, who have been a continual source of intellectual support and encouragement and have provided me with many opportunities for which I am deeply grateful. Brad's boundless enthusiasm, meticulousness, and care over the last five years have improved me as a researcher, writer, scientist and engineer. I am grateful for Brad's numerous excellent academic and industrial partnerships and friendships, which provided me with many friendships of my own and invaluable opportunities to travel. Brad has been a constant source of support, mentorship, and an example for me as I finish my PhD and embark into the broader scientific world.

Sadly, Prof. Jacob Israelachvili passed away in September, 2018, during the late stages of my PhD. Jacob was an intellectual leader in the fields of soft matter, surface interactions, intermolecular physics, and surface interactions, as well as a role model and mentor. Jacob's humor, wit, and attention to detail made working with him a pleasure and taught me the value of both organization and kindness in a research setting. I am profoundly lucky to be among Jacob's students. His reassuring presence and quiet, continual optimism are sorely missed.

I additionally want to express my gratitude to the other members of my committee, Mike Gordon and Horia Metiu, for valuable insights during our annual meetings.

Over the course of my PhD, I have had the opportunity to collaborate closely with numerous world-class researchers who have supported or contributed to my work. I am continually astounded by the kindness, creativity, and intellectual excellence of the scientific community as a whole, and the following people in particular. I am particularly grateful to Anne Lesage for enabling my annual visits to her lab at the Centre de RMN à Très Hautes Champs in Lyon, France, as well as the other researchers with whom I have worked at CRMN: Guido Pintacuda, David Gajan, Daniela Lalli, and Kevin Sanders. I have enjoyed discussing the frontiers of solid-state NMR spectroscopy with the Alicia Lund, from UCSB to CRMN. I thank James Yesinowski for his mentorship during the early years of my PhD and for hosting me on my visit to Washington, DC and the Naval Research Lab. I thank Lynne McCusker and Christian Baerlocher for graciously welcoming me into their home in Switzerland on more than one occasion and for many excellent conversations in California, Zurich, and Ljubljana. I thank Ulrike Werner-Zwanziger, who taught me much about solid-state NMR during the year she spent at UCSB as a visiting researcher. I am also grateful to Subramanian Prasad, for his continued interest and enthusiasm in our collaborative work.

This work would not have been possible without the support of the excellent staff of the NMR facility at UCSB, Jerry Hu, Jaya Nolt, and Shamon Walker.

I acknowledge the diverse funding sources which provided support for different aspects of my PhD work. The UCSB Regents Special Fellowship provided funding support during the first three years of my PhD. The Chevron Energy Technology Corporation supported the work presented in Chapters 2-4, the BASF Corporation supported the work presented in Chapter 5, the US Department of Energy (Award No. DE-FG02-87ER45331) supported the work presented in Chapter 6, and the US National Science Foundation (Award No. DMR-

1121053) supported the work presented in Chapter 9. All chapters of this dissertation made use of the MRL Shared Experimental Facilities, which are supported by the MRSEC Program of the NSF under Award No. DMR 1720256.

I am grateful to the members of the Chmelka and Israelachvili research groups for their support, encouragement, and friendship over the years. I particularly want to acknowledge the mentorship and continuing encouragement of Rahul Sangodkar, who exemplified for me the ideal graduate student for many years. It has been a pleasure to work alongside the excellent company of Matthew Idso, Niels Zussblatt, Thomas Farmer, Howard Dobbs, Nathan Prisco, George Degen, Madeline Beeson, Tsatsa Battsengel, and Shona Becwar.

I would like to thank my family: Lisa Berkson, Steve Bokenkamp, Nathaniel and Eliza Forsythe, Anastasia, Ashton, Ayley, Jessa, and Samara Shortridge, and Sean Bokenkamp. And I would like to thank E. Nastacia Schmoll for her love and support.

Curriculum vitae of Zachariah J. Berkson

zberkson@engineering.ucsb.edu

Updated December, 2018

EDUCATION

2013 - present **Doctor of Philosophy in Chemical Engineering**,
expected December, 2018
University of California, Santa Barbara, CA

2009 - 2013 **Bachelor of Science in Engineering, Chemical Engineering**
Fulton Schools of Engineering & Barrett, the Honors College
Arizona State University, Tempe, AZ
Summa cum laude

Research Experience

Jan. 2014 - present **Ph. D. Candidate**
University of California, Santa Barbara, CA
Advisors: Profs. Bradley F. Chmelka and Jacob N. Israelachvili
−Dissertation: *Understanding atomic-scale compositions, structures, and properties of semi-crystalline inorganic nanomaterials*

June 2018 **Visiting researcher**
National High Magnetic Field Laboratory, Tallahassee, FL

Aug., 2018
Sep., 2017
Jul., 2016 **Visiting researcher**
Centre de RMN à Très Hauts Champs (European Center for High Field NMR), Lyon, France

2011 - 2013 **Fulton Undergraduate Research Internship**
Arizona State University, Tempe, AZ
Advisor: Prof. Jean Andino, Atmospheric Chemistry Laboratory
−Honors thesis: *Charge separation in titanium dioxide photocatalysts for the reduction of carbon dioxide to fuels*

Publications and Manuscripts in Submission

1) D. Jung, L. M. A. Saleh, Z. J. Berkson, *et al*. "A Molecular Doping Approach for Hybrid Metal Oxide Materials." *Nature Materials,* **2018**, 17 (4) 341-350.
2) Z. J. Berkson, R. J. Messinger, K. Na, Y. Seo, R. Ryoo, B. F. Chmelka. "Non-Topotactic Transformation of Silicate Nanolayers into Mesostructured MFI Zeolite Frameworks During Crystallization." *Angewandte Chemie International Edition, **2017**, 56 (19), 5146-5241.*
3) S. Smeets, Z. J. Berkson, D. Xie, S. I. Zones, W. Wan, X. Zou, M. Hsieh, B. F. Chmelka, L. B. McCusker, C. Baerlocher. "Well-defined silanols in the structure of the calcined high-silica zeolite SSZ-70: new understanding of a successful catalytic material." *Journal of the American Chemical Society*, **2017**, 139(46), 16803-16812.

4) J. P. Yesinowski, Z. J. Berkson, S. Cadars, A. P. Purdy, B. F. Chmelka. "Spatially Correlated Distributions of Local Metallic Properties in Bulk & Nanocrystalline GaN." *Physical Review B*, **2017**, 95 (23), 235201.
5) Z. J. Berkson, M.-F. Hsieh, S. Smeets, D. Gajan, A. Lund, A. Lesage, D. Xie, S. I. Zones, L. B. McCusker, C. Baerlocher, B. F. Chmelka. "Preferential siting of Al heteroatoms in the zeolite catalyst Al-SSZ-70." Submitted to *Angewandte Chemie.*
6) -S.-H. Cho*, S. Gosh*, Z. J. Berkson*, J. Hachtel, J. Shi, L. Gilbert, Y. Ho, A. Yang, B. F. Chmelka, D. Milliron. "Synthesis of colloidal F:In_2O_3 cubes: fluorine induced faceting and infrared plasmonic response." Submitted to *Journal of the American Chemical Society*. *Equal contribution. Preprint available on *ChemRxiv* under DOI: 10.26434/chemrxiv.7355042.v1
7) H. Dobbs, K. Kristiansen, A. Schrader, Z. J. Berkson, G. Degen, B. F. Chmelka, J. N. Israelachvili. "Electrochemically enhanced dissolution of silica and alumina in alkaline solutions." Submitted to *Proceedings of the National Academy of Sciences.*
8) K. Gottschling, L. Stegbauer, G. Savasci, N. Prisco, Z. J. Berkson, C. Ochsenfeld, B. F. Chmelka, B. V. Lotsch, "Tailoring CO_2 uptake by tertiary amine-modified hydrazone-linked covalent organic frameworks." Submitted to *Chemistry of Materials*.

Manuscripts in Preparation

1) Z. J. Berkson, D. C. Upham, S. Prasad, D. Gajan, U. Werner-Zwanziger, A. Lesage, E. McFarland, B. F. Chmelka. "Hydrocarbon adsorption, reaction, and deactivation sites in aluminosilicate USY zeolite catalysts." In preparation for *Science.*
2) Z. J. Berkson, S. Becwar, N. P. Zussblatt, N. A. Prisco, N. Fechler, B. F. Chmelka, "Atomic-scale origins of oxygen reduction activity in non-precious-metal mesoporous Fe,N-carbon electrocatalysts with high nitrogen contents." In preparation for *Nature Materials.*
3) Z. J. Berkson, M. Beeson, D. Lalli, N. A. Prisco, H. Dobbs, D. Gajan, E. H. Poniatowski, M. Sanchez del Rio, F. Sánchez-Ochao, Jacob N. Israelachvili, A. Lesage, G. Pintacuda, B. F. Chmelka. "Atomic-scale compositions and structures that account for the optical and stability properties of the historic pigment Maya Blue." In preparation for *Nature Materials.*
4) Z. J. Berkson, S. Prasad, K. Sanders, N. Prisco, D. C. Upham, D. Gajan, A. Lesage, E. McFarland, G. Pintacuda, B. F. Chmelka. "Atomic insights into the active sites and catalytic properties of copper-chabazite zeolite catalysts." In preparation for *Journal of the American Chemical Society.*
5) M. Kumar, Z. J. Berkson, R. J. Clark, Y. Shen, N. A. Prisco, H. Zheng, L. B. McCusker, J. Palmer, B. F. Chmelka J. Rimer. "Cooperative organic structure directing agents direct suprananoscale mordenite zeolite crystallization." In preparation for *Science.*
6) Z. J. Berkson, H. Dobbs, G. Degen, K. Kristiansen, A. Schrader, J. N. Israelachvili, B. F. Chmelka,. "Network formation and strength development in alkali-activated aluminosilica cements." In preparation for *J. Amer. Chem. Soc*.
7) N. P. Zussblatt, Z. J. Berkson, N. A. Prisco, N. Fechler, A. Lund, B. F. Chmelka, "Correlated molecular compositions, structures, and electrochemical properties of nitrogen-containing carbon materials." In preparation for *Chemistry of Materials.*

Selected Honors and Awards

- Travel Fellowship, 10th Alpine Conference on Solid-State NMR in Chamonix, France, 2017
- Outstanding Teaching Assistant Award, UCSB Department of Chemical Engineering. 2014-2015.
- UCSB Regents Special Fellowship. 2013-2015.
- Center for Biology and Society Travel Award, ASU. 2013.
- Air and Waste Management Association (AWMA) Scholarship, Grand Canyon Section. 2012.

Teaching and Mentorship

2016-2018	Mentored undergraduate student researcher, Madeline Beeson (UCSB ChE, '18)
Fall, 2016	Teaching assistant for *Advanced Process Control*, instructed lab section
Fall, 2015	Teaching assistant for *Process Dynamics and Control*, gave 1/4 of lectures
Fall, 2014	Teaching assistant for *Chemical Reaction Engineering*, gave 1/5 of lectures
Fall, 2012	Undergraduate teaching assistant for *Intro. to Chemical Reactor Design*

Patents and Inventions

1) Z.J. Berkson, S. Prasad, I. Petrovic, B. F. Chmelka. "*Cu/H-chabazite catalyst prepared through back-exchange of Cu-chabazite for MTO applications.*" Invention disclosure submitted, 2018.

Selected Presentations and Conferences

1) Framework structures and heteroatom sites of zeolite SSZ-70 established by solid-state DNP-NMR and synchrotron XRPD. SMARTER-6 conference, Ljubljana, Slovenia. 6 September 2018. Talk.

2) Understanding heteroatom and cation influences on zeolite catalyst properties. BASF California Research Alliance Summer Symposium. 11 July 2018. Poster. Student poster award, 3rd place.

3) Opportunities for high-field NMR and DNP for elucidating surface and heteroatom environments in complex heterogeneous materials. BigMag@UCSB workshop, May 17-19, 2018. Poster.

4) Atomic-level crystallization, adsorption, and reaction properties of zeolite catalysts established by solid-state J-mediated DNP-NMR and synchrotron XRPD. Experimental NMR Conference, Orlando, FL. 1-3 June 2018. Poster.

5) *Understanding network formation and strength development in alkali-activated aluminosilica cements.* American Chemical Society Spring Meeting, 21 March 2018. Talk.

6) *Molecular compositions and structures of heteroatom and cation-exchange sites in zeolite catalysts.* BASF California Research Alliance Review, Berkeley, CA, 17 November 2017. Talk.

7) *Identification of specific adsorption and deactivation sites in aluminosilicate USY zeolite catalysts.* American Institute of Chemical Engineers (AIChE) Annual Meeting, Minneapolis, MN, 31 October 2017. Talk.

8) *Solid-state DNP-NMR studies of molecular adsorption environments and interactions of distinct heteroatom sites in aluminosilicate zeolite catalysts.* 10th Alpine Conference for Solid-State NMR, Chamonix-Mont Blanc, France, 12 September 2017. Round-table.
9) *Measuring and understanding the atomic-scale environments and interactions of heteroatom sites in zeolite catalysts.* Materials Research Society (MRS) Spring Meeting, Phoenix, AZ, 21 April 2017. Talk.
10) *Non-topotactic transformation of silicate nanolayers into mesostructured MFI zeolite frameworks determined by solid-state DNP-NMR.* Experimental NMR Conference, Pacific Grove, CA, 26-31 March 2017. Poster.
11) *Correlating atomic-scale compositions, structures, and properties of heterogeneous zeolite catalysts.* Clorox-Amgen Chemical Engineering Graduate Student Symposium, University of California, Santa Barbara, CA. 30 September 2016. Talk.
12) *Atomic-scale interactions and compositions of electrically- and catalytically-active nanostructured materials*. U.S. Naval Research Laboratory, Washington, D.C. 18 April 2016. Invited talk.
13) *Correlated local electronic properties and photoluminescence of annealed gallium nitride nanoparticles.* Materials Research Outreach Program, University of California, Santa Barbara, CA. 2 February 2016. Poster.
14) *Engineering nanomaterials for a sustainable world.* UCSB Nano Days science outreach event, Santa Barbara Museum of Natural History, CA. 2 April, 2016. Talk.
15) *Solid-state ^{71}Ga and ^{15}N NMR evidence for electron carriers in annealed gallium nitride nanoparticles.* Experimental NMR Conference, Pacific Grove, CA. 19-24 April, 2015. Poster.
16) *Molecular assembly and properties of semiconducting nanostructures.* Chemical Engineering First-Year Graduate Student Symposium, University of California, Santa Barbara, CA. 29 September, 2014. Talk.
17) *EPR study of charge separation within novel TiO_2 photocatalysts for the conversion of CO_2 to fuels.* Air and Waste Management Association Annual Conference and Exhibition, San Antonio, TX. 19-22 June, 2012. Poster. Undergraduate student poster award, 1st place.

ABSTRACT

Understanding Atomic-Scale Compositions, Structures, and Properties of Semi-Crystalline Inorganic Nanomaterials

by

Zachariah J. Berkson

Many important material properties are determined by the surface layer (0.5-100 nm); these include optoelectronic properties like conductivity, absorptivity, and reflectance as well as physiochemical properties such as molecular adsorption, hydrophobicity, and surface diffusivity. Furthermore, the crystallization or assembly processes of technologically-important nanomaterials are mediated by surface interactions and influence the surface compositions and properties of the resultant material, including zeolites, colloidal semiconductors, carbon-based electrocatalysts, and mesoporous inorganic oxides. Catalytic reaction properties of diverse porous heterogeneous materials are determined by molecular interactions of adsorbates, reactants, or product species at pore or exterior surface sites.

Despite the broad importance of surface interactions in determining material properties, fundamental questions remain regarding the physiochemical interactions at surfaces that determine crystallization, adsorption, optoelectronic, and/or reaction properties. This is because such properties often depend on dilute surface moieties, defect species, and/or molecular adsorbates that occupy distributions that are partially- or non-ordered and are therefore challenging or impossible to characterize by conventional scattering techniques. Developing atomic-level insights into the types, interactions, and distributions of such dilute non-ordered species is crucial to elucidate the molecular-level origins of the properties and

synthesis pathways of materials such as zeolites, semiconductor nanoparticles, and mesoporous electrocatalysts. By understanding the crystallization, synthesis, and assembly processes of these materials, as well as the resulting structures and active species, the resulting insights can be applied to develop new synthetic or post-synthetic treatments to generate more effective, stable, and/or active materials with desirable properties.

The objective of this dissertation is to measure, understand, and correlate the atomic-scale compositions, structures, and properties of heterogenous materials with diverse applications, including heterogeneous catalysis and solid-state lighting. Recently-developed solid-state nuclear magnetic resonance (NMR) techniques with complementary X-ray diffraction and electron microscopy analyses are applied to elucidate the structures and compositions of dilute surface, defect, or heteroatom species, which are correlated to the macroscopic properties of interest. These techniques are applied to analyze diverse heterogeneous inorganic nanomaterials, including aluminosilicate zeolites, cementitious solids, precious-metal-free electrocatalysts, and nanocrystalline semiconductors. Though the material systems vary in composition and application, in each case the important optical, electronic, and/or catalytic properties arise from dilute partially- or non-ordered defect or heteroatom species in a semi-crystalline lattice. The overall unifying themes are: (1) analysis of order and disorder in semi-crystalline inorganic solids using state-of-the-art diffraction and spectroscopic characterization techniques; (2) determining the distributions and structures of non-stoichiometric species, particularly at surfaces and interfaces; and (3) correlating atomic-level structures and compositions with macroscopic material properties. The insights provided are of broad importance and relevance to diverse material systems of technological interest for sustainable energy storage, conversion, and utilization.

TABLE OF CONTENTS

Acknowledgements iv

Curriculum vitae vii

Abstract xi

Table of contents xiii

List of figures xx

1. Introduction, background, and scope 1

1.1 Motivation and objections 1

1.2 Aluminosilicate zeolite catalysts 4

1.2.1 Crystallization of mesoporous (alumino)silicate zeolite catalysts 7

1.2.2 Deactivation processes of aluminosilicate zeolites 11

1.3 Network formation in inorganic polymer binders 13

1.4 Non-precious-metal-containing electrocatalysts 16

1.5 The historical pigment Maya Blue 19

1.6 Heavily-doped nanocrystalline semiconductors 21

1.7 Experimental approaches 22

1.7.1 Solid-state nuclear magnetic resonance 23

1.7.2 Dynamic-nuclear-polarization-enhanced NMR 25

1.8 References 27

2. Non-topotactic transformation of silicate nanolayers into mesostructured MFI zeolite frameworks during crystallization 32

2.1 Abstract 32

2.2 Introduction 33

2.3 Results and discussion 37

2.4 Conclusions 45

2.5 Materials and methods 47

2.6 References 48

3. Well-defined silanols in the structure of the calcined high-silica zeolite SSZ-70 50

3.1 Abstract 50

3.2 Introduction 51

3.3 Results and discussion 55

3.3.1 Long-range order in Si-SSZ-70 55

3.3.2 Relationship between SSZ-70 and ITQ-1 58

3.3.3 Initial structural model of calcined SSZ-70 59

3.3.4 Model 1 or Model 2? 61

3.3.5 Structure of calcined SSZ-70 69

3.3.6 Catalytic aspects 70

3.4 Conclusions 71

3.5 Materials and methods 73

3.6 References 76

4. Preferential siting of Al heteroatoms in the zeolite catalyst Al-SSZ-70 79

4.1 Abstract 79

4.2 Introduction 80

4.3 Results and discussion 83

4.3.1 ^{29}Si environments in calcined Si- and Al-SSZ-70 83

4.3.2 ^{27}Al-O-^{29}Si T-site connectivities in calcined Al-SSZ-70 85

4.3.3 Strong hydrogen bonds in calcined Al-SSZ-70 90

4.3.4 Isotropic ^{27}Al chemical shifts in calcined Al-SSZ-70 92

4.3.5 Positions of Al heteroatoms in Al-SSZ-70 98

4.4 Conclusions 100

4.5 Materials and methods 101

4.6 References 104

5. Hydrocarbon adsorption, reaction, and deactivation sites in aluminosilicate USY zeolite catalysts 107

5.1 Abstract 107

5.2 Introduction 108

5.3 Results and discussion 110

5.3.1 Long-range and local order in 'ultrastable' Y zeolite catalyst materials 110

5.3.2 Molecular interactions of toluene and methanol with H^+-USY zeolite frameworks 116

5.3.3 Toluene alkylation reaction properties of H^+-USY 121

5.3.4 Types and interactions of deactivation products in post-reaction USY zeolite catalysts 123

5.3.5 Direct identification of H^+-USY deactivation sites 126

5.4 Conclusions 127

5.5 Materials and methods 129

5.6 References 132

6. Network formation and strength development in alkali-activated aluminosilica cements 135

6.1 Abstract 135

6.2 Introduction 136

6.3 Results and discussion 140

6.3.1 Morphology and long-range order in alkali-activated IPBs 140

6.3.2 Local ^{1}H, ^{27}Al, and ^{29}Si environments in alkali-activated IPB networks formed at early reaction times 142

6.3.3 Atomic-scale rearrangements of the aluminosilica networks 147

6.4 Conclusions 151

6.5 Materials and methods 153

6.6 References 154

7. Atomic-scale origins of oxygen reduction activity in non-precious-metal mesoporous Fe,N-carbon electrocatalysts with high N contents 156

7.1 Abstract 156

7.2 Introduction 157

7.3 Results and discussion 160

7.3.1 Synthesis, surface compositions, and long-range order of mesoporous high-N-content carbon electrocatalysts 160

7.3.2 Electrocatalytic activities of mesoporous Fe,N-carbon electrocatalysts 164

7.3.3 Local ^{15}N heteroatom environments in mesoporous high-N-content carbon electrocatalysts 166

7.3.4 Structure and ^{15}N and ^{57}Fe heteroatom environments of mesoporous Fe,N-carbon electrocatalysts 171

7.4 Conclusions 176

7.5 Materials and methods 177

7.6 References 182

8. Atomic-scale compositions and structures that account for the stability of the historic pigment Maya Blue 185

8.1 Abstract 185

8.2 Introduction 186

8.3 Results and discussion 187

8.3.1 Synthesis, long-range order, and morphology of Maya Blue 187

8.3.2 Framework-indigo interactions in Maya Blue 190

8.4 Conclusions 199

8.5 Materials and methods 201

8.6 References 204

9. Spatially correlated distributions of local metallic properties in bulk and nanocrystalline GaN 206

9.1 Abstract 206

9.2 Introduction 207

9.3 Results and discussion 209

9.3.1 Bulk polycrystalline GaN:Ge 209

9.3.2 Korringa T_1 relaxation of ^{71}Ga in GaN:Ge 212

9.3.3 Photoluminescence properties, ^{71}Ga Knight shifts and Korringa-type T_1 relaxation in nanocrystalline GaN 214

9.3.4 Spatial correlation of ^{71}Ga and ^{15}N Knight shifts 218

9.3.5 Likely shallow donors in nanocrystalline GaN 221

9.4 Conclusions 223

9.5 Materials and methods 224

9.6 References 228

10. Conclusions and outlook 230

A1. Ultrathin mordenite crystals synthesized using cooperative organic structure-directing agents 235

A1.1 Abstract 235

A1.2 Introduction 235

A1.3 Results and discussion 238

A1.3.1 Synthesis and morphology of mordenite crystallites prepared using cooperative OSDAs 238

A1.3.2 Quantifying and locating the organic structure-directing molecules 240

A1.3.3 Site-specific organic-inorganic interactions in mordenite prepared using cooperative OSDAs 243

A1.3.4 Catalytic properties of ultrathin mordenite 246

A1.4 Conclusions 248

A1.5 Materials and methods 248

A1.6 References 254

A2. Colloidal F:In_2O_3 cubes: Fluorine-induced faceting and infrared plasmonic response 258

A2.1 Abstract 258

A2.2 Introduction 259

A2.3 Results and discussion 261

A2.3.1 Synthesis and shape behavior of F:In_2O_3 cubes 261

A2.3.2 Influences of fluorine on F:In_2O_3 nanocrystal shape 263

A2.3.1 Fluorine as an anionic dopant 271

A2.3.1 Optical Properties of F:In_2O_3 NCs 280

A2.4 Conclusions 283

A2.5 Materials and methods 284

A2.6 References 289

LIST OF FIGURES

1.1. *Framework structures of the zeolites studied in this dissertation*..... 5

1.2. *Schematic of a zeolite catalyst pellet and surface structure*..... 12

1.3. *Dissolution, reprecipitation, and condensation processes involved in inorganic polymer binder formation*..... 16

1.4. *The Cacaxtla Mural from Tlaxcala, Mexico (600-950 C.E.), an historical example of the Maya Blue pigment*..... 19

1.5. *Polarization transfer pathways in DNP-NMR experiments*..... 26

2.1. *XRD patterns, ^{29}Si CP-MAS NMR spectra, and TEM images of intermediate products of hydrothermal MFI-type zeolite nanosheet crystallization*..... 35

2.2. *Schematic structures of 2D nanolayered siicates and the MFI zeolite framework structure*..... 35

2.3. *2D ^{29}Si{^{29}Si} DNP-J-mediated correlation spectrum and SEM and TEM images of the intermediate product of MFI zeolite nanosheet crystallization after 8.5 days of hydrothermal synthesis*..... 39

2.4. *2D ^{29}Si{^{29}Si} dipolar- and DNP-J-mediated correlation spectrum and TEM images of the intermediate product of MFI zeolite nanosheet crystallization after 10 days of hydrothermal synthesis*..... 42

2.5. *2D ^{29}Si{^{29}Si} J-mediated correlation spectrum of 99% ^{29}Si-labeled MFI zeolite nanosheets after 13 days of hydrothermal synthesis*..... 46

2.6. *Schematic depiction of the non-topotactic rearrangement and condensation of 2D nanolayered silicates to form MFI zeolite nanosheets*..... 47

3.1. *N,N'-diisobutyl imidazolium cation used as the organic structure-directing agent in the syntheses of SSZ-70* 52

3.2. *Representative SEM image of as-synthesized SSZ-70* 54

3.3. *Synchrotron XRPD patterns of as-synthesized and calcined Si- and Al-SSZ-70* 56

3.4. *HRTEM images of as-synthesized Al-SSZ-70* 57

3.5. *Schematic representations of ITQ-1p, ITQ-1, and calcined SSZ-70* 59

3.6. *Schematic of the interlayer regions of calcined Si-SSZ-70* 60

3.7. *2D $^{29}Si\{^{1}H\}$ DNP-HETCOR spectra of calcined Si-SSZ-70* 64

3.8. *2D $^{29}Si\{^{29}Si\}$ DNP-J-mediated correlation and quantitative 1D single-pulse ^{29}Si MAS NMR spectra of calcined Si-SSZ-70* 65

3.9. *Observed and simulated synchrotron powder XRD patterns for calcined Si-SSZ-70* 69

3.10. *Effective pore diameter of the interlayer channel in calcined SSZ-70* 70

4.1. *SEM image, synchrotron powder XRD patterns, and framework structure of Al-SSZ-70* 83

4.2. *1D ^{29}Si MAS NMR spectra of calcined Si- and Al-SSZ-70* 85

4.3. *2D $^{27}Al\{^{29}Si\}$ J-mediated NMR heteronuclear correlation spectrum of calcined Al-SSZ-70 acquired at 18.8 T* 88

4.4. *2D $^{27}Al\{^{29}Si\}$ J-mediated NMR heteronuclear correlation spectrum of calcined Al-SSZ-70 acquired at 9.4* 89

4.5. *2D $^{27}Al\{^{1}H\}$ HETCOR spectrum of calcined Al-SSZ-70* 91

4.6. *2D $^{29}Si\{^{1}H\}$ HETCOR spectra of calcined Si- and Al-SSZ-70* 93

4.7. *2D ^{27}Al MQMAS spectrum of calcined Al-SSZ-70 acquired at 18.8 T and 295 K* 94

4.8. *2D ^{27}Al MQMAS spectrum of calcined Al-SSZ-70 acquired at 9.4 T and 298 K or 93 K* 98

4.9. *1D quantitative single-pulse ^{27}Al spectrum of calcined Al-SSZ-70 and positions of Al heteroatoms* 100

5.1. *Structure and long-range order of USY zeolite catalysts* 111

5.2. *1D ^{29}Si MAS NMR spectra of USY zeolite catalysts* 114

5.3. *2D ^{27}Al{^{29}Si} J- and dipolar-mediated NMR correlation spectra of H^+-USY* 115

5.4. *2D ^{13}C{^{29}Si} and ^{27}Al{^{13}C} correlation spectra of methanol-adsorbed H^+-USY* 118

5.5. *2D ^{13}C{^{29}Si} correlation spectrum of toluene-adsorbed H^+-USY* 120

5.6. *Schematic diagram of toluene methylation reactor setup* 122

5.7. *Product distributions for toluene alkylation with methanol catalyzed by H^+-USY* 124

5.8. *2D ^{13}C{^{1}H} DNP-HETCOR spectra of post-reaction H^+-USY* 125

5.9. *2D ^{13}C{^{29}Si} and 1D ^{27}Al{^{13}C} correlation spectra of post-reaction H^+-USY* 128

6.1. *Schematic diagram of the coupled and transient processes involved in IPB formation* 139

6.2. *XRD patterns and SEM images of alkali-activated IPBs formed after reaction times of 24, 72, and 384 h* 141

6.3. *Solid-state 1D single-pulse ^{27}Al MAS NMR spectra of alkali-activated IPBs formed after reaction times of 24, 72, and 384 h* 143

6.4. *Solid-state 2D $^{29}Si\{^{1}H\}$ DNP-HETCOR spectra of alkali-activated IPBs formed after reaction times of 24 and 72 h* 147

6.5. *Solid-state DNP-enhanced 2D $^{27}Al\{^{29}Si\}$ dipolar-mediated correlation spectra of alkali-activated IPBs formed after reaction times of 24, 72, and 384 h* 149

6.6. *Schematic diagram of the aluminosilica IPB network formed in highly alkaline media at early reaction times* 152

7.1. *Schematic diagram of the synthesis of the mesoporous Fe,N-containing electrocatalysts* 161

7.2. *XRD patterns, Raman spectra, and TEM images of high-N-content mesoporous carbon materials* 164

7.3. *Electrocatalytic potential curves for the mesoporous Fe,N-carbon materials* 165

7.4. *Solid-state 2D $^{13}C\{^{15}N\}$ correlation and 1D single-pulse ^{15}N MAS NMR spectra of mesoporous high-N-content carbon materials* 170

7.5. *XRD pattern and Raman spectrum of the mesoporous Fe,N-carbon material* 172

7.6. *Solid-state relaxation-resolved ^{15}N MAS NMR and ^{57}Fe Mössbauer spectra of the mesoporous Fe,N-carbon material* 174

8.1. *Synthesis and acid stability of Maya Blue* 188

8.2. *XRD patterns and electron microscopy images of Maya Blue and palygorskite* 190

8.3. *^{1}H environments and indigo-framework interactions in Maya Blue established by 1D and 2D ^{1}H NMR at high fields and fast MAS* 193

8.4. *Solid-state 2D ^{29}Si{^{1}H} and ^{13}C{^{1}H} DNP-HETCOR spectra of Maya Blue* 196

8.5. *Relative surface proximities of indigo/dehydroindigo and indoxyl molecules in Maya Blue determined by DNP-NMR signal intensity buildup times* 200

9.1. *^{71}Ga and ^{14}N MAS NMR spectra of GaN:Ge* 211

9.2. *^{71}Ga Korringa relaxation in GaN:Ge* 214

9.3. *XRD patterns, TEM images, and photoluminescence spectra of nanocrystalline GaN* 216

9.4. *^{71}Ga MAS NMR spectra of nanocrystalline GaN* 217

9.5. *Korringa T_1 relaxation in nanocrystalline GaN* 217

9.6. *2D ^{15}N{^{71}Ga} NMR correlation spectrum of nanocrystalline GaN* 220

A1.1. *Structures, SEM images, and XRD patterns of SSZ-13, ZSM-5, and mordenite (HOU-4)* 239

A1.2. *TEM images, SAED, and AFM analyses of ultrathin mordenite crystallites* 240

A1.3. *OSDA and Na^{+} positions in mordenite (HOU-4) from synchrotron PXRD analysis* 241

A1.4. *Quantitative 1D single-pulse ^{13}C MAS NMR spectrum of HOU-4* 242

A1.5. *2D $^{27}Al\{^{29}Si\}$, $^{27}Al\{^{1}H\}$, and $^{13}C\{^{1}H\}$ spectra of HOU-4* 244

A1.6. *Quantitative 1D single-pulse ^{29}Si and $^{29}Si\{^{1}H\}$ CPMAS spectra of HOU-4* 246

A1.7. *Comparison of catalytic properties of H-HOU-4 and conventional H-mordenite for cumene cracking* 247

A2.1. *Synthesis, morphology, and atomic positional order of F:In_2O_3 NCs* 262

A2.2. *XPS of F:In_2O_3 NCs and DFT simulations of surface F environments* 264

A2.3. *1D ^{19}F echo and 2D $^{1}H\{^{29}F\}$ correlation NMR spectra of F:In_2O_3 NCs* 268

A2.4. *Quantitative 1D single-pulse ^{19}F MAS NMR spectrum of F:In_2O_3 NCs* 270

A2.5. *^{19}F Knight shifts and Korringa T_1 relaxation in F:In_2O_3 NCs* 274

A2.6. *MAS and temperature dependences of ^{19}F T_1 relaxation times in F:In_2O_3 NCs* 276

A2.7. *Wideline ^{115}In solid-state NMR spectra of undoped and F-doped In_2O_3* 247

A2.8. *FTIR spectra of F:In_2O_3 NCs and STEM-EELS maps of edge and corner LSPR modes* 281

Chapter 1. Introduction, background, and scope

1.1 Motivation and objectives

With the environmental and economic challenges facing the world today, it is clear that the future will rely on the development of new technologies that can provide, convert, store, and utilize energy in a sustainable fashion. To meet the goal of long-term sustainability for the entire world, the US National Academy of Engineering has issued a list of fourteen 'Grand Engineering Challenges," which include removal of CO_2 from the atmosphere (or mitigation of its release) and improved storage and utilization of solar energy.[1] The processes by which we capture, store, and utilize energy (from renewable or conventional resources) rely on materials with relevant adsorption, catalytic, or optoelectronic properties that have been optimized for these applications. For example, much of our liquid fuels for transportation applications are produced by catalytic cracking of heavy oil feedstocks, which use heterogeneous solid-acid catalysts comprised in part of nanoporous zeolites.[2] Zeolites are also important for numerous separation, catalytic, and environmental remediation processes including separation of oxygen and nitrogen in air,[3,4] adsorption of pollutants from water,[5,6] processing of cellulosic plant byproducts to biofuels,[7,8] removal of gas-phase pollutants,[9] and capture/sequestration of carbon dioxide.[10,11] Current commercial solar-to-electrical energy conversion and high-efficiency lighting processes utilize doped semiconductors that adsorb or emit light at UV, visible, or IR wavelengths. Semiconductors with controllable features on the nanoscale such as nanoparticles, nanosheets, and hierarchical nanostructures are emerging for commercial applications including solar cells,[12] photocatalysts,[13,14] and light emitting diodes (LEDs).[15,16] Engineering new energy technologies requires a detailed understanding of the physiochemical origins of the properties of such nanostructured

materials. By obtaining fundamental insights into the atomic-level origins of the macroscopic properties of materials for energy conversion, utilization, and storage, new design rules can be developed for engineering materials with improved efficiencies and desirable properties to meet the grand engineering challenges of the 21st century.

Many important material properties are determined by the surface layer (0.5-100 nm). These include optoelectronic properties like conductivity, absorptivity, and reflectance[17] as well as physiochemical properties such as molecular adsorption,[18] hydrophobicity,[19,20] and surface diffusivity.[21] Furthermore, the crystallization or assembly processes of technologically-important nanomaterials are mediated by surface interactions and influence the surface compositions and properties of the resultant material, e.g. zeolites,[22,23] colloidal semiconductors,[24,25] carbon-based electrocatalysts,[26,27] and mesoporous inorganic oxides.[28,29] Catalytic reaction properties of diverse porous heterogeneous materials are determined by the molecular interactions of adsorbates, reactants, or product species at pore or exterior surface active sites.[30]

Despite the broad importance of surface interactions in determining material properties, fundamental questions remain regarding the physiochemical interactions at surfaces that determine the crystallization, adsorption, optoelectronic, and/or reaction properties. This is because such properties are often determined by dilute surface moieties, defect species, and/or molecular adsorbates that occupy distributions that are partially- or non-ordered and are therefore challenging or impossible to characterize by conventional scattering techniques. Developing atomic-level insights into the types, interactions, and distributions of such dilute non-ordered species is crucial to elucidate the molecular-level origins of the properties and synthesis pathways of materials such as zeolites, semiconductor nanoparticles, and carbon-

based electrocatalysts. For example, many important technological materials, including biominerals, nanoparticles, zeolites, and organic systems,[31] are now recognized to crystallize through complex non-classical pathways, which yield distributions of surface active sites that govern their macroscopic properties. By understanding the crystallization, synthesis, and assembly processes of these materials, as well as the resulting structures and active species, the resulting insights can be applied to develop new synthetic or post-synthetic treatments to generate more effective, stable, or active materials targeted to exploit specific structural features with desirable properties.[32]

The objective of this dissertation is to measure, understand, and correlate the atomic-scale compositions, structures, and properties of heterogenous materials with diverse applications, including as catalysts, structural materials, and optoelectronic materials. The present chapter provides a brief introduction of each of the material systems discussed in subsequent chapters in this dissertation. The last section of this chapter provides an overview of the experimental techniques used throughout the work presented here. Chapters 2 and 3 elucidate the structures and crystallization processes of recently-developed zeolite molecular sieves, specifically MFI-type mesoporous zeolite nanosheets and the zeolite catalyst SSZ-70. Chapters 4 and 5 report newly-developed solid-state nuclear magnetic resonance (NMR) techniques to determine the distributions and molecular interactions of heteroatom active sites in zeolite Al-SSZ-70 and Y catalysts, which are correlated to the macroscopic catalytic reaction properties. Chapter 6 explores the molecular-scale dissolution, precipitation, and condensation processes that yield non-ordered metal oxide inorganic polymer binders under highly alkaline conditions, which are attractive as low-CO_2 cementitious materials. Chapter 7 elucidates the active sites of mesoporous iron- and nitrogen-containing carbon materials with

very high activities for the oxygen reduction reaction and applications as fuel cell electrocatalysts. Chapter 8 shows that the stability of the historical pigment Maya Blue arises from strong hydrogen bonding interactions between an inorganic framework and dilute organic dye molecules. Chapter 9 correlates the atomic-scale electronic environments and the macroscopic optoelectronic properties of nanocrystalline gallium nitride materials. Though the material systems discussed in this dissertation vary in composition and application, in each case their important structural, optoelectronic, and/or catalytic properties arise from partially- or non-ordered defect, dopant, and/or heteroatom species in a semi-crystalline lattice. Structural insights into such non-ordered but important species have been severely limited in the past, but are enabled here by state-of-the-art solid-state NMR techniques, complemented by X-ray and electron diffraction techniques and correlations to the macroscopic materials properties of interest. The insights provided here are of broad importance and relevance to diverse material systems of technological importance.

1.2 Aluminosilicate zeolite catalysts

Aluminosilicate zeolites are porous nanostructured inorganic materials that are of high industrial interest because of their well-defined nanopore dimensions (<1 nm), high surface areas, and framework ion-exchange sites, which enable diverse applications including in air-gas separation,[4,33] water purification,[5] and heterogeneous catalysis.[2] Aluminosilicate zeolites are composed of corning-sharing SiO_4^{2-} that are partially substituted by AlO_4^{3-} tetrahedra. This substitution introduces negative framework charges associated with the Al species that may be balanced by exchangeable cations, which can introduce strong Brønsted (for H^+) or Lewis (e.g., La^{3+}) acid species that act as molecular adsorption/reaction sites. The different

well-defined framework structures (see Figure 1 for examples), high surface areas, and active sites of aluminosilicate zeolites enable diverse applications as heterogeneous catalysts, including for hydrocarbon rearrangement reactions[34–36] and removal of pollution from automotive exhaust streams.[37,38] By adjusting the framework composition of zeolite catalysts using synthetic or post-synthetic methods, the density and nature of the catalytic sites can be influenced to generate different types of catalytic reaction centers.[36,39,40] As zeolite frameworks are composed of earth-abundant elements (e.g., Si, Al, O, B), zeolite catalysts are attracting attention as replacements for expensive precious-metal catalysts (e.g., Pt, Ir, Rh), which are currently used for applications such as pollution removal. When zeolite catalysts are used as supports for precious metal catalysts, their high surface areas and well-defined nanopore/nanochannel systems can enable high dispersion and accessibility of reaction sites even for very low precious metal loadings.[41]

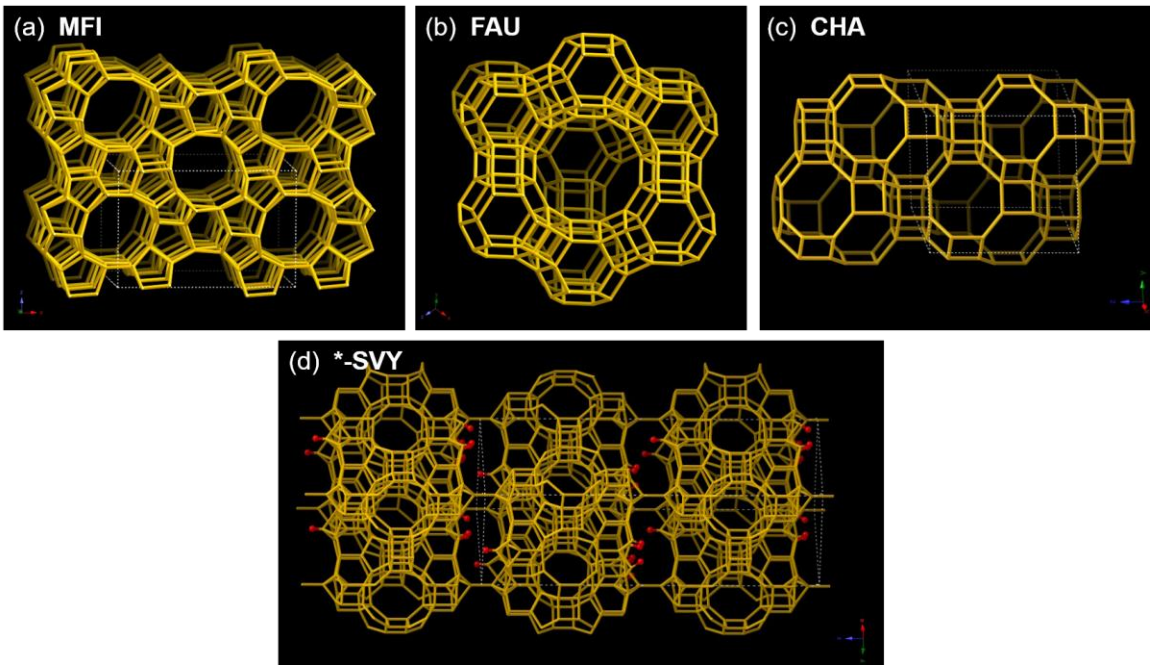

Figure 1.1. Framework structures of several zeolites discussed in this dissertation: (a) the **MFI** framework structure of zeolites ZSM-5 and silicalite, (b) the **FAU** framework structure of zeolite Y (faujasite), (c) the **CHA** framework structure of zeolite SSZ-13 (chabazite), and

(d) the ***-SVY** framework structure of zeolite SSZ-70. In these representation, each vertex is a tetrahedral site that may be occupied by a Si or Al atom, while each line is a bridging oxygen atom. The red dots in (d) represent hydroxyl groups associated with incompletely-crosslinked species. The schematic structures were adapted from the databases of the International Zeolite Association.[42]

The molecular diffusion, reaction, and adsorption properties of aluminosilicate zeolite catalysts are strongly influenced by the dimensions of the nanopores, the aluminosilicate framework architectures, and the types and distributions of heteroatom sites (e.g, Al) and associated cations. Understanding and controlling heteroatom distributions in zeolite catalysts has been severely limited by the non-stoichiometric substitution of heteroatoms into the framework and their complicated distributions, which can be challenging to characterize. Determining the types and distributions of Al heteroatom sites in different zeolite frameworks has been a long-standing challenge in correlating their local compositions to the macroscopic adsorption and/or catalytic reaction properties.

Heteroatom distributions in zeolites have long been recognized to depend strongly on synthesis conditions, including the compositions of the precursor materials and organic and inorganic structure directing cations.[43] Information on heteroatom distributions in zeolites has been accessed previously in favorable cases utilizing several different scattering and spectroscopic techniques, generally requiring combinations of methods. Different Al heteroatom sites in 8-member ring (MR) and 12-MR environments may be identified by deconvolution of Fourier transform infrared (FTIR) spectra of dehydrated zeolite frameworks,[44] though such spectra are generally poorly resolved and the resulting assignments inconclusive. While the similar electron densities of Al and Si atoms make distinguishing them through diffraction or scattering techniques challenging,[45] Al occupancies at different tetrahedral (T) sites have been determined for large single crystals of

the zeolite mineral scolecite by synchrotron X-ray standing wave diffraction.[46] For as-synthesized zeolites containing organic structure directing agents that orient preferentially with respect to specific heteroatom sites, information on framework Al distributions may be extracted by the refinement of synchrotron X-ray diffraction data, for example as has been demonstrated for ferrierite zeolite[47] and systematically for a series of borosilicate zeolites.[48] Relative positions and proximities of Al atoms and their associated cations within chabazite zeolite materials have been determined through the adsorption of probe molecules such as CO and NO, paired with FTIR spectroscopy.[49] Exchange of aluminosilicate zeolites with divalent cations such as Co^{2+}, paired with ultraviolet-visible (UV-vis) spectroscopy enables quantification of Al heteroatom pairs that are positioned within the same aluminosilicate rings.[50] Several synthetic techniques for influencing heteroatom distributions in zeolites have been established, including exchange of B heteroatoms for Al, which can lead to preferential siting of Al at surface sites.[51] In favorable cases, Al distributions may be influenced by the careful selection of organic structure directing agent and synthesis conditions, as has been demonstrated for ferrierite[47] and chabazite.[39,52]

Developing new insights into the siting of Al heteroatoms in aluminosilicate zeolite frameworks remains important and is of high interest, especially for recently-developed molecular sieves that exhibit promising catalytic properties. One such material is the **MWW**-type zeolite SSZ-70,[53] which exhibits interesting molecular adsorption and hydrocarbon conversion characteristics[54] and has been developed as a versatile synthetic platform for diverse heterogeneous catalyst materials.[55]

1.2.1 Crystallization of mesoporous (alumino)silicate zeolite catalysts

Design of zeolite catalyst materials with improved mass transport properties requires new synthetic protocols. Zeolites are typically prepared under alkaline hydrothermal conditions from solution- or solid-phase silicate and aluminate sources in the presence of cationic structure directing agents (SDAs). Zeolite frameworks form through co-assembly of the (alumino)silicate species and the SDAs, which may be inorganic (e.g., Na^+, K^+) or organic.[56] By varying the composition of the synthesis mixture, including the type and molecular architecture of the SDA species, a range of different zeolite framework structures have been generated. As of December, 2018, 245 different zeolite framework structures have been reported and assigned unique framework codes by the International Zeolite Association.[42] Recent efforts in prediction of hypothetical zeolite frameworks have indicated that millions of unique structures are theoretically stable,[57,58] many of which may be of industrial interest if synthetic routes can be developed. Discovery of new zeolite materials and optimization of their structures and properties has been largely empirical in past decades, with more effort recently on rational design of desirable zeolite structures with specific properties.[32,59]

In particular, recent synthetic and post-synthetic protocols have focused on preparation of zeolites with hierarchical structures including pore size diameters that are in both the meso range (1-100 nm) and sub-nanometer range. A notable example by Ryoo and coworkers is the synthesis of mesostructured zeolitic nanosheets with crystallite thicknesses as small as a single unit cell[22] and with controllable mesopore diameters of 1-50 nm.[60] Such mesostructured zeolite nanosheets are prepared by using organic SDA species with charged imidazolium moieties that direct the assembly of the crystalline zeolite framework and with long alkyl chains that guide the mesoscale ordering. Mesostructured zeolite nanosheets

exhibit improved catalytic properties and lifetimes for reactions involving large molecules, including catalytic cracking,[22] due to reduced mass transport limitations and improved accessibility of the mesopore and nanopore surface active sites.[61] The initial discovery of mesostructured zeolitic nanosheets has sparked great interest in development of new zeolite synthesis methods to prepare different mesostructured catalyst materials with different framework structures and mesopore diameters for diverse industrial applications. Development of new mesostructured zeolite materials requires detailed understanding of the hydrothermal co-assembly processes of the organic and inorganic components and corresponding development of the mesoscopic and atomic order during the synthesis of such mesostructured zeolites. However, the assembly processes of mesostructured zeolite nanosheets have previously been poorly understood and debated. In general, zeolites crystallize through coupled classical and non-classical pathways, including dissolution/reprecipitation, particle-attachment, Ostwald ripening, and solid-state transformation.[23,31]

In Chapter 2 of this dissertation, mesostructured MFI-type zeolite nanosheets are demonstrated to assemble through non-topotactic condensation and solid-state transformation of intermediate nanolayered silicate species during the hydrothermal crystallization. Such non-topotactic transformations involve subtle atomic-level rearrangement and condensation processes that are challenging to elucidate, but are resolved here by powerful solid-state NMR measurements, with sensitivity enhanced by dynamic-nuclear-polarization (DNP). The new insights provided on the crystallization mechanisms of such important zeolite catalyst materials offer new means to adjust their synthesis and assembly processes, resultant

structures, and correspondingly their macroscopic adsorption and catalytic reaction properties.

A second class of recently-developed mesoporous zeolitic nanosheets are derived from zeolites materials comprised of **MWW**-type layers such as ITQ-1, MCM-22, and SSZ-70. These **MWW**-type zeolites are synthesized through zeolitic layered silicate precursors that condense on calcination, forming three-dimensional nanoporous (0.74 nm pore diameter) zeolite frameworks. Alternatively, the layered silicate precursor materials can be delaminated and exfoliated, yielding lamellar zeolite nanosheets with large accessible surface areas (~700 m^2/g), with emerging catalytic applications for hydrocarbon cracking, alkylation, and olefin metathesis reactions.[54,55,62,63] However, the complicated interlayer structures of the layered silicate precursor materials have long eluded characterization. In the case of SSZ-70, the complete 3D zeolite structure formed on calcination was also previously unknown. Detailed understanding of the local compositions and structures of the zeolite interlayer regions is crucial in order to understand and improve the catalytic properties of zeolites derived from SSZ-70, which rely on the interlayer surfaces exposed on delamination. In Chapter 3 of this dissertation, the structure of the calcined form of SSZ-70 is determined by a combination of high-resolution transmission electron microscopy, synchrotron X-ray powder diffraction (XRD), and solid-state NMR analyses. Notably, 2D DNP-enhanced solid-state NMR spectra establish two types of silanol groups in the interlayer channel regions, the presence of which helps explain the catalytic properties of SSZ-70-derived materials and provides new targets for design of future catalysts. The aluminosilicate form of calcined SSZ-70 is examined in Chapter 4 of this dissertation, where it is shown that Al heteroatoms are preferentially sited at specific framework sites at the interlayer channel surfaces of SSZ-70. Though the structures

of the incompletely-condensed layered precursors of SSZ-70 (and other **MWW**-type polymorphs such as ITQ-1 and MCM-22) are still under investigation, the detailed insights provided here on the interlayer structures and heteroatom positions in calcined SSZ-70 are expected to further the understanding of the structures, properties, and applications of these important catalytic materials.

A different approach to improving internal mass transport properties in zeolites is adjusting synthetic conditions to tailor crystal properties for optimal performance. Various approaches have been explored to precisely tune the anisotropic growth of zeolite crystals, including the alteration of synthesis conditions, though achieving materials with well-controlled properties is often challenging owing to the complex and poorly understood mechanisms of zeolite crystallization. In Appendix A1 of this disseration, a combination of high resolution characterization and modeling methods are applied to examine the role of OSDAs in the formation of ultrathin (<100 nm) mordenite crystallites, which are typically difficult to prepare with sub-micron dimensions.

1.2.2 Deactivation processes of aluminosilicate zeolites

One of the most important applications of zeolites for heterogeneous catalysis is fluidized catalytic cracking (FCC), where high-molecular-weight heavy oil feedstocks are converted to lower-molecular-weight hydrocarbons, including C6-C8 alkanes used as automotive fuels (gasoline).[2,64] In FCC processes, large bulky polyaromatic reactants are cracked through a series of thermal and acid-catalyzed processes to distributions of smaller hydrocarbons. Though mesostructured zeolite catalyst materials such as those discussed above are finding emerging applications for FCC, the most common industrial practice for

introducing mesoporosity into zeolite catalyst particles is steam treatment, which results in fissuring of the zeolite particles and dealumination of the framework, generating non-ordered mesopores and complex distributions of framework and extraframework heteroatom species (Figure 2).[65–67] Under high-temperature FCC reaction conditions (typically 500-600 °C), aromatic intermediate species oligomerize at the zeolite particle surfaces and within the zeolite nanochannels, forming polyaromatic carbonaceous deposits (coke) that inhibit diffusion through the zeolite nanopores and block access to framework active sites. For FCC applications, the formation of surface-adsorbed coke and corresponding deactivation of the catalyst materials occurs on millisecond time scales.[2,68] In industrial FCC processes, FCC catalyst pellets deactivated in this way are regenerated by combustion of the adsorbed coke, which also generates the heat required for the endothermic cracking reactions. Combustion of coke in FCC catalyst regenerators is responsible for the release of ~100 million tons of CO_2 every year.[2]

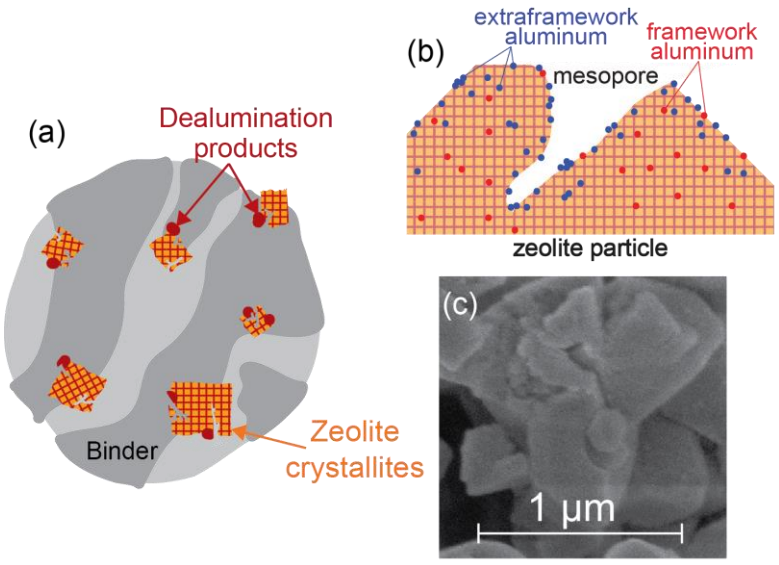

Figure 1.2 Schematic diagram of (a) an FCC catalyst pellet containing zeolite microcrystals embedded in a porous binder and (b) a zeolite particle surface, showing a mesoporous fissure and the distributions of framework and extraframework aluminum species generated on steam-aging. (c) A representative SEM image of steam-aged Y zeolite particles.

To reduce the environmental impact and improve the efficiency and selectivity of FCC processes requires molecular insights into the deactivation processes to develop new synthetic or post-synthetic protocols for improved catalyst lifetime and stability. In Chapter 5 of this dissertation, the molecular organic-inorganic interactions of adsorbed coke species and aluminozeolite catalyst materials are elucidated using powerful sensitivity-enhanced solid-state NMR techniques with complementary electron microscopy, X-ray diffraction, and catalytic reaction tests. Specifically, the steam-treatment processes are shown to generate different types of surface- and sub-surface Al heteroatom sites that have different molecular adsorption and reaction properties. Specific moieties associated with defect sites at the mesopore surfaces are shown to be particularly prone to adsorption of bulky reaction byproducts. These insights provide new design rules for the synthesis of new, highly stable zeolite catalysts.

1.3 Network formation in inorganic polymer binders

Aluminum, silicon, and oxygen are three of the most earth-abundant elements and compose a wide variety of natural and technological systems with diverse industrial applications in catalysis, structural materials, and separations.[33,69–71] The physiochemical and mechanical properties of aluminosilicate materials vary dramatically depending on their local structures and compositions, even for materials with similar bulk chemical compositions. By adjusting the synthesis conditions of aluminosilicate materials, different structures and properties can be achieved for different applications. For example, aluminosilicate zeolites (such as discussed above) and aluminosilica inorganic polymer binders (IPBs) are two types of highly condensed materials composed of non-stoichiometric corner-sharing AlO_4^- and

SiO_4^{2-} tetrahedra and charge-balancing cationic species (e.g., H^+, Na^+, Ca^{2+}, etc.), though which exhibit very different degrees of local and long-range order. While both zeolites and IPBs are formed by condensation of solid- or solution-phase aluminate and silicate species in aqueous media (e.g., gels or colloidal suspensions), they differ in their density and corresponding mechanical properties. Zeolites are generally formed under elevated pressures and temperatures and mildly alkaline solution conditions over intermediate time scales (hours-days), yielding well-defined nanoporous framework structures with high extents of long-range periodic ordering.[72–74] By comparison, IPBs are formed from partial dissolution, reprecipitation, and gradual condensation under highly alkaline conditions (*ca*. 16 M NaOH) of dense inorganic oxides such as fly ash, a waste product of coal combustion, or natural clays.[71] Under these reaction conditions, a network of polymerized aluminate and silicate tetrahedra forms and gradually condenses between the metal oxide particles over long timescales (days-months).

The condensation of the aluminosilica network in IPBs is concomitant with development of macroscopic compressive strength,[75] leading to interest in their application as new low-CO_2 structural materials. Conventional structural materials (e.g., ordinary Portland cement, OPC) are produced through high-temperature calcination of lime ($CaCO_3$), resulting in the release of 0.9 ton CO_2 per ton of cement produced and accounting for 8-10% of global anthropogenic CO_2 emissions. By comparison, IPB-based cements can be produced using common waste products (fly ash), releasing little to no CO_2 in their production. However, the current methods of IPB cement production are commercially untenable because of the very slow reaction kinetics and highly alkaline reaction conditions needed for the development of macroscopic strength. Slight variations in IPB precursor composition and crystallinity can

yield materials with compressive strengths ranging from relatively poor to almost three times greater than that of OPC.[76] In general, aluminosilicate networks, including those present in IPBs, are poorly understood because they are difficult to characterize.[77] The difficulty in preparing IPBs with desirable structural properties arises from a lack of molecular-level understanding of the formation and condensation processes of aluminosilica networks, as well as the relations between IPB structures, compositions, and the development of micro- and macroscopic compressive strength.[78]

In order to develop a fundamental understanding of the molecular changes occurring during dissolution, oligomerization, and condensation of IPBs and, more broadly, aluminate and silicate materials, state-of-the-art surface characterization techniques are applied to identify and understand the different molecular-level transformations that accompany silicate and aluminate dissolution, oligomerization, and condensation. In Chapter 6 of this dissertation, the early network formation of aluminosilica networks prepared from amorphous silica and alumina sources in strongly alkaline (6 M NaOH) reaction conditions is elucidated to obtain a detailed understanding of IPB network formation and evolution during the initial condensation and growth of the aluminosilica network. Tracking the evolution of such aluminosilica networks and the corresponding development of interparticle adhesion and macroscopic material strength has been challenging due to the heterogeneous surface compositions and small (~nm) particle-particle distances under realistic reaction conditions. Newly developed solid-state NMR techniques and advances in the surfaces forces apparatus (SFA) enable detection and correlation of atomic bonding and hydration environments in aluminosilica networks formed at different reaction times (hours to weeks) as well as elucidation of the nanoscopic interparticle adhesion energies and strength properties. *Ex-situ*

solid-state DNP-enhanced NMR techniques yield dramatic improvements in NMR signal intensity from particle surfaces. The signal enhancements provided by DNP-NMR enable acquisition of two-dimensional (2D) heteronuclear DNP-NMR correlation spectra that establish the nanoscale proximities and interactions of ^{1}H, ^{27}Al, and ^{29}Si species in the aluminosilica networks formed at different reaction times. The combined DNP-NMR and SFA analyses yield new insights into the development of strength in IPBs, with implications for improved control of the mechanical properties of low-CO_2 cements.

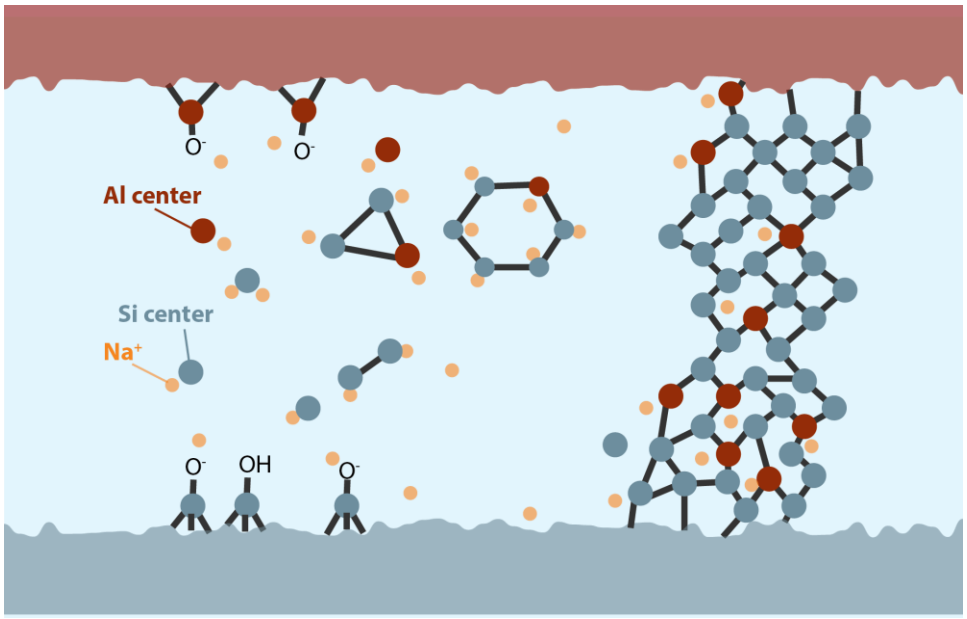

Figure 1.3. Schematic diagram showing the complex coupled and transient processes involved in dissolution and formation of inorganic polymer binders for silica (blue) and alumina (red) surfaces in highly alkaline conditions, including monomer detachment from the surfaces, solution-phase speciation and oligomerization, and reprecipitation of the condensed network.

1.4 Non-precious-metal-containing electrocatalysts

Carbon materials containing heteroatoms such as Fe and N have received significant attention in recent years as inexpensive and environmentally-inert materials for catalytic and electrochemical applications, such as electrodes,[79–81] electrocatalysts,[82–84] and catalyst

supports.[26,85,86] A promising application is in the electrochemical reduction of oxygen, where heteroatom-containing carbon materials have been proposed as replacements for Pt-based catalysts at the cathode of fuel cells.[87–90] Due to the poor selectivity and sluggish kinetics of the oxygen reduction reaction (ORR), conventional Pt-based catalysts (typically Pt supported on activated carbon) require very high Pt loadings (up to 15 wt%), which significantly increases the overall costs of fuel cells and has limited their applications.[91] By comparison, heteroatom-containing carbon electrocatalysts can be prepared inexpensively by high-temperature condensation of macrocycles or small molecule precursors,[92,93] and have been shown to exhibit properties approaching Pt/C under some reaction conditions.[94] Although inexpensive and scalable, the condensation reactions used to synthesize heteroatom-containing carbon materials are difficult to control and tend to result in materials with distributions of graphitic domain sizes[95] as well as types, quantities, and locations of nitrogen moieties.[96] In addition, high-temperature condensation-based methods generally lead to low quantities of retained heteroatoms, such as nitrogen, which introduce desired functional properties to the carbonized product materials.[97]

Previous work reported the preparation of a high-N-content (28 wt% N) carbon material, which also exhibited a moderately high conductivity of 2.0 S/cm.[98] The molecular precursors used to synthesize this material, urea and cyclohexanehexone octahydrate, were shown to form a low-melting eutectic phase and cross-link into materials with N moieties that resist volatilization during condensation at elevated temperatures. These features allowed facile preparation of high-surface-area, high-N-content, and porous carbon materials using either SBA-15 mesoporous silica or a mixture of $ZnCl_2$-NaCl salts as sacrificial templating agents.[98]

While the high N contents, high electrical conductivities, and high surface areas of these N- carbon materials are expected to make them attractive for use as fuel cell electrocatalysts, much remains unknown regarding the active moieties that catalyze oxygen reduction. For example, in different N-containing carbon materials, pyrrolic nitrogen,[99] pyridinic nitrogen,[95,99,100] and/or graphitic nitrogen[101,102] species have been proposed as ORR active sites. In carbon-based electrocatalyst materials prepared with both Fe- and N-containing precursors, the disorder in heteroatom-containing carbon materials has left the types and structures of the ORR active sites and the role of Fe open to debate. Some propose that Fe atoms act only to catalyze the formation of active nitrogen moieties[103] and others propose that Fe-containing moieties such as $Fe_2N_xC_y$[104] or porphyrinic planar FeN_4[90,105] species serve as electrocatalytic active sites. Indeed, different active moieties may be present to different extents in Fe,N-carbon materials as a result of different synthesis conditions and precursor compositions.

Chapter 7 of this dissertation reports the local environments of Fe and N active sites in high-surface-area mesoporous Fe,N-carbon materials with high heteroatom contents, which are correlated to the electrocatalytic activities. These insights are provided by comprehensive combined analyses including Mössbauer spectroscopy, X-ray diffraction, electron microscopy, and solid-state one- (1D) and two-dimensional (2D) ^{15}N and $^{13}C\{^{15}N\}$ NMR spectroscopy. The analyses elucidate the macroscopic electrocatalytic properties of the material, and show that electrocatalytic activity correlates to both the presence of isolated pyridinic N sites as well as square-planar iron porphyrrinic environments, suggesting that overall ORR activity may be improved by preparation of materials with a diversity of catalytically-active sites.

1.5 The historical pigment Maya Blue

Organic-inorganic interactions at nanostructured surfaces determine the macroscopic properties of diverse materials, including heterogeneous catalysts,[36,106] battery materials,[107] optoelectronic devices,[108,109] and biominerals.[110] An example of cultural and historic significance is the pigment Maya Blue, an organic-inorganic hybrid material prepared from mixtures of the natural clay palygorskite (also known as attapulgite) and organic dyes derived from the leaves of the *Indigofera suffruticosa* plant.[111,112] Maya Blue was developed and used by Mesoamerican civilizations between the 6th and 16th century.[113–115] Remarkably, the pigment retains its vibrant blue-turquoise color when exposed to aging, weathering, thermal degradation, concentrated acid, and chemical solvents.[115,116] As a result, many Mesoamerican murals, artifacts, and sculptures that incorporate Maya Blue still retain their coloration, long after pigments of other hues have faded due to weathering (Figure 1.4).[111] These exceptional properties have prompted theoretical and experimental studies to investigate the composition, structure, and stability of the organic-inorganic complex of indigo and palygorskite,[112,117–124] but its precise nature and the molecular origins of its durability have remained elusive.

Figure 1.4. The Cacaxtla Mural from Tlaxcala, Mexico, 600-950 C.E, an example of the use of Maya Blue. Photo taken by Hajor, July, 2003. Released under cc.by.sa and/or GFDL.

The exact procedures used historically to prepare Maya Blue pigments have been lost,[111] though pigments with analogous optical properties and stability may be prepared by thermal treatment of macroscopic mixtures of indigo and palygorskite at temperatures greater than 130˚C.[121] Previous diffract, electrochemical, and spectroscopic studies[118,120,123] have identified the organic components of Maya Blue as indigo and dehydroindigo, which together account for the green-blue hue of the Maya Blue pigments. Indigo and dehydroindigo are typically present in dilute quantities in Maya Blue (<1 wt%) and occupy non-ordered surface- and near-surface distributions, making determination of their environments and interactions challenging. The different organic components of Maya Blue are present to different relative extents depending on the synthesis conditions and precursor compositions,[112] which yield different hues in different samples of archaeological Maya Blue that likely arise from different historical preparation methods and precursor material compositions from region to region.[112]

In Chapter 8 of this dissertation, the stability of Maya Blue pigments is shown to arise from very strong hydrogen bonding interactions between indigo/dehydroindigo molecules and the inorganic palygorskite framework. Solid-state 2D $^{1}H\{^{1}H\}$, $^{13}C\{^{1}H\}$, and $^{29}Si\{^{1}H\}$ NMR spectra, with sensitivity enhanced by very high magnetic field strengths and/or DNP-NMR techniques, unambiguously establish the incorporation of indigo/dehydroindigo molecules into near-surface environments in the palygorskite nanopores. Additionally, the spectra resolve signals from strongly-H-bonded -OH moieties that interact with the dilute organic molecules. The combined analyses provide the first experimental evidence for strong H-bonds stabilizing indigo within the palygorskite matrix in Maya Blue.

1.6 Heavily-doped nanocrystalline semiconductors

Semiconducting nanoparticles, with characteristic lengths less than 100 nm, can exhibit markedly different properties compared to bulk, non-structured materials of similar compositions.[24] This enables a variety of emerging applications including biological sensing, catalysis, solid-state lighting, and solar photovoltaics.[12,16,125,126] Understanding the synthesis and structure-property relations of nanostructured materials is critical to their engineering for industrial/commercial applications. Group III-V nanocrystalline semiconductors such as GaN, InGaP, and In_2O_3, are particularly attractive for optoelectronic applications, including solid-state lighting[127,128] and power electronics,[129] because their wide bandgaps and electronic structures that can be tuned by the introduction of dopants or defects. For example, semiconductors heavily doped with shallow donors become metallic, acquiring useful electronic and photonic properties. Mott provided a quantitative estimate of the donor concentration required to induce such a transition,[130] known as the metal-insulator transition (MIT) or Mott transition. Physically, this corresponds to a transition between two extrema: (1) dilute isolated and independent shallow donors, that at low temperatures are un-ionized and have weakly bound electrons whose wave functions[131] typically extend over several lattice constants; and (2) concentrated and interacting shallow donors, whose overlapping wave functions form an impurity band that can lie below the conduction band or, at higher concentrations, enter into it. The optoelectronic properties of semiconductors therefore depend strongly on the types, quantities, and distributions lattice or surface defects as well as particle size and structure.

In Chapter 9, the local electronic environments of ^{71}Ga and ^{15}N atoms in annealed nanocrystalline GaN materials are investigated using 1D and 2D ^{71}Ga and ^{15}N NMR

techniques, with complementary X-ray diffraction, electron microscopy, and photoluminescence measurements. Defects introduced during the annealing process are found to generate a defect band that yields local conductivity and metallic properties, similar to heavily-doped bulk GaN. Furthermore, the photoluminescence intensity and wavelength is shown to correlate to the presence of metallic environments. The techniques described here provide a promising tool for understanding heavily doped semiconductor nanomaterials, for which bulk electrical characterization methods are often infeasible due to the difficulties associated with making electrical contacts. This is demonstrated in Appendix A2 for F-doped In_2O_3 nanocrystals with near-IR plasmonic responses, where the F additives are shown to both direct the crystallite morphology and act as n-type dopants that contribute electron carriers to the In_2O_3 conduction band.

1.7 Experimental approaches

Each of the different material systems analyzed in this dissertation involves complicated extents of order and disorder, where the macroscopic optical or catalytic properties arise from non-stoichiometric distributions of heteroatoms and/or interactions at dilute surface sites. Detailed atomic-level insights are provided by combinations of spectroscopic and scattering techniques. Powder X-ray diffraction (XRD) provides unit cell dimensions and atom positions for materials that exhibit periodic ordering over relatively large length scales (>10 nm). Scanning electron microscopy (SEM) provides information on morphology and surface topology, as well as particle size distributions for particles typically >50 nm in size. Transmission electron microscopy (TEM) provides nanometer-scale details of the morphology and atomic positioning and is capable of atom-level resolution for materials with

high extents of local ordering. The forces between two extended surfaces are measured as a function of distance using the surface forces apparatus (SFA), which can detect inter-surface forces with sub-nanometer resolution under different solution conditions.[132] Recent advances in SFA instrumentation have enabled the application of electrostatic fields to probe fundamental physiochemical forces of electrochemical phenomena at surfaces.[132–134] The advanced solid-state NMR spectroscopy techniques used in this work are described in the following sections. Specific experimental details for each chapter are provided in the "Materials and Methods" sections.

1.7.1 Solid-state nuclear magnetic resonance

NMR spectroscopy probes the local chemical, electronic, and structural environments of atomic nuclei with nuclear spin numbers $I \neq 0$, including isotopes of nearly every element (e.g., ^{1}H, ^{13}C, ^{14}N, ^{15}N, ^{17}O, ^{23}Na, ^{27}Al, ^{29}Si, ^{71}Ga, ^{115}In, etc.). When such non-zero-spin nuclei are placed in an external magnetic field, the degenerate energy levels of the nuclear spins are split and unevenly populated according to Boltzmann statics, with dependencies on the temperature and the strength of the external magnetic field. At thermal equilibrium, the net polarization vector of the nuclear spins is aligned with the magnetic field. This equilibrium state is perturbed by the application of short (~μs), high-power radio-frequency (rf) pulses that match the Larmor frequencies of the nuclei at the given magnetic field strength, after which the nuclear spins magnetization vector recovers toward the equilibrium position. Simultaneously, the nuclear spin magnetization vector precesses as a function of time at a specific frequency in the plane perpendicular to the external magnetic field. The precise frequency of the precession is induces a current in the rf coil around the sample that

is measured in an NMR experiment. This frequency is highly sensitive to the chemical, physical, and electronic interactions of the nucleus and yields information about the local (sub-nm) environment of the nuclear spins. A Fourier transform of the time-domain NMR signal allows different NMR signals from nuclear species in different local environments to be resolved in the frequency domain. Typically, NMR spectra are plotted with normalized frequency axes with units of ppm (=Hz/MHz). In solutions, isotropic motion of the molecular species yields well-resolved NMR signals with narrow linewidths due to motional averaging of nuclear couplings to local magnetic fields.[135] However, solid-state materials typically yield very broad NMR signals that are poorly resolved due to strong nuclear-nuclear dipolar couplings and orientation dependencies of the NMR signals of individual nuclei with respect to the external magnetic field (e.g., chemical shift anisotropy). Consequently, methods to improve the spectral resolution of solid-state NMR spectra are of high importance for obtaining structural or physiochemical information about a material.

Resolution may be improved by imposing motion on the nuclear spin ensemble within the NMR magnet by rotating the sample rapidly about the so-called "magic-angle," 54.74°. This is because many nuclear spin interactions (including dipolar interactions and chemical shift anisotropy) are described by second-order Hamiltonians that have $3\cos^2(\theta)-1$ terms that reduce to zero at $\theta = 54.7°$. Under magic-angle-spinning (MAS) conditions, these nuclear spin interactions are partially or completely averaged, yielding well-resolved solid-state NMR spectra that manifest the isotropic chemical shifts (for spin ½ nuclei). Resolution may be further improved by powerful 2D NMR methods, which correlate the isotropic shifts of different nuclear species in a material and may be mediated by nuclear dipole-dipole-couplings through space or *J*-couplings through covalent bonds. Of these two interactions,

dipole-dipole couplings are stronger and vary as the inverse cube of the separation distance between two nuclei, while *J* couplings are typically selective for interactions over one or two covalent bond lengths.[136–139]

Atomic nuclei with spin numbers >|1/2| are "quadrupolar" nuclei that have anisotropic distributions of nuclear charge. Such nuclei couple to local electric field gradients at the nuclear sites and typically yield broad and poorly-resolved NMR signals. These nuclei include ^{27}Al (I = 5/2) and ^{71}Ga (I = 3/2). The resolution of NMR signals from quadrupolar may be improved by conducting NMR measurements at very high magnetic fields (>18.8 T), or by using 2D multiple-quantum MAS (MQMAS) methods to mitigate the effects of anisotropic second-order quadrupolar broadening associated with the quadrupolar nuclei.[22]

1.7.2 Dynamic-nuclear-polarization-enhanced NMR

Due to the low polarizability of NMR-active spins in commercially-available NMR magnets (field strengths typically 7.0-18.8 T), the low sensitivity of NMR measurements is a primary challenge, particularly for measuring nuclear isotopes with low natural abundances such as ^{13}C (1.1 %), ^{15}N (0.5 %), ^{17}O (0.04 %), and ^{29}Si (4.7 %). Due to the Boltzmann distribution of nuclear spin polarization in an external magnetic field, NMR sensitivity is improved by measurement under low-temperature conditions and by application of higher magnetic fields (>18.8 T). The most notable recent advance in solid-state NMR instrumentation is dynamic-nuclear-polarization (DNP)-enhanced MAS NMR techniques at low temperatures (ca. 100 K),[140–143] which provide significantly enhanced NMR signal sensitivity particularly of surface species. The DNP-enhanced NMR experiments use continuous microwave irradiation at <100 K to transfer high electron spin polarization from

stable exogeneous biradicals such as TEKPol[144] via electron-nuclear hyperfine interactions to ^{1}H nuclei of frozen 1,1,2,2-tetrachloroethane (TCE) DNP solvent molecules. The hydrophobic solvent TCE is typically chosen for analysis of hydrophilic materials so as to minimize perturbation of the structure or hydration environments of the particle surfaces.[145] The DNP-enhanced ^{1}H spin polarization is distributed by ^{1}H-^{1}H spin diffusion through the frozen solvent to other molecularly proximate (<1 nm) solvent molecules and to the surfaces of the material. Subsequently, DNP-enhanced ^{1}H polarization is transferred via conventional cross-polarization techniques to proximate nuclei. The polarization transfer pathways involved in DNP-NMR experiments are depicted schematically in Figure 1.5. For more information on the fundamental principles and diverse applications of DNP-NMR spectroscopy, the reader is referred to recent review papers.[146,147]

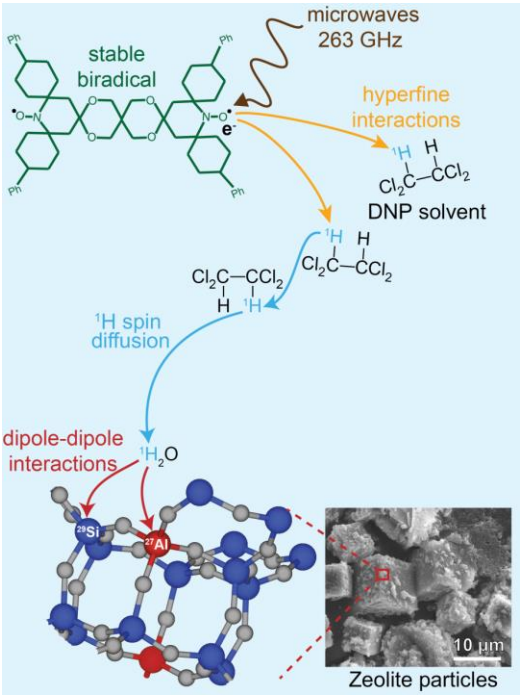

Figure 1.5. Schematic depiction of polarization transfer pathways in DNP-NMR experiments. First, hyperpolarization is generated by high-frequency microwave irradiation at of an exogeneous stable biradical in a frozen organic solvent. Polarization is transferred from electron spins to proximate nuclear spins via electron-nuclear hyperfine interactions (yellow arrows). The hyperpolarization subsequently diffuses through the frozen organic

solvent matrix by spin diffusion (blue arrows) to the surface of the sample particles (an aluminosilicate zeolite particle surface is shown in the present case). Polarization is transferred to atomic nuclei such as ^{29}Si or ^{27}Al at the zeolite particle surfaces by conventional cross-polarization techniques that are mediated by ^{1}H-^{29}Si or ^{1}H-^{27}Al nuclear dipole-dipole interactions (red arrows).

1.8 References

(1) NAE Grand Challenges for Engineering http://www.engineeringchallenges.org/challenges.aspx (accessed Feb 9, 2018).
(2) Vogt, E. T. C.; Weckhuysen, B. M. *Chem. Soc. Rev.* **2015**, *44* (20), 7342.
(3) Nugent, P.; Belmabkhout, Y.; Burd, S. D.; Cairns, A. J.; Luebke, R.; Forrest, K.; Pham, T.; Ma, S.; Space, B.; Wojtas, L.; Eddaoudi, M.; Zaworotko, M. J. *Nature* **2013**, *495* (7439), 80.
(4) Morris, R. E.; Wheatley, P. S. *Angew. Chemie - Int. Ed.* **2008**, *47* (27), 4966.
(5) Babel, S.; Kurniawan, T. A. *J. Hazard. Mater.* **2003**, *97* (1–3), 219.
(6) Borai, E. H.; Harjula, R.; malinen, L.; Paajanen, A. *J. Hazard. Mater.* **2009**, *172* (1), 416.
(7) Huber, G. W.; Corma, A. *Angew. Chemie - Int. Ed.* **2007**, *46* (38), 7184.
(8) Stöcker, M. *Angew. Chemie - Int. Ed.* **2008**, *47* (48), 9200.
(9) Paolucci, C.; Khurana, I.; Parekh, A. A.; Li, S.; Shih, A. J.; Li, H.; Di Iorio, J. R.; Albarracin-Caballero, J. D.; Yezerets, A.; Miller, J. T. *Science.* **2017**, *357*, 898.
(10) Choi, S.; Drese, J. H.; Jones, C. W. *ChemSusChem* **2009**, *2* (9), 796.
(11) Phan, A.; Doonan, C. J.; Uribe-Romo, F. J.; Knobler, C. B.; O'Keeffe, M.; Yaghi, O. M. *Acc Chem Res* **2010**, *43* (1), 58.
(12) Nozik, A. J.; Beard, M. C.; Luther, J. M.; Law, M.; Ellingson, R. J.; Johnson, J. C. *Chem. Rev.* **2010**, *110* (11), 6873.
(13) Linic, S.; Christopher, P.; Ingram, D. B. *Nat. Mater.* **2011**, *10* (12), 911.
(14) Tong, H.; Ouyang, S.; Bi, Y.; Umezawa, N.; Oshikiri, M.; Ye, J. *Adv. Mater.* **2012**, *24* (2), 229.
(15) Fortunato, E.; Barquinha, P.; Martins, R. *Adv. Mater.* **2012**, *24* (22), 2945.
(16) Jariwala, D.; Sangwan, V. K.; Lauhon, L. J.; Marks, T. J.; Hersam, M. C. *ACS Nano* **2014**, *8* (2), 1102.
(17) Min, Y.; Akbulut, M.; Kristiansen, K.; Golan, Y.; Israelachvili, J. *Nat. Mater.* **2008**, *7* (7), 527.
(18) Fuchs, A. H.; Cheetham, A. K. *J. Phys. Chem. B* **2001**, *105* (31), 7375.
(19) Donaldson, S. H.; Lee, C. T.; Chmelka, B. F.; Israelachvili, J. N. *Proc. Natl. Acad. Sci.* **2011**, *108* (38), 15699.
(20) Schrader, A. M.; Monroe, J. I.; Sheil, R.; Dobbs, H. A.; Keller, T. J.; Li, Y.; Jain, S.; Shell, M. S.; Israelachvili, J. N.; Han, S. *Proc. Natl. Acad. Sci.* **2018**, *115* (12), 201722263.
(21) Xiao, J.; Wei, J. *Chem. Eng. Sci.* **1992**, *47*, 1123.
(22) Choi, M.; Na, K.; Kim, J.; Sakamoto, Y.; Terasaki, O.; Ryoo, R. *Nature* **2009**, *461* (7261), 246.
(23) Lupulescu, A. I.; Rimer, J. D. *Science.* **2014**, *344* (6185), 729.
(24) Alivisatos, A. P. *Science.* **1996**, *271* (5251), 933.
(25) Sánchez-Iglesias, A.; Grzelczak, M.; Altantzis, T.; Goris, B.; Pérez-Juste, J.; Bals, S.; Van Tendeloo, G.; Donaldson, S. H.; Chmelka, B. F.; Israelachvili, J. N.; Liz-Marzán, L. M. *ACS Nano* **2012**, *6* (12), 11059.
(26) Joo, S. H.; Choi, S. J.; Oh, I.; Kwak, J.; Liu, Z.; Terasaki, O.; Ryoo, R. *Nature* **2001**, *412* (6843), 169.
(27) Fechler, N.; Fellinger, T. P.; Antonietti, M. *Adv. Mater.* **2013**, *25* (1), 75.
(28) Zhao, D.; Feng, J.; Huo, Q.; Melosh, N.; Fredrickson, G. H.; Chmelka, B. F.; Stucky, G. D. *Science* **1998**, *279* (5350), 548.
(29) Yang, P.; Zhao, D.; Margolese, D. I.; Chmelka, B. F.; Stucky, G. D. *Nature* **1998**, *396*, 152.
(30) Corma, A.; Garcfa, H. *Catal. Today* **1997**, *38*, 257.
(31) De Yoreo, J. J.; Gilbert, P. U. P. A.; Sommerdijk, N. A. J. M.; Penn, R. L.; Whitelam, S.;

Joester, D.; Zhang, H.; Rimer, J. D.; Navrotsky, A.; Banfield, J. F.; Wallace, A. F.; Michel, F. M.; Meldrum, F. C.; Colfen, H.; Dove, P. M. *Science.* **2015**, *349* (6247), 6760.
(32) Gallego, E. M.; Portilla, M. T.; Paris, C.; León-Escamilla, A.; Boronat, M.; Moliner, M.; Corma, A. *Science.* **2017**, *355* (6329), 1051.
(33) Davis, M. E. *Nature* **2002**, *417*, 813.
(34) Meirer, F.; Kalirai, S.; Weker, J. N.; Liu, Y.; Andrews, J. C.; Weckhuysen, B. M. *Chem. Commun.* **2015**, *51* (38), 8097.
(35) Tian, P.; Wei, Y.; Ye, M.; Liu, Z. *ACS Catal.* **2015**, *5* (3), 1922.
(36) Gallego, E. M.; Portilla, M. T.; Paris, C.; León-Escamilla, A.; Boronat, M.; Moliner, M.; Corma, A. *Science.* **2017**, *355* (6329), 1051.
(37) Gao, F.; Kwak, J. H.; Szanyi, J.; Peden, C. H. F. *Top. Catal.* **2013**, *56* (15–17), 1441.
(38) Lomachenko, K. A.; Borfecchia, E.; Negri, C.; Berlier, G.; Lamberti, C.; Beato, P.; Falsig, H.; Bordiga, S. *J. Am. Chem. Soc.* **2016**, *138* (37), 12025.
(39) Di Iorio, J. R.; Gounder, R. *Chem. Mater.* **2016**, *28* (7), 2236.
(40) Paolucci, C.; Khurana, I.; Parekh, A. A.; Li, S.; Shih, A. J.; Li, H.; Di Iorio, J. R.; Albarracin-Caballero, J. D.; Yezerets, A.; Miller, J. T.; Delgass, W. N.; Ribeiro, F. H.; Schneider, W. F.; Gounder, R. *Science.* **2017**, *357* (6354), 898.
(41) Flytzani-Stephanopoulos, M.; Gates, B. C. *Annu. Rev. Chem. Biomol. Eng.* **2012**, *3* (1), 545.
(42) Baerlocher, C.; McCusker, L. B. Database of Zeolite Structures.
(43) Gábová, V.; Dědeček, J.; čejka, J. *Chem. Commun.* **2003**, *3* (10), 1196.
(44) Gounder, R.; Iglesia, E. *J. Am. Chem. Soc.* **2009**, *131* (5), 1958.
(45) Dědeček, J.; Sobalík, Z.; Wichterlová, B. *Catal. Rev. - Sci. Eng.* **2012**, *54* (2), 135.
(46) Van Bokhoven, J. A.; Lee, T. L.; Drakopoulos, M.; Lamberti, C.; Thie, S.; Zegenhagen, J. *Nat. Mater.* **2008**, *7* (7), 551.
(47) Pinar, A. B.; Gómez-Hortigüela, L.; McCusker, L. B.; Pérez-Pariente, J. *Chem. Mater.* **2013**, *25* (18), 3654.
(48) Smeets, S.; McCusker, L. B.; Baerlocher, C.; Elomari, S.; Xie, D.; Zones, S. I. *J. Am. Chem. Soc.* **2016**, *138* (22), 7099.
(49) Hun Kwak, J.; Zhu, H.; Lee, J. H.; Peden, C. H. F.; Szanyi, J. *Chem. Commun.* **2012**, *48* (39), 4758.
(50) Dědeček, J.; Kaucký, D.; Wichterlová, B.; Gonsiorová, O. *Phys. Chem. Chem. Phys.* **2002**, *4* (21), 5406.
(51) Zones, S. I.; Benin, A.; Hwang, S. J.; Xie, D.; Elomari, S.; Hsieh, M. F. *J. Am. Chem. Soc.* **2014**, *136* (4), 1462.
(52) Di Iorio, J. R.; Nimlos, C. T.; Gounder, R. *ACS Catal.* **2017**, *7* (10), 6663.
(53) Archer, R. H.; Zones, S. I.; Davis, M. E. *Microporous Mesoporous Mater.* **2010**, *130* (1–3), 255.
(54) Archer, R. H.; Carpenter, J. R.; Hwang, S.-J.; Burton, A. W.; Chen, C.-Y.; Zones, S. I.; Davis, M. E. *Chem. Mater.* **2010**, *22* (8), 2563.
(55) Aigner, M.; Grosso-Giordano, N. A.; Okrut, A.; Zones, S.; Katz, A. *React. Chem. Eng.* **2017**, *2* (6), 842.
(56) Lupulescu, A. I.; Rimer, J. D. *Angew. Chem.* **2012**.
(57) Earl, D. J.; Deem, M. W. *Ind. Eng. Chem. Res.* **2006**, *45* (16), 5449.
(58) Li, Y.; Yu, J. *Chem. Rev.* **2014**, *114* (14), 7268.
(59) Smeets, S.; Berkson, Z. J.; Xie, D.; Zones, S. I.; Wan, W.; Zou, X.; Hsieh, M. F.; Chmelka, B. F.; McCusker, L. B.; Baerlocher, C. *J. Am. Chem. Soc.* **2017**, *139* (46), 16803.
(60) Na, K.; Jo, C.; Kim, J.; Cho, K.; Jung, J.; Seo, Y.; Messinger, R. J.; Chmelka, B. F.; Ryoo, R. *Science.* **2011**, *333* (6040), 328.
(61) Seo, Y.; Cho, K.; Jung, Y.; Ryoo, R. *ACS Catal.* **2013**, *3* (4), 713.
(62) Ogino, I.; Nigra, M. M.; Hwang, S.-J.; Ha, J.-M.; Rea, T.; Zones, S. I.; Katz, A. *J. Am. Chem. Soc.* **2011**, *133* (10), 3288.

(63) Runnebaum, R. C.; Ouyang, X.; Edsinga, J. A.; Rea, T.; Arslan, I.; Hwang, S. J.; Zones, S. I.; Katz, A. *ACS Catal.* **2014**, *4* (7), 2364.
(64) Blay, V.; Louis, B.; Miravalles, R.; Yokoi, T.; Peccatiello, K. A.; Clough, M.; Yilmaz, B. *ACS Catal.* **2017**, *7* (10), 6542.
(65) Beyerlein, R. A.; Choi-feng, C.; Hall, J. B.; Huggins, B. J.; Ray, G. J. **1997**, *4*, 27.
(66) Wouters, B. H.; Chen, T.; Grobet, P. J. *J. Phys. Chem. B* **2001**, *105* (6), 1135.
(67) Van Donk, S.; Janssen, A. H.; Bitter, J. H.; De Jong, K. P. *Catal. Rev. - Sci. Eng.* **2003**, *45* (2), 297.
(68) Al-Khattaf, S.; Rabiu, S.; Tukur, N. M.; Alnaizy, R. *Chem. Eng. J.* **2008**, *139* (3), 622.
(69) Sherman, J. D. *Proc. Natl. Acad. Sci.* **1999**, *96* (7), 3471.
(70) Taguchi, A.; Schüth, F. *Ordered mesoporous materials in catalysis*; 2005; Vol. 77.
(71) Duxson, P.; Fernández-Jiménez, A.; Provis, J. L.; Lukey, G. C.; Palomo, A.; Van Deventer, J. S. J. *J. Mater. Sci.* **2007**, *42* (9), 2917.
(72) Cundy, C. S.; Cox, P. A. *Chem. Rev.* **2003**, *103* (3), 663.
(73) Cundy, C. S.; Cox, P. A. *Microporous Mesoporous Mater.* **2005**, *82* (1–2), 1.
(74) Grand, J.; Awala, H.; Mintova, S. *CrystEngComm* **2016**, *18* (5), 650.
(75) Fernández-Jiménez, A.; Palomo, A.; Sobrados, I.; Sanz, J. *Microporous Mesoporous Mater.* **2006**, *91* (1–3), 111.
(76) Aughenbaugh, K. L.; Williamson, T.; Juenger, M. C. G. *Mater. Struct.* **2015**, *48* (3), 607.
(77) Khale, D.; Chaudhary, R. *J. Mater. Sci.* **2007**, *42* (3), 729.
(78) Duxson, P.; Provis, J. L.; Lukey, G. C.; Mallicoat, S. W.; Kriven, W. M.; Van Deventer, J. S. J. *Colloids Surfaces A Physicochem. Eng. Asp.* **2005**, *269* (1–3), 47.
(79) Zhang, L. L.; Zhao, X. S. *Chem. Soc. Rev.* **2009**, *38*, 2520.
(80) Zhao, Y.; Hu, C.; Hu, Y.; Cheng, H.; Shi, G.; Qu, L. *Angew. Chemie - Int. Ed.* **2012**, *51* (45), 11371.
(81) Xu, Y.; Lin, Z.; Zhong, X.; Huang, X.; Weiss, N. O.; Huang, Y.; Duan, X. *Nat. Commun.* **2014**, *5*.
(82) Gong, K.; Du, F.; Xia, Z.; Durstock, M.; Dai, L. *Science* **2009**, *323* (5915), 760.
(83) Zhao, Y.; Nakamura, R.; Kamiya, K.; Nakanishi, S.; Hashimoto, K. *Nat. Commun.* **2013**, *4*, 1.
(84) Lu, Z.; Chen, G.; Siahrostami, S.; Chen, Z.; Liu, K.; Xie, J.; Liao, L.; Wu, T.; Lin, D.; Liu, Y.; Jaramillo, T. F.; Nørskov, J. K.; Cui, Y. *Nat. Catal.* **2018**, *1*, 156.
(85) He, L.; Weniger, F.; Neumann, H.; Beller, M. *Angew. Chemie - Int. Ed.* **2016**, *55* (41), 12582.
(86) Sahoo, B.; Surkus, A. E.; Pohl, M. M.; Radnik, J.; Schneider, M.; Bachmann, S.; Scalone, M.; Junge, K.; Beller, M. *Angew. Chemie - Int. Ed.* **2017**, *56* (37), 11242.
(87) Yang, W.; Fellinger, T.-P.; Antonietti, M. *J. Am. Chem. Soc.* **2011**, *133* (2), 206.
(88) Li, Y.; Zhou, W.; Wang, H.; Xie, L.; Liang, Y.; Wei, F.; Idrobo, J.-C.; Pennycook, S. J.; Dai, H. *Nat. Nanotechnol.* **2012**, *7* (6), 394.
(89) Chung, H. T.; Won, J. H.; Zelenay, P. *Nat. Commun.* **2013**, *4*, 1922.
(90) Chung, H. T.; Cullen, D. A.; Higgins, D.; Sneed, B. T.; Holby, E. F.; More, K. L.; Zelenay, P. *Science.* **2017**, *357* (6350), 479.
(91) Othman, R.; Dicks, A. L.; Zhu, Z. *Int. J. Hydrogen Energy* **2012**, *37* (1), 357.
(92) Zhu, Y. P.; Guo, C.; Zheng, Y.; Qiao, S.-Z. *Acc. Chem. Res.* **2017**, *50*, 915−923.
(93) Dombrovskis, J. K.; Palmqvist, A. E. C. *J. Power Sources* **2017**, *357*, 87.
(94) Kim, D.; Zussblatt, N. P.; Chung, H. T.; Zelenay, P.; Chmelka, B. F. *ACS Appl. Mater. Interfaces* **2018**, submitted.
(95) Guo, D.; Shibuya, R.; Akiba, C.; Saji, S.; Kondo, T.; Nakamura, J. *Science* **2016**, *351* (6271), 361.
(96) Wang, D.-W.; Su, D. *Energy Environ. Sci.* **2014**, *7* (2), 576.
(97) Wang, X.; He, Z.; Shi, Y.; Li, B. *J. Electrochem. Soc.* **2017**, *164* (6), F620.
(98) Fechler, N.; Zussblatt, N. P.; Rothe, R.; Schlögl, R.; Willinger, M.-G. G.; Chmelka, B. F.; Antonietti, M.; Schlögl, R.; Willinger, M.-G. G.; Chmelka, B. F.; Antonietti, M. *Adv. Mater.*

2016, *28* (6), 1287.
(99) Ding, W.; Wei, Z.; Chen, S.; Qi, X.; Yang, T.; Hu, J.; Wang, D.; Wan, L.-J.; Alvi, S. F.; Li, L. *Angew. Chemie - Int. Ed.* **2013**, *52* (45), 11755.
(100) Wu, J.; Ma, L.; Yadav, R. M.; Yang, Y.; Zhang, X.; Vajtai, R.; Lou, J.; Ajayan, P. M. *ACS Appl. Mater. Interfaces* **2015**, *7* (27), 14763.
(101) Liu, G.; Li, X.; Ganesan, P.; Popov, B. N. *Electrochim. Acta* **2010**, *55* (8), 2853.
(102) Lai, L.; Potts, J. R.; Zhan, D.; Wang, L.; Poh, C. K.; Tang, C.; Gong, H.; Shen, Z.; Lin, J.; Ruoff, R. S. *Energy Environ. Sci.* **2012**, *5* (7), 7936.
(103) Subramanian, N. P.; Li, X.; Nallathambi, V.; Kumaraguru, S. P.; Colon-Mercado, H.; Wu, G.; Lee, J. W.; Popov, B. N. *J. Power Sources* **2009**, *188* (1), 38.
(104) Tributsch, H.; Koslowski, U. I.; Dorbandt, I. *Electrochim. Acta* **2008**, *53* (5), 2198.
(105) Zitolo, A.; Goellner, V.; Armel, V.; Sougrati, M. T.; Mineva, T.; Stievano, L.; Fonda, E.; Jaouen, F. *Nat. Mater.* **2015**, *14* (9), 937.
(106) Meirer, F.; Kalirai, S.; Morris, D.; Soparawalla, S.; Liu, Y.; Mesu, G.; Andrews, J. C.; Weckhuysen, B. M. *Sci. Adv.* **2015**, *1* (3), e1400199.
(107) Goodenough, J. B.; Park, K. S. *J. Am. Chem. Soc.* **2013**, *135* (4), 1167.
(108) Shirasaki, Y.; Supran, G. J.; Bawendi, M. G.; Bulović, V. *Nat. Photonics* **2013**, *7* (1), 13.
(109) Osterloh, F. E. *Chem. Soc. Rev.* **2013**, *42* (6), 2294.
(110) Gebbie, M. A.; Wei, W.; Schrader, A. M.; Cristiani, T. R.; Dobbs, H. A.; Idso, M.; Chmelka, B. F.; Herbert Waite, J.; Israelachvili, J. N. *Nat. Chem.* **2017**, *9* (5), 473.
(111) Reyes-Valerio, C. *De Bonampak al Templo Mayor : el azul maya en Mesoamérica*, 1st ed.; México, D.F. : Siglo Veintiuno Editores : Agro Asemex, 1993.
(112) Doménech, A.; Doménech-Carbõ, M. T.; Vidal-Lorenzo, C.; De Agredos-Pascual, M. L. V. *Angew. Chemie - Int. Ed.* **2012**, *51* (3), 700.
(113) Van Olphen, H. *Science* **1966**, *154* (3749), 645.
(114) Puche, S.; Carmen, M. *Science. 273* **1996**, 223.
(115) Del Río, M. S.; Doménech, A.; Doménech-Carbó, M. T.; De Agredos Pascual, M. L. V.; Suárez, M.; García-Romero, E. *Dev. Clay Sci.* **2011**, *3* (1962), 453.
(116) Del Río, M. S.; Martinetto, P. *Archeometry*, **2006**, *1*, 115.
(117) Hubbard, B.; Kuang, W.; Moser, A.; Facey, G. A.; Detellier, C. *Clays Clay Miner.* **2003**, *51* (3), 318.
(118) Doménech, A.; Doménech-Carbó, M. T.; De Agredos Pascual, M. L. V. *J. Phys. Chem. C* **2007**, *111* (12), 4585.
(119) Del Río, M. S.; Gutiérrez-León, A.; Castro, G. R.; Rubio-Zuazo, J.; Solís, C.; Sánchez-Hernández, R.; Robles-Camacho, J.; Rojas-Gaytán, J. *Appl. Phys. A Mater. Sci. Process.* **2008**, *90* (1), 55.
(120) Domenech, A.; Domenech-Carbo, M. T.; Ŕo, M. S. Del; Goberna, S.; Lima, E. *J. Phys. Chem. C* **2009**, *113* (28), 12118.
(121) Del Río, M.S.; Boccaleri, E.; Milanesio, M.; Croce, G.; Van Beek, W.; Tsiantos, C.; Chyssikos, G. D.; Gionis, V.; Kacandes, G. H.; Suárez, M.; García-Romero, E. *J. Mater. Sci.* **2009**, *44* (20), 5524.
(122) Giustetto, R.; Levy, D.; Wahyudi, O.; Ricchiardi, G.; Vitillo, J. G. *Eur. J. Mineral.* **2011**, *23* (3), 449.
(123) Lima, E.; Guzman, A.; Vera, M.; Rivera, J. L.; Fraissard, J. *J. Phys. Chem. C* **2012**, *116* (7), 4556.
(124) Sánchez-Ochoa, F.; Cocoletzi, G. H.; Canto, G. *Microporous Mesoporous Mater.* **2017**, *249*, 111.
(125) Panda, A. B.; Acharya, S.; Efrima, S.; Golan, Y. *Langmuir* **2007**, *23* (2), 765.
(126) Cadars, S.; Smith, B. J.; Epping, J. D.; Acharya, S.; Belman, N.; Golan, Y.; Chmelka, B. F. *Phys. Rev. Lett.* **2009**, *103* (13).
(127) Denbaars, S. P.; Feezell, D.; Kelchner, K.; Pimputkar, S.; Pan, C. C.; Yen, C. C.; Tanaka, S.;

Zhao, Y.; Pfaff, N.; Farrell, R.; Iza, M.; Keller, S.; Mishra, U.; Speck, J. S.; Nakamura, S. *Acta Mater.* **2013**, *61* (3), 945.
(128) Kaur, G.; Denninger, G. *Appl. Magn. Reson.* **2010**, *39* (1), 185.
(129) Mishra, U. K.; Shen, L.; Kazior, T. E.; Wu, Y. F. *Proc. IEEE* **2007**, *96* (2), 287.
(130) Mott, N. F. *Adv. Phys.* **1972**, *21* (94), 785.
(131) Kohn, W.; Luttinger, J. M. *Phys. Rev.* **1955**, *98* (4), 915.
(132) Israelachvili, J.; Min, Y.; Akbulut, M.; Alig, A.; Carver, G.; Greene, W.; Kristiansen, K.; Meyer, E.; Pesika, N.; Rosenberg, K.; Zeng, H. *Reports Prog. Phys.* **2010**, *73* (3).
(133) Valtiner, M.; Banquy, X.; Kristiansen, K.; Greene, G. W.; Israelachvili, J. N. *Langmuir* **2012**, *28* (36), 13080.
(134) Dobbs, H. A.; Kaufman, Y.; Scott, J.; Kristiansen, K.; Schrader, A. M.; Chen, S. Y.; Duda, P.; Israelachvili, J. N. *Adv. Eng. Mater.* **2018**, *20* (2), 1.
(135) Slichter, C. P. *Principles of Magnetic Resonance, Third Edition*; Springer-Verlag: Berlin, 1990.
(136) Lesage, A.; Bardet, M.; Emsley, L. *J. Am. Chem. Soc.* **1999**, *121* (47), 10987.
(137) Lesage, A.; Sakellariou, D.; Steuernagel, S.; Emsley, L. *J. Am. Chem. Soc.* **1998**, *120* (7), 13194.
(138) Hu, B.; Trébosc, J.; Amoureux, J. P. *J. Magn. Reson.* **2008**, *192* (1), 112.
(139) Brouwer, D. H.; Kristiansen, P. E.; Fyfe, C. A.; Levitt, M. H. *J. Am. Chem. Soc.* **2005**, *127* (2), 542.
(140) Maly, T.; Debelouchina, G. T.; Bajaj, V. S.; Hu, K.-N.; Joo, C.-G.; Mak–Jurkauskas, M. L.; Sirigiri, J. R.; van der Wel, P. C. A.; Herzfeld, J.; Temkin, R. J.; Griffin, R. G. *J. Chem. Phys.* **2008**, *128* (5), 052211.
(141) Lesage, A.; Lelli, M.; Gajan, D.; Caporini, M. A.; Vitzthum, V.; Mieville, P.; Alauzun, J.; Roussey, A.; Thieuleux, C.; Mehdi, A.; Bodenhausen, G.; Coperet, C.; Emsley, L. *J. Am. Chem. Soc.* **2010**, *132*, 15459.
(142) Rossini, A. J.; Zagdoun, A.; Lelli, M.; Lesage, A.; Copéret, C.; Emsley, L. *Acc. Chem. Res.* **2013**, *46* (9), 1942.
(143) Ni, Q. Z.; Daviso, E.; Can, T. V.; Markhasin, E.; Jawla, S. K.; Swager, T. M.; Temkin, R. J.; Herzfeld, J.; Griffin, R. G. *Acc. Chem. Res.* **2013**, *46* (9), 1933.
(144) Zagdoun, A.; Casano, G.; Ouari, O.; Schwarzwälder, M.; Rossini, A. J.; Aussenac, F.; Yulikov, M.; Jeschke, G.; Coperet, C.; Lesage, A.; Tordo, P.; Emsley, L. *J. Am. Chem. Soc.* **2013**, *135*, 12790.
(145) Sangodkar, R. P.; Smith, B. J.; Gajan, D.; Rossini, A. J.; Roberts, L. R.; Funkhouser, G. P.; Lesage, A.; Emsley, L.; Chmelka, B. F. *J. Am. Chem. Soc.* **2015**, *137* (25), 8096.
(146) Liao, W. C.; Ghaffari, B.; Gordon, C. P.; Xu, J.; Copéret, C. *Curr. Opin. Colloid Interface Sci.* **2018**, *33*, 63.
(147) Rossini, A. J. *J. Phys. Chem. Lett.* **2018**, *9*, DOI: acs. jpclett.8b01891.

Chapter 2

Non-topotactic transformation of silicate nanolayers into mesostructured MFI zeolite frameworks during crystallization

Adapted from: Z. J. Berkson, R. J. Messinger, K. Na, Y. Seo, R. Ryoo, and B.F. Chmelka, *Angewandte Chemie International Edition* **2017**, *56* (19), 5164-5169

2.1 Abstract

Mesostructured zeolite nanosheets with well-defined nano- and mesopores exhibit improved mass transport properties compared to conventional zeolite materials, with important implications for their use as supports for heterogeneous catalysts. However, their crystallization properties are poorly understood and challenging to control, limiting their industrial application. Here, mesostructured MFI-type zeolite frameworks are established to crystallize non-topotactically through a nanolayered silicate intermediate during hydrothermal synthesis by complementary X-ray diffraction (XRD), electron microscopy, and solid-state nuclear magnetic resonance (NMR) analyses. Notably, solid-state 2D NMR spectra, with sensitivity enhanced by dynamic nuclear polarization (DNP), reveal shared covalent ^{29}Si-O-^{29}Si bonds between intermediate nanolayered silicate moieties and the crystallizing MFI zeolite nanosheet framework at intermediate stages of the hydrothermal synthesis. The results and analyses establish the condensation of the 2D nanolayered silicates to form the 3D framework of the zeolite nanosheets.

2.2 Introduction

Zeolites are porous nanostructured inorganic materials that are of high industrial interest because their well-defined nanopore dimensions (<1 nm), high surface areas, and framework ion-exchange sites for diverse applications including air-gas separation,[1,2] water purification,[3] and heterogeneous catalysis.[4] The acidity and diverse functionalities of aluminosilicate zeolites makes them ideal as heterogeneous catalysts for diverse applications, including hydrocarbon rearrangement reactions.[5–7] However, slow diffusion through the zeolite nanopores limits their stability and longevity for catalytic applications.[8] Recently, surfactant-directed mesostructured zeolite nanosheets have been reported with controllable mesopore diameters in the 1-50 nm range[9–11] that exhibit improved transport, adsorption, and reaction properties compared to conventional zeolites. The hydrothermal crystallization of the mesostructured zeolite nanosheets involves complicated and coupled framework crystallization and surfactant assembly processes that are poorly understood and challenging to characterize, limiting further development of mesostructured zeolite catalysts.

Mesostructured zeolite nanosheets crystallize via co-assembly of the inorganic (alumino)silicate framework and organic structure-directing agents (OSDAs) with nanopore- and mesopore-directing functionalities under hydrothermal conditions. Much previous work on mesostructured zeolite nanosheets has focused on mesostructured silicalite-1, the siliceous analog of the important aluminosilicate zeolite ZSM-5 with **MFI**-type structure. However, the complicated assembly and crystallization processes that lead to the development of both nanoscopic and meso-scale ordering are challenging to measure and elucidate.

Previous work has identified two-dimensional (2D) nanolayered silicates as intermediates in the synthesis of mesostructured **MFI**-type zeolite frameworks,[12] though the

roles of these intermediates in the crystallization and assembly of the mesostructured materials have been contentious. A primary issue is whether zeolite crystallization can proceed through non-topotactic rearrangement of such intermediate structures. Small- and wide-angle X-ray diffraction (XRD) patterns, solid-state ^{29}Si nuclear magnetic resonance (NMR) spectra, and transmission electron microscopy (TEM) images of the intermediate products (1-12 days) of mesostructured **MFI**-type zeolite crystallization were recently reported,[12] and are reproduced in Figure 2.1. At early stages of the synthesis (1 day) a hexagonal silica mesophase is formed that exhibits no short-range or crystalline ordering. At intermediate stages of crystallization (7-10 days), 2D nanolayered silicate species form that are characterized by five relatively narrow ^{29}Si signals in the ^{29}Si CPMAS spectra. These signals are assigned to the five distinct ^{29}Si sites in intermediate 2D nanolayered silicate species, the structure of which has been established by extensive previous studies on materials formed under similar hydrothermal synthesis conditions but using monovalent quaternary ammonium cations,[13–16] shown in Figure 2.2a. After 8.5 days of hydrothermal synthesis, wide-angle XRD reflections are detected (Fig. 2.1a) that are indexable to the crystalline mesostructured **MFI**-type zeolite nanosheets (Fig. 2.2b). Importantly, TEM images of the intermediate crystallization products (8.5-10 days, Fig. 2.1c) showed regions where the nanolayered silicate intermediates are in the process of transforming into the crystalline MFI zeolite products. Furthermore, 2D solid-state ^{29}Si{^{29}Si} NMR correlation analyses provided direct evidence for the distortion of ^{29}Si bonding environments in the 2D nanolayered silicate intermediates, consistent with their transformation into the crystallizing MFI zeolite frameworks with which they were also correlated over sub-nanometer distances.[12]

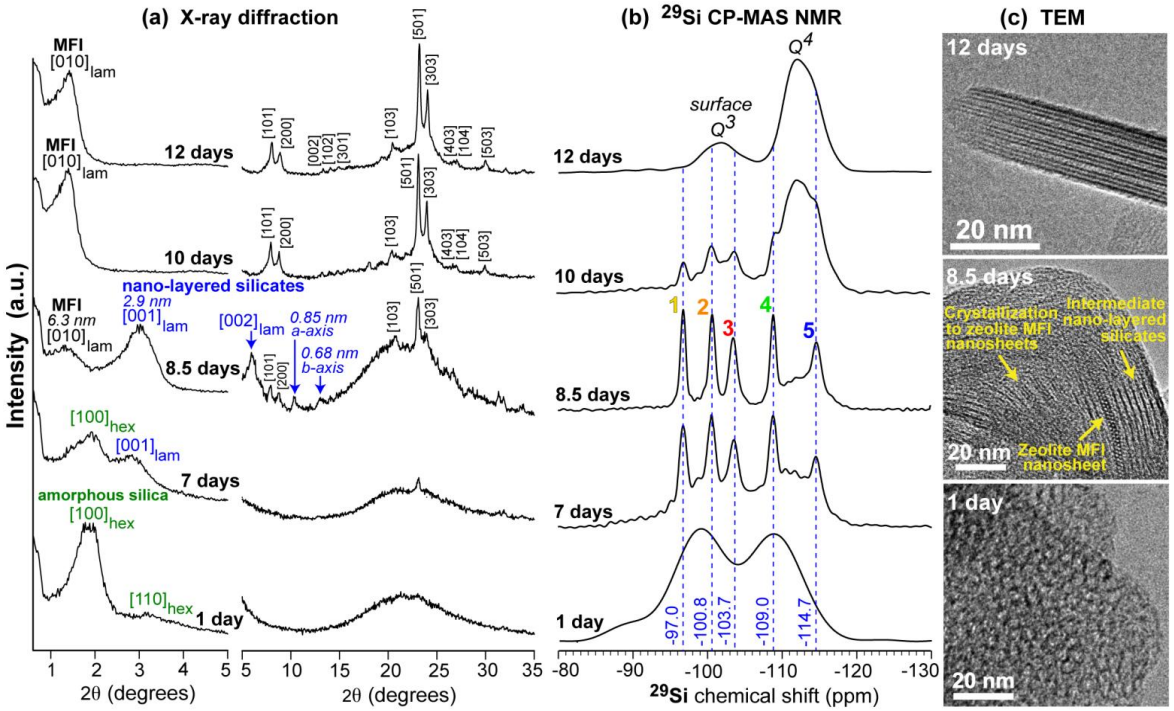

Figure 2.1. (a) Small- and wide-angle powder XRD patterns, (b) solid-state ^{29}Si CP-MAS NMR spectra, and c) representative TEM images of the products obtained after 1, 7, 8.5, 10, and 12 days during hydrothermal synthesis (130 °C) of mesostructured **MFI**-type zeolite nanosheets. XRD reflections are labeled with respect to the different characteristic material structures: initially amorphous silica frameworks with weak hexagonal mesophase ordering (green), intermediate nanolayered silicates (blue), and **MFI**-type zeolite nanosheets (black). Reproduced with permission from Messinger, et al., *Angew. Chem. Int. Ed.* **2015**, *54*, 927-931. Copyright 2015 Wiley Ltd.

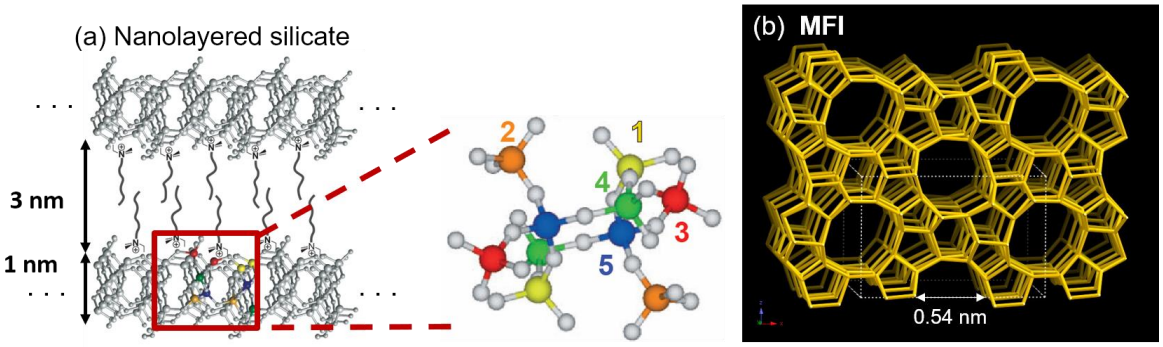

Figure 2.2. (a) Structure of the 2D nanolayered silicates, as determined by extensive previous studies on materials formed under similar hydrothermal synthesis conditions but using monovalent quaternary ammonium cations.[13–16] Schematic diagram courtesy of Prof. Brad Chmelka. (b) Framework structure of MFI-type zeolites (e.g., silicalite-1, ZSM-5). Adapted from the databases of the International Zeolite Association.[18]

Despite the above evidence for the role of the nanolayered silicate species as intermediates in the crystallization of mesostructured MFI-type zeolite frameworks, the sharing of covalent bonds between the layered silicate intermediates and the crystallizing **MFI** frameworks were not established, and other researchers have recently contended that no such non-topotactic transformation occurs.[17] Instead, they hypothesize that mesostructured **MFI**-type zeolite frameworks crystallize through dissolution of the initially formed mesostructured (non-crystalline) silica and the nanolayered silicate, followed by reprecipitation of the **MFI**-type zeolite nanosheets.[17]

Here, mesostructured **MFI**-type zeolite frameworks are established to crystallize non-topotactically through a nanolayered silicate intermediate during hydrothermal synthesis. Complementary electron microscopy and solid-state NMR analyses establish the co-existence of 2D nanolayered silicate species and the crystallizing zeolite framework at intermediate stages of the synthesis. Solid-state 2D NMR analyses, with sensitivity enhanced by dynamic nuclear polarization (DNP), reveal shared covalent ^{29}Si-O-^{29}Si bonds between intermediate nanolayered silicate moieties and the crystallizing MFI zeolite nanosheet framework at intermediate stages of the hydrothermal synthesis. The results and analyses establish the condensation of the 2D nanolayered silicate intermediates to form the 3D framework of the zeolite nanosheets. The new insights provided here on the crystallization mechanisms of industrially-important mesostructured zeolite catalyst materials offer new means to adjust the synthesis and assembly processes, resultant structures, and correspondingly their macroscopic adsorption and catalytic reaction properties.

2.3 Results and discussion

While observation of non-topotactic transformations in zeolite syntheses have been rare in the past,[19,20] there has until now been a lack of experimental probes capable of detecting such subtle molecular rearrangements. 2D ^{29}Si{^{29}Si} NMR techniques provide information on the atomic-level interactions of dipolar- and *J*-coupled pairs of ^{29}Si nuclear spins, whose local (<1 nm) bonding environments are manifested by their respective isotropic chemical shifts. In one-dimensional (1D) NMR spectra, such as 1D ^{29}Si{^{1}H} cross-polarization (CP) magic-angle spinning (MAS) spectra, the ^{29}Si isotropic shifts often overlap. By comparison, 2D ^{29}Si{^{29}Si} NMR spectra provide significantly higher spectral resolution that yield direct information on the local chemical environments and interconnectivities of ^{29}Si framework moieties. These insights are achieved by correlating the isotropic chemical shifts of pairs of ^{29}Si framework sites that are dipole-dipole-coupled through space or *J*-coupled through ^{29}Si-O-^{29}Si covalent bonds. Of these two interactions, dipole-dipole couplings are stronger and vary as the inverse cube of the separation distance between ^{29}Si nuclei. Such couplings in silicates tend to be localized over distances of less than 1 nm,[21,22] which correspond to nearest or next-nearest tetrahedral (T) site neighbors of ^{29}Si nuclei in silicates and zeolites. 2D ^{29}Si{^{29}Si} NMR spectra are typically presented as contour plots with two ^{29}Si chemical shift axes, where pairs of 2D signal intensity from ^{29}Si nuclei are correlated across the spectrum diagonal. Such correlated signal intensities in 2D dipolar-mediated ^{29}Si{^{29}Si} NMR spectra thus identify pairs of dipole-dipole-coupled ^{29}Si nuclei within 1 nm of each other or, in 2D *J*-mediated spectra, pairs of *J*-coupled ^{29}Si nuclei that are connected via covalent (e.g., ^{29}Si-O-^{29}Si) bonds.

That the transforming nanolayered silicate and **MFI**-type zeolite frameworks are

covalently bonded and accompanied by non-topotactic transformation of their structures is proven by the 2D *J*-mediated ^{29}Si{^{29}Si} NMR spectra in Figures 1b, 2, and 3a. In contrast to the relatively strong dipole-dipole interactions (ca. 200 Hz), through-bond *J* interactions are an order-of-magnitude weaker (ca. 10-15 Hz),[21,23] so that the distances probed by 2D ^{29}Si{^{29}Si} *J*-mediated NMR experiments are shorter (ca. 0.5 nm), in practice being sensitive principally to ^{29}Si-O-^{29}Si nearest-neighbor T site pairs.[15] Until now, the weak *J* interactions and low natural isotopic abundance of ^{29}Si (4.7%), have made solid-state 2D *J*-mediated ^{29}Si{^{29}Si} NMR spectra of ^{29}Si-O-^{29}Si through-bond connectivities impractical to acquire without expensive isotopic enrichment of ^{29}Si.

However, recent advances in solid-state NMR spectroscopy, most notably dynamic-nuclear-polarization (DNP)-enhanced MAS NMR techniques at low temperatures (ca. 100 K),[24–27] provide significantly enhanced NMR signal sensitivity that allows the detection and analysis of heteroatom and ^{29}Si environments[28–32] in zeolites at natural abundance ^{29}Si. These advances enable the detection and correlation of ^{29}Si signals from dilute covalently bonded ^{29}Si-O-^{29}Si moieties in the intermediate products of **MFI**-type zeolite crystallization. This is demonstrated, for example, by the 2D DNP-enhanced *J*-mediated ^{29}Si{^{29}Si} spectrum in Figure 2.3 of the intermediate product of mesostructured **MFI**-type zeolite framework crystallization obtained after 8.5 days of hydrothermal synthesis. All of the intensity in the 2D *J*-mediated spectrum arises from pairs of covalently-bonded (through bridging oxygen atoms) *J*-coupled ^{29}Si nuclei, whose isotropic chemical shifts are correlated across the spectrum diagonal (black dashed line). The low temperature conditions required for the DNP-NMR measurements result in broader and slightly displaced ^{29}Si signals at 95 K compared to the 1D ^{29}Si CPMAS spectrum acquired at 298 K due to the freezing of motions

of the diquaternary-ammonium structure-directing species,[15] which do not affect ^{29}Si-O-^{29}Si framework connectivities.

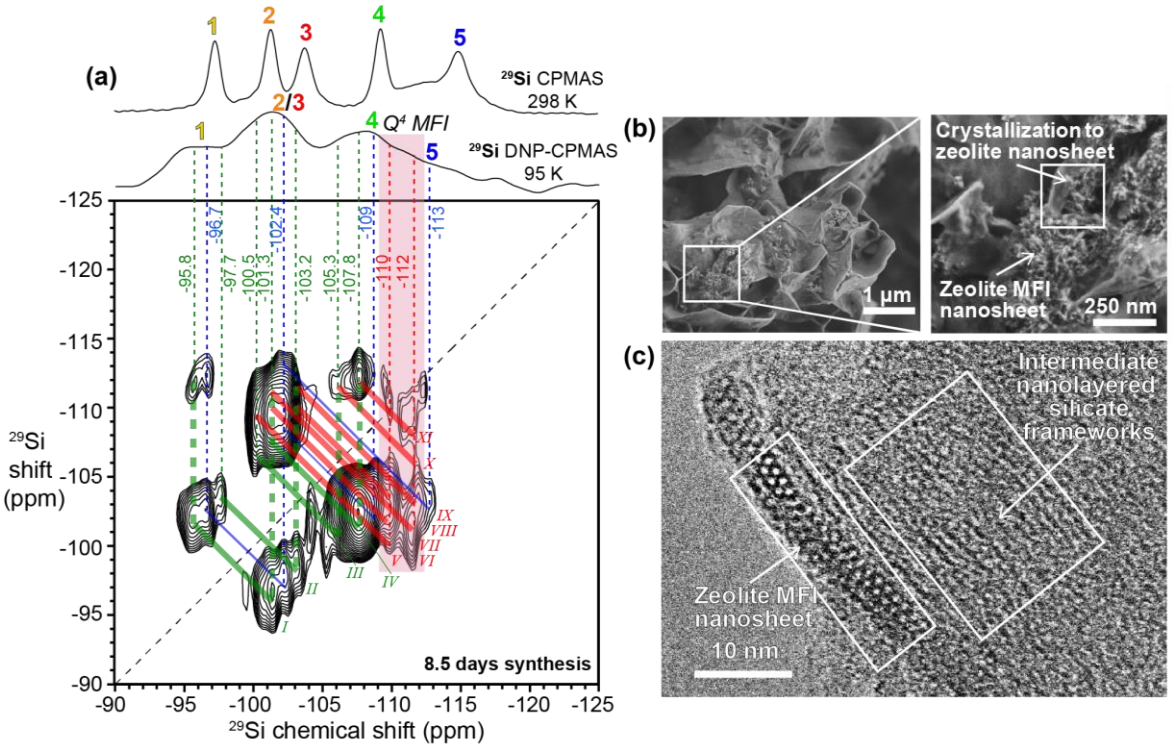

Figure 2.3. (a) Solid-state 2D DNP-enhanced *J*-mediated (through-bond) ^{29}Si{^{29}Si} correlation spectrum of the intermediate product of crystallizing MFI zeolite nanosheets after 8.5 days of hydrothermal synthesis. The spectrum was acquired at 9.4 T, 95 K, 8 kHz MAS, in the presence of 16 mM TEKPol biradical in frozen tetrachloroethane (DNP solvent), and under microwave irradiation at 263 GHz. A 1D ^{29}Si{^{1}H} DNP-enhanced CPMAS spectrum acquired at the same conditions is shown above the 2D spectrum for comparison, as is a 1D ^{29}Si{^{1}H} CPMAS spectrum acquired at 11.7 T, 298 K, and 12.5 kHz MAS. Pairs of correlated signals discussed in the text are indicated by the solid blue, red, and green anti-diagonal lines. Representative **(b)** SEM images and **(c)** TEM image showing regions in which intermediate nanolayered silicate sheets are transforming into MFI zeolite nanosheets.

The nanoscale proximities and shared covalent bonds of the transforming nanolayered silicate and MFI zeolite frameworks are established by 2D dipolar- and *J*-mediated ^{29}Si{^{29}Si} NMR spectra of intermediate products obtained at different stages of hydrothermal synthesis of mesostructured MFI-type zeolite crystallization (Figures 2.3a, 2.4a,b, and 2.5). Despite the broad ^{29}Si signals in the 1D ^{29}Si{^{1}H} DNP-CPMAS spectrum of the intermediate

crystallization product (8.5 days), the 2D ^{29}Si{^{29}Si} *J*-mediated correlation spectrum in Figure 2.3a resolves numerous pairs of correlated signal intensity. These intensities arise from ^{29}Si moieties in the intermediate nanolayered silicates (blue dotted lines), the crystallizing MFI zeolite frameworks (red dotted lines, pink band), and, notably nanolayered silicate species that are undergoing transformation/rearrangement processes (green dotted lines). Specifically, the ^{29}Si signals at -96.7, -102.4, -109, and -113 ppm (blue lines) arise from the intermediate nanolayered silicate species. The signals from sites 2 and 3 of the nanolayered silicates overlap at 95 K due to inhomogeneous broadening of the signals at low temperature (< 253 K).[15] Resolved 2D *J*-mediated ^{29}Si{^{29}Si} signals at -95.8, -97.7, -100.5, -101.3, -103.2, -105.3, and -107.8 ppm associated with transforming nanolayered silicate moieties are correlated with each other (green lines) and signals in the range of -110 to -112 ppm (red lines) from Q^4 species in the crystallizing **MFI**-type zeolite nanosheets. Several of these are especially noteworthy. In particular, the signal at -95.8 from transforming nanolayered silicate site 1 moieties is correlated with the signal at -101.3 from transforming site 2 and 3 moieties (Roman numeral *I*, thick green line), which is also correlated with signal intensities at -110 and -112 ppm (Roman numerals *III* and *IV*, thick red lines) that arise from Q^4 species in the crystallizing MFI-type zeolite nanosheet framework. Similarly, the ^{29}Si signal at -102.4 ppm from transforming nanolayered silicate site 2 and 3 moieties is correlated with the signal at -107.8 ppm from transforming site 4 moieties (Roman numeral *II*, thick green line), the latter of which is also correlated with the signal at -112 ppm from the crystallizing MFI zeolite (Roman numeral *V*, thick red line). These correlated signals provide direct evidence for covalent ^{29}Si-O-^{29}Si bonding between the transforming nanolayered silicates and the mesostructured MFI zeolite nanosheets and, correspondingly, their non-

topotactic rearrangement during crystallization.

The 2D ^{29}Si{^{29}Si} NMR results for the 8.5-day sample are consistent with electron microscopy measurements that probe the morphologies and proximities of the intermediate nanolayered silicate and **MFI**-type zeolite nanosheet products. For example, the representative SEM images in Figure 2.3b show the flower-petal-like morphologies of the nanolayered silicates and the finer MFI zeolite nanosheets, both of which are intimately associated and with no evidence of macroscopically segregated products. The TEM image in Figure 2.3c, shows the nanoscale proximities of the MFI zeolite nanosheets and the transforming nanolayered silicates, similar to the image of the 10-day sample in Figure 2.1, but in a different local orientation. Under the synthetic conditions used here, there is no evidence for the crystallization through dissolution-reprecipitation-type mechanisms.

These insights are corroborated by 2D ^{29}Si{^{29}Si} NMR and TEM analyses of the products of **MFI**-type zeolite hydrothermal crystallization after longer time periods. For example, Figure 2.4a shows the 2D dipolar-mediated ^{29}Si{^{29}Si} correlation spectrum of the product of 10 days of hydrothermal crystallization at 130 °C, adapted from Messinger, et al,[12] which establishes the atomic-level interactions of ^{29}Si sites 1, 2, and 3 in the transforming nanolayered silicates with the ^{29}Si Q^4 sites in the developing **MFI**-type zeolite framework. Significantly, the correlated signal intensities from the crystallizing nanolayered silicates are displaced by approximately 0.5 ppm (red dashed lines in Figure 2.4a) and appear as shoulders alongside the signals at -96.6, -100.7, -103.3, -108.8, and -114.9 ppm (blue dashed lines) from the five resolved ^{29}Si sites in the nanolayered silicates, which have been previously characterized and assigned.[13,16] These displacements in the ^{29}Si signals establish

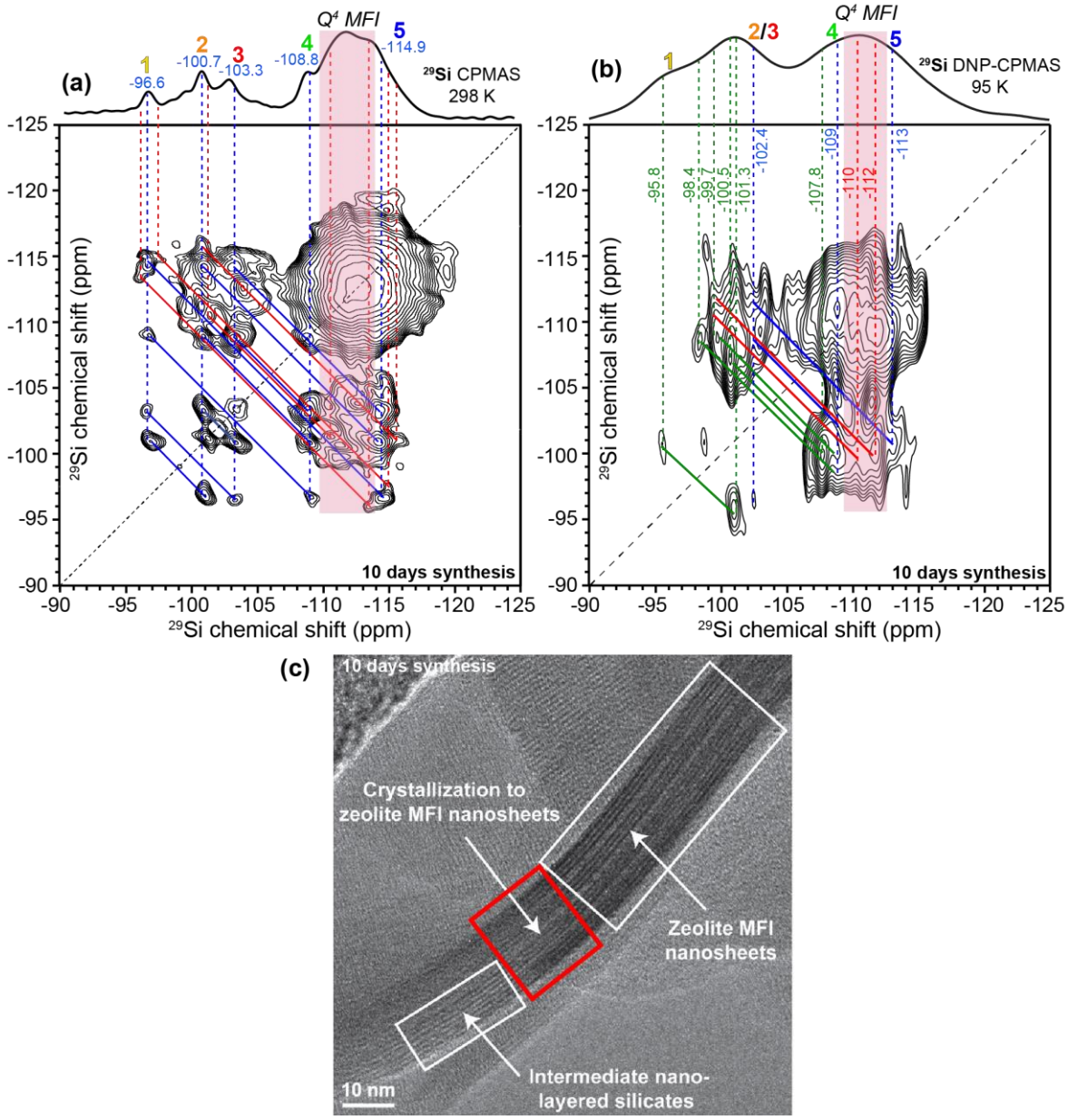

Figure 2.4. (a) Solid-state 2D dipolar-mediated (through-space, <1 nm) $^{29}Si\{^{29}Si\}$ correlation spectrum of the intermediate product of crystallizing MFI zeolite nanosheets after 10 days of hydrothermal synthesis (modified from ref. [12]). The spectrum was acquired at 11.7 T, 298 K, and under MAS conditions of 12.5 kHz. A 1D $^{29}Si\{^{1}H\}$ CPMAS spectrum acquired under the same conditions is shown above for comparison. (b) Solid-state 2D DNP-enhanced J-mediated (through-bond) $^{29}Si\{^{29}Si\}$ correlation spectrum, acquired at 9.4 T, 95 K, 8 kHz MAS, in the presence of 16 mM TEKPol biradical in frozen tetrachloroethane (DNP solvent), and under microwave irradiation at 263 GHz. Pairs of several correlated signals discussed in the text are indicated by the solid blue, red, and green anti-diagonal lines. (c) Representative TEM image showing a region in which intermediate nanolayered silicate sheets are transforming into MFI zeolite nanosheets (modified from ref. 12).

that the local bonding environments of the nanolayered silicates are transforming and, as they do so, are correlated with Q^4 ^{29}Si signals (pink band) that are in the spectral region -110 to -114 ppm of MFI zeolite frameworks that is distinct from any of the Q^4 nanolayered silicate signals (specifically sites 4 and 5 at -108.8 and -114.9 ppm). The displaced signals are associated with regions of the nanolayered silicate frameworks that are rearranging to form mesostructured **MFI** zeolite frameworks.

Furthermore, multiple covalent connectivities among distinct nanolayered silicate and **MFI** zeolite moieties are resolved in the 2D DNP-enhanced *J*-mediated ^{29}Si{^{29}Si} spectrum in Figure 2.4b. As in Figure 2.4a, the 2D *J*-mediated spectrum shows broad correlated intensity that straddles the diagonal over the range -107 to -116 ppm, which arises from overlapping signals associated with covalently bonded ^{29}Si-O-^{29}Si moieties among the 24 crystallographically distinct Q^4 sites of the MFI zeolite frameworks. The advantages of the 2D NMR results are evident in the high spectral resolution that is obtained, even at 95 K, from locally ordered pairs of *J*-coupled, and therefore covalently bonded, ^{29}Si-O-^{29}Si moieties. Specifically, pairs of correlated signals at -102.4, -109, and -113 ppm are observed between the distinct ^{29}Si sites in the nanolayered silicates (blue lines), which are consistent with previously published results, including the known temperature dependencies of the chemical shifts[15] and site connectivities.[13,16,33] Well-resolved 2D ^{29}Si signals are also present at -95.8, -98.4, -99.7, and -100.5, and 101.3 ppm, with distributions of intensity that reflect similar, but distinct, framework bonding environments that are associated with transforming sites 1, 2, and 3 of the nanolayered silicate (green lines). Importantly, these latter signals exhibit intensity correlations with 2D maxima at -107.8 from transforming site 4 moieties and at -110 and -112 ppm from Q^4 ^{29}Si species in the crystallizing MFI zeolite frameworks

(red lines). The 2D *J*-mediated NMR results thus unambiguously establish that ^{29}Si species in the transforming nanolayered silicates are covalently bonded to the crystallizing MFI zeolite frameworks.

If the MFI zeolite frameworks formed only through dissolution and reprecipitation, the nanolayered silicate and MFI-type zeolite moieties would not be covalently bonded to any significant extent. The presence of the *J*-mediated ^{29}Si signals in Figure 2.3a and 2.4b is instead consistent with the non-topotactic rearrangement of nanolayered silicates to form the MFI zeolite frameworks. The regions over which such transformations occur are sufficiently numerous and large that they can be resolved in the representative TEM images shown in Figure 2.3b and 2.4c The transition domains (such as that depicted in the red-boxed region in Figure 2.4c) contain many rearranging ^{29}Si-O-^{29}Si moieties, which are within the ca. 0.5 nm needed for effective *J* coupling and yield correlated ^{29}Si{^{29}Si} signals in the 2D *J*-mediated NMR spectra. The 2D ^{29}Si{^{29}Si} NMR and TEM results provide complementary and consistent information over their complementary length scales.

Importantly, the ^{29}Si signals from the Q^3 mesopore surface moieties of the fully-crystalline MFI zeolite nanosheets (Fig. 2.5) are correlated to those of the transforming nanolayered silicate moieties (Figs. 2.3a and 2.4b). The solid-state 2D *J*-mediated ^{29}Si{^{29}Si} NMR spectrum in of the final mesostructured MFI zeolite nanosheet product after 13 days of hydrothermal synthesis (prepared with 99% isotopic ^{29}Si enrichment for increased sensitivity) shows broad correlated intensity across the diagonal in the region -109 to -117 ppm that arises from covalently connected ^{29}Si-O-^{29}Si pairs of Q^4 sites within the MFI zeolite framework. The red band indicates the sub-portion of this spectral region that does not overlap with any of the nanolayered silicate signals. Individual ^{29}Si resonances associated

with the 24 crystallographically distinct ^{29}Si T-sites within the MFI zeolite structure largely overlap, though several are partially resolved, as indicated by the correlated 2D intensity maxima labeled by Roman numerals *x-xii* (orange lines) in Figure 2.5, which are consistent with previous 2D NMR analyses of bulk MFI zeolite.[34] The 2D spectrum also reveals narrow ^{29}Si signals at -99.7, -101.1, -102.5, and -103.6 ppm, which are attributed to locally ordered Q^3 sites on the mesopore surfaces of the MFI nanosheets, that are correlated with intensity in the range of -114 to -115 ppm (orange lines, Roman numerals *iv-vi*), which corresponds to covalently bonded Q^4 sites within the MFI zeolite nanosheets. Additional narrow ^{29}Si signals are resolved at -105.5, -106.7, and -107.5 ppm that are attributed to locally ordered sub-surface Q^3 sites and are correlated with intensity in the range of -113 to -114 (orange lines, Roman numerals *vii-ix*) from covalently bonded Q^4 sites in the MFI zeolite nanosheets. Intensity correlations are also observed between pairs of Q^3 ^{29}Si signals at -99.7 and -102.5 ppm, at -101.1 and -103.6 ppm, and at -102.5 and -103.6 ppm (orange lines, Roman numerals *i-iii*) in the boxed region of Fig. 2,5), which establishes that their respective Q^3 moieties are covalently bonded, consistent with their mesopore surface locations.

2.4 Conclusions

In summary, the small- and wide-angle X-ray scattering, electron microscopy and 2D NMR results and analyses show that mesostructured MFI zeolite nanosheets form from nanolayered silicates that rearrange non-topotactically under the conditions studied here. In particular, the 2D ^{29}Si{^{29}Si} *J*-mediated NMR analyses establish unambiguously the covalent connectivities of transforming intermediate nanolayered silicate moieties and crystallizing mesostructured MFI zeolite nanosheets. While we cannot rule out dissolution-

recrystallization processes, which may contribute partially here (or under different synthesis conditions[19]), the 2D ^{29}Si{^{29}Si} *J*-mediated NMR results provide strong and direct evidence for non-topotactic rearrangement and condensation of a substantial fraction of the Q^3 and Q^4 Si T-sites in the nanolayered silicates during the mesostructured MFI zeolite crystallization process. This is likely aided by the high density of partially condensed Q^3 moieties in the intermediate nanolayered silicates, as well as in the mesostructured MFI zeolite product. The non-topotactic transformation, rearrangement, and condensation processes of the 2D nanolayered silicates to form the mesostructured 3D MFI zeolite framework is depicted schematically in Figure 2.6. The measurements of structural rearrangements during crystallization of zeolites have been previously difficult to characterize, though are enabled here by the combination of high spectral resolution and unprecedented sensitivity provided by newly available DNP-enhanced 2D *J*-mediated ^{29}Si{^{29}Si} NMR methods.

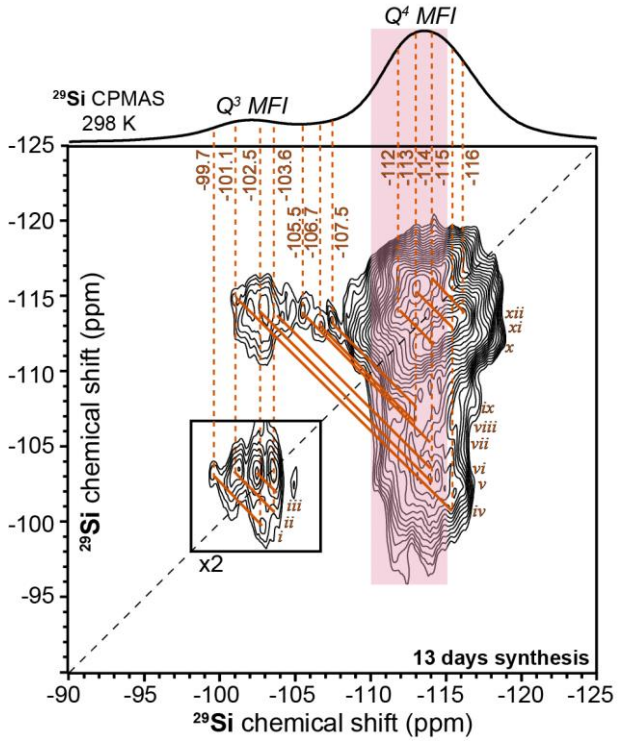

Figure 2.5. Solid-state 2D J-mediated (through-covalent-bond) ^{29}Si{^{29}Si} correlation spectrum of MFI zeolite nanosheets after 13 days of hydrothermal synthesis, isotopically

enriched to 99% abundance in ^{29}Si. The spectrum was acquired at 11.7 T, 298 K, and under MAS conditions of 12.5 kHz. Pairs of correlated signal intensity discussed in the text are indicated by the solid orange anti-diagonal lines.

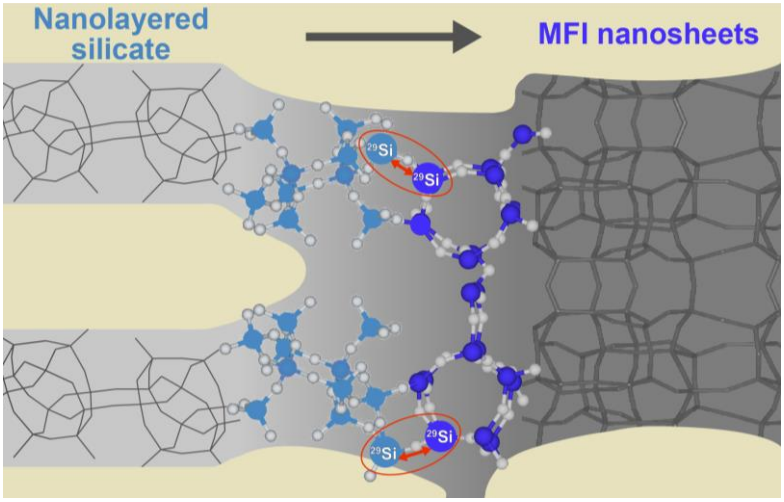

Figure 2.6. Schematic depiction of the non-topotactic rearrangement and condensation of 2D nanolayered silicates to form MFI zeolite nanosheets.

2.5 Materials and methods

The synthesis, X-ray diffraction, and microscopy characterization methods of the final and intermediate products of siliceous MFI zeolite nanosheet crystallization have been described previously.[10,12]

All solid-state DNP-enhanced ^{29}Si{^{29}Si} and ^{29}Si{^{1}H} NMR experiments were carried out on a Bruker ASCEND 400 DNP-NMR spectrometer with a 9.4 Tesla superconducting magnet operating at 399.95 and 79.46 MHz for ^{1}H and ^{29}Si nuclei, respectively, and equipped with a gyrotron and microwave transmission line capable of providing 263 GHz microwave irradiation at the sample and a low-temperature 3.2 mm MAS probe. The DNP-enhanced ^{29}Si{^{1}H} and ^{29}Si{^{29}Si} spectra were acquired at 95 K, 8 kHz MAS, under continuous microwave irradiation at 263 GHz, and in the presence of 16 mM TEKPol biradical[35] in frozen 1,1,2,2-tetrachloroethane (DNP solvent), which do not influence the surface structures

of the material.[36] The ^{29}Si DNP NMR signal enhancements were quantified as the ratio of the fully-relaxed ^{29}Si{^{1}H} CPMAS signal intensities obtained with and without microwave irradiation, which was measured to be ca. 9 and 23 for the intermediate products obtained after 10 and 8.5 days of hydrothermal synthesis, respectively. Solid-state 2D DNP-enhanced *J*-mediated ^{29}Si{^{29}Si} spectra[15,37] were acquired using ^{29}Si{^{1}H} cross-polarization with a contact time of 4 ms to circumvent the effects of the long longitudinal ^{29}Si spin relaxation times. An experimentally optimized half-spin-echo (τ) delay of 16 ms and a repetition time of 8.5 s were used for best overall efficiency.

The solid-state 2D *J*-mediated ^{29}Si{^{29}Si} spectrum of MFI zeolite nanosheets after 13 days of hydrothermal synthesis, isotopically enriched to 99% abundance in ^{29}Si, was acquired on a Bruker AVANCE IPSO 500 NMR spectrometer with an 11.74 Tesla widebore superconducting magnet operating at 500.13 and 99.35 MHz for ^{1}H and ^{29}Si nuclei, respectively. The spectrum was acquired at 298 K, using ^{29}Si{^{1}H} cross-polarization with a contact time of 4 ms, with an experimentally-optimized τ delay of 5 ms, and a repetition time of 1.2 s.

2.6 References

(1) Davis, M. E. *Nature.* **2002**, *417*, 813.
(2) Morris, R. E.; Wheatley, P. S. *Angew. Chemie - Int. Ed.* **2008**, *47*, 4966.
(3) Babel, S.; Kurniawan, T. A. *J. Hazard. Mater.* **2003**, *97*, 219.
(4) Vogt, E. T. C.; Weckhuysen, B. M. *Chem. Soc. Rev.* **2015**, *44*, 7342.
(5) Meirer, F.; Kalirai, S.; Weker, J. N.; Liu, Y.; Andrews, J. C.; Weckhuysen, B. M. *Chem. Commun.* **2015**, *51*, 8097.
(6) Tian, P.; Wei, Y.; Ye, M.; Liu, Z. *ACS Catal.* **2015**, *5*, 1922.
(7) Gallego, E. M.; Portilla, M. T.; Paris, C.; León-Escamilla, A.; Boronat, M.; Moliner, M.; Corma, A. *Science.* **2017**, *355*, 1051.
(8) Runnebaum, R. C.; Ouyang, X.; Edsinga, J. A.; Rea, T.; Arslan, I.; Hwang, S. J.; Zones, S. I.; Katz, A. *ACS Catal.* **2014**, *4*, 2364.
(9) Choi, M.; Na, K.; Kim, J.; Sakamoto, Y.; Terasaki, O.; Ryoo, R. *Nature* **2009**, *461*, 246.
(10) Na, K.; Chol, M.; Park, W.; Sakamoto, Y.; Terasakl, O.; Ryoo, R. *J. Am. Chem. Soc.* **2010**, *132* , 4169.
(11) Na, K.; Jo, C.; Kim, J.; Cho, K.; Jung, J.; Seo, Y.; Messinger, R. J.; Chmelka, B. F.; Ryoo, R.

Science. **2011**, *333* (6040), 328.
(12) Messinger, R. J.; Na, K.; Seo, Y.; Ryoo, R.; Chmelka, B. F. *Angew. Chemie - Int. Ed.* **2014**, *54*, 927.
(13) Christiansen, S. C.; Zhao, D.; Janicke, M. T.; Landry, C. C.; Stucky, G. D.; Chmelka, B. F. *J. Am. Chem. Soc.* **2001**, *123*, 4519.
(14) Hedin, N.; Graf, R.; Christiansen, S. C.; Gervais, C.; Hayward, R. C.; Eckert, J.; Chmelka, B. F. *J. Am. Chem. Soc.* **2004**, *126*, 9425.
(15) Cadars, S.; Mifsud, N.; Lesage, A.; Epping, J. D.; Hedin, N.; Chmelka, B. F.; Emsley, L. *J. Phys. Chem. C* **2008**, *112*, 9145.
(16) Cadars, S.; Allix, M.; Brouwer, D. H. H.; Shayib, R.; Suchomel, M.; Garaga, M. N. N.; Rakhmatullin, A.; Burton, A. W. W.; Zones, S. I. I.; Massiot, D.; Chmelka, B. F. F. *Chem. Mater.* **2014**, *26*, 6994.
(17) Goesten, M. G.; Zhu, X.; Mezari, B.; Hensen, E. J. M. *Angew. Chemie - Int. Ed.* **2017**, *56*, 5160.
(18) Baerlocher, C.; McCusker, L. B. Database of Zeolite Structures.
(19) Lupulescu, A. I.; Rimer, J. D. *Science.* **2014**, *344*, 729.
(20) De Yoreo, J. J.; Gilbert, P. U. P. A.; Sommerdijk, N. A. J. M.; Penn, R. L.; Whitelam, S.; Joester, D.; Zhang, H.; Rimer, J. D.; Navrotsky, A.; Banfield, J. F.; Wallace, A. F.; Michel, F. M.; Meldrum, F. C.; Colfen, H.; Dove, P. M. *Science.* **2015**, *349*, 6760.
(21) Brouwer, D. H.; Kristiansen, P. E.; Fyfe, C. A.; Levitt, M. H. *J. Am. Chem. Soc.* **2005**, *127*, 542.
(22) Brouwer, D. H.; Darton, R. J.; Morris, R. E.; Levitt, M. H. **2005**, *11*, 10365.
(23) Cadars, S.; Brouwer, D. H.; Chmelka, B. F. *Phys. Chem. Chem. Phys.* **2009**, *11*, 1825.
(24) Maly, T.; Debelouchina, G. T.; Bajaj, V. S.; Hu, K.-N.; Joo, C.-G.; Mak–Jurkauskas, M. L.; Sirigiri, J. R.; van der Wel, P. C. A.; Herzfeld, J.; Temkin, R. J.; Griffin, R. G. *J. Chem. Phys.* **2008**, *128*, 52211.
(25) Lesage, A.; Lelli, M.; Gajan, D.; Caporini, M. A.; Vitzthum, V.; Mieville, P.; Alauzun, J.; Roussey, A.; Thieuleux, C.; Mehdi, A.; Bodenhausen, G.; Coperet, C.; Emsley, L. *J. Am. Chem. Soc.* **2010**, *132*, 15459.
(26) Rossini, A. J.; Zagdoun, A.; Lelli, M.; Lesage, A.; Copéret, C.; Emsley, L. *Acc. Chem. Res.* **2013**, *46*, 1942.
(27) Ni, Q. Z.; Daviso, E.; Can, T. V.; Markhasin, E.; Jawla, S. K.; Swager, T. M.; Temkin, R. J.; Herzfeld, J.; Griffin, R. G. *Acc. Chem. Res.* **2013**, *46*, 1933.
(28) Gunther, W. R. *J. Am. Chem. Soc.* **2014**, *136*, 6219.
(29) Wolf, P.; Valla, M.; Rossini, A. J.; Comas-Vives, A.; Núñez-Zarur, F.; Malaman, B.; Lesage, A.; Emsley, L.; Copéret, C.; Hermans, I. *Angew. Chemie - Int. Ed.* **2014**, *53*, 10179.
(30) Lee, D.; Monin, G.; Duong, N. T.; Lopez, I. Z.; Bardet, M.; Mareau, V.; Gonon, L.; De Paëpe, G. *J. Am. Chem. Soc.* **2014**, *136*, 13781.
(31) Wolf, P.; Valla, M.; Núñez-Zarur, F.; Comas-Vives, A.; Rossini, A. J.; Firth, C.; Kallas, H.; Lesage, A.; Emsley, L.; Copéret, C.; Hermans, I. *ACS Catal.* **2016**, *6*, 4047.
(32) Smeets, S.; Berkson, Z. J.; Xie, D.; Zones, S. I.; Wan, W.; Zou, X.; Hsieh, M. F.; Chmelka, B. F.; McCusker, L. B.; Baerlocher, C. *J. Am. Chem. Soc.* **2017**, *139*, 16803.
(33) Brouwer, H. W.; Cadars, S.; Eckert, J.; Liu, Z.; Terasaki, O.; Chmelka, B. F. *J. Am. Chem. Soc.* **2013**, *135*, 5641.
(34) Fyfe, C. A.; Grondey, H.; Feng, Y.; Kokotailo, G. T. *Chem. Phys. Lett.* **1990**, *173*, 211.
(35) Zagdoun, A.; Casano, G.; Ouari, O.; Schwarzwälder, M.; Rossini, A. J.; Aussenac, F.; Yulikov, M.; Jeschke, G.; Coperet, C.; Lesage, A.; Tordo, P.; Emsley, L. *J. Am. Chem. Soc.* **2013**, *135*, 12790.
(36) Sangodkar, R. P.; Smith, B. J.; Gajan, D.; Rossini, A. J.; Roberts, L. R.; Funkhouser, G. P.; Lesage, A.; Emsley, L.; Chmelka, B. F. *J. Am. Chem. Soc.* **2015**, *137*, 8096.
(37) Lesage, A.; Bardet, M.; Emsley, L. *J. Am. Chem. Soc.* **1999**, *121*, 10987.

Chapter 3

Well-defined silanols in the structure of the calcined high-silica zeolite SSZ-70

Adapted from: S. Smeets, Z. J. Berkson, D. Xie, S. I. Zones, W. Wan, X. Zou, M.-F. Hsieh, B. F. Chmelka, L. B. McCusker, C. Baerlocher, *Journal of the American Chemical Society* **2017**, *139* (46), 16803-16812

3.1 Abstract

Recently, layered **MWW**-type zeolites such as SSZ-70 have been established as versatile supports for diverse catalytic materials, especially for reactions involving large molecules. However, their structures, and particularly the features at the interlayer surfaces, have been elusive. Here, the structure of the calcined form of the high-silica zeolite SSZ-70 has been elucidated by combining synchrotron X-ray powder diffraction (XRPD), high resolution transmission electron microscopy (HRTEM), and two-dimensional (2D) dynamic nuclear polarization (DNP)-enhanced NMR techniques. The framework structure of SSZ-70 is a polytype of **MWW** and can be viewed as a disordered ABC-type stacking of **MWW**-layers. HRTEM and XRPD simulations show that the stacking sequence is almost random, with each layer being shifted by ±1/3 along the <110> direction with respect to the previous one but with a small preponderance of ABAB stacking. DNP-enhanced 2D ^{29}Si{^{29}Si} *J*-mediated NMR analyses of calcined Si-SSZ-70 at natural ^{29}Si isotopic abundance (4.7%) establish the through-covalent-bond ^{29}Si-O-^{29}Si connectivities of distinct Si sites in the framework. The DNP-NMR results corroborate the presence of **MWW**-layers and, more importantly, identify two distinct types of Q^3 silanol species at the surfaces of the interlayer regions. In the first, an

isolated silanol group protrudes into the interlayer space pointing towards the pocket in the adjacent layer. In the second, the surrounding topology is the same, but the isolated -SiOH group is missing, leaving a nest of three Si-O-H groups in place of the three Si-O-Si linkages. The analyses clarify the structure of this complicated material, including features that do not exhibit long-range order. With these insights, the novel catalytic behavior of SSZ-70 can be better understood and opportunities for enhancement recognized.

3.2 Introduction

Zeolite molecular sieves have nanoporous architectures with pore openings that are typically less than a nanometer in diameter. The tetrahedrally coordinated Si atoms in the silicate zeolite framework structure may also be replaced with other elements such as Al, leading to charge imbalance and an opportunity for additional cations to be introduced into the structure. If protons are used to counterbalance such framework negative charges, very strong acid catalysts can be created that have great impact in a large variety of chemical and petrochemical processes.[1] In particular, they are used to promote catalytic rearrangement reactions in which the location of the acid sites within the zeolite structure have a strong effect on selectivity and activity for a given reaction.[2] The nanopore architecture and composition of a zeolite are important factors in controlling the transition states between reactants and products within the confining nanopores.[3] Furthermore, the diffusion pathways for the products, which are influenced by the structure of the zeolite framework and crystallite sizes, also play a significant role in the selectivity.[4]

Indeed, there is an increasing understanding that instead of focusing on the entire zeolite structure, portions of the internal zeolite architecture can be exploited in an optimal fashion

to design the catalytic sites. Notable recent examples include (1) the development of a novel carbonylation catalyst using only a sub-domain of the zeolite mordenite,[5,6] (2) the creation of acid sites in only the large pores of a borosilicate zeolite where there are both large and small pores and boron has been selectively replaced post-synthetically with aluminum,[2,7] and (3) an elegant effort to synthesize a zeolite using an organic structure directing agent (OSDA) designed to mimic the structure of the desired transition state of a reaction.[8] These advances broaden our view of how to use zeolites as catalysts, going beyond the previous boundaries of just focusing on the size of the pores. Consequently, understanding the fine and local structural details of a new zeolite is essential for designing an optimal catalyst.

Here, we present a comprehensive structural analysis of the novel zeolite SSZ-70, which has already begun to emerge as an important and novel catalytic material. SSZ-70 was first synthesized in borosilicate form when Zones and Hwang were exploring a system featuring both borosilicate inorganic reaction conditions and HF as a mineralizer (in contrast to the conventional alkaline type of reaction normally used in zeolite syntheses).[9] In this environment and using *N*,*N*′-diisopropyl imidazolium (Figure 3.1), which has very high selectivity for **MTT**-type frameworks under alkaline conditions,[10] as the OSDA, the novel phase B-SSZ-70 was formed.[11]

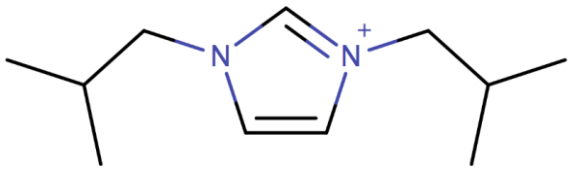

Figure 3.1. *N*,*N*′-diisobutyl imidazolium cation used as the organic structure-directing agent in the syntheses of SSZ-70.

In a later study, Archer and coworkers[12] extended the range of imidazolium-type OSDAs that favor the formation of SSZ-70. They also showed that aluminosilicate analogs (Al-SSZ-70) could be made, and developed the synthesis chemistry to allow alkaline media to be used instead of HF. Scanning electron microscopy (SEM) images of these materials showed them to be platelets, as would be expected for a layered material, and their X-ray powder diffraction (XRPD) patterns contained both broad and sharp peaks, which would be consistent with well-ordered layers stacked in a somewhat disordered fashion. Further characterization by magic angle spinning (MAS) nuclear magnetic resonance (NMR) showed that SSZ-70 was related to, but distinctly different from, MCM-22[13] (**MWW**-type framework structure),[14] which has already been developed as a commercial catalyst for the alkylation of aromatics.[15] MCM-22 and its **MWW**-type analogs (e.g. ITQ-1[16] and SSZ-25[17]) are unique among the known zeolites in that they only form the fully 4-connected **MWW**-type framework upon calcination. The as-synthesized materials are layered (alumino)silicates that lend themselves to exfoliation.

In view of these observations, it appeared that as-synthesized SSZ-70 was likely to be organized in layers, supported by electron microscopy images (Figure 3.2). Exfoliation procedures were applied, and indeed, exfoliated Al-SSZ-70 was found to exhibit enhanced catalysis rates for alkylation reactions.[18] In the calcined form, Al-SSZ-70 exhibits high activity as a cracking catalyst, and subsequent deactivation is different from that of SSZ-25 (**MWW)**, which becomes more selective with coking.[19] This difference in catalytic performance indicates that there are some key differences in the structural details of zeolites SSZ-25 and 70, even though both are built from similar layers. With more structural information, we hoped to rationalize the different activities of SSZ-70 as a catalyst when the

material has been delaminated and certain external features at the surface of the crystalline zeolite modified. The replacement of boron sites located in wells along the interlayer surface of B-SSZ-70 with other heteroatoms, for example, has proven to be particularly effective in creating catalysts that are suitable for larger reactant molecules, while retaining the important confinement features of a zeolite catalyst.[18,20] We also wanted to understand why the structure of SSZ-70 lends itself to delamination via more gentle, non-destructive conditions, which allow the integrity of the boron replacement sites in the surface structure to be retained.[21] Most of the previous delamination work on other zeolite materials required harsh basic conditions that led to some amorphisation of the materials, which is detrimental to the catalytic properties.[22]

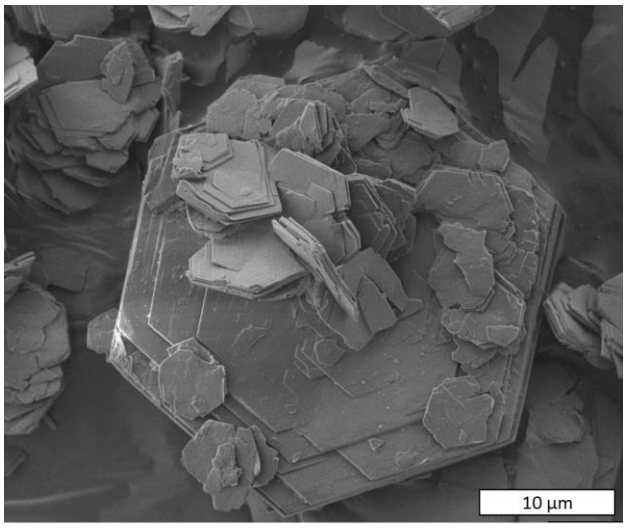

Figure 3.2. Representative SEM image of as-synthesized Al-SSZ-70.

We realized early on that a straightforward determination of the structure of SSZ-70 from diffraction data alone would not be possible because of the disorder in the material. Therefore, we combined three highly complementary state-of-the-art techniques to elucidate the structure. Here, we present the structure of calcined siliceous SSZ-70, as determined from

a combination of high-resolution transmission electron microscopy (HRTEM), synchrotron X-ray powder diffraction (XRPD), and dynamic-nuclear-polarization (DNP)-enhanced MAS NMR spectroscopy data.

3.3 Results and discussion

3.3.1 Long-range order in Si-SSZ-70

Analyses of synchrotron X-ray powder diffraction (XRPD) data (Figure 3) yields the unit cell parameters of as-made and calcined SSZ-70 (Table 3.1). Although the XRPD pattern of as-synthesized SSZ-70 contains a mixture of broad and sharp reflections, it could still be indexed with a hexagonal unit cell ($P6_3/mmc$, a = 14.223 Å, c = 53.786 Å). SSZ-70 crystallizes in the form of well-defined hexagonal flakes approximately 50 nm in thickness (Figure 3.2), consistent with the unit cell and space group symmetry. The *a* lattice parameter is similar to and the *c* parameter is approximately double that of the high-silica **MWW**-type precursor ITQ-1p (Table 3.1). A further indication of a structural relationship could be found in the HRTEM images, which show the presence of layers similar to those in **MWW**-type materials (Figure 3.4a), and also reveal the irregular stacking of these layers (Figure 3.4b). Each layer is shifted by approximately ±1/3 in the horizontal direction (<110>) with respect to the previous one, while in the **MWW** framework structure the layers are aligned directly above one another. The dark band observed between the **MWW**-layers does not necessarily indicate the presence of additional siliceous species in the interlayer region, as HRTEM images simulated using a structure model built by stacking the **MWW**-layers only (overlay in Figure 3.4a) match the experimental image very well (Supporting Information).

Determination of the fine structural details of the interlayer regions of as-made SSZ-70 (and, ITQ-1p as well), remains elusive and is the subject of future study.

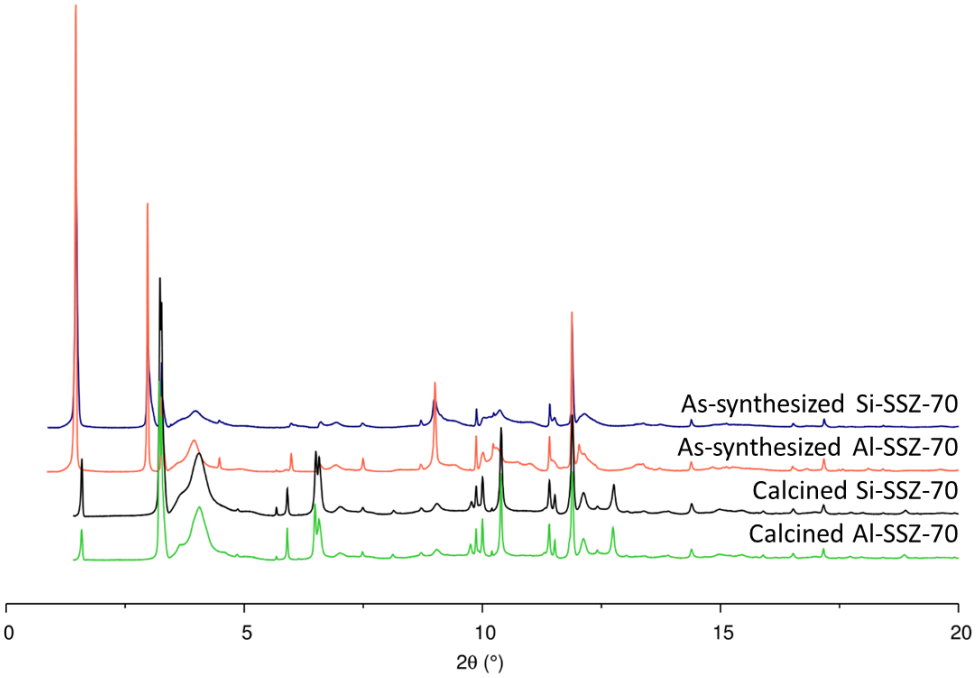

Figure 3.3. From top to bottom: Synchrotron XRPD data collected on as-synthesized Si-SSZ-70 and Al-SSZ-70 and calcined Si-SSZ-70 and Al-SSZ-70.

Table 3.1. Unit cell parameters of as-synthesized and calcined Si-SSZ-70 and ITQ-1

	Space group	*a* (Å)	*c* (Å)	Vol. (Å^3)
ITQ-1P (as-synth.)[20]	*P6/mmm*	14.2091	27.4877	4806.39
ITQ-1 (calcined)[16]	*P6/mmm*	14.2081	24.9450	4361.00
SSZ-70 (as-synth.)	*P6$_3$/mmc*	14.223	53.786	9422.85
SSZ-70 (calcined)	*P6$_3$/mmc*	14.227	49.806	8730.64

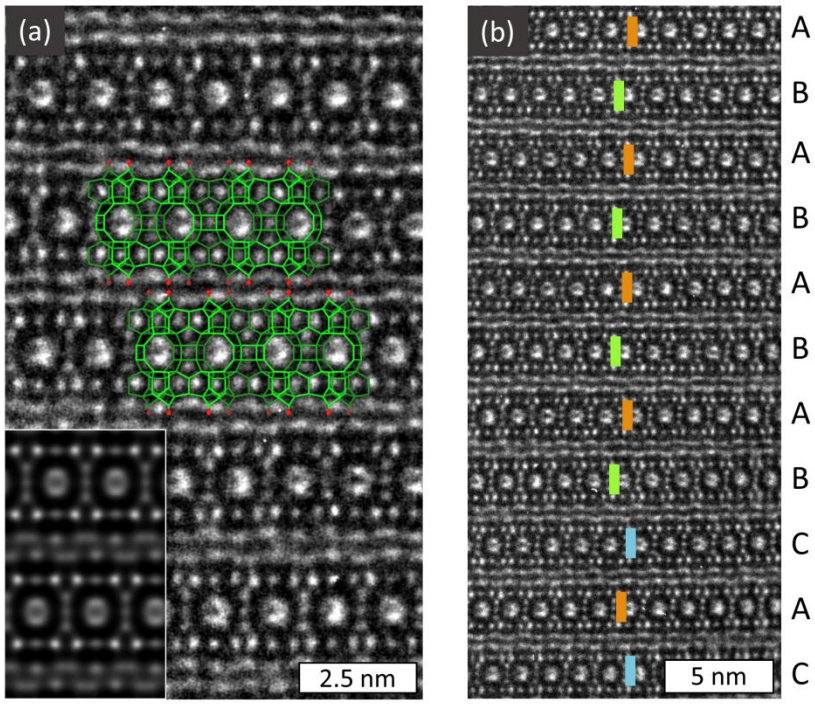

Figure 3.4. HRTEM images along the *b*-axis of as-synthesized Al-SSZ-70. (a) Image with an outline of the **MWW**-layers overlaid. Each layer is shifted by ±1/3 along <100> with respect to the neighboring one. The inset in the lower left corner shows an image simulation using a structure model built by stacking the **MWW**-layers only. (b) Larger area with a schematic description of the ABC stacking disorder. The colored lines indicate the position of the center of the 10-ring pore.

The XRPD pattern of the calcined material also yields a hexagonal unit cell ($P6_3/mmc$, a = 14.227 Å, c = 49.806 Å). The contraction of approximately 4 Å in the c direction with respect to the as-synthesized form is similar to that found in ITQ-1 (Table 1), supporting the hypothesis that SSZ-70 consists of silicate layers that condense upon calcination. The broadened reflection around 4°2θ (013) in the XRPD patterns of both the as-synthesized and the calcined materials (Figure 3.3) provides clear evidence that stacking disorder is present in SSZ-70, and that this disorder persists through calcination. Unfortunately, this also prevents its structure from being determined and refined in a conventional manner. Therefore, we first looked at what is known about its ordered **MWW**-type counterpart, ITQ-1.[16]

3.3.2 Relationship between SSZ-70 and ITQ-1

ITQ-1P is the layered precursor to the pure silica **MWW**-type material ITQ-1, which is formed only upon calcination, when the layers condense to form an ordered three-dimensional framework (Figure 3.5). The relationship between as-synthesized and calcined SSZ-70 is similar. Solid-state ^{29}Si MAS-NMR spectra reported for high-silica ITQ-1P show an intense signal (ca. 30% of the total ^{29}Si signal intensity) around -95 ppm, which is characteristic of Q^3 (Si with three O-Si linkages) silicate species.[16] Camblor and coworkers showed that this peak disappears completely upon calcination, consistent with a condensation of the silicate layers. Structure refinement using XRPD data confirmed that calcined ITQ-1 has low defect concentrations, and a three-dimensional, fully 4-connected framework structure. In the same study, they hypothesized that the distribution of Q^3 Si sites in the precursor is not random. Indeed, in the follow-up study by Njo,[23] the Q^3 sites in ITQ-1P were assigned to Si1 silanol groups protruding from the surface of the layer (Figure 3.5c), and the best XRPD agreement values were obtained with partial occupation (occupancy = 0.5) of these Si sites. It should be noted that the *c* lattice parameter of ITQ-1P is too small to accommodate the simultaneous occupation of opposing Si1 silanol groups in adjacent layers, consistent with a Si1 occupancy of 0.5. An attempt was made to determine the nature of the species in the interlayer region of the precursor, in order to better understand what happens during calcination, but the results were inconclusive.

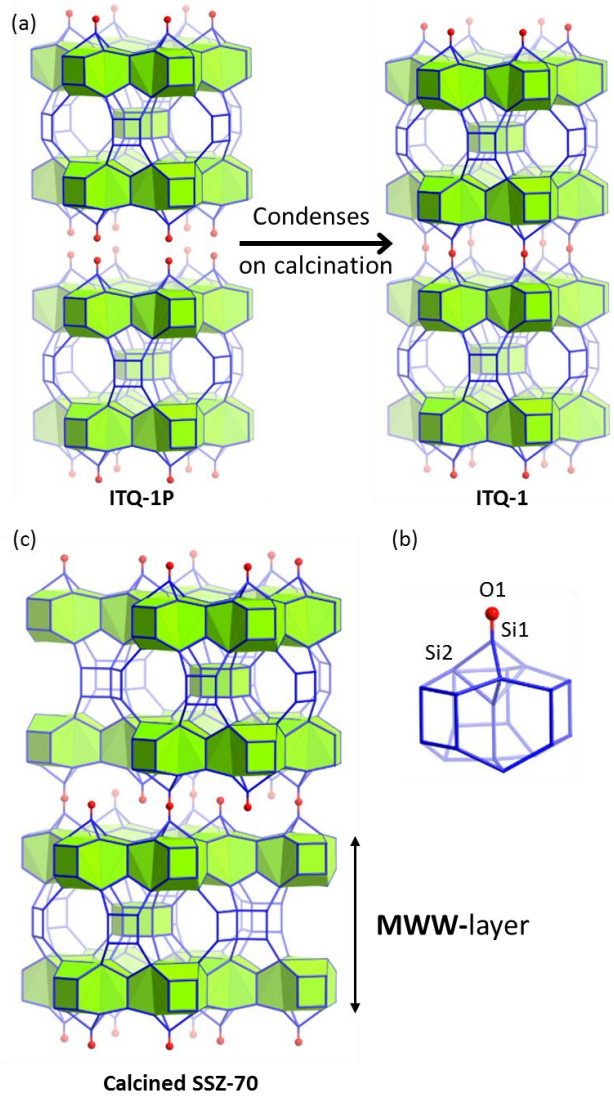

Figure 3.5. (a) Schematic representation of ITQ-1P and its transformation into ITQ-1 (**MWW**) upon calcination. (b) Schematic representation of the structure of calcined SSZ-70, showing the **MWW**-layers. (c) Building unit of **MWW** showing the terminal -SiOH group responsible for linking the layers.

3.3.3 Initial structural model of calcined SSZ-70

Conventional ^{29}Si MAS-NMR spectra for as-synthesized and calcined SSZ-70 have been reported as part of the study by Archer and coworkers.[14] The spectrum for as-synthesized SSZ-70 is very similar to that of ITQ-1P. The ^{29}Si signal at -95 ppm present in ITQ-1P can also be found in the spectrum of as-synthesized Si-SSZ-70, with the key difference that it

does not disappear completely upon calcination. Based on the intensity of this peak, the population of Q^3 Si sites for as-synthesized SSZ-70 was estimated to be approximately 10%, and after calcination, 5%. This indicates that approximately half of the terminal –SiOH species condense on calcination to form Q^4 Si species that connect the **MWW**-layers.

With the constraint that only half of the terminal Si atoms in adjacent **MWW** layers need to align with one another for condensation, a model was proposed for calcined SSZ-70 (Figure 3.6a). In this model, which we refer to as Model 1, half of the interlayer Si atoms are connected to form an oxygen bridge to the neighboring layer, while the other half point into the pocket of that layer. The coordinates for the atoms in the second layer are $x + 1/3$, $y + 2/3$ or $x + 2/3$, $y + 1/3$ where x and y are those for the first layer (Figure 3.6). This model fits well with the disorder observed in the HRTEM images of the as-synthesized material, because there are two possible positions for each layer, just as in the ABC-type stacking of spheres.

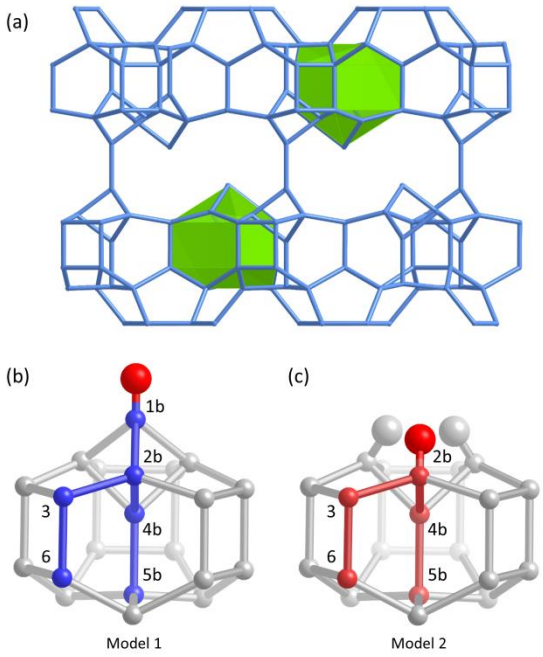

Figure 3.6. (a) Projection of the interlayer region of calcined Si-SSZ-70 highlighting the cages with silanol groups. (b) The cage structure for Model 1 showing the four-site

connectivity path with blue lines, and (c) for Model 2 showing the three-site connectivity path with red lines.

Previous ^{29}Si MAS-NMR results indicated the presence of approximately 3.3 Q^3 Si species per layer, but in our working model (Model 1; Figure 3.6a), there are only two. Therefore, a second model with all of these silanol groups removed to create nests of three silanol groups (Figure 3.6b) was constructed. The simulated diffraction patterns corresponding to Model 1 and Model 2 are very similar to that of Model 1, but neither reproduce the observed data perfectly, perhaps because residual OSDA species or adsorbed H_2O are not accounted for in the model. Ultimately, the XRPD data cannot distinguish Model 1 from Model 2 definitively, so we turned to NMR to learn more.

3.3.4 Model 1 or Model 2?

By taking advantage of the large enhancements in signal sensitivity provided by DNP-enhanced MAS NMR techniques at low temperatures,[24–27] powerful 2D NMR methods can be applied to measure and understand the compositions, structures, covalent interconnectivities, and molecular-level interactions of ^{29}Si species in zeolite frameworks at natural isotopic abundance (4.7%). This precludes the need for expensive isotopic enrichment in ^{29}Si and allows 2D NMR analyses to be conducted on the same calcined Si-SSZ-70 sample as characterized by synchrotron XRPD.

Molecular interactions among the organic DNP solvent molecules, adsorbed water, and framework Q^3 and Q^4 silicate species in calcined zeolite Si-SSZ-70 are established by using 2D DNP-enhanced NMR methods to measure and correlate their respective isotropic chemical shifts. For example, 2D ^{29}Si{^{1}H} DNP-enhanced HETeronuclear CORrelation

(HETCOR) methods selectively detect ^{29}Si species that are dipole-dipole-coupled to ^{1}H nuclei that are in close molecular proximities (<1 nm). The resulting 2D NMR spectra are plotted as 2D frequency contour maps with normalized ^{1}H and ^{29}Si chemical shift axes (Hz/MHz or ppm), such as shown in Figure 3.7, where the 2D intensity correlations establish the site-specific interactions and relative proximities of dipole-dipole coupled ^{29}Si and ^{1}H nuclei. For example, the 2D DNP-enhanced ^{29}Si{^{1}H} HETCOR spectra in Figures 3.7 demonstrate that Q^3 -SiOH moieties in the calcined zeolite Si-SSZ-70 framework exhibit hydrogen bonding interactions that are consistent with structural Models 1 and 2. The 2D spectra yield improved spectral resolution compared to the 1D ^{29}Si{^{1}H} CPMAS spectra shown above the 2D contour maps, which enables the detection of a number of distinct correlated ^{1}H-^{29}Si signals. In the 2D spectrum acquired at very short ^{29}Si{^{1}H} contact times (0.2 ms, Figure 3.7a), ^{1}H signals are detected in the chemical shift range 2.0 to 4.4 ppm from relatively isolated -SiOH groups that are correlated with ^{29}Si signals in the range -95 to -103 ppm from silanol Q^3 ^{29}Si species, and also at -105 ppm from Q^4 ^{29}Si species that are in close proximities to silanol moieties such as Si2b in Model 1. The presence of isolated silanol groups that exhibit little hydrogen bonding is consistent with Model 1 of calcined Si-SSZ-70 shown in Figure 3.6a. There are also ^{1}H signals at 6.5 and 7.2 ppm which arise from the DNP solvent (1,1,2,2-tetrachloroethane, TCE) which are correlated with all of the ^{29}Si signals, indicating that the TCE solvent molecules have entered into the zeolite nanopores, and are present both in the inter- and intralayer channel systems.

Importantly, high frequency ^{1}H signals in the chemical shift range 8 to 10 ppm arise from H-bonded -SiOH groups that are correlated with ^{29}Si signals from Q^3 silanol species at -93 to -103 ppm, and also with ^{29}Si signals from Q^4 species at -105 to -115 ppm. ^{1}H signals

from H-bonded -SiOH groups over this range of ^{1}H frequencies are consistent with predictions based on empirical relations for ^{1}H isotropic chemical shifts as functions of -SiOH··OSi- distance in silicate glasses and minerals.[28,29] The shortest -OH··O distances (2.8 Å) associated with -SiOH··OHSi- hydrogen bonds in Model 2 are consistent with the ^{1}H signals in the region 8-10 ppm. The presences of both isolated and strongly H-bonded -SiOH species are consistent with both of the candidate structures proposed for calcined zeolite Si-SSZ-70.

All of the distinct ^{29}Si moieties present in the calcined zeolite Si-SSZ-70 are in close molecular proximities to each other, as established by the 2D $^{29}Si\{^{1}H\}$ DNP-HETCOR spectrum acquired at a longer contact time (5 ms, Figure S3b). The spectral resolution is reduced at the longer contact time because the spectrum manifests longer range ^{29}Si-^{1}H interactions, such that each ^{29}Si signal is correlated with a broader distribution of ^{1}H signals than at shorter contact times. Nevertheless, different ^{1}H signals are detected at 2.2 to 3.0 ppm from isolated -SiOH groups, 6.3 to 6.7 ppm from frozen TCE solvent molecules, and 9.5 ppm from H-bonded -SiOH groups. Importantly, these ^{1}H signals are all correlated with broad ^{29}Si signals with partially-resolved peak maxima at -96, -99, -105, -111, and -113 ppm, establishing the close mutual proximities (<1 nm) of the corresponding ^{29}Si and ^{1}H environments. These results suggest that the different types of -SiOH moieties are intermixed over nanoscale dimensions.

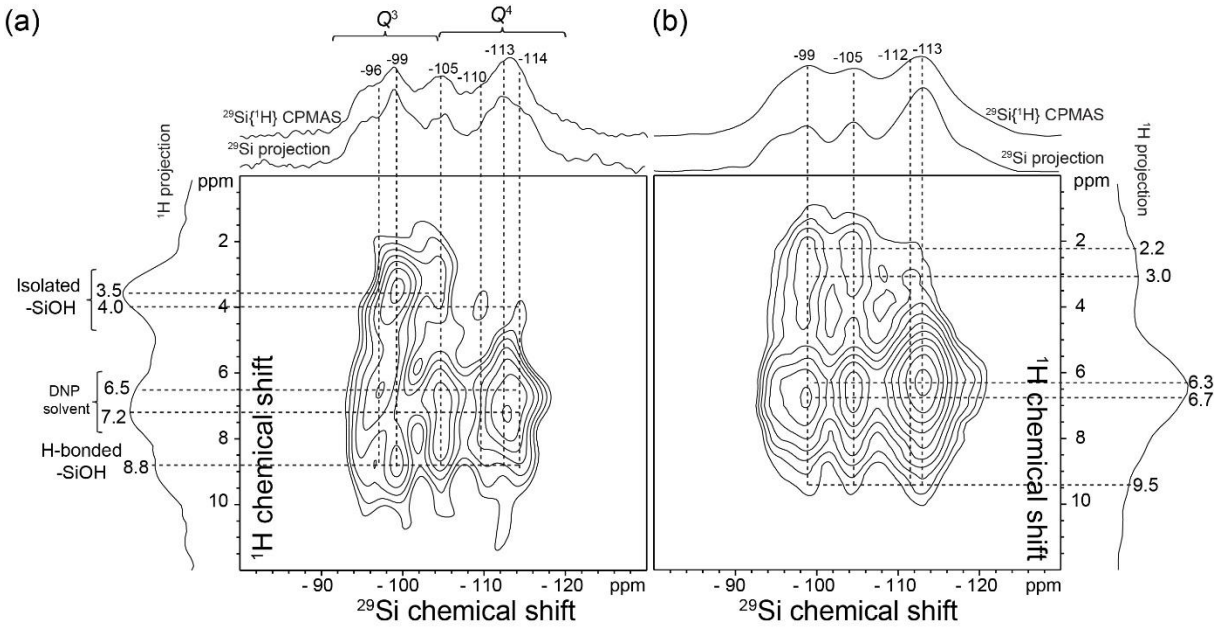

Figure 3.7. Solid-state DNP-enhanced 2D ^{29}Si{^{1}H} dipolar-mediated HETCOR spectra of calcined Si-SSZ-70 acquired in the presence of 16 mM TEKPol biradical in frozen tetrachloroethane, at 9.4 T, 95 K, 8 kHz MAS, with microwave irradiation at 263 GHz, and with different contact times of (a) 0.2 ms and (b) 5 ms. 1D ^{29}Si{^{1}H} DNP-CPMAS spectra acquired under the same conditions are shown along the horizontal axes for comparison with the 1D projections of the 2D spectra.

Though the different candidate structures in Figure 3.6 are very similar, they are distinguished by the different local bonding environments associated with their respective interlayer Q^3 silanol moieties. In particular, the Q^3 Si sites are covalently linked to three equivalent Q^4 Si sites (Si2b) in Model 1 and to two different Q^4 Si sites (Si3 and Si4b) in Model 2. Therefore, the different interlayer surface structures are expected to lead to distinct pairs of correlated intensities in 2D *J*-mediated ^{29}Si{^{29}Si} NMR spectra. Such spectra resolve and correlate inhomogeneously broadened ^{29}Si signals, which substantially overlap in 1D ^{29}Si spectra. Correlated pairs of ^{29}Si signal intensity unambiguously establish the covalent ^{29}Si-O-^{29}Si connectivities of nearest-neighbor Q^3 and Q^4 ^{29}Si sites, which were previously infeasible to measure for natural abundance ^{29}Si (4.7%) materials.

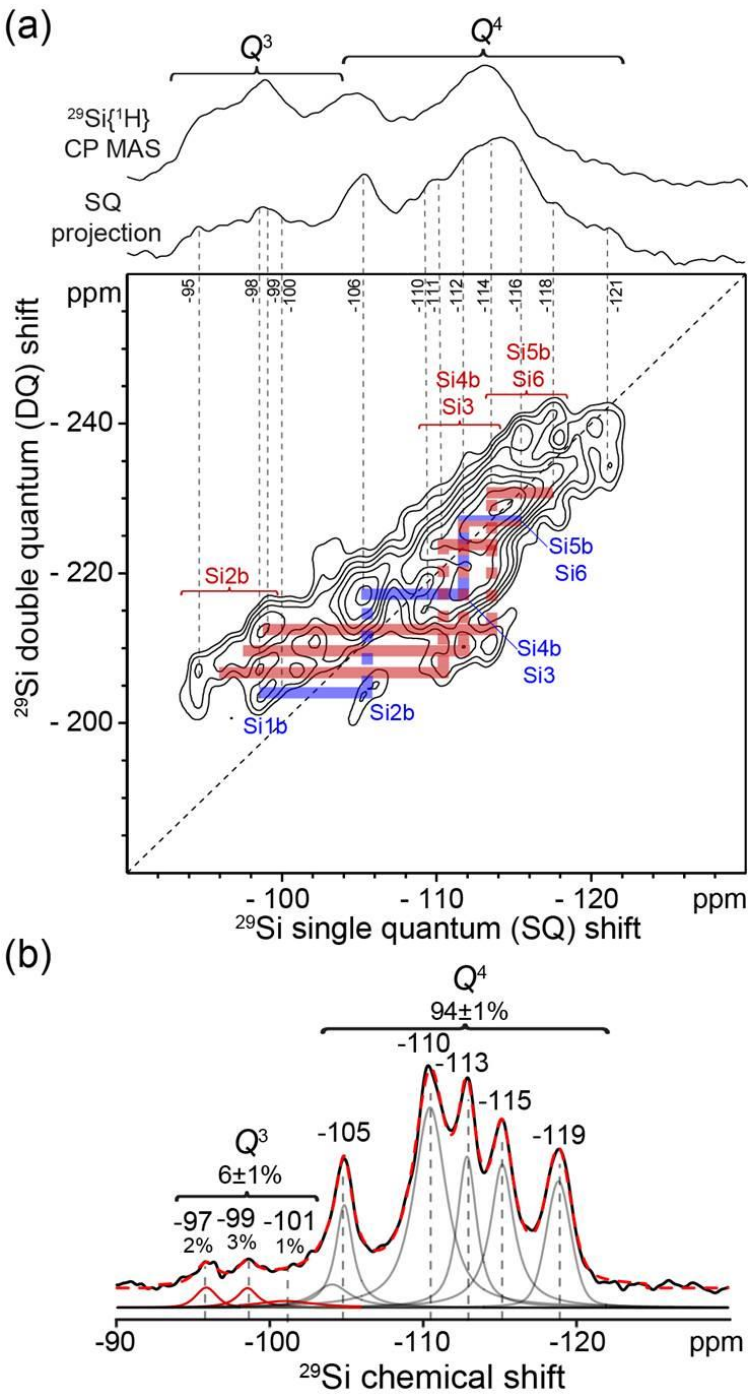

Figure 3.8. (a) Solid-state DNP-enhanced 2D ^{29}Si{^{29}Si} *J*-mediated correlation spectrum of calcined Si-SSZ-70. A 1D ^{29}Si{^{1}H} DNP-CPMAS spectrum acquired under the same conditions is shown along the vertical axis for comparison with the 1D projection of the 2D spectrum. 2D intensity correlations associated with covalent connectivities of Q^3 and Q^4 ^{29}Si species that are consistent with Model 1 and Model 2 are indicated by blue and red lines, respectively. (b) Solid-state quantitative 1D single-pulse ^{29}Si MAS NMR spectrum acquired at 11.7 T, 298 K, and 10 kHz MAS. The simulated spectrum is the dotted red line with the fit deconvolution offset below.

The sensitivity enhancements provided by DNP-NMR enabled acquisition of the 2D *J*-mediated ^{29}Si{^{29}Si} correlation spectrum shown in Figure 3.8a, which resolves multiple intensity correlations that correspond to covalent connectivities between distinct Q^3 and Q^4 ^{29}Si framework species. The spectrum is dominated by broad ^{29}Si signal intensity straddling the diagonal from -110 to -121 ppm, which arises from overlapping signals associated with covalently bonded ^{29}Si-O-^{29}Si moieties that are fully cross-linked and can be assigned to Q^4 ^{29}Si sites in the **MWW**-layers. Their shift values are consistent with (1) previous results on similar zeolites,[16,30] (2) chemical shieldings calculated using the proposed models for calcined zeolite Si-SSZ-70 and well-established semi-empirical relationships,[31,32] and (3) signals detected in a similar DNP-enhanced 2D ^{29}Si{^{29}Si} *J*-mediated spectrum of calcined ITQ-1. While the signals are broadened by interactions with frozen TCE solvent molecules in the zeolite nanopores, the resolution provided by the 2D spectrum is nevertheless sufficient to resolve pairs of correlated signal intensity that arise from the covalent interconnectivities of different framework Q^4 sites. These signals are tabulated in Table 3.2.

Of most interest here are the pairs of correlated ^{29}Si signals associated with the Q^3 –SiOH moieties that are not present in **MWW**-type zeolites and that enable the candidate models for calcined SSZ-70 to be distinguished. While the ^{29}Si signals from the Q^3 species overlap in the range -94 to -101 ppm in the conventional 1D ^{29}Si MAS spectrum (Figure 3.8b), they are resolved in the 2D DNP-enhanced ^{29}Si{^{29}Si} *J*-mediated spectrum. The ^{29}Si signals in the -105 to -106 ppm range are assigned to Si2b Q^4 sites in Model 1, while ^{29}Si signals from Si4b and Si3 sites overlap in the -109 to -113 ppm range. In the 2D spectrum in Figure 3.8a, the broad ^{29}Si signals in the Q^3 range (-98 to -100 ppm) are correlated (lower blue line) with

signals that can be attributed to Q^4 Si2b sites in Model 1. These Si2b ^{29}Si signals are themselves correlated with the broad intensity maximum at ca. -112 ppm attributed to Si4b and Si3 sites, and these in turn with intensity at ca. -116 ppm attributed to Si5b and Si6 sites. These three pairs of ^{29}Si intensity correlations are indicated by the blue lines in Figure 3.8a. In Model 1, there are two paths of three Si-O-Si covalent linkages connecting the Q^3 Si1b silanol moieties at the interlayer surface with the Q^4 species at the surface of the channel system within the layer (Si1b-O-Si2b-O-Si4b-O-Si5b and Si1b-O-Si2b-O-Si3-O-Si6). These relatively long four-site connectivity paths are shown in blue in Figure 3.6b.

Table 3.2. ^{29}Si NMR signal assignments to ^{29}Si sites in calcined Si-SSZ-70, based on the DNP-enhanced 2D ^{29}Si{^{29}Si} *J*-mediated NMR results.

^{29}Si chemical shift (ppm)	**Type**	**Assignment**
-94.5	Q^3	Si2b (Model 2)
-96.0		
-97.5	Q^3	Si2b (Model 2) Si1b (Model 1)
-98.5		
-99.0		
-101.0		
-105.5	Q^4	Si2b (Model 1) Si2a
-105.7		
-108	Q^4	Si5a
-110	Q^4	Si4b, Si4a
-111	Q^4	Si4b, Si4a, Si3
-112		
-113		
-114	Q^4	Si4b, Si4a, Si3, Si5b
-116	Q^4	Si5b, Si6
-118	Q^4	Si7a, Si7b, Si8a, Si8b
-120		
-121		

However, there are further ^{29}Si intensity correlations from distinct covalently-linked Q^3 and Q^4 moieties in Figure 3.8a that cannot be assigned to Model 1, and are instead consistent

with Model 2. Specifically, partially-resolved Q^3 ^{29}Si signals in the range -94 to -99 ppm are each correlated with intensity from -110 to -114 ppm in the Q^4 region of the spectrum that can be assigned to Si4b and Si3 sites (lower red lines in Figure 3.8a). These in turn are correlated with ^{29}Si signals in the range -114 to -118 ppm (upper red lines), which are assigned to overlapping signals from sites Si5b and Si6. These results reflect the two shorter Si-O-Si covalent interconnectivity paths between the Q^3 S2b silanol moieties and Q^4 sites at the intralayer channel surfaces (Si2b-O-Si4b-O-Si5b and Si2b-O-Si3-O-Si6). These relatively short three-site connectivity paths are consistent with Model 2 and shown in red in Figure 3.6c.

The high signal sensitivity and spectral resolution of the 2D DNP-enhanced *J*-mediated ^{29}Si{^{29}Si} spectrum of calcined zeolite Si-SSZ-70 thus provide direct evidence of the presence of two distinct types of interlayer Q^3 silanol species in the material. One has covalent connectivities that are consistent with Model 1 and the other with Model 2. Neither model alone is consistent with all of the observed connectivities. Although the ^{29}Si signals overlap in the quantitative 1D single-pulse ^{29}Si MAS NMR spectrum in Figure 3.8b, the enhanced resolution of the 2D DNP-NMR spectrum enables the positions and linewidths of partially resolved ^{29}Si signals in the single-pulse spectrum to be deconvoluted with confidence and their relative integrated intensities and site populations quantified. Noting that the percentages of Q^3 sites in Models 1 and 2 are distinct (3% and 9%, respectively), we estimate that 50±10% of the calcined Si-SSZ-70 material is structurally consistent with Model 1 and 50±10% with Model 2. The estimated uncertainties arise from the low absolute quantities of Q^3 moieties in the material (ca. 6±1%) and the ^{29}Si signal fits.

3.3.5 Structure of calcined SSZ-70

The framework structure of calcined SSZ-70 can then be described as a polytype of **MWW**, with an almost random ABC-type stacking of **MWW**-layers. Each layer is translated by (x + 1/3, y + 2/3) or (x + 2/3, y + 1/3) with respect to the previous one, with a probability of 50% for either translation. Simulation of the XRPD patterns[33] evidence some short-range ordering of the stacking of the layers, where ABA has a slightly higher chance of occurring (60%) than ABC (40%), is present. The isolated silanol groups protruding into the interlayer space and pointing towards the pocket of the adjacent layer in Figureb are only present 50% of the time. When they are absent, a nest of three silanol groups is present (Figure 3.6c). A model for calcined Si-SSZ-70 with these stacking probabilities and a 50% occupancy of the Si1b and O1b sites results in a diffraction pattern that shows good agreement with the observed data (Figure 3.9). The average structure can be described in $P6_3/mmc$ symmetry with a = 14.227 Å and c = 49.806 Å as an ABAB stacking of **MWW**-layers. Prominent examples in zeolite structures with similar stacking disorder include the ABC-6 family[34] and the **FAU**/**EMT** systems.[35]

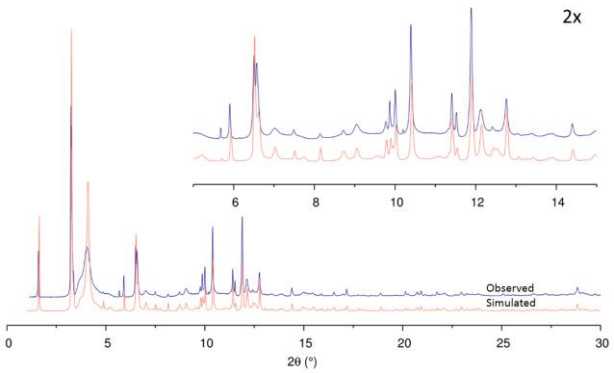

Figure 3.9. Observed (blue), and simulated (red) pattern generated by DIFFaX for calcined Si-SSZ-70, corresponding to a 50/50 mixture of Model 1 and Model 2 with a 60% chance of short-range ABAB ordering of the layers.

Despite the disorder, the regions between the layers are topologically identical. The layers are connected via widely spaced bridging oxygen atoms, forming elongated 14-ring windows lying along <110>, with free dimensions of 4.0 Å × 11.5 Å (Figure 3.10). The terminal SiOH groups in Models 1 and 2 act as additional obstacles for diffusion through the channels. These pores form a 2D channel system between the **MWW**-layers that is very different from that in the **MWW** framework structure. In calcined Si-SSZ-70, there are only half as many oxygen bridges between the layers as in ITQ-1 (**MWW**). The other half are replaced by silanol groups (either isolated or nests of three) opposite the 12-ring pockets of the adjacent layer. From the NMR results, we estimate that there are approximately equal numbers of the two types of silanol species (Figure c). This corresponds to four –SiOH groups per **MWW** layer in the unit cell, in good agreement with the value of 3.3 estimated in earlier work[14] and the NMR results in Figure 3.8.

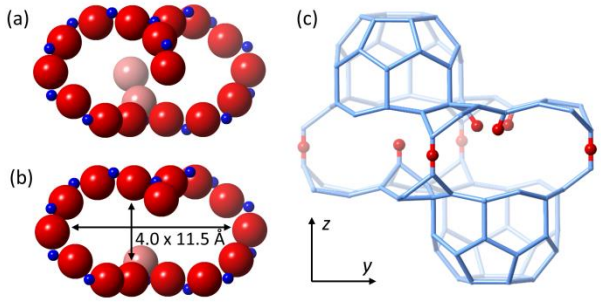

Figure 3.10. Effective pore opening of the 14-ring window for (a) Model 1, and (b) Model 2. The van der Waals radius of O (1.35 Å) has been taken into account in calculating the distances. (c) Schematic representation of the interlayer region along <110> showing the two possible arrangements. The terminal and layer-bridging O atoms are shown in red, but the others have been omitted for clarity.

3.3.6 Catalytic aspects

With this greater insight into the organization and distinction of silanol groups at the SSZ-70 interlayer surfaces, new opportunities and challenges for the development of newer

catalysts based upon SSZ-70 arise. The reduced number of potential linkages between **MWW**-layers in the as-synthesized form of SSZ-70 (compared with **MWW**-type materials) may explain why it is such a good candidate for delamination using milder non-aqueous treatment conditions. A high degree of externally exposed surface area is achieved while leaving the intrinsic structure intact. Even without the detailed understanding presented here, Katz and co-workers have already produced some exceptional Lewis Acid catalysts based on SSZ-70 by inserting tin[36] or titanium[37] (in place of boron in B-SSZ-70) into the cups on the interlayer surface. The latter catalyst seems to exceed commercial materials in performance for partial oxidation reactions.

With the structural details of Si-SSZ-70 that have been learned in this study, new possibilities for enhancing the performance of a class of catalysts that are already active and performing well can be envisaged. Indeed, Aigner *et al.* recently showed that the delamination procedure for Ti-SSZ-70 materials has a significant effect on catalytic performance.[38] Another question is whether the location of the substituting heteroatom can be controlled differentially to create single-site catalysts with a variation in the environment around the site.

3.4 Conclusions

For the determination of the structures of complex polycrystalline materials, conventional methods are rarely sufficient, so information from different sources must be combined.[41–52] This process is much like solving a puzzle, where data and constraints over multiple length scales must be analyzed to establish a structure (or distribution of structures) that is consistent with all data. Sometimes such data simply provide independently corroborative

information, but for SSZ-70, the HRTEM images, synchrotron XRPD data, and DNP-enhanced 2D NMR spectra, each provided crucial and complementary insights. Specifically, the HRTEM images provided evidence that the calcined Si-SSZ-70 is a polytype of **MWW** and consists of disordered **MWW**-layers, the initial XRPD data analysis yielded the unit cell and space group symmetry, and 1D ^{29}Si MAS NMR data indicated that only half of the silanol groups condensed upon calcination. With this information, it was possible to build an initial model of the structure. A more accurate description of the disordered stacking of the **MWW**-layers could then be derived from the XRPD data. Finally, the combined sensitivity and resolution of the DNP-enhanced 2D ^{29}Si{^{1}H} and ^{29}Si{^{29}Si} NMR analyses established the types and bonding environments of terminal -SiOH groups at the interlayer surfaces. Three state-of-the-art characterization techniques were used to probe different structural aspects of calcined SSZ-70, ranging from the long-range average structure (> 500 nm) to short-range stacking sequences (ca. 50 nm) to local atomic-level compositions and structures (< 1 nm). The combination is particularly well suited to the investigation of materials with complex partially disordered structures that cannot be resolved with conventional X-ray diffraction analysis alone.

Obtaining detailed structural information for zeolites at natural isotopic abundance of ^{29}Si (4.7%) from solid-state ^{29}Si NMR has previously been challenging, because the low sensitivity of conventional methods made it unfeasible to determine the covalent ^{29}Si-O-^{29}Si interconnectivities within the framework. However, by exploiting DNP-enhanced NMR techniques, which dramatically increase ^{29}Si NMR signal sensitivity, the interconnectivities and the relative proximities of different framework silicate sites have been established, even for natural abundance ^{29}Si in calcined zeolite Si-SSZ-70. The deeper understanding of the

structural details of SSZ-70 realized in this study are expected to enable further development towards new single-site selective heterogeneous catalysts via carefully controlled chemical modification.

3.5 Materials and methods

Synthesis of Si-SSZ-70

6 mmol of tetraethylorthosilicate (1.26 g) and 3 mmol of *N*,*N*′-diisobutyl imidazolium hydroxide (Figure 3.1, 6.66 g of solution) were added to a tared cup and cap (Teflon^{TM}) of a small Parr reactor. The top was tightly closed and the reactants were allowed to hydrolyze the silicate for 3 days. Afterwards, the top wa s lifted and the internal reactor contents were exposed to an air draft in a hood to remove ethanol and water slowly. When the reactor contents had been reduced to near dryness (requiring several days) the reactor and top were weighed again. The H_2O/SiO_2 molar ratio was then adjusted to 7 by adding water in small amounts to the reaction mixture. After stirring, 50% HF was added by mass to add 3 mmol (about 0.12 g) of reagent. The reactor was closed and heated to 150 °C while being tumbled at 43 rpm for 8 days. The reactor was then removed from the oven and allowed to cool to room temperature.

The Al-SSZ-70 material was synthesized according to the protocol described in reference 12 using *N*,*N*′-diisobutyl imidazolium hydroxide as the OSDA.

Calcination

To simplify the complicated structure analysis, the material was calcined to remove the OSDA. A thin bed of the zeolite sample was calcined in air in a muffle furnace with a controlled ramp program: temperature increased at a rate of 1 °C per minute up to 120 °C;

held for 2 h; increased at the same rate up to 540 °C; held for 5 h; and finally allowed to cool down slowly in the oven.

X-ray Powder Diffraction

Synchrotron XRPD data were collected on both calcined and as-synthesized samples of Si-SSZ-70 and Al-SSZ-70 in a rotating 0.3 mm capillary on the MS-Powder beamline at the Swiss Light Source in Villigen, Switzerland (wavelength 0.70848 Å, MYTHEN II detector).[53]

Electron microscopy

Scanning electron micrographs (Figure 3.2) were obtained using a JEOL JSM 6700F instrument. For high-resolution transmission electron microscopy (HRTEM) analysis, a sample of as-synthesized Al-SSZ-70 was mixed with ethanol, treated by ultrasonication, then transferred to a copper grid covered with lacey carbon and dried in air. Using a 200 kV JEOL JEM-2100F transmission electron microscope equipped with a Gatan UltraScan 1000 camera, 20 HRTEM images were taken under the same conditions (close to the Scherzer focus) with a weak electron beam. These were then summed together into a single image, after correcting for sample drift by cross correlation, to improve the signal-to-noise ratio, following the approach described by Xie and coworkers.[54]

Solid-state NMR spectroscopy

DNP-enhanced MAS NMR techniques at low temperatures (*ca.* 100 K)[26,55–58,24,25,27] provide significantly enhanced NMR signal sensitivity that allows the detection and analysis of ^{29}Si environments in zeolite frameworks at natural isotopic abundance (4.7%).[59–64]

All solid-state DNP-enhanced ^{29}Si{^{29}Si} and ^{29}Si{^{1}H} NMR experiments were carried out on a Bruker ASCEND 400 DNP-NMR spectrometer with a 9.4 Tesla superconducting

magnet operating at 399.95 and 79.46 MHz for ^{1}H and ^{29}Si nuclei, respectively, and equipped with a gyrotron and microwave transmission line capable of providing 263 GHz microwave irradiation at the sample and a low-temperature 3.2 mm triple-resonance MAS probehead. The DNP-enhanced ^{29}Si{^{1}H} and ^{29}Si{^{29}Si} spectra were acquired at 95 K, 8 kHz MAS, under continuous microwave irradiation at 263 GHz, and in the presence of 16 mM TEKPol biradical[65] in frozen 1,1,2,2-tetrachloroethane (TCE). Before NMR analyses, the calcined Si-SSZ-70 material was dried overnight at 200 °C to remove adsorbed water. The sample was prepared in a dry glovebox and was mixed under incipient wetness conditions.[66,62] The ^{29}Si DNP-NMR signal enhancement was quantified as the ratio of the fully-relaxed ^{29}Si{^{1}H} CPMAS signal intensities obtained with and without continuous microwave irradiation, and was measured to be ca. 16.

The DNP-enhanced solid-state 2D *J*-mediated ^{29}Si{^{29}Si} spectrum[64,67,68] was acquired using ^{29}Si{^{1}H} cross-polarization with a 2.5 μs ^{1}H excitation pulse and a contact time of 4 ms to circumvent the effects of the long ^{29}Si spin-lattice relaxation times. The efficiency of the 2D ^{29}Si{^{29}Si} *J*-mediated experiment depends on the ratio of ^{29}Si relaxation parameters T_2'/T_2^*, which was measured to be 11 or greater for all of the ^{29}Si signals (Supporting Information). The spectrum was acquired with an experimentally optimized half-spin-echo (τ) delay of 8 ms, ^{29}Si $\pi/2$ and π pulse lengths of 5 and 10 μs, respectively, a repetition time of 3 s, 32 t_1 increments, a rotor-synchronized incremental step size of 125 μs, and 2048 transients for a total acquisition time of 54 h. Additional experimental details are provided in the Supporting Information.

The DNP-enhanced 2D ^{29}Si{^{1}H} HETeronuclear CORrelation (HETCOR) spectra were acquired using 0.2 or 5 ms contact times, 80 or 160 t_1 increments, an incremental step size of

64 μs, 64 or 16 transients, and repetition times of 3 s for total acquisition times of 4 or 2 h. The $^{29}Si\{^{1}H\}$ DNP-HETCOR spectra were acquired using eDUMBO-1_{22} homonuclear coupling during the ^{1}H evolution period to improve resolution in the ^{1}H dimension.[69] All ^{29}Si NMR spectra were acquired using 100 kHz SPINAL-64 ^{1}H decoupling during the acquisition period.[70]

3.6 References

(1) Zones, S. I. *Micropor. Mesopor. Mat.* **2011**, *144*, 1.
(2) Zones, S. I.; Chen, C. Y.; Benin, A.; Hwang, S.-J. *J. Catal.* **2013**, *308*, 213.
(3) Gounder, R.; Iglesia, E. *Angew. Chemie - Int. Ed.* **2010**, *49* (4), 808.
(4) Corma, A. *J. Catal.* **2003**, *216* (1–2), 298.
(5) Cheung, P.; Bhan, A.; Sunley, G. J.; Iglesia, E. *Angew. Chemie Int. Ed.* **2006**, *45* (10), 1617.
(6) Boronat, M.; Martínez-Sánchez, C.; Law, D.; Corma, A. *J. Am. Chem. Soc.* **2008**, *130* (48), 16316.
(7) Zones, S. I.; Benin, A.; Hwang, S. J.; Xie, D.; Elomari, S.; Hsieh, M. F. *J. Am. Chem. Soc.* **2014**, *136* (4), 1462.
(8) Gallego, E. M.; Portilla, M. T.; Paris, C.; León-Escamilla, A.; Boronat, M.; Moliner, M.; Corma, A. *Science.* **2017**, *355* (6329), 1051.
(9) Zones, S. I.; Hwang, S.-J. *Micropor. Mesopor. Mat.* **2011**, *146* (1), 48.
(10) Zones, S. I. *Zeolites* **1989**, *9* (6), 458.
(11) Zones, S. I.; Burton, A. W. Molecular sieve SSZ-70 composition of matter and synthesis thereof. US7108843 B2, September 2006.
(12) Archer, R. H.; Zones, S. I.; Davis, M. E. *Microporous Mesoporous Mater.* **2010**, *130* (1–3), 255.
(13) Leonowicz, M. E.; Lawton, J. A.; Lawton, S. L.; Rubin, M. K. *Science.* **1994**, *264* (5167), 1910.
(14) Archer, R. H.; Carpenter, J. R.; Hwang, S.-J.; Burton, A. W.; Chen, C.-Y.; Zones, S. I.; Davis, M. E. *Chem. Mater.* **2010**, *22* (8), 2563.
(15) Chu, P.; Landis, M. E.; Le, Q. N. Production of ethylbenzene. US5334795 A, August 1994.
(16) Camblor, M. A.; Corma, A.; Díaz-Cabañas, M.-J.; Baerlocher, C. *J. Phys. Chem. B* **1998**, *102* (1), 44.
(17) Zones, S. I.; Holtermann, D. I.; Innes, R. A.; Pecoraro, T. A.; Santilli, D. S.; Ziemer, J. N. Zeolite SSZ-25. US4826667 A, May 1989.
(18) Runnebaum, R. C.; Ouyang, X.; Edsinga, J. A.; Rea, T.; Arslan, I.; Hwang, S. J.; Zones, S. I.; Katz, A. *ACS Catal.* **2014**, *4* (7), 2364.
(19) Zones, S. I.; Harris, T. V. *Microporous Mesoporous Mater.* **2000**, *35–36*, 31.
(20) Ouyang, X.; Hwang, S.-J.; Runnebaum, R. C.; Xie, D.; Wanglee, Y.-J.; Rea, T.; Zones, S. I.; Katz, A. *J. Am. Chem. Soc.* **2014**, *136* (4), 1449.
(21) Ogino, I.; Nigra, M. M.; Hwang, S.-J.; Ha, J.-M.; Rea, T.; Zones, S. I.; Katz, A. *J. Am. Chem. Soc.* **2011**, *133* (10), 3288.
(22) Maheshwari, S.; Martínez, C.; Teresa Portilla, M.; Llopis, F. J.; Corma, A.; Tsapatsis, M. *J. Catal.* **2010**, *272* (2), 298.

(23) Njo, S. L. Computational Chemistry Approaches to Zeolite Frameworks and their Interactions with Structure Directing Agents. PhD thesis, TU Delft, The Netherlands, 1998.
(24) Maly, T.; Debelouchina, G. T.; Bajaj, V. S.; Hu, K.-N.; Joo, C.-G.; Mak–Jurkauskas, M. L.; Sirigiri, J. R.; van der Wel, P. C. A.; Herzfeld, J.; Temkin, R. J.; Griffin, R. G. *J. Chem. Phys.* **2008**, *128* (5), 52211.
(25) Lesage, A.; Lelli, M.; Gajan, D.; Caporini, M. A.; Vitzthum, V.; Mieville, P.; Alauzun, J.; Roussey, A.; Thieuleux, C.; Mehdi, A.; Bodenhausen, G.; Coperet, C.; Emsley, L. *J. Am. Chem. Soc.* **2010**, *132*, 15459.
(26) Ni, Q. Z.; Daviso, E.; Can, T. V.; Markhasin, E.; Jawla, S. K.; Swager, T. M.; Temkin, R. J.; Herzfeld, J.; Griffin, R. G. *Acc. Chem. Res.* **2013**, *46* (9), 1933.
(27) Rossini, A. J.; Zagdoun, A.; Lelli, M.; Lesage, A.; Copéret, C.; Emsley, L. *Acc. Chem. Res.* **2013**, *46* (9), 1942.
(28) Yesinowski, J. P.; Eckert, H.; Rossman, G. R. *J. Am. Chem. Soc.* **1988**, *110* (5), 1367.
(29) Xue, X.; Kanzaki, M. *J. Am. Ceram. Soc.* **2009**, *92* (12), 2803.
(30) Camblor, M. A.; Corell, C.; Corma, A.; Díaz-Cabañas, M.-J.; Nicolopoulos, S.; González-Calbet, J. M.; Vallet-Regí, M. *Chem. Mater.* **1996**, *8* (10), 2415.
(31) Lewis, J. E.; Freyhardt, C. C.; Davis, M. E. *J. Phys. Chem.* **1996**, *100* (12), 5039.
(32) Brouwer, D. H.; Darton, R. J.; Morris, R. E.; Levitt, M. H. **2005**, No. 11, 10365.
(33) Smeets, S.; Berkson, Z. J.; Xie, D.; Zones, S. I.; Wan, W.; Zou, X.; Hsieh, M. F.; Chmelka, B. F.; McCusker, L. B.; Baerlocher, C. *J. Am. Chem. Soc.* **2017**, *139* (46), 16803.
(34) Millward, G. R.; Ramdas, S.; Thomas, J. M. *Proc. R. Soc. Lond. A* **1985**, *399* (1816), 57.
(35) Treacy, M. M. J.; Vaughan, D. E. W.; Strohmaier, K. G.; Newsam, J. M. *Proc. R. Soc. Lond. A* **1996**, *452* (1947), 813.
(36) Ouyang, X.; Wanglee, Y.-J.; Hwang, S.-J.; Xie, D.; Rea, T.; I. Zones, S.; Katz, A. *Dalt. Trans.* **2014**, *43* (27), 10417.
(37) Aigner, M.; Grosso-Giordano, N. A.; Okrut, A.; Zones, S.; Katz, A. *React. Chem. Eng.* **2017**, *2* (6), 842.
(38) Aigner, M.; Grosso-Giordano, N.; Schöttle, C.; Okrut, A.; Zones, S.; Katz, A. *React. Chem. Eng.* **2017**, doi: 10.1039/C7RE00138J.
(39) Xu, L.; Ji, X.; Jiang, J.-G.; Han, L.; Che, S.; Wu, P. *Chem. Mater.* **2015**, *27* (23), 7852.
(40) Roth, W. J.; Dorset, D. L. *Micropor. Mesopor. Mat.* **2011**, *142* (1), 32.
(41) Fyfe, C. A.; Gies, H.; Kokotailo, G. T.; Pasztor, C.; Strobl, H.; Cox, D. E. *J. Am. Chem. Soc.* **1989**, *111* (7), 2470.
(42) Wright, P. A.; Natarajan, S.; Thomas, J. M.; Bell, R. G.; Gai-Boyes, P. L.; Jones, R. H.; Chen, J. *Angew. Chemie Int. Ed. English* **1992**, *31* (11), 1472.
(43) Eiden-Aßmann, S.; Schneider, A. M.; Behrens, P.; Engelhardt, G.; Mändar, H.; Felsche, J. *Eur. J. Inorg. Chem.* **2001**, *2001* (6), 1527.
(44) Cao, G.; Afeworki, M.; Kennedy, G. J.; Strohmaier, K. G.; Dorset, D. L. *Acta Crystallogr. Sect. B Struct. Sci.* **2007**, *63* (1), 56.
(45) Wu, P.; Ruan, J.; Wang, L.; Wu, L.; Wang, Y.; Liu, Y.; Fan, W.; He, M.; Terasaki, O.; Tatsumi, T. *J. Am. Chem. Soc.* **2008**, *130* (26), 8178.
(46) Milanesio, M.; Croce, G.; Viterbo, D.; Pastore, H. O.; Mascarenhas, A. J. dos S.; Munsignatti, E. C. de O.; Meda, L. *J. Phys. Chem. A* **2008**, *112* (36), 8403.
(47) Sun, J.; Bonneau, C.; Cantin, A.; Corma, A.; Díaz-Cabañas, M. J.; Moliner, M.; Zhang, D.; Li, M.; Zou, X. *Nature* **2009**, *458* (7242), 1154.
(48) Inge, A. K.; Huang, S.; Chen, H.; Moraga, F.; Sun, J.; Zou, X. *Cryst. Growth Des.* **2012**, *12* (10), 4853.
(49) Kong, X.; Deng, H.; Yan, F.; Kim, J.; Swisher, J. A.; Smit, B.; Yaghi, O. M.; Reimer, J. A. *Science.* **2013**, *341* (6148), 882.
(50) Smeets, S.; Xie, D.; Baerlocher, C.; McCusker, L. B.; Wan, W.; Zou, X.; Zones, S. I. *Angew. Chemie Int. Ed.* **2014**, *53* (39), 10398.

(51) Krajnc, A.; Kos, T.; Zabukovec Logar, N.; Mali, G. *Angew. Chemie Int. Ed.* **2015**, *54* (36), 10535.
(52) Morris, S. A.; Bignami, G. P. M.; Tian, Y.; Navarro, M.; Firth, D. S.; Čejka, J.; Wheatley, P. S.; Dawson, D. M.; Slawinski, W. A.; Wragg, D. S.; Morris, R. E.; Ashbrook, S. E. *Nat. Chem.* **2017**, *9* (10), 1012.
(53) Bergamaschi, A.; Cervellino, A.; Dinapoli, R.; Gozzo, F.; Henrich, B.; Johnson, I.; Kraft, P.; Mozzanica, A.; Schmitt, B.; Shi, X. *J. Synchrotron Radiat.* **2010**, *17* (5), 653.
(54) Xie, D.; McCusker, L. B.; Baerlocher, C.; Zones, S. I.; Wan, W.; Zou, X. *J. Am. Chem. Soc.* **2013**, *135* (28), 10519.
(55) Perras, F. A.; Kobayashi, T.; Pruski, M. *J. Am. Chem. Soc.* **2015**, *137* (26), 8336.
(56) Perras, F. A.; Padmos, J. D.; Johnson, R. L.; Wang, L.-L. L.; Schwartz, T. J.; Kobayashi, T.; Horton, J. H.; Dumesic, J. A.; Shanks, B. H.; Johnson, D. D.; Pruski, M. *J. Am. Chem. Soc.* **2017**, *139* (7), 2702.
(57) Copéret, C.; Liao, W.-C.; Gordon, C. P.; Ong, T.-C. *J. Am. Chem. Soc.* **2017**, *139* (31), 10588.
(58) Kobayashi, T.; Singappuli-Arachchige, D.; Wang, Z.; I. Slowing, I.; Pruski, M. *Phys. Chem. Chem. Phys.* **2017**, *19* (3), 1781.
(59) Lee, D.; Monin, G.; Duong, N. T.; Lopez, I. Z.; Bardet, M.; Mareau, V.; Gonon, L.; De Paëpe, G. *J. Am. Chem. Soc.* **2014**, *136* (39), 13781.
(60) Wolf, P.; Valla, M.; Rossini, A. J.; Comas-Vives, A.; Núñez-Zarur, F.; Malaman, B.; Lesage, A.; Emsley, L.; Copéret, C.; Hermans, I. *Angew. Chemie Int. Ed.* **2014**, *53* (38), 10179.
(61) Gunther, W. R. *J. Am. Chem. Soc.* **2014**, *136* (17), 6219.
(62) Sangodkar, R. P.; Smith, B. J.; Gajan, D.; Rossini, A. J.; Roberts, L. R.; Funkhouser, G. P.; Lesage, A.; Emsley, L.; Chmelka, B. F. *J. Am. Chem. Soc.* **2015**, *137* (25), 8096.
(63) Wolf, P.; Valla, M.; Núñez-Zarur, F.; Comas-Vives, A.; Rossini, A. J.; Firth, C.; Kallas, H.; Lesage, A.; Emsley, L.; Copéret, C.; Hermans, I. *ACS Catal.* **2016**, *6* (7), 4047.
(64) Berkson, Z. J.; Messinger, R. J.; Na, K.; Seo, Y.; Ryoo, R.; Chmelka, B. F. *Angew. Chemie - Int. Ed.* **2017**, No. 2, 2.
(65) Zagdoun, A.; Casano, G.; Ouari, O.; Schwarzwälder, M.; Rossini, A. J.; Aussenac, F.; Yulikov, M.; Jeschke, G.; Copéret, C.; Lesage, A.; Tordo, P.; Emsley, L. *J. Am. Chem. Soc.* **2013**, *135* (34), 12790.
(66) Zagdoun, A.; J. Rossini, A.; Gajan, D.; Bourdolle, A.; Ouari, O.; Rosay, M.; E. Maas, W.; Tordo, P.; Lelli, M.; Emsley, L.; Lesage, A.; Copéret, C. *Chem. Commun.* **2012**, *48* (5), 654.
(67) Lesage, A.; Bardet, M.; Emsley, L. *J. Am. Chem. Soc.* **1999**, *121* (47), 10987.
(68) Cadars, S.; Mifsud, N.; Lesage, A.; Epping, J. D.; Hedin, N.; Chmelka, B. F.; Emsley, L. *J. Phys. Chem. C* **2008**, *112* (25), 9145.
(69) Elena, B.; de Paëpe, G.; Emsley, L. *Chem. Phys. Lett.* **2004**, *398* (4–6), 532.
(70) Fung, B. M.; Khitrin, A. K.; Ermolaev, K. **2000**, *101*, 97.

Chapter 4

Preferential siting of aluminum heteroatoms in the zeolite catalyst Al-SSZ-70

Adapted from: Z. J. Berkson, M.-F. Hsieh, S. Smeets, D. Gajan, A. Lund, A. Lesage, D. Xie, S. I. Zones, A. Lesage, L. B. McCusker, C. Baerlocher, B. F. Chmelka, *submitted to Angewandte Chemie.*

4.1 Abstract

The macroscopic adsorption and catalytic reaction properties of aluminosilicate zeolites arise from non-stoichiometric distributions of Al atoms substituted for Si at tetrahedral framework sites, which are associated with exchangeable cations that act as molecular adsorption/reaction sites. Understanding the distributions of Al atoms and corresponding cationic species is crucial to relating the overall catalytic performance of a zeolite catalyst to its atomic-level structure and composition. However, Al distributions in zeolites are challenging to determine, due in part to their non-stoichiometric distributions, complicated framework architectures, and the absence of long-range positional ordering. These challenges are exacerbated for zeolites with complicated framework structures such as SSZ-70, which has 14 distinct framework tetrahedral (T) sites that may be occupied by Si or Al atoms. Here, Here, Al atoms are shown to be located preferentially in certain framework sites in the zeolite catalyst Al-SSZ-70 by combined solid-state NMR and synchrotron X-ray powder diffraction analyses. Through-covalent-bond 2D $^{27}Al\{^{29}Si\}$ J-correlation NMR spectra allow distinct framework Al sites to be identified and their relative occupancies quantified. The analyses show that 94% of the Al atoms are located at the surfaces of the large-pore interlayer

channels of Al-SSZ-70, while only 6% are in the sub-nm intralayer channels. The selective siting of Al atoms accounts for the reaction properties of catalysts derived from SSZ-70.

4.2 Introduction

Nanoporous aluminosilicate zeolites are of considerable technological interest because their high surface areas, well-defined sub-nanometer pore dimensions, and exchangeable cation molecular adsorption or reaction sites enable important industrial and technological applications, including for air-gas separations[1] and as heterogeneous catalysts for reactions such as hydrocarbon conversion[2,3] and pollution removal.[4] Aluminosilicate zeolites are composed of corner-sharing SiO_4^{2-} and AlO_4^{3-} tetrahedra, the latter of which are associated with catalytically-active sites when the excess negative framework charges are balanced by acidic countercations such as H^+ or La^{3+}. The molecular diffusion, reaction, and adsorption properties of zeolite catalysts are strongly influenced by the nanopore dimensions, the aluminosilicate framework architectures, and the types and distributions of heteroatom sites (e.g, Al) and associated cations. Understanding and controlling the heteroatom distributions in zeolite catalysts has been severely limited by the non-stoichiometric substitution of heteroatoms into the framework and their complicated distributions which are challenging to characterize. Determining the types and distributions of Al heteroatom sites in different zeolite frameworks has been a long-standing challenge in understanding the structures of zeolite catalysts and correlating their molecular compositions to their macroscopic adsorption and/or catalytic reaction properties.

Heteroatom distributions in zeolites have long been recognized to depend strongly on the synthesis conditions, including the compositions of the precursor materials and organic

and inorganic structure directing cations.[5] Information on heteroatom distributions in zeolites has been accessed previously in favorable cases utilizing several different scattering and spectroscopic techniques. For example, different Al heteroatom sites in 8-member ring (MR) and 12-MR environments may be identified by deconvolution of Fourier transform infrared (FTIR) spectra of zeolite frameworks,[6] though such spectra are generally poorly resolved. While the similar electron densities of Al and Si atoms make distinguishing them challenging using diffraction or scattering techniques,[7] Al occupancies at different tetrahedral (T) sites have been determined for large single crystals of the zeolite mineral scolecite by synchrotron X-ray standing wave diffraction.[8] For as-synthesized zeolites containing organic structure directing agents that orient preferentially with respect to heteroatom sites, information on framework Al distributions may be extracted by the refinement of synchrotron X-ray diffraction data, as has been demonstrated for ferrierite zeolite[9] and systematically for a series borosilicate zeolites.[10] Relative positions and mutual proximities of Al atoms and their associated cations within chabazite zeolite materials have been determined through adsorption of probe molecules such as CO and NO and subsequent FTIR spectroscopy.[11] Exchange of aluminosilicate zeolites with divalent cations such as Co^{2+}, paired with ultraviolet-visible (UV-vis) spectroscopy, enables quantification of Al heteroatom pairs that are positioned within the same aluminosilicate rings.[12] Several synthetic techniques for influencing heteroatom distributions in zeolites have been established, including exchange of B heteroatoms for Al, which can lead to preferential siting of Al at surface sites.[13] In favorable cases, Al distributions may be influenced by the careful selection of organic structure directing agent and synthesis conditions, as has been demonstrated for ferrierite[9] and chabazite.[14,15]

Here, analysis of solid-state two-dimensional (2D) NMR spectra with complementary synchrotron X-ray powder diffraction analyses establish the preferential siting of Al heteroatoms in calcined zeolite Al-SSZ-70. The layered zeolite SSZ-70 has recently emerged as a promising platform for new catalysts because it can be exfoliated to generate high-surface-area active materials that have been shown to exhibit enhanced catalysis rates for alkylation reactions,[16] while calcined Al-SSZ-70 exhibits high catalytic activity for hydrocarbon cracking.[17] The structure of calcined SSZ-70 has recently been shown to have 14 crystallographically distinct T sites.[18] SSZ-70 crystallizes into hexagonal flakes (Fig. 4.1a) and has two types of 2-dimensional channel systems with effective cross-sectional pore openings of 4.4 x 5.9 $Å^2$ (between the **MWW**-type layers) and 4.0 x 11.5 $Å^2$ (within the **MWW**-type layers). However, in contrast to other **MWW**-type zeolite catalysts the catalytic selectivity of calcined Al-SSZ-70 for hydrocarbon cracking does not change substantially with time on stream,[17] characteristic of reactions occurring in a single type of nanochannel system.[19] Calcined SSZ-70 exhibits two types of silanol species that protrude into the interlayer channels (Fig. 4.1b): "nests" of three closely-spaced silanols (Fig. 4.1c) and isolated silanols (Fig. 4.1d). The different T sites in SSZ-70 differ with respect to their covalent bonding configurations and positions relative to the inter- and intralayer channel surfaces. For example, T1a,b, T2a,b, and T3 are at the surfaces of the interlayer channels, while T5a,b, T6, T7a,b, and T8a,b are at the surfaces of the intralayer channels. As a consequence, Al heteroatoms located in such different T sites are expected to exhibit distinct adsorption and reaction properties. The synchrotron X-ray powder diffraction (XRPD) patterns of calcined Si- and Al-SSZ-70 are virtually identical (Fig. 4.1e), indicating that the

long-range ordering of T-atoms in SSZ-70 is indistinguishable in silicate and aluminosilicate forms, despite their different compositions.

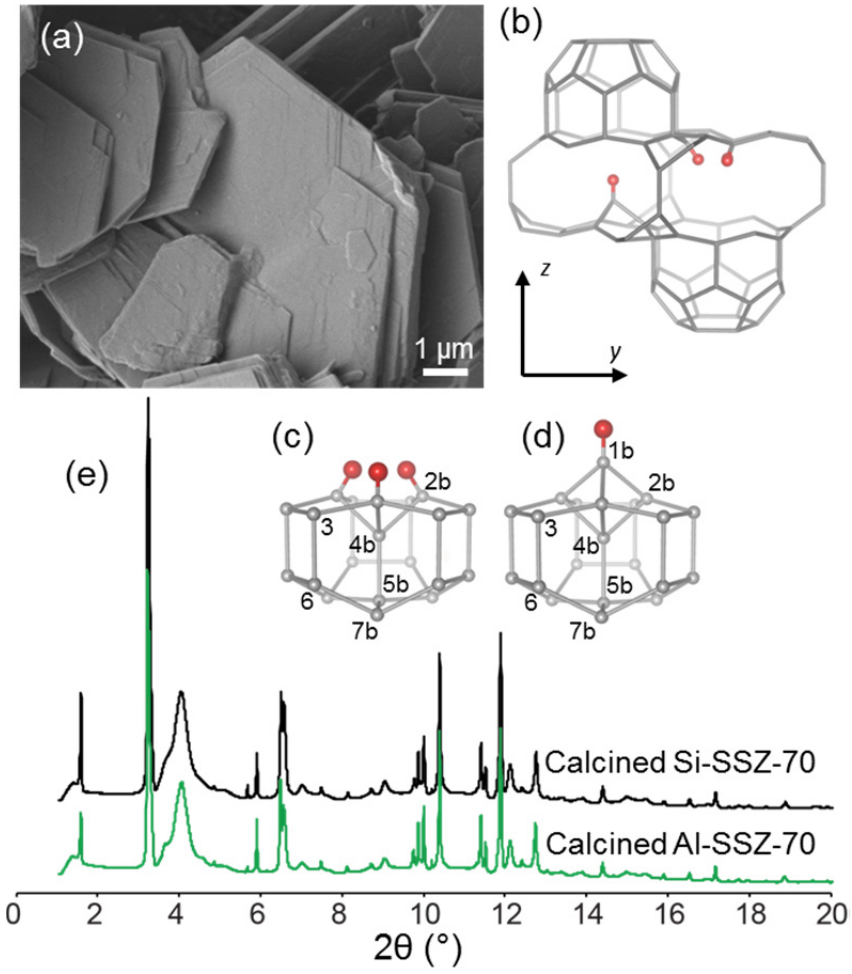

Figure 4.1. (a) SEM image of Al-SSZ-70. (b) Interlayer structure of calcined SSZ-70, with the two different types of interlayer hydroxyl species (c,d). Synchrotron XRPD patterns (e) of calcined Si- (black) and Al-SSZ-70 (green).

4.3 Results and discussion

4.3.1 ^{29}Si environments in calcined Si- and Al-SSZ-70

Analyses of the 1D ^{29}Si MAS NMR spectra show that the local ^{29}Si framework environments in calcined SSZ-70 are almost identical in the siliceous and aluminosilicate forms. The quantitative 1D single-pulse ^{29}Si NMR spectrum of calcined Si-SSZ-70 (Fig.

4.2a) exhibits ^{29}Si signals in the Q^4 region at -105 ppm, -110 ppm, -113 ppm, -115 ppm, and -119 ppm from different fully-crosslinked Q^4(0Al) framework ^{29}Si species. The Q^m(nAl) notation indicates a tetrahedrally-coordinated Si atom covalently linked through bridging oxygen atoms to m other Si or Al atoms, of which n are Al. The partially-crosslinked ^{29}Si silanol species at the interlayer channel surfaces give rise to ^{29}Si signals in the Q^3(0Al) region at -97 ppm, -99 ppm, and -101 ppm. These ^{29}Si signals were previously discussed and partially assigned on the basis of dynamic nuclear polarization (DNP-)enhanced solid-state 2D ^{29}Si{^{29}Si} and ^{29}Si{^{1}H} NMR correlation spectra.[18] In the quantitative single-pulse ^{29}Si MAS NMR spectrum of calcined Al-SSZ-70 (Fig. 4.2b), all of the same ^{29}Si signals are detected, with the same peak positions and linewidths as the spectrum of the siliceous form. Subtle differences in the relative intensities of the different ^{29}Si signals in the ^{29}Si NMR spectra of Al- and Si-SSZ-70 are attributed to the influences of incorporation of Al heteroatoms into the Al-SSZ-70 framework. Bonding of framework ^{29}Si atoms through bridging oxygen atoms to Al atoms in zeolites is well-known to displace the ^{29}Si NMR signals by +6-7 ppm:[20] a Q^4(1Al) ^{29}Si species at a given T site will exhibit an isotropic ^{29}Si chemical shift that is 6-7 ppm greater than the isotropic ^{29}Si chemical shift of the corresponding Q^4(0Al) ^{29}Si species at the same T site. The ^{29}Si signals at -113 and -115 ppm in the ^{29}Si spectrum of Al-SSZ-70 exhibit diminished relative intensity compared to the ^{29}Si spectrum of Si-SSZ-70, which is attributed to the displacement of ^{29}Si signals from Q^4(1Al) species to higher ppm values. Due to the small absolute quantity of Al in the Al-SSZ-70 material (Si/Al = 16.6[17]) and overlapping ^{29}Si NMR signals from the diversity of Q^4(0Al) and Q^3(0Al) species in SSZ-70, the ^{29}Si signals from Q^4(1Al) species are not resolved and cannot be quantified from the 1D ^{29}Si MAS NMR spectra alone.

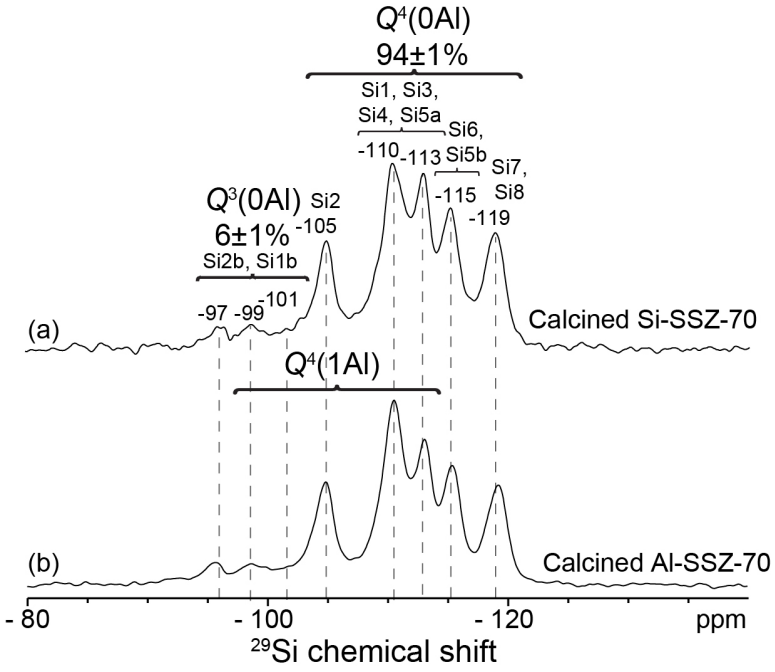

Figure 4.2. Solid-state 1D quantitative single pulse ^{29}Si MAS NMR spectra of calcined (a) Si- and (b) Al-SSZ-70 acquired at 11.7 T, 298 K, and 12.5 kHz MAS.

4.3.2 ^{27}Al-O-^{29}Si T-site connectivities in calcined Al-SSZ-70

Solid-state ^{27}Al NMR spectroscopy is sensitive to the local environments of the crucial Al heteroatoms in zeolite frameworks and is in principle capable of distinguishing between ^{27}Al species in different T sites in aluminosilicate zeolites.[21] However, the resolution of such spectra is often limited owing to strong quadrupolar interactions of ^{27}Al (I=5/2) nuclei, as well as inhomogeneous distributions of ^{27}Al environments species at different framework sites. The resolution of solid-state ^{27}Al NMR spectra can be improved by using high magnetic fields (>18 Tesla) and two-dimensional (2D) NMR techniques.[22] For example, high-field ^{27}Al multiple-quantum magic-angle-spinning (MQMAS) NMR analyses of different samples of aluminosilicate zeolite ZSM-5, which has 24 crystallographically-distinct T sites, have led to the identification and assignment of at least 12 different ^{27}Al signals associated with different T sites.[23–25] In addition, recent 2D ^{27}Al{^{29}Si} NMR analyses

of ZSM-5[26] provided evidence of Al incorporation into 4 of the 24 T sites, though these analyses were mediated by through-space ^{27}Al-^{29}Si internuclear dipole-dipole couplings, which can manifest signal intensities from next-nearest neighbor T sites, and were further complicated by poorly-resolved ^{27}Al signals from ZSM-5. General methods for determining the distributions and relative populations of Al heteroatoms in zeolites have been elusive, particularly for materials of high catalytic importance that often exhibit exceptional structural complexity, such as Al-SSZ-70.

Here, we report the preferential siting of Al heteroatoms in 5 of the 14 T sites in calcined Al-SSZ-70 established by analyses of solid-state 2D NMR heteronuclear correlation spectra,[26,27] which resolve distinct signals from different framework ^{27}Al moieties and provide direct evidence for the incorporation of Al atoms into specific sites. The 1D and 2D ^{27}Al MAS NMR spectra of calcined Al-SSZ-70 in Fig. 4.3 show well-resolved ^{27}Al signals at 60 ppm, 55 ppm, and 49 ppm from ^{27}Al atoms in tetrahedrally-coordinated environments, as well as a signal at -5 ppm from octahedrally-coordinated ^{27}Al species. The well-resolved and relatively narrow (2-3 ppm full-width half-maximum, fwhm) ^{27}Al signals suggest that the ^{27}Al heteroatoms are sited in specific T sites, rather than being randomly distributed.

Specific locations of Al heteroatoms in calcined Al-SSZ-70 are determined by identification of the nearest-neighbor ^{29}Si sites to which the different ^{27}Al species are covalently bonded. This is achieved by measuring 2D ^{27}Al{^{29}Si} heteronuclear multiple quantum correlation (HMQC) NMR spectra,[28–30] which here correlate the shifts of ^{27}Al-O-^{29}Si spin pairs that are mediated by through-covalent-bond $J_{\text{Al-Si}}$ couplings.[31] For example, the 2D ^{27}Al{^{29}Si} *J*-HMQC spectrum of calcined Al-SSZ-70 in Fig. 4.3a shows correlated signal intensities at ^{27}Al shifts of 60 ppm, 55 ppm, and 49 ppm (denoted *A, B,* and *C,*

respectively) that are correlated with ^{29}Si signals in the chemical shift range -105 ppm to -107 ppm (red band) from different Q^4(1Al) ^{29}Si species. The ^{27}Al signal at 55 ppm is additionally correlated with ^{29}Si signals in the -99 to -101 ppm range (blue band), which also arise from Q^4(1Al) species. The different correlated ^{27}Al-^{29}Si signals in the 2D ^{27}Al{^{29}Si} *J*-mediated spectrum in Fig. 4.3a are assigned based on comparisons with previous 2D ^{29}Si{^{29}Si} and ^{29}Si{^{1}H} NMR analyses of calcined Si-SSZ-70,[18] analyses of 2D ^{27}Al MQMAS spectra of Al-SSZ-70 (Fig. 4.7, 4.8 Table 4.1), well-established semi-empirical correlations relating the isotropic ^{27}Al and ^{29}Si chemical shift values to the -T-O-T- bond angles and T-O bond lengths,[32–34] and prior literature.[20,35] On the basis of isotropic ^{29}Si chemical shift values calculated for Q^4(1Al) species in each T site in calcined Al-SSZ-70, the correlated signals at -99 to -101 ppm in the ^{29}Si dimension (blue band) are assigned to framework Al-O-Si2 Q^4(1Al) moieties, while those at -105, -107, and -108 ppm (red band) are assigned respectively to Al-O-Si3 and Al-O-Si1a, Al-O-Si6, and Al-O-Si4 and Al-O-Si7 Q^4(1Al) moieties. The correlated ^{27}Al-^{29}Si signals at 60, 55, and 49 ppm in the ^{27}Al dimension must therefore arise respectively from ^{27}Al species that are covalently bonded (through bridging O atoms) to Si1a and Si3, Si6 and Si2, and Si4 and Si7 Q^4(1Al) species. The positions of the ^{27}Al heteroatoms are further constrained by analysis of the isotropic ^{27}Al chemical shifts determined by 2D ^{27}Al MQMAS analyses at different magnetic field strengths and temperatures (4.8), which are compared with calculated values for ^{27}Al atoms in each T site in Table 4.1. With the constraints provided by the 2D ^{27}Al{^{29}Si} *J*-mediated correlation spectrum, these analyses enable the ^{27}Al signals at 60, 55, and 49 ppm to be confidently assigned to fully-crosslinked Al2a/b, Al3, and Al5b sites, respectively. The

unambiguous identification of the different ^{27}Al-O-^{29}Si connectivities enables the specific locations of Al heteroatoms to be established, even for a complex zeolite like Al-SSZ-70.

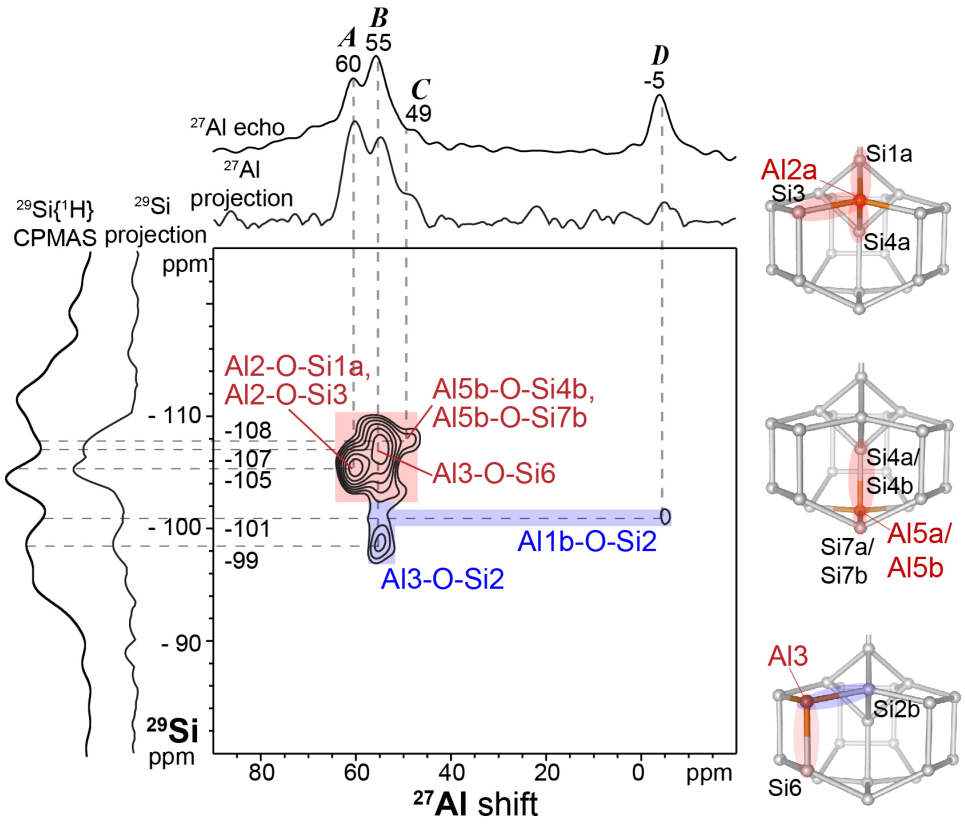

Figure 4.3. Solid-state 2D ^{27}Al{^{29}Si} *J*-HMQC spectrum of calcined Al-SSZ-70 acquired at 18.8 Tesla, 10 kHz MAS, and 97 K. Solid-state 1D ^{27}Al echo and ^{29}Si{^{1}H} CPMAS spectra acquired under the same conditions are shown along the corresponding axes for comparison with the 1D projections of the 2D spectra. The accompanying insets show the *J*-coupling between ^{27}Al atoms (orange) and ^{29}Si atoms (grey) at nearest-neighbor T sites consistent with the correlated intensities in the 2D spectrum.

Interestingly, octahedrally-coordinated ^{27}Al species are also covalently bonded to Q^4(1Al) Si2 species within the aluminosilicate zeolite framework, as established by the correlation of the ^{27}Al signal at -5 ppm and a ^{29}Si signal at -101 ppm (blue band). The presence of this weak correlated signal is confirmed by the 2D ^{27}Al{^{29}Si} *J*-HMQC spectrum of Al-SSZ-70 acquired at 9.4 Tesla and 91 K (Fig. 4.4). Octahedrally-coordinated framework ^{27}Al species in aluminosilicate zeolites are generally associated with framework defect sites

and/or partial dealumination of the framework.[36] Here, the correlation of the ^{29}Si signal at -101 ppm from Si2 Q^4(1Al) species and the ^{27}Al signal at -5 ppm establishes that the octahedrally-coordinated ^{27}Al species are in fact covalently linked to Si2 Q^4(1Al) species and therefore in T1a/b or T3 sites. Because of steric hindrance near framework T1a and T3 sites, the presence of octahedrally-coordinated Al1a or Al3 species is considered unlikely. By comparison, T1b is a partially-crosslinked site that protrudes into the interlayer channels, where ^{27}Al atoms could coordinate to adsorbed water and/or hydroxyl groups. Octahedrally-coordinated Al1b species are therefore expected to be associated with significant hydrogen bonding.

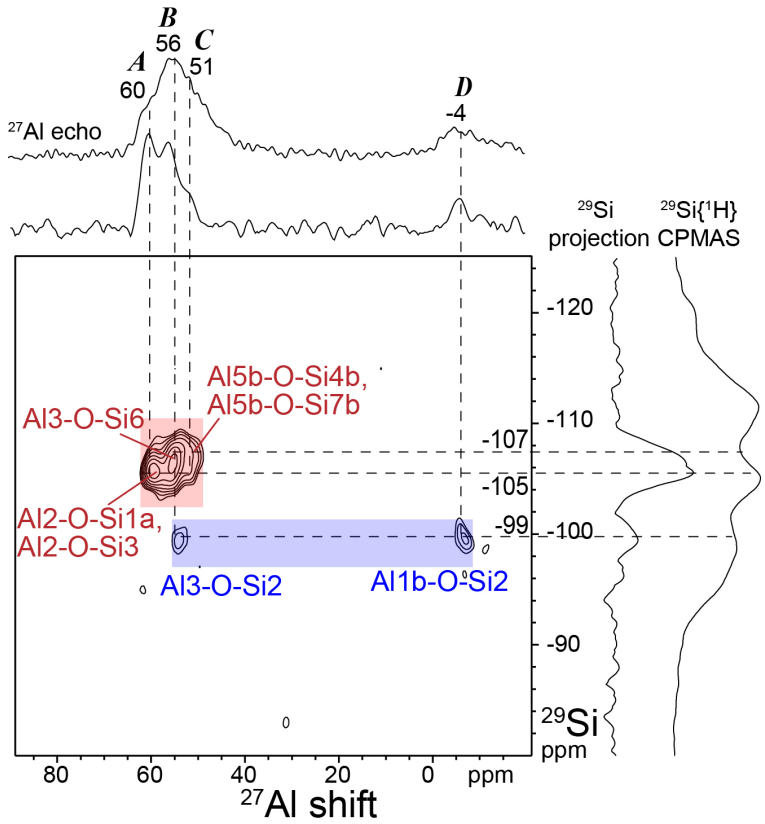

Figure 4.4. Solid-state 2D ^{27}Al{^{29}Si} *J*-HMQC spectrum of calcined Al-SSZ-70 acquired at 9.4 Tesla, 8 kHz MAS, and 91 K. Solid-state 1D ^{27}Al echo and ^{29}Si{^{1}H} CPMAS spectra acquired under the same conditions are shown along the corresponding axes for comparison with the 1D projections of the 2D spectra.

4.3.3 Strong hydrogen bonds in calcined Al-SSZ-70

Strong H-bonds associated with the octahedrally-coordinated ^{27}Al species in T1b sites in calcined Al-SSZ-70 are identified by analysis of the 2D ^{27}Al{^{1}H} HETeronuclear CORrelation (HETCOR) spectrum (Fig. 4.5), which manifests correlated ^{27}Al{^{1}H} signal intensities from ^{27}Al-^{1}H nuclear spin pairs that are dipole-dipole coupled through space. Such spectra are principally sensitive to interactions over distances of <5 Å.[37] Analyses of 2D ^{29}Si{^{1}H} HETCOR spectra of calcined Si- and Al-SSZ-70 (Fig. 4.6) show that both materials possess isolated and strongly H-bonded interlayer -OH species. The 2D ^{27}Al{^{1}H} HETCOR spectrum of calcined Al-SSZ-70 shows correlated intensity at 55 and 60 ppm in the ^{27}Al dimension and at 2.8-5.6 ppm in the ^{1}H dimension, which arises from tetrahedrally-coordinated ^{27}Al species proximate to isolated interlayer -OH groups (green band) and nanopore-adsorbed water (grey band).[18,37] These signals are consistent with the assignment of the ^{27}Al signals at 55 and 60 ppm to fully-crosslinked Al2a/b and Al3 sites, respectively, which are expected to be *ca*. 5 Å from isolated Si-OH species at Si1b sites.[18] By comparison, the ^{27}Al signal at -5 ppm is correlated with a broad, continuous distribution of ^{1}H signals from 2.8-14.3 ppm. The ^{1}H signals at 2.8-4.0 ppm (green band) are assigned to isolated Si-OH or Al-OH moieties, those at 5.1-6.0 ppm (grey band) to adsorbed water molecules, and those at 8.8-14.3 ppm (purple band) to different types of strongly H-bonded silanol groups with approximate -OH···O- distances of 2.8 Å to 2.5 Å as estimated from the ^{1}H chemical shift values and semi-empirical correlations.[38,39] The correlated ^{27}Al{^{1}H} signal intensities establish that the octahedrally-coordinated ^{27}Al species are in close proximities to isolated and strongly H-bonded -OH moieties, as expected for ^{27}Al sites at the surfaces of the interlayer channels. All of the solid-state NMR results are therefore consistent with the

assignment of the ^{27}Al signal at -5 ppm to partially-crosslinked Al1b sites in calcined Al-SSZ-70, which protrude into the interlayer channel regions and are able to adopt octahedral configurations by coordinating with water molecules or hydroxyl groups.

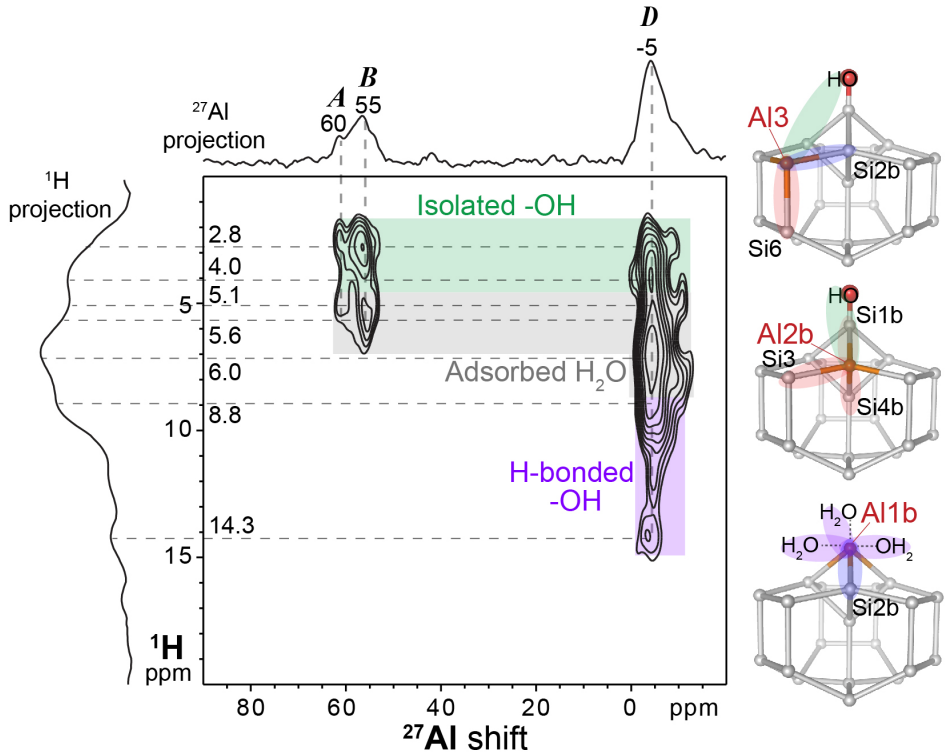

Figure 4.5. Solid-state 2D ^{27}Al{^{1}H} HETCOR spectrum of calcined Al-SSZ-70 acquired at 18.8 Tesla, 10 kHz MAS, and 97 K. The 1D ^{1}H and ^{27}Al projections of the 2D spectra are shown along the corresponding ^{1}H and ^{27}Al axes. The accompanying insets show the *J*-coupling between ^{27}Al atoms (orange) and ^{29}Si atoms (grey) at nearest-neighbor T sites consistent with the correlated intensities in the 2D spectrum in Fig. 4.3, as the ^{27}Al-^{1}H proximities consistend with the 2D HETCOR spectrum.

The presence of different types of isolated and H-bonded -OH moieties in calcined Al-SSZ-70 is corroborated by the 2D ^{29}Si{^{1}H} HETCOR spectra in Fig. 4.6. The 2D ^{29}Si{^{1}H} HETCOR spectrum of calcined Si-SSZ-70 (acquired under DNP-NMR conditions, Fig. 4.6a) shows ^{29}Si signals in the -96 to -99 ppm range from partially-crosslinked Q3(0Al) 29Si species that are correlated with 1H signals at 3.0 ppm, 7.0 ppm, and 8.8 ppm, which arise respectively from isolated Si-OH moieties, DNP solvent molecules, and nests of H-bonded

Si-OH species.[18] Partially resolved ^{29}Si signals in the -105 to -112 ppm range arise from fully-crosslinked Q^4 species in the Si-SSZ-70 zeolite framework. By comparison, the 2D ^{29}Si{^{1}H} HETCOR spectrum of calcined Al-SSZ-70 (Fig. 4.6b) shows correlated signal intensities at ^{29}Si chemical shifts of -98 to -102 ppm from Q^3(0Al) species that are correlated to ^{1}H signals from isolated -OH groups in the 0-3.7 ppm range and from H-bonded -OH groups in the 7.6 to 11.1 ppm range. Additional correlated signal intensities at ^{29}Si chemical shifts of -104 to -114 ppm arise from overlapping ^{29}Si signals from fully-crosslinked Q^4(0Al) and Q^4(1Al) species, while the broad correlated signals at 6.9 ppm in the ^{1}H dimension and at -98 to -107 ppm in the ^{29}Si dimension are attributed to interactions of adsorbed water molecules and framework ^{29}Si species. The relatively low signal-to-noise ratio (S/N ~ 3) of the 2D ^{29}Si{^{1}H} HETCOR spectrum is likely due to the low density of ^{1}H sites interacting with ^{29}Si atoms in the calcined Al-SSZ-70 material and the inhomogeneously-broadened ^{29}Si and ^{1}H signals. Despite the low sensitivity, the resolution of the 2D ^{29}Si{^{1}H} HETCOR spectrum is sufficient to determine that different types of isolated and strongly H-bonded -OH species are present in calcined Al-SSZ-70, similar to its siliceous analogue.

4.3.4 Isotropic ^{27}Al chemical shifts in calcined Al-SSZ-70

The ^{27}Al heteroatoms at different T sites in calcined Al-SSZ-70 are expected to exhibit different isotropic ^{27}Al chemical shifts that will yield different ^{27}Al NMR signals in the solid-state ^{27}Al NMR spectra, enabling the T site positions and occupancies of the different Al species to be identified when analyzed in conjunction with the 2D correlation spectra discussed above. The ^{27}Al quadrupolar and chemical shift parameters for the different ^{27}Al species in Al-SSZ-70 are determined by using 2D ^{27}Al triple-quantum MAS (3QMAS)

techniques.[22] The 2D ^{27}Al 3QMAS spectra of Al-SSZ-70 (Fig. 4.7 and 4.8) are presented as 2D contour plots, with ^{27}Al signals plotted across MAS and isotropic dimensions with frequency units of Hz/MHz or ppm. The MAS dimension manifests the same MAS NMR lineshape as detected in conventional 1D ^{27}Al NMR MAS experiments, while the isotropic dimension reflects only the isotropic contributions to the ^{27}Al signals, with anisotropic second-order quadrupolar broadening effects removed.[22] The isotropic chemical shifts, $\delta_{CS,\mathrm{iso}}$, are determined for each ^{27}Al signal by fitting the ^{27}Al lineshapes extracted from the 2D MQMAS spectrum in Fig. 4.7a at TQ shifts 62, 57, 50, and 1.3 ppm (horizontal dotted lines in Fig. 4.7a). The extracted slices and simulated ^{27}Al lineshapes for the ^{27}Al signals *A*-*C* from tetrahedrally-coordinated ^{27}Al species are shown in Fig. 4.3b, with the isotropic ^{27}Al chemical shift values indicated.

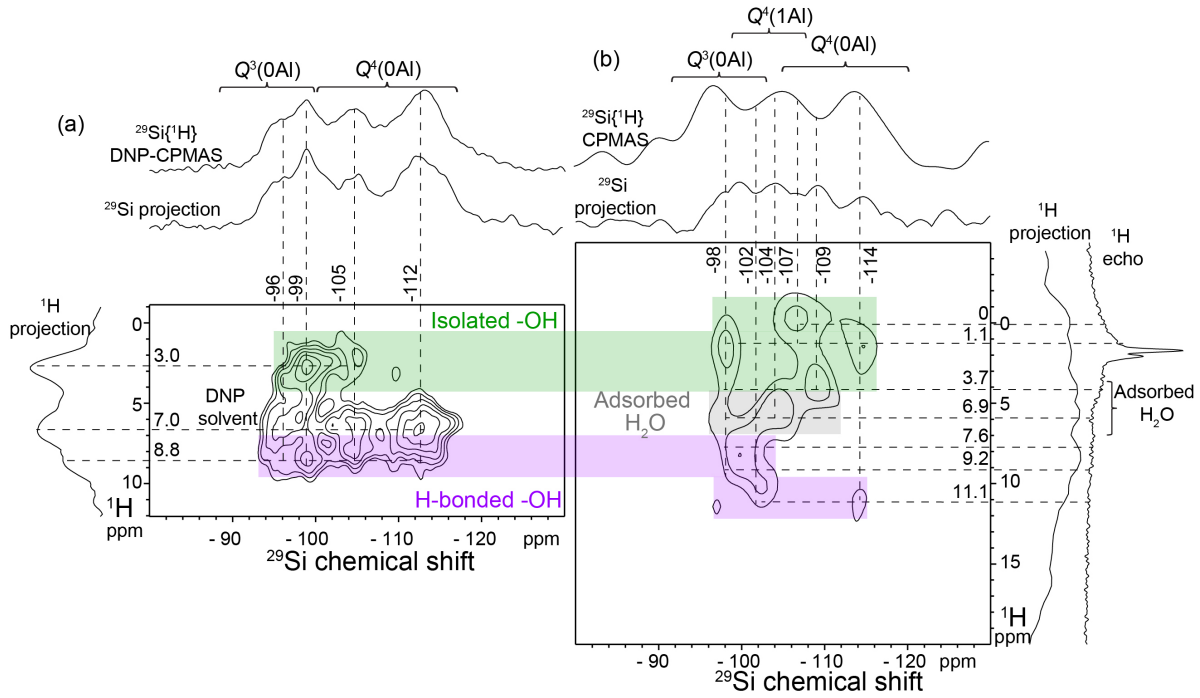

Figure 4.6. Solid-state 2D ^{29}Si{^{1}H} HETCOR spectra of calcined (a) Si-SSZ-70 and (b) Al-SSZ-70. Solid-state 1D ^{29}Si{^{1}H} CPMAS or ^{1}H echo spectra are shown along the horizontal or vertical axes, respectively, for comparison with the 1D projections of the 2D spectra. The spectra in (a) were acquired under DNP-NMR conditions at 9.4 T, 10 kHz MAS, 95 K, with ^{29}Si{^{1}H} contact time of 0.2 ms, in the presence of 16 mM TEKPol biradical in TCE (DNP

solvent), and under 263 GHz microwave irradiation (adapted from Ref. [18]). The spectra in (b) were acquired under low-temperature NMR conditions of 9.4 T, 10 kHz MAS, 93 K, and with $^{29}Si\{^{1}H\}$ contact times of 0.2 ms.

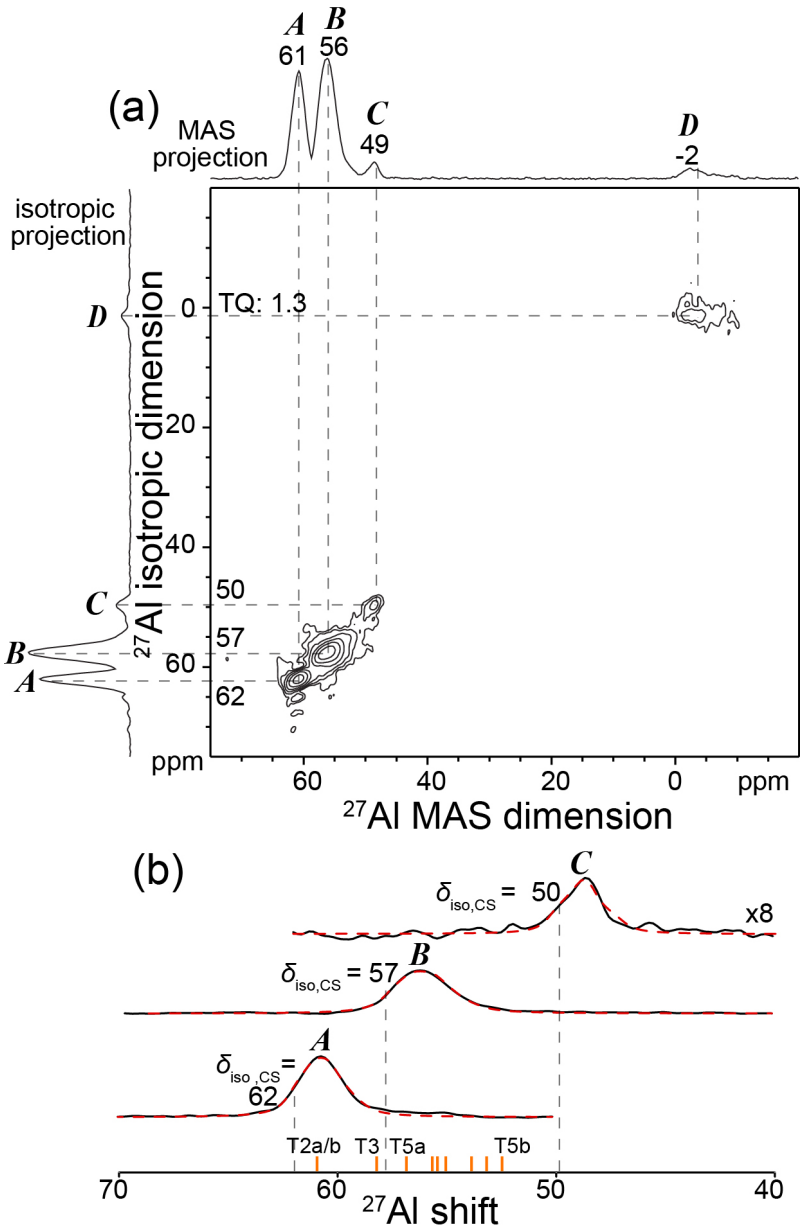

Figure 4.7. (a) Solid-state 2D 3QMAS NMR spectrum of calcined Al-SSZ-70 acquired at 18.8 T, 298 K, and 35 kHz MAS, with SQ and TQ projections shown along the horizontal and vertical axes, respectively. Horizontal cross-sections at TQ shifts of 50, 58, and 62 ppm are extracted from the 2D ^{27}Al 3QMAS spectrum and shown in (b). The red dotted lines are simulations of the ^{27}Al lineshapes using the parameters listed in Table 1 and the orange lines are predicted ^{27}Al isotropic chemical shifts for ^{27}Al heteroatoms sited at each of the different T sites in Al-SSZ-70, calculated using Eqn. 4.1.

Isotropic ^{27}Al chemical shifts of tetrahedrally-coordinated ^{27}Al species in aluminosilicate materials correlate linearly to the mean T-O-T bond angle, θ', for a given T site. A commonly applied semi-empirical correlation, developed by Lippmaa, et al,[33,40] is:

$$\delta_{\mathrm{CS,iso}} = -0.5\theta' + 132 \text{ (ppm)} \qquad \text{(Eqn. 4.1)}$$

While this equation relies on the average T site geometry obtained from powder diffraction measurements, which are not always representative of the local geometry around Al sites that make up a small fraction of the overall number of T sites,[7] it provides a first approximation for assigning the different ^{27}Al signals in the ^{27}Al NMR spectra of Al-SSZ-70. The predicted isotropic ^{27}Al chemical shifts, calculated from the known structure of calcined Si-SSZ-70 and Eqn. 4.1 are provided in Table 4.2 and compared with the experimentally-determined $\delta_{\mathrm{CS,iso}}$ values for signals *A*-*C* in Fig. 4.7b. On the basis of this comparison, ^{27}Al signal *A* at $\delta_{\mathrm{CS,iso}}$ = 62 ppm is tentatively assigned to ^{27}Al species at fully-crosslinked T2a and T2b sites, which have predicted $\delta_{\mathrm{CS,iso}}$ values of 61 ppm. ^{27}Al signal *B* at $\delta_{\mathrm{CS,iso}}$ = 57 ppm is assigned to ^{27}Al species at T3 and/or T5a sites, which have calculated $\delta_{\mathrm{CS,iso}}$ values of 58 and 57 ppm, respectively. Signal *C* at $\delta_{\mathrm{CS,iso}}$ = 50 ppm is closest to the predicted isotropic chemical shift value for T5b (53 ppm), but the agreement between the calculated and experimental ^{27}Al $\delta_{\mathrm{CS,iso}}$ values is relatively poor and so a confident assignment cannot be made. Further confidence in the assignments of ^{27}Al signals *A*-*C* are provided by complementary analyses of 2D ^{27}Al 3QMAS spectra acquired at different magnetic field strengths and temperatures, shown in Fig. 4.4. At lower magnetic field strengths (9.4 T) and temperatures (95 K) the ^{27}Al signals are displaced and broadened by comparison to the spectra obtained at 18.8 T due to the greater quadrupolar interactions at the lower magnetic field strength and inhomogeneous temperature-dependent broadening effects. The quadrupolar coupling constants C_{Q}, asymmetry parameters η, and $\delta_{\mathrm{CS,iso}}$ values for each ^{27}Al

signals, determined by fitting the horizontal ^{27}Al slices extracted from the 2D ^{27}Al 3QMAS spectra, are provided in Table 4.1.

Table 4.1. ^{27}Al quadrupolar parameters and isotropic chemical shifts for calcined Al-SSZ-70[a]

^{27}Al signal:	***A***	***B***	***C***	***D***
$\delta_{CS,iso}$ (ppm)	62	57	50	1.3
C_Q (MHz)	2.2	3.0	2.4	5.5[c]
η[b]	0.5	0	0.6	-[c]

[a] Extracted from analysis of the 2D ^{27}Al MQMAS spectrum in Fig. S2.
[b] The fits of the ^{27}Al NMR lineshapes were found to be generally insensitive to the asymmetry parameter η, similar to previous ^{27}Al 3QMAS NMR analyses of aluminosilicate zeolites.[41]
[c] The ^{27}Al signal *D* in the six-coordinate region was fitted by using a single quadrupolar Czjzek lineshape, which reflects a distribution of quadrupolar parameters characterized by a maximum C_Q value of 5.5 MHz.

Table 4.2. Predicted ^{27}Al $\delta_{CS,iso}$ values for ^{27}Al atoms at each T site in Al-SSZ-70[a]

T-site	1a	1b	2a	2b	3	4a	4b	5a	5a	6	7a	7b	8a	8b
^{27}Al $\delta_{CS,iso}$ (ppm)	56	-[b]	61	61[c]	58	55	55	57	52	53	53	55	55	54

[a] Calculated using the mean -T-O-T- angles for each T site from the structure of calcined Si-SSZ-70[18] and Eqn. S1.
[b] T1b is a partially-crosslinked site protruding into the interlayer channels of calcined Al-SSZ-70 and is associated with at least one hydroxyl group. Eqn. S1 does not account for Al-OH bonds, which are expected to influence the ^{27}Al isotropic shifts.
[c] T2b may be either completely- or partially- crosslinked. This value is for completely-crosslinked Al2b sites.

Elucidating the nature of the octahedrally-coordinated ^{27}Al species that give rise to ^{27}Al signal *D* is more challenging, as octahedrally-coordinated ^{27}Al species in zeolite frameworks are rare, though may arise as products of partial reversible dealumination.[42] Signal *D* could also be attributed to extra-framework alumina species such as residual alumina gel remaining in the material after the hydrothermal synthesis and calcination.

However, though signal *D* is relatively broad in the MAS dimension of the 2D 27Al MQMAS spectrum, this broadening arises primarily from anisotropic quadrupolar interactions, as evidenced by the relatively narrow linewidth (2 ppm full-width half-maximum, fwhm) associated with the signal in the isotropic dimension in Fig. 4.7a. This indicates that signal *D* arises from a narrow distribution of ^{27}Al species in well-ordered environments, which is inconsistent with extraframework alumina species. The ^{27}Al lineshape of signal *D* is fit well using a Czjzek lineshape,[43] which is characteristic of a distribution of ^{27}Al quadrupolar parameters as previously observed in aluminosilica glasses[44] or aluminosilicate zeolites with non-ordered Al distributions.[45] The 2D ^{27}Al{^{29}Si} through-bond-mediated NMR correlation spectra and analyses discussed above provide further evidence that the ^{27}Al signal in the octahedral region is associated with ^{27}Al species that are covalently linked to fully-condensed ^{29}Si species and are therefore located within the aluminosilicate zeolite framework, consistent with its assignment to partially-crosslinked Al1b species.

At lower temperatures (<100 K), ^{27}Al NMR signal sensitivity is improved due to an increase in the Boltzmann distribution of nuclear spin polarization, which enables acquisition of 2D ^{27}Al{^{29}Si} through-bond-mediated correlation spectra that provide detailed structural insights into the bonding environments of the different ^{27}Al species in calcined Al-SSZ-70. The 2D ^{27}Al 3QMAS spectrum of calcined Al-SSZ-70 acquired at 9.4 T and 93 K (Fig. 4.8b) exhibits the same signal intensities as the corresponding spectrum acquired at 295 K (Fig. 4.8a), but with ^{27}Al signals that are modestly displaced and broadened in both the isotropic and MAS dimensions. The spectral broadening indicates a broader distribution of ^{27}Al environments under the low-temperature measurement conditions, likely arising from the

freezing out of interactions of ^{27}Al species with adsorbed water molecules. Similar temperature-dependent broadening effects in NMR of silicate materials have been attributed to the freezing out of interactions with organic surfactant or structure-directing molecules in layered silicates[46] and **MFI**-type zeolite nanosheets[47] and with DNP solvent molecules in calcined Si-SSZ-70 measured under DNP-NMR conditions.[18] The 2D ^{27}Al MQMAS spectra acquired at different temperatures and magnetic field strengths allow the ^{27}Al signals detected and resolved under different measurement conditions to be more confidently assigned.

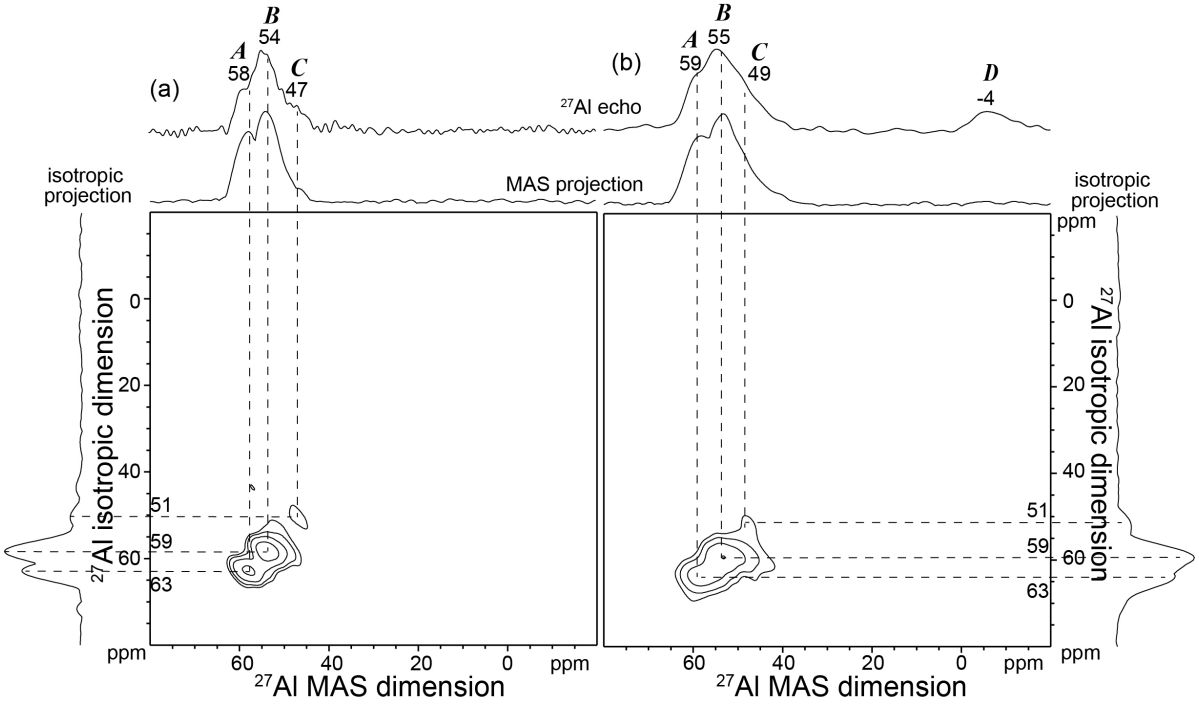

Figure 4.8. Solid-state 2D 3QMAS NMR spectrum of calcined Al-SSZ-70 acquired at 9.4 T, 10 kHz MAS, and (a) 298 K or (b) 93 K. Solid-state 1D ^{27}Al echo NMR spectra acquired under the same conditions are shown along the horizontal axes for comparison with the MAS projections, and the isotropic projection is shown along the vertical axis.

4.3.5 Positions of Al heteroatoms in Al-SSZ-70

Interestingly, the majority of the Al heteroatoms in calcined Al-SSZ-70 are located at sites at the surfaces of the interlayer channels, as determined by analysis of the quantitative

1D ^{27}Al MAS NMR spectrum of the material (Fig. 4.8a). On the basis of the analyses of the 2D ^{27}Al 3QMAS spectra, as well as the 2D ^{27}Al{^{29}Si}, ^{29}Si{^{1}H}, and ^{27}Al{^{1}H} heteronuclear correlation spectra, each of the ^{27}Al signals is confidently assigned to an individual T site within the zeolite framework structure. Specifically, ^{27}Al signal *I* is assigned to ^{27}Al atoms at T2a or fully-crosslinked T2b sites, ^{27}Al signal *II* is assigned to ^{27}Al atoms at T3 sites, ^{27}Al signal *III* is assigned to T5b sites, and ^{27}Al signal *IV* is assigned to ^{27}Al atoms at T1b sites within the interlayer channels that are octahedrally-coordinated. The different ^{27}Al species are quantified by deconvolution of the 1D single-pulse ^{27}Al spectrum in Fig. 4.8a, which shows that the ^{27}Al species located at sites T2a, T3, T5b, and T1b respectively account for 25%, 53%, 6%, and 16% of all of the ^{27}Al species in the material. The positions of each of these T sites in the Al-SSZ-70 framework structure are indicated by orange dots in the schematic structure of calcined Al-SSZ-70 Fig. 4.8b. Notably, the great majority of the ^{27}Al species (94%) are sited at T2a, T3, or T1b sites, which are located at the surfaces of the interlayer channels. The remainder of the ^{27}Al species (6%) are at T5b sites, which are located at the surfaces of the intralayer channels. Due to their different positions and local structures within the SSZ-70 framework, the distinct Al heteroatom sites are expected to be associated with very different properties for molecular adsorption and catalysis. These results elucidate the high catalytic activities of catalysts derived from delamination of SSZ-70 materials:[16,48] nearly all of the heteroatoms associated with the cation-exchange sites in Al-SSZ-70 are at the surfaces of the intralayer channels that are exposed on exfoliation and therefore are accessible for post-synthetic modification and/or catalysis.

The reason for the well-defined positions of Al heteroatoms in calcined Al-SSZ-70 is unclear. The positioning of the majority of the Al heteroatoms at sites at the surfaces of the

interlayer channels indicates that the bulky N,N'-diisobutylimidazolium cations used as organic structure directing agents (OSDAs) during the zeolite synthesis must direct the Al heteroatoms to specific sites at the surfaces of the interlayer channels. As the positions of the Al heteroatoms in Al-SSZ-70 are not expected to change on calcination (though their coordination might), the above analyses are expected to be very useful for further studies on as-synthesized SSZ-70, the interlayer structure of which is still unknown.

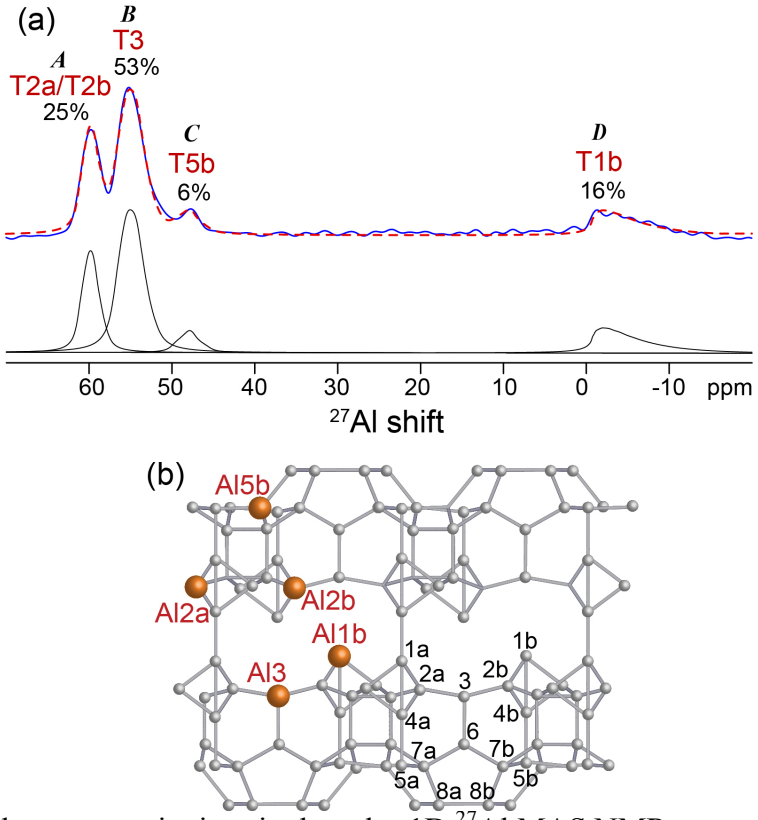

Figure 4.9. (a) Solid-state quantitative single-pulse 1D ^{27}Al MAS NMR spectrum of calcined Al-SSZ-70, acquired at 18.8 T, 35 kHz MAS, and 295 K. The red dotted line is a simulation of the spectrum, with the deconvolution shown offset below. (b) Schematic of the framework structure of Al-SSZ-70, with orange dots indicating the T sites that may be occupied by Al heteroatoms as identified by the solid-state NMR analyses.

4.4 Conclusions

In summary, the preferential siting of Al heteroatoms at 5 of the 14 T sites in calcined Al-SSZ-70 has been established by comprehensive analysis of solid-state 1D and 2D ^{1}H, ^{27}Al, and ^{29}Si NMR spectra. Notably, 2D ^{27}Al{^{29}Si} and ^{27}Al{^{1}H} heteronuclear correlation spectra establish the T-site connectivities and hydration environments of the different ^{27}Al sites. The methods described here are fully extendable to diverse other technologically-relevant aluminosilicate materials to understand the atomic origins of their macroscopic properties. The insights provided here on Al siting in calcined Al-SSZ-70 provide a deeper understanding of this emerging catalytic material, and are expected to aid in the future design of new catalytic materials with improved activity, selectivity, and stability.

4.5 Materials and methods

4.5.1 Synthesis of Al-SSZ-70

The Al-SSZ-70 material was synthesized according to the protocol described in reference 17 using *N*,*N*′-diisobutyl imidazolium hydroxide as the OSDA.

4.5.2 Calcination

The material was calcined to remove the OSDA and condense the layered aluminosilicate precursor. A thin bed of the zeolite sample was calcined in air in a muffle furnace with a controlled ramp program: temperature increased at a rate of 1 °C per minute up to 120 °C; held for 2 h; increased at the same rate up to 540 °C; held for 5 h; and finally allowed to cool down slowly in the oven.

4.5.3 X-ray Powder Diffraction

Synchrotron XRPD data were collected on both calcined and as-synthesized samples of Si-SSZ-70 and Al-SSZ-70 in a rotating 0.3 mm capillary on the MS-Powder beamline at the Swiss Light Source in Villigen, Switzerland (wavelength 0.70848 Å, MYTHEN II detector).[49]

4.5.4 Electron microscopy

Scanning electron micrographs of Al-SSZ-70 were obtained using a JEOL JSM 6700F instrument.

4.5.5 Solid-state NMR spectroscopy

Solid-state 1D and 2D MAS NMR spectroscopy was used to analyze the ^{1}H, ^{27}Al, and ^{29}Si environments in calcined Al-SSZ-70. The ^{1}H and ^{29}Si chemical shifts were referenced to trimethylsilane (TMS) at 0.0 ppm, using tetrakis(trimethylsilyl)silane as a secondary external chemical shift reference. The ^{27}Al shifts were referenced to a 0.5 M solution of $Al(NO_3)_3$ as a secondary external shift reference. The 1D single-pulse ^{27}Al and 2D ^{27}Al 3QMAS spectra measured at 295 K and 18.8 T were acquired on a Bruker AVANCE-III Ultrashield Plus 800 MHz (18.8 T) narrow-bore spectrometer operating at a Larmor frequency of 208.520 MHz for ^{27}Al and using a Bruker 2.5 mm broadband double-resonance H-X probehead. The ^{27}Al spin-lattice T_1 relaxation times were measured using a saturation recovery experiment to be 40 ms or less at 295 K and 650 ms or less at 90-100 K for all the ^{27}Al signals. The 2D ^{27}Al 3QMAS spectrum was obtained using 2400 transients, a repetition time of 0.1 s, a rotor-synchronized incremental t_1 step size of 14.29 μs, and 200 increments in the indirect dimension for a total acquisition time of 27 h. The 1D quantitative single-pulse ^{27}Al spectrum was acquired using a 0.27 μs π/12 pulse, 512 transients, and a repetition time of 0.2

s. The 2D ^{27}Al{^{29}Si} *J*-HMQC spectrum measured at 100 K and 18.8 T was acquired on a Bruker ASCEND 800 MHz (18.8 T) DNP NMR spectrometer operating at Larmor frequencies of 208.387 and 158.864 for ^{27}Al and ^{29}Si, respectively, and equipped with a 3.2 mm triple-resonance HXY low-temperature MAS probehead. The spectrum was acquired with an experimentally-optimized τ delay of X ms to refocus the weak (ca. 10 Hz) ^{27}Al-O-^{29}Si scalar *J* couplings, a repetition time of 2 s 512 transients, a rotor-synchronized incremental t_1 step size of 80 μs, and 50 increments in the indirect dimension for a total acquisition time of 14 h. The 2D ^{27}Al 3QMAS, ^{27}Al{^{1}H} HETCOR, ^{29}Si{^{1}H} HETCOR, and ^{27}Al{^{29}Si} *J*-HMQC spectra measured at 9.4 T were acquired on a Bruker ASCEND 400 MHz (9.4 T) DNP NMR spectrometer operating at Larmor frequencies of 400.203, 104.283, and 79.501 MHz for ^{1}H, ^{27}Al, and ^{29}Si nuclei, respectively and equipped with a 3.2 mm triple-resonance HXY low-temperature MAS probehead. The 2D ^{27}Al 3QMAS spectrum acquired at 9.4 T and 295 K was obtained using 2400 transients, a repetition time of 0.2 s, an incremental t_1 step size of 50 μs, and 50 increments in the indirect dimension for a total acquisition time of 7 h. The 2D ^{27}Al 3QMAS spectrum acquired at 9.4 T and 93 K was obtained using 960 transients, a repetition time of 1 s, an incremental t_1 step size of 50 μs, and 50 increments in the indirect dimension for a total acquisition time of 13 h. The 2D ^{29}Si{^{1}H} HETCOR spectrum of calcined Si-SSZ-70 was acquired under DNP-NMR conditions as previously reported.[18] The 2D ^{29}Si{^{1}H} HETCOR spectrum of calcined Al-SSZ-70 was acquired using a ^{29}Si{^{1}H} contact time of 0.2 ms, 512 transients, a repetition time of 1.2 s, an incremental t_1 step size of 64 μs, and 32 increments in the indirect dimension for a total acquisition time of 5.5 h. The 2D ^{27}Al{^{1}H} HETCOR spectrum of calcined Al-SSZ-70 was acquired using a ^{27}Al{^{1}H} cross-polarization contact time of 0.2 ms, 512

transients, a repetition time of 1.2 s, an incremental t_1 step size of 64 μs, and 32 increments in the indirect dimension for a total acquisition time of 5.5 h. All of the 2D HETCOR spectra were acquired using homonuclear ^{1}H-^{1}H eDUMBO-1_{22} decoupling[50] during the ^{1}H evolution periods to improve resolution in the ^{1}H dimensions. For all of the 2D ^{27}Al{^{29}Si} *J*-HMQC spectra, 100 kHz of continuous wave ^{1}H decoupling was applied during the rotor-synchronized tau delay periods. The signal sensitivity of the 2D ^{27}Al{^{29}Si} *J*-HMQC spectra was enhanced by applying a 1 ms ^{27}Al adiabatic double-frequency sweep (DFS) pulse during the preparation period to invert the ^{27}Al satellite transitions.[51] All of the 2D ^{27}Al 3QMAS spectra were obtained using a 20 μs z-filter to eliminate zero-quantum coherences and processed using a shearing transformation to scale the isotropic TQ frequency axes. All of the 1D and 2D spectra, with the exception of the 2D ^{27}Al 3QMAS spectra, were acquired with 100 kHz heteronuclear SPINAL-64[52] ^{1}H decoupling during the acquisition period. All NMR lineshape simulations and spectral deconvolutions were performed using dmfit software.[53]

4.6 References

(1) Nugent, P.; Belmabkhout, Y.; Burd, S. D.; Cairns, A. J.; Luebke, R.; Forrest, K.; Pham, T.; Ma, S.; Space, B.; Wojtas, L.; Eddaoudi, M.; Zaworotko, M. J. *Nature* **2013**, *495* (7439), 80.

(2) Vogt, E. T. C.; Weckhuysen, B. M. *Chem. Soc. Rev.* **2015**, *44* (20), 7342.

(3) Gallego, E. M.; Portilla, M. T.; Paris, C.; León-Escamilla, A.; Boronat, M.; Moliner, M.; Corma, A. *Science.* **2017**, *355* (6329), 1051.

(4) Paolucci, C.; Khurana, I.; Parekh, A. A.; Li, S.; Shih, A. J.; Li, H.; Di Iorio, J. R.; Albarracin-Caballero, J. D.; Yezerets, A.; Miller, J. T.; Delgass, W. N.; Ribeiro, F. H.; Schneider, W. F.; Gounder, R. *Science.* **2017**, *357* (6354), 898.

(5) Gábová, V.; Dědeček, J.; Čejka, J. *Chem. Commun.* **2003**, *3* (10), 1196.

(6) Gounder, R.; Iglesia, E. *J. Am. Chem. Soc.* **2009**, *131* (5), 1958.

(7) Dědeček, J.; Sobalík, Z.; Wichterlová, B. *Catal. Rev. - Sci. Eng.* **2012**, *54* (2), 135.

(8) Van Bokhoven, J. A.; Lee, T. L.; Drakopoulos, M.; Lamberti, C.; Thie, S.; Zegenhagen, J. *Nat. Mater.* **2008**, *7* (7), 551.

(9) Pinar, A. B.; Gómez-Hortigüela, L.; McCusker, L. B.; Pérez-Pariente, J. *Chem. Mater.* **2013**, *25* (18), 3654.

(10) Smeets, S.; McCusker, L. B.; Baerlocher, C.; Elomari, S.; Xie, D.; Zones, S. I. *J. Am. Chem. Soc.* **2016**, *138* (22), 7099.

(11) Hun Kwak, J.; Zhu, H.; Lee, J. H.; Peden, C. H. F.; Szanyi, J. *Chem. Commun.* **2012**, *48* (39), 4758.

(12) Dědeček, J.; Kaucký, D.; Wichterlová, B.; Gonsiorová, O. *Phys. Chem. Chem. Phys.* **2002**, *4*

(21), 5406.
(13) Zones, S. I.; Benin, A.; Hwang, S.-J. J.; Xie, D.; Elomari, S.; Hsieh, M.-F. F. *J. Am. Chem. Soc.* **2014**, *136* (4), 1462.
(14) Di Iorio, J. R.; Gounder, R. *Chem. Mater.* **2016**, *28* (7), 2236.
(15) Di Iorio, J. R.; Nimlos, C. T.; Gounder, R. *ACS Catal.* **2017**, *7* (10), 6663.
(16) Runnebaum, R. C.; Ouyang, X.; Edsinga, J. A.; Rea, T.; Arslan, I.; Hwang, S.-J. J.; Zones, S. I.; Katz, A. *ACS Catal.* **2014**, *4* (7), 2364.
(17) Archer, R. H.; Carpenter, J. R.; Hwang, S.-J.; Burton, A. W.; Chen, C.-Y.; Zones, S. I.; Davis, M. E. *Chem. Mater.* **2010**, *22* (8), 2563.
(18) Smeets, S.; Berkson, Z. J.; Xie, D.; Zones, S. I.; Wan, W.; Zou, X.; Hsieh, M. F.; Chmelka, B. F.; McCusker, L. B.; Baerlocher, C. *J. Am. Chem. Soc.* **2017**, *139* (46), 16803.
(19) Zones, S. I.; Harris, T. V. *Microporous Mesoporous Mater.* **2000**, *35–36*, 31.
(20) Kodakari, N.; Tomita, K.; Iwata, K.; Katada, N.; Niwa, M. *Langmuir* **1998**, *14* (16), 4623.
(21) Haouas, M.; Taulelle, F.; Martineau, C. *Prog. Nucl. Magn. Reson. Spectrosc.* **2016**, *94–95*, 11.
(22) Frydman, L.; Grant, D. M.; Harris, R. K. *Encycl. Nucl. Magn. Reson. Vol. 9 Adv. NMR* **2002**, *9*, 262.
(23) Sklenak, S.; Dědeček, J.; Li, C.; Wichterlová, B.; Gábová, V.; Sierka, M.; Sauer, J. *Angew. Chemie - Int. Ed.* **2007**, *46* (38), 7286.
(24) Sklenak, S.; Dědeček, J.; Li, C.; Wichterlová, B.; Gábová, V.; Sierka, M.; Sauer, J. *Phys. Chem. Chem. Phys.* **2009**, *11* (8), 1237.
(25) Holzinger, J.; Beato, P.; Lundegaard, L. F.; Skibsted, J. *J. Phys. Chem. C* **2018**, *122* (27), 15595.
(26) Dib, E.; Mineva, T.; Veron, E.; Sarou-Kanian, V.; Fayon, F.; Alonso, B. *J. Phys. Chem. Lett.* **2018**, *9* (1), 19.
(27) Rankin, A. G. M.; Webb, P. B.; Dawson, D. M.; Viger-Gravel, J.; Walder, B. J.; Emsley, L.; Ashbrook, S. E. *J. Phys. Chem. C* **2017**, *121* (41), 22977.
(28) Lesage, A.; Sakellariou, D.; Steuernagel, S.; Emsley, L. *J. Am. Chem. Soc.* **1998**, *120* (7), 13194.
(29) Florian, P.; Veron, E.; Green, T. F. G.; Yates, J. R.; Massiot, D. **2012**.
(30) Valla, M.; Rossini, A. J.; Caillot, M.; Chizallet, C.; Raybaud, P.; Digne, M.; Chaumonnot, A.; Lesage, A.; Emsley, L.; Van Bokhoven, J. A.; Copéret, C. *J. Am. Chem. Soc.* **2015**, *137* (33), 10710.
(31) Massiot, D.; Fayon, F.; Deschamps, M.; Cadars, S.; Florian, P.; Montouillout, V.; Pellerin, N.; Hiet, J.; Rakhmatullin, A.; Bessada, C.; Massiot, D.; Fayon, F.; Deschamps, M.; Cadars, S.; Florian, P.; Massiot, D.; Fayon, F.; Deschamps, M.; Cadars, S.; Florian, P. **2010**.
(32) Ramdas; Klinosski. *Nature* **1984**, *308*, 521.
(33) Lippmaa, E.; Samoson, A.; Magi, M. *J. Am. Chem. Soc.* **1986**, *108* (8), 1730.
(34) Dawson, D. M.; Moran, R. F.; Ashbrook, S. E. *J. Phys. Chem. C* **2017**, *121* (28), 15198.
(35) Camblor, M. A.; Corma, A.; Díaz-Cabañas, M.-J.; Baerlocher, C. *J. Phys. Chem. B* **1998**, *102* (1), 44.
(36) Omegna, A.; van Bokhoven, J. a.; Prins, R. *J. Phys. Chem. B* **2003**, *107* (34), 8854.
(37) Janicke, M. T.; Landry, C. C.; Christiansen, S. C.; Kumar, D.; Stucky, G. D.; Chmelka, B. F. *J. Am. Chem. Soc.* **1998**, *120* (28), 6940.
(38) Yesinowski, J. P.; Eckert, H.; Rossman, G. R. *J. Am. Chem. Soc.* **1988**, *110* (5), 1367.
(39) Xue, X.; Kanzaki, M. *J. Am. Ceram. Soc.* **2009**, *92* (12), 2803.
(40) Samoson, A.; Lippmaa, E.; Engelhardt, G.; Lohse, U.; Jerschkewitz, H. G. *Chem. Phys. Lett.* **1987**, *134* (6), 589.
(41) Fyfe, C. A.; Bretherton, J. L.; Lam, L. Y. *J. Am. Chem. Soc.* **2001**, *123* (22), 5285.
(42) Van Bokhoven, J. A.; Koningsberger, D. C.; Kunkeler, P.; Van Bekkum, H.; Kentgens, A. P. M. *J. Am. Chem. Soc.* **2000**, *122* (51), 12842.
(43) d'Espinose de Lacaillerie, J. B.; Fretigny, C.; Massiot, D. *J. Magn. Reson.* **2008**, *192* (2), 244.

(44) Le Caër, G.; Bureau, B.; Massiot, D. *J. Phys. Condens. Matter* **2010**, *22* (6), 065402.
(45) Klein, P.; Pashkova, V.; Thomas, H. M.; Whittleton, S. R.; Brus, J.; Kobera, L.; Dedecek, J.; Sklenak, S.; Heyrovsky, J. *J. Phys. Chem. C* **2016**, *120* (26), 14216.
(46) Cadars, S.; Mifsud, N.; Lesage, A.; Epping, J. D.; Hedin, N.; Chmelka, B. F.; Emsley, L. *J. Phys. Chem. C* **2008**, *112* (25), 9145.
(47) Berkson, Z. J.; Messinger, R. J.; Na, K.; Seo, Y.; Ryoo, R.; Chmelka, B. F. *Angew. Chemie - Int. Ed.* **2017**, No. 2, 2.
(48) Aigner, M.; Grosso-Giordano, N. A.; Okrut, A.; Zones, S.; Katz, A. *React. Chem. Eng.* **2017**, *2* (6), 842.
(49) Bergamaschi, A.; Cervellino, A.; Dinapoli, R.; Gozzo, F.; Henrich, B.; Johnson, I.; Kraft, P.; Mozzanica, A.; Schmitt, B.; Shi, X. *J. Synchrotron Radiat.* **2010**, *17* (5), 653.
(50) Elena, B.; de Paëpe, G.; Emsley, L. *Chem. Phys. Lett.* **2004**, *398* (4–6), 532.
(51) Van Veenendaal, E.; Meier, B. H.; Kentgens, A. P. M. *Mol. Phys.* **1998**, *93* (2), 195.
(52) Fung, B. M.; Khitrin, A. K.; Ermolaev, K. *J. Magn. Reson.* **2000**, *142*, 97.
(53) Massiot, D.; Fayon, F.; Capron, M.; King, I.; Le Calvé, S.; Alonso, B.; Durand, J. O.; Bujoli, B.; Gan, Z.; Hoatson, G. *Magn. Reson. Chem.* **2002**, *40* (1), 70.

Chapter 5

Hydrocarbon adsorption, reaction, and deactivation sites in aluminosilicate USY zeolite catalysts

Adapted from: Z. J. Berkson, D. C. Upham, S. Prasad, U. Werner-Zwanziger, A. Lesage, E. W. McFarland, B. F. Chmelka, *in preparation.*

5.1 Abstract

Determining the molecular interactions of dilute molecular adsorbates and heterogeneous zeolite catalyst materials is challenging, in part due to the complicated distributions of surface and framework heteroatom adsorption/reaction sites in zeolites. Here, the distributions of Al heteroatoms in steam-aged 'ultrastable' Y (USY) aluminosilicate zeolite materials are established by solid-state 2D $^{27}Al\{^{29}Si\}$ NMR spectra, acquired at high fields and low temperatures, with complementary X-ray diffraction and electron microscopy analyses. Furthermore, the interactions of different catalytically-relevant molecular species (methanol, toluene, and catalytic reaction byproducts) and the USY zeolite frameworks are elucidated by solid-state 2D $^{13}C\{^{1}H\}$, $^{13}C\{^{27}Al\}$, and $^{27}Al\{^{13}C\}$ NMR correlation spectra. Notably, bulky carbonaceous reaction byproducts shown to interact preferentially at partially-crosslinked -Si-OH-Al-O-Si-OH surface mesopore moieties that form on steam-aging of the zeolite catalyst materials. The molecular-level insights are correlated with the macroscopic catalytic reaction properties (toluene methylation) of the USY zeolite materials. It is shown that the adsorption of deactivation products on the USY particle surfaces correlates to reduced selectivity for catalytic cracking reactions. These insights, and especially the identification of specific surface defects that act as deactivation sites, are

expected to aid crucially in the development of new catalyst materials with improved reaction properties.

5.2 Introduction

The adsorption and catalytic reaction properties of many technologically-important porous materials depend on the nanoscale interactions of adsorbed or guest molecules at surface sites. For example, semi-crystalline aluminosilicate zeolites are high-surface-area nanoporous materials with solid-acid or ion-exchange properties that enable diverse applications, including hydrocarbon conversions,[1,2] air-gas separations,[3] ion-exchange,[4] and pollution mitigation.[4,5] Aluminum atoms at tetrahedrally-coordinated sites in zeolite frameworks introduce negative charges that must be charge-balanced by exchangeable cations (e.g., Na^+, NH_4^+, H^+, La^{3+}, etc.), which can act as Brønsted or Lewis acid sites for molecular adsorption and catalysis [6]. One of the most industrially important applications of aluminosilicate zeolites is as solid-acid catalysts for fluidized catalytic cracking (FCC) of petroleum,[7] to convert high-molecular-weight hydrocarbon molecules to lighter, higher value products, including C5-C8 alkanes for automotive fuels. Commercial FCC catalysts typically include steam-aged "ultrastable" aluminosilicate zeolite Y (USY) in H^+- or La^{3+}-exchanged form as a primary component, which shows high activities and good selectivities for gasoline production from petroleum feedstocks.[7] Such FCC catalysts are manufactured and used industrially on a large scale of *ca.* 840,000 metric tons per year (as of 2013), and are responsible for >5 billion barrels per year of valuable liquid hydrocarbon products.[7] Importantly and undesirably, however, USY catalysts are deactivated very rapidly, on millisecond timescales, by the formation of carbonaceous reaction byproducts ("coke") in

and on the catalyst particles. These deposits adsorb at and poison zeolite active sites, block zeolite nanopore entrances, and inhibit macroscopic mass transport through and reactions within the catalyst pellets, which deactivate the catalysts and impose severe and costly process design strategies to overcome. This is particularly for the processing of coke-prone heavy oil feedstocks,[7] as well as for numerous other technologically important hydrocarbon conversion processes, including for the production of polymer precursors from methanol[8,9] and xylenes via toluene alkylation or disproportionation.[10]

To influence catalytic selectivity and mitigate such deactivation reactions, it is crucial to identify and understand the natures of different adsorption and reaction sites and their associated deactivation processes. However, determining the atomic-scale interactions of hydrocarbon reaction products with adsorption/reaction sites on and in zeolite catalyst particles has been exceedingly challenging, in part due to the complicated distributions of surface species, Al heteroatoms and associated active sites, and dilute quantities of adsorbed species, especially at early stages of deactivation. In recent years, the characterization of zeolite catalyst materials has largely focused on obtaining spatially-resolved information on distributions of acid sites, contaminants, or reaction byproducts in single catalyst particles by applying characterization techniques such as X-ray fluorescence microscopy/tomography, X-ray adsorption near-edge structure, atom probe tomography or confocal/single-molecule fluorescence microscopy.[11–14] These techniques have provided insights on the meso- or pellet-scale distributions of catalytically-active species, ion-exchange sites, metal poison contaminants, or carbonaceous reaction byproducts for both fresh and reacted catalyst materials. Such techniques are however limited to relatively long length scales (>50 nm) and large single particles. Here, new atomic-level insights on the site-specific interactions of

adsorbed deactivation products with zeolite active sites in H^+-USY catalysts are obtained by X-ray diffraction (XRD), electron microscopy, and solid-state nuclear magnetic resonance (NMR) spectroscopy analyses. In combination with catalytic toluene alkylation reaction tests, the results establish the preferential adsorption of carbonaceous deactivation products at acid sites on the surfaces of mesopores in H^+-USY zeolite catalyst particles. Such insights are expected to enable surface modification of the USY zeolite catalysts to target and selectively passivate these mesopore surface adsorption sites to improve product selectivity, reduce coke formation, and increase catalyst lifetime.[15]

5.3 Results and discussion

5.1 Long-range and local order in 'ultrastable' Y zeolite catalyst materials

Ultrastable USY catalyst materials are prepared by steam treatment of microcrystalline zeolite Y at elevated temperatures (400-750 °C), which dealuminates the zeolite framework and leads to overall reduction in the number of catalytically active sites, but improves the hydrothermal stability and catalytic properties of the remaining framework aluminum species.[16–20] The USY zeolite catalyst materials studied here consisted of microcrystals that were dealuminated by hydrothermal steam treatment at 500 °C. The long-range crystalline order of the framework structure is predominantly retained after steam-aging, as evidenced by the X-ray diffraction (XRD) pattern in Figure 1a, which shows only reflections indexable to the **FAU**-type structure of zeolite Y (inset to Fig. 1a, ref. 21). Steam treatment results in the formation of mesoporous fissures in the zeolite particles, such as shown in the representative scanning electron micrograph in Fig. 1b, which generally improve molecular diffusion through the catalyst particles and accessibility catalytically active sites in the

nanopore interior.[22] However, dealumination of the framework also exacerbates the complexity of non-stoichiometric distributions of nano- and mesopore surface species that lack long range order, including extra-framework aluminum atoms that migrate to the surfaces of the zeolite particles.[18,19,22] The mesoscale distribution of aluminum atoms in steamed USY particles is established by the scanning tunneling electron microscope (STEM) image in Fig. 1c, where the blue color contrast arises from high local aluminum density. The high color contrast at the particle surfaces arises from surface and near-surface extra-framework aluminum species that form as a result of the dealumination processes. The molecular-level adsorption, reaction, and deactivation properties of different framework and extra-framework aluminum species have been largely unknown due to the challenges associated with atomic-scale characterization of such dilute and non-ordered surface active sites.

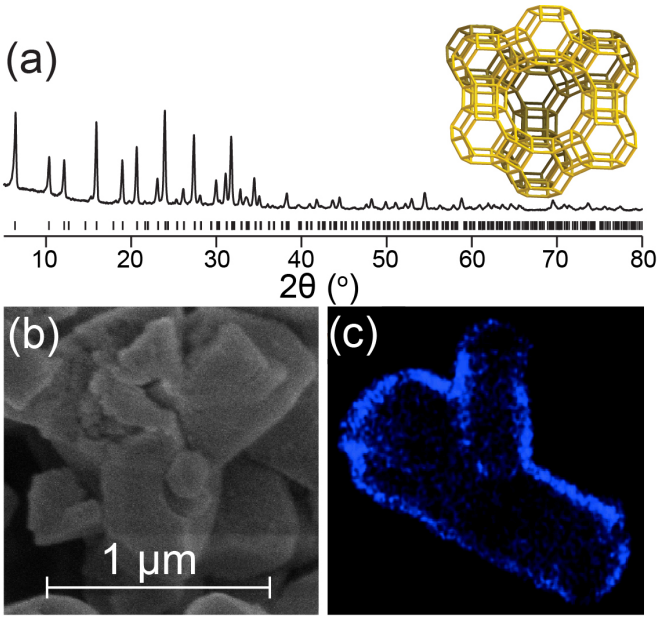

Figure 5.1. (a) XRD pattern of USY zeolite steam aged at 500 °C, with reflections indexable to the FAU crystal structure (JCPDS Card No. 39-0218) indicated by the solid black lines. Inset: framework structure of zeolite Y (framework code **FAU**) viewed along the [111] axis, adapted from the International Zeolite Association (*iza-structures.org/databases*). Each vertex represents a tetrahedral site occupied by a Si or Al atom, and each line represents a

bridging oxygen atom. (b) Representative SEM micrograph of zeolite USY microcrystals, showing a region where dealumination has led to fissuring/fracturing of the crystalline particles. (c) Representative Al-contrast STEM image of steam-aged USY zeolite particles. The blue color contrast indicates regions of high aluminum concentration, which are predominantly at the particle exterior surfaces, due to dealumination of the zeolite framework and the subsequent formation and migration of extra-framework aluminum species.

The influence of the steam-aging treatment on the quantities of framework Al heteroatoms is established by analysis of quantitative solid-state 1D single-pulse ^{29}Si MAS NMR spectra of zeolite USY materials steam aged at different temperatures, shown in Figure 5.2. The 1D ^{29}Si spectrum of NH^{4+}-USY steam aged at 500 °C (Fig. 5.2a) shows four ^{29}Si signals at -106, -102, -95, and -91 ppm, which arise respectively from Q^4(0Al), Q^4(1Al), Q^4(2Al), and Q^3(1Al) species. The Q^m(nAl) notation refers to an Si atom linked through bridging O atoms to m other Si or Al atoms, of which n are Al. These assignments are corroborated by analysis of the 2D ^{27}Al{^{29}Si} spectra discussed below. The high relative quantities of partially-crosslinked Q^3(1Al) species are associated with silanol defect sites at the surfaces of the USY mesopores formed as a result of the steam-aging process. While the bulk Si/Al ratio of the NH_4^+-USY material determined by elemental analysis is 2.5, the framework Si/Al ratio determined by integration of the quantitative 1D ^{29}Si MAS NMR spectrum is 7.5, suggesting that more than half of the Al species are extra-framework after steam aging at 500 °C. After steam aging at 600 °C, the same ^{29}Si signals are detected (Fig. 5.2b), with diminished intensity from the signals corresponding to Q^4(1Al), Q^4(2Al), and Q^3(1Al) ^{29}Si species, consistent with greater dealumination of the framework. Integration of the 1D ^{29}Si MAS NMR spectrum indicates an Si/Al ratio of ~13. Though the 1D ^{29}Si MAS NMR spectra provide insights into the quantities of framework Al and extent of

dealumination, they are incapable of providing direct information on the types and distributions of framework and extraframework Al species.

To establish the types, distributions, and molecular interactions of zeolite surface environments that influence the catalyst activity and deactivation, recently developed two-dimensional (2D) NMR techniques are applied with signal sensitivity enhanced by dynamic-nuclear-polarization (DNP) and/or low temperature (<100 K) magic-angle-spinning (MAS) conditions.[23–25] DNP-NMR techniques provide dramatically improved signal sensitivity that enables the detection and identification of dilute adsorbed surface species[26,27] and (alumino)silicate materials at natural isotopic abundance ^{29}Si (4.7 %),[28–32] which are otherwise exceedingly challenging to analyze spectroscopically or otherwise. Here, multinuclear 2D NMR techniques exploit internuclear *J* (through-bond) couplings to determine framework ^{27}Al-O-^{29}Si connectivities[33] or dipole-dipole (through-space) couplings[34,35] to correlate ^{27}Al, and ^{29}Si NMR signals arising from the zeolite framework to ^{1}H and ^{13}C signals from proximate (<1 nm) organic molecules, including after exposure to catalytic reaction conditions. The solid-state 2D NMR correlation spectra are presented as 2D contour maps with two frequency axes having normalized frequency units of Hz/MHz or ppm. Correlated signal intensity in the 2D spectra manifests the through-covalent-bond (for *J*-mediated spectra) or through-space (for dipolar-mediated spectra) interactions of the nuclear spins with the corresponding frequency shifts.

Framework ^{27}Al atoms in H^+-USY zeolite are distributed in the nanopore framework exterior as well as at surface/mesopore exterior defect sites. This is evidenced by the solid-state 2D ^{27}Al{^{29}Si} HMQC NMR spectra of H^+-USY zeolite steam-aged at 500 °C in Figure 5.3, which manifest correlated signal intensity from ^{27}Al and ^{29}Si nuclei that are *J* coupled

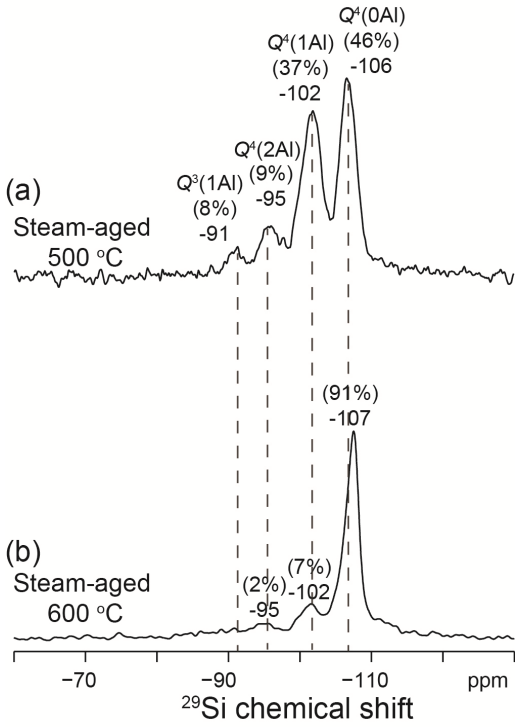

Figure 5.2. Solid-state 1D quantitative single-pulse ^{29}Si NMR spectra of (A) NH_4^+-USY zeolite after steaming at 500 °C (framework Si/Al ~ 8) and (B) H^+-USY zeolite after steaming at 600 °C (framework Si/Al ~ 16).

through covalent ^{27}Al-O-^{29}Si linkages or dipolar coupled through space over distances of less than 1 nm. For example, the 2D ^{27}Al{^{29}Si} *J*-mediated HMQC spectrum (Fig. 5.3a) shows ^{27}Al signals at 57 ppm from tetrahedral ^{27}Al that are correlated with ^{29}Si signals at -102, -96, and -93 ppm from ^{29}Si Q^4(1Al), Q^4(2Al), and Q^3(1Al) species that are in the zeolite framework. Though ^{27}Al signals are detected at 26 or -1 ppm from five- and six-coordinate ^{27}Al species in the 1D ^{27}Al echo spectrum shown in Fig. 5.3a, no correlated signal intensities in these shift regions are detected in the 2D ^{27}Al{^{29}Si} correlation spectra. This indicates that the five- and six-coordinate ^{27}Al species are not bonded to a detectable extent with ^{29}Si atoms in the zeolite framework, confirming that they are extra-framework species. The ^{27}Al signals at 57 ppm correlated with ^{29}Si signals at -102 and -96 ppm arise from four-coordinate ^{27}Al species that are bonded through bridging oxygen atoms to fully-crosslinked Q^4(1Al) or Q^4(2Al) silicate species, and are therefore within the nanopore framework interior of the

USY zeolite. By comparison, the relatively weak correlated signal intensity at a ^{29}Si shift of -93 ppm arises from four-coordinated ^{27}Al atoms that are bonded through bridging oxygen atoms to Q^3(1Al) silicate species (e.g., -O-Al-OH-Si-OH moieties) that are partially-crosslinked and predominantly associated with mesopore or exterior surface sites.

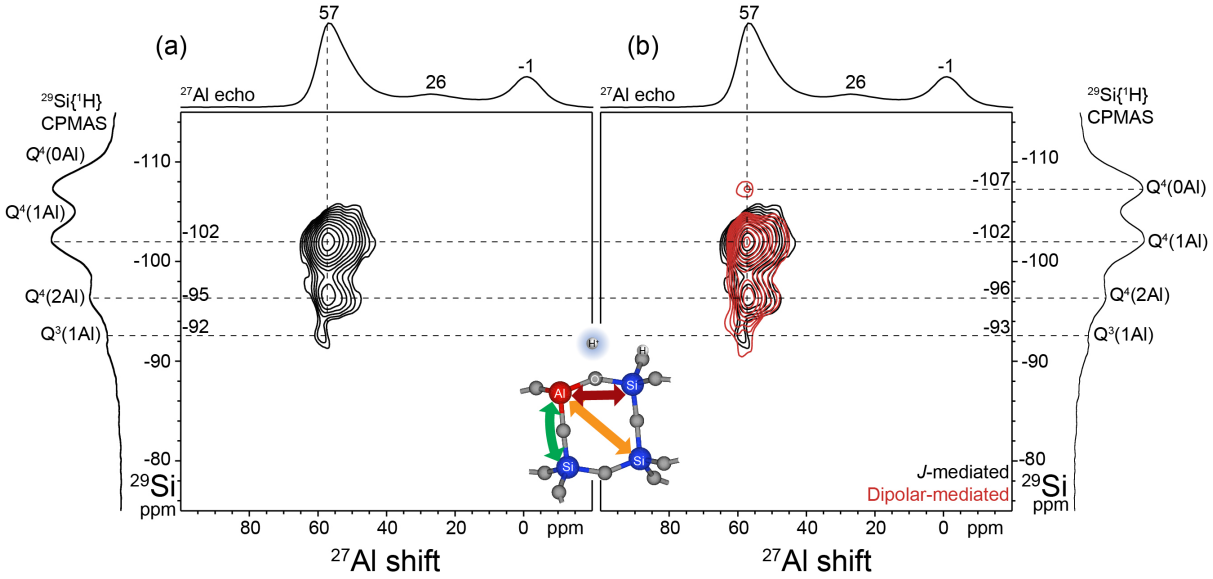

Figure 5.3. Solid-state 2D ^{27}Al{^{29}Si} (a) through-covalent-bond *J*-mediated and (b) through-space dipolar mediated (red) NMR correlation spectra of H^+-USY zeolite steam aged at 500 °C. The spectra were acquired at 18.8 T, 100 K, and 10 kHz MAS. Solid-state 1D ^{27}Al echo and ^{29}Si{^{1}H} CPMAS spectra acquired under the same conditions are shown along the horizontal and vertical axes, respectively, for comparison with the 2D spectra. The schematic inset shows the interactions of a framework ^{27}Al heteroatom with framework Q^4(1Al), Q^3(1Al), and Q^4(0Al) ^{29}Si species, indicated by green, red, and yellow arrows, respectively.

These insights into the distributions of aluminum species in the zeolite framework interior and at exterior/mesopore surface sites are supported and extended by analysis of the 2D ^{27}Al{^{29}Si} dipolar-mediated HMQC spectrum in Figure 5.3b, which selectively detects pairs of ^{27}Al and ^{29}Si nuclei that are dipole-dipole coupled over distances of less than 1 nm. The 2D spectrum shows the same correlated signal intensities that are observed in the *J*-mediated analogue (Fig. 5.3a), consistent with the covalent connectivities of Q^4(1Al) and Q^4(2Al) silicate species in the nanopore framework interior and Q^3(1Al) silicate species at particle exterior/mesopore surfaces with four-coordinate ^{27}Al species. An additional

correlated signal intensity is detected at ^{27}Al and ^{29}Si shifts of 57 and -107 ppm, respectively, arising from interactions between four-coordinate ^{27}Al and next-nearest T site Q^4(0Al) silicate neighbors, as shown schematically in the inset to Fig. 5.3. Interestingly, no correlated intensities are observed from five- or six-coordinate ^{27}Al species, indicating that the corresponding species are not located within the USY zeolite nanopores in the form of extraframework Al cations, as has been observed for other Y zeolite materials.[36,37] The combined 2D ^{27}Al{^{29}Si} dipolar- and *J*-mediated NMR analyses reveal different types of framework ^{27}Al heteroatom sites: those within the nanopore framework interior, and those at the surfaces of the USY mesopores, which are hypothesized to exhibit different adsorption and reaction properties.

5.3.2 Molecular interactions of methanol and toluene with H^+-USY

The zeolite framework adsorption environments of molecular guest species such as organic reactant molecules can be determined by advanced solid-state dynamic-nuclear-polarization (DNP) enhanced NMR techniques at low temperatures, which provide dramatic enhancements in NMR signal sensitivity. The enhancements provided by DNP-NMR techniques enable acquisition of powerful 2D ^{13}C{^{29}Si} correlation spectra that exploit the through-space nuclear dipole-dipole couplings of proximate (< 1 nm) ^{13}C and ^{29}Si nuclei to selectively detect and correlate ^{13}C atoms on adsorbed organic molecules and ^{29}Si atoms near zeolite framework adsorption sites. For example, the methanol adsorption environments in H^+-USY zeolite are identified by the DNP-enhanced 2D ^{13}C{^{29}Si} spectrum in Figure 5.4a. The methanol-adsorbed zeolite USY sample was prepared by steam treatment of Na-Y zeolite at 500 °C, ion-exchange to the NH_4^+ form, calcination at 500 °C to produce the H^+

form, then subsequently dried at 500 °C and exposed to argon saturated with ^{13}C-labeled methanol vapor. In the 2D spectrum, the ^{13}C NMR signal at 50 ppm arises from adsorbed methanol molecules and is correlated to partially-resolved ^{29}Si signals at -106, -103, -97, and -92 ppm, which arise respectively from Q^4(0Al), Q^4(1Al), Q^4(2Al), and Q^3(1Al) silicate moieties. These assignments are confirmed by the ^{27}Al{^{29}Si} dipolar-mediated correlation spectrum in Fig. 5.4b, which shows the same signals as 5.3b but modestly broadened due to partial dehydration of the USY zeolite framework. Notably, the correlated signals in Fig. 5.4a at ^{29}Si chemical shifts of -92 and -96 ppm exhibit the greatest relative signal intensities, as can be seen by comparison of the 1D ^{29}Si projection of the 2D spectrum and the 1D ^{29}Si{^{1}H} CPMAS spectrum in Fig. 5.4a. Approximately 50% of the difference in relative intensity can be accounted for by the differences in DNP enhancements as a function of distance from the particle surface; the ^{29}Si signals at -92 ppm from Q^3(1Al) exterior/mesopore surface sites exhibit DNP enhancements of *ca*. 6 while the ^{29}Si signals at -108 ppm from Q^4(0Al) nanopore interior are enhanced by a factor of *ca*. 3. As the dinitroxide polarizing agent[38] is too bulky to enter the zeolite Y nanopores, the differences in ^{29}Si DNP-NMR signal enhancements are due in part to ^{1}H relaxation processes, which limit the diffusion of ^{1}H spin polarization more than 100 nm into the zeolite particle. However, the correlated signal at -92 ppm from surface mesopore adsorption sites is ca. 12 times greater in relative intensity than the signal at -103 ppm from adsorption sites in the nanopore framework interior, and thus the relative intensity difference cannot be accounted for entirely by the greater signal enhancement of the zeolite particle surface. Instead, the difference in relative intensities indicates preferential adsorption of the methanol at surface adsorption sites with which the ^{29}Si signals from Q^3(1Al) species are associated. The strong association of methanol with

partially-crosslinked surface acid sites is likely due to the two closely-spaced -OH interaction sites, which are expected to interact strongly with alcohols due to hydrogen-bonding and/or electrostatic interactions.[39]

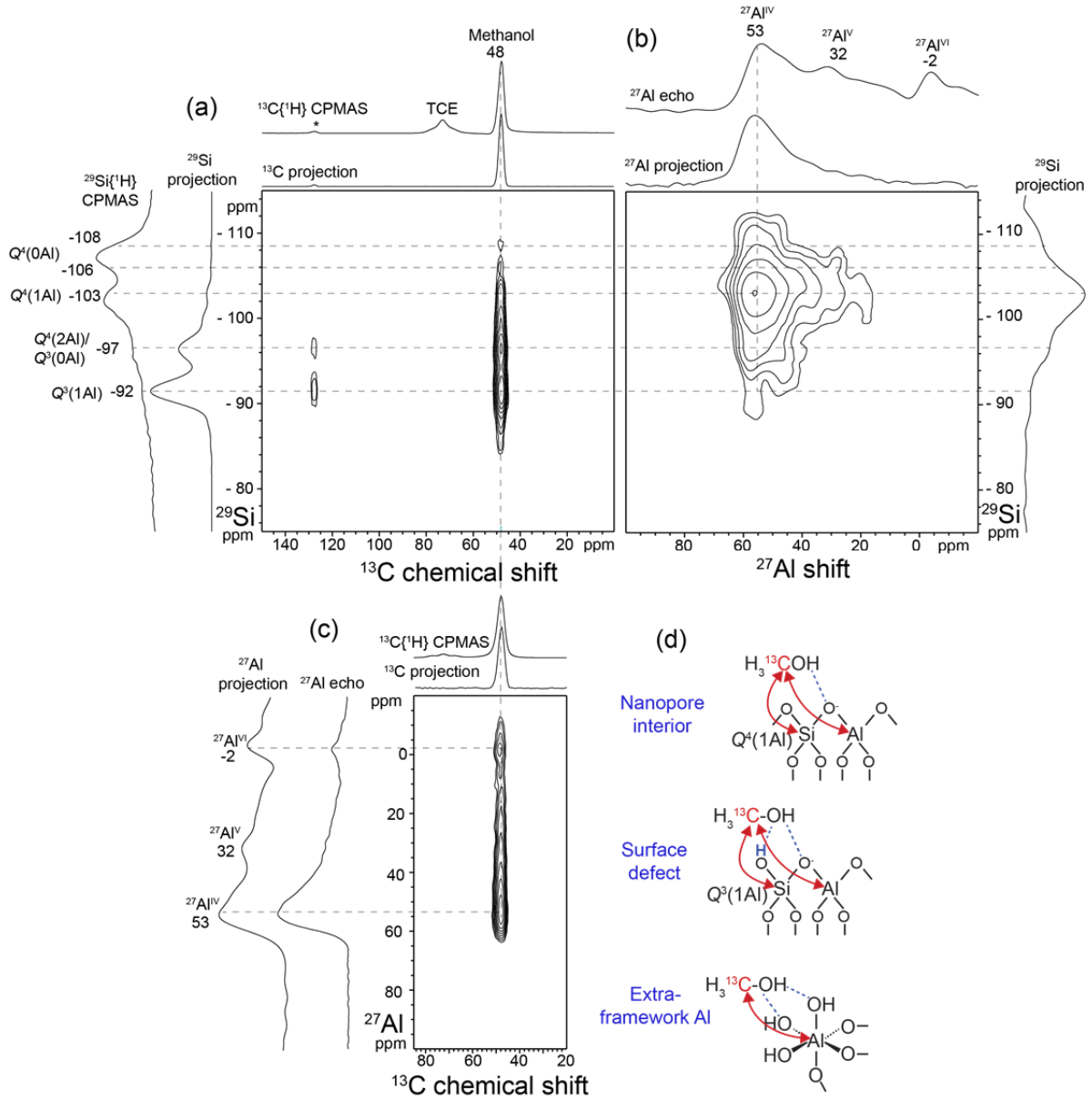

Figure 5.4. Solid-state DNP-enhanced 2D dipolar-mediated (through-space) (a) ^{13}C{^{29}Si}, (b) ^{27}Al{^{29}Si}, and (c) ^{27}Al{^{13}C} NMR correlation spectrum of H$^+$-USY zeolite steam aged at 500 °C, subsequently dried and exposed to saturated methanol vapor (enriched to 99.9 % isotopic abundance of ^{13}C). The spectra were acquired at 9.4 T, 89-94 K, 8 kHz MAS, in the presence of 16 mM TEKPol biradical polarizing agent in 1,1,2,2-tetrachloroethane, and under microwave irradiation at 263 GHz. Solid-state 1D ^{13}C{^{1}H}, ^{29}Si{^{1}H} DNP-CPMAS or ^{27}Al echo spectra acquired under the same conditions are shown along the horizontal and

vertical axes, respectively, for comparison with the 1D projections of the 2D spectrum. The asterisk indicates a spinning side band. (d) Schematic diagrams of ^{13}C-methanol interacting with ^{29}Si and ^{27}Al atoms at nanopore interior (top), surface defect (middle), and extra-framework Al (bottom) adsorption sites.

In addition to interacting with adsorption sites at the surfaces and within the zeolite USY frameworks, methanol molecules also adsorb at extra-framework aluminum sites, as determined by the 2D ^{27}Al{^{13}C} dipolar-mediated NMR correlation spectrum in Fig. 5.4c. Such ^{13}C-^{27}Al double-resonance NMR correlation measurements have been exceptionally limited in the past due to the very similar Larmor frequencies of ^{13}C and ^{27}Al (101.6 and 105.4 MHz at 9.4 T, respectively) and have only recently been enabled by new developments in NMR instrumentation.[40–42] The 2D spectrum shows that the narrow ^{13}C signal at 48 ppm from adsorbed methanol molecules is correlated with broad and overlapping ^{27}Al signals at 53, 32, and -2 ppm from four-, five-, and six-coordinate ^{27}Al species, respectively. These correlated intensities establish that adsorbed methanol interacts over sub-nanometer distances with five- and six-coordinate extraframework ^{27}Al species, in addition to the four-coordinate framework ^{27}Al species. The different adsorption sites of ^{13}C-methanol in USY zeolite are depicted schematically in Fig. 5.4d.

Toluene exhibits preferential adsorption at surface acid sites similar to methanol, as determined by DNP-enhanced 2D ^{13}C{^{29}Si} NMR analyses of toluene adsorbed H^+-USY zeolite materials (Fig. 5.5). The 1D ^{13}C{^{1}H} DNP-CPMAS spectrum of this material shows ^{13}C signals at 19, 124, 127, and 137 ppm from the different ^{13}C atoms in the adsorbed ^{13}C-toluene molecules and 73 ppm from the DNP solvent, 1,1,2,2-tetrachloroethane. The signals from the aromatic ^{13}C atoms in the 124-137 ppm range are diminished in intensity compared to the signals from methyl groups at 19 ppm in the DNP-enhanced 2D ^{13}C{^{29}Si} spectrum, likely because of the shorter spin-lattice and spin-spin relaxation times of the aromatic ^{13}C

species. Nevertheless, the 2D spectrum shows several partially-resolved regions of correlated intensity from ^{13}C-enriched toluene molecules adsorbed in the zeolite nanopore framework and at surface adsorption sites. Specifically, correlated signals at ^{29}Si chemical shifts of -101 and -92 ppm arise from toluene in close proximity to nanopore interior Q^4(1Al) and surface/mesopore exterior Q^3(1Al) species, respectively. Similar to the corresponding analysis of methanol-adsorbed H$^+$-USY (Fig. 5.4a), toluene preferentially adsorbs at surface/mesopore exterior sites associated with Q^3(1Al) species, which is reflected by the greater correlated signal intensity in the 2D ^{13}C{^{29}Si} spectrum at -92 ppm in the ^{29}Si dimension. The interactions of toluene with partially-crosslinked -O-Al-OH-Si-OH surface sites are shown schematically in the inset to Figure 5.5.

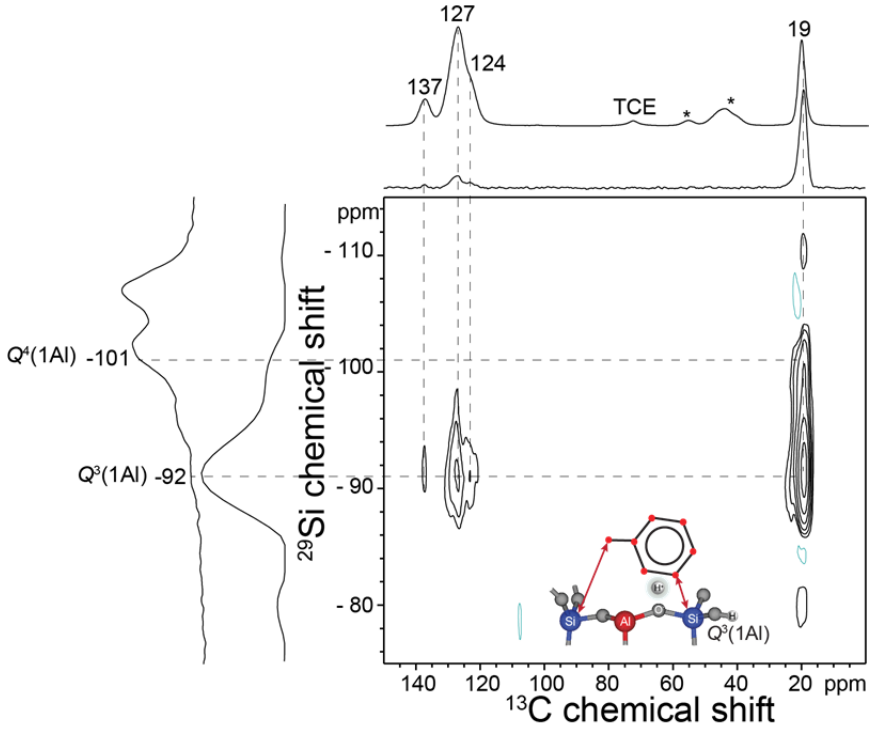

Figure 5.5. Solid-state DNP-enhanced 2D ^{13}C{^{29}Si} dipolar-mediated (through-space) NMR correlation spectrum of H$^+$-USY zeolite steam aged at 500 °C, subsequently dried and exposed to saturated toluene vapor (uniformly enriched to 99.9% isotopic abundance in argon at atmospheric pressure. The spectrum was acquired at 9.4 T, 89 K, 8 kHz MAS, in the presence of 16 mM TEKPol biradical polarizing agent in 1,1,2,2-tetrachloroethane, and under microwave irradiation at 263 GHz. Solid-state 1D ^{13}C{^{1}H} and ^{29}Si{^{1}H} DNP-

CPMAS spectra acquired under the same conditions are shown along the horizontal and vertical axes, respectively, for comparison with the 1D projections of the 2D spectrum. The asterisks indicate spinning side bands. The interactions of adsorbed toluene and framework ^{29}Si atoms are depicted schematically in the inset.

5.3.3 Toluene alkylation reaction properties of USY zeolite catalysts

To obtain insights on the origins of the deactivation processes and identify surface deactivation sites of H^+-USY zeolites, a series of H^+-USY zeolite catalyst materials were examined after toluene methylation at 500 °C. Toluene methylation by methanol is used in the commercial production of xylenes, which have important applications as plasticizers, solvents, and polymer precursors.[10,43] Under high-temperature reaction conditions, toluene disproportionation, catalytic cracking, and deactivation by coke deposition occur rapidly.[10,43] At the relatively high reaction temperature (500 °C) used here, deactivation reactions are expected to favor bulky polyaromatic coke products similar to those formed during FCC processes, in contrast to more aliphatic coke expected at lower temperatures.[10,43,44]

Analyses of the products of toluene methylation with H^+-USY zeolite catalysts indicate that deactivation occurs at early reaction times (< 1 min) due to deposition of aromatic side-products at zeolite adsorption sites. The reactor setup used for the toluene methylation reaction tests is shown schematically in Figure 5.6. The toluene methylation reaction product distributions (Fig. 5.7a) show that at early reaction times (1 min), conversion of toluene is high, with high selectivity for straight-chain alkanes (86%), indicating that catalytic cracking reactions of toluene dominate. At these early reaction times, the catalytic cracking of toluene is thought to be due to reactions at highly reactive surface acid sites on the zeolite USY catalyst particles that are hypothesized to be associated with both catalytic cracking and deactivation processes. By comparison, at intermediate reaction times (5 min) the selectivity

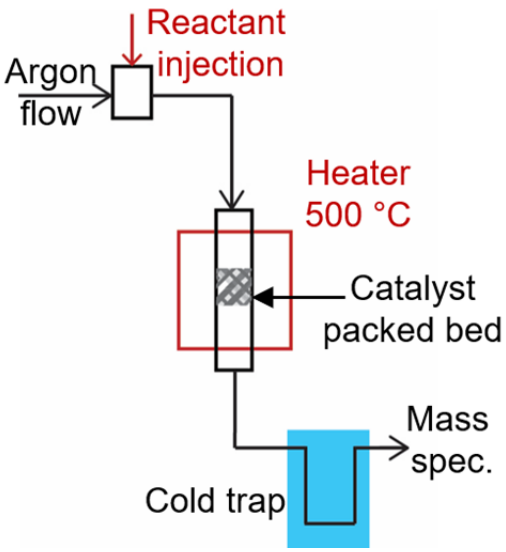

Figure 5.6. Schematic diagram of the reactor setup used to examine the deactivation and reaction properties of H^+-USY zeolite catalyst materials. A droplet of known volume of a reactant mixture (3:1 stoichiometric ratio of methanol:toluene) was injected into flowing argon and passed through a packed bed reactor at 500 °C. The high-molecular-weight reaction products were trapped in a cold bath of deuterated acetone for *ex-situ* analysis by solution-state NMR. The light gas-phase reaction products were analyzed by *in-situ* mass spectrometry.

for xylenes is high (26%), with smaller quantities of benzene (15%) and alkanes (4%) also formed. At longer reaction times (9 min), the percentage of formed xylenes decreases to 5%, with smaller overall conversion of toluene and large quantities of benzene and alkanes also formed (25% and 10%, respectively). The total quantity of coke (mg/mg catalyst) deposited on the zeolite catalyst particles increases linearly with reaction time (Fig. 5.7b, blue). The conversion of reactants to coke is high at early reaction times (0.075 mg/mg reactant after 1 min), but decreases to 0.04 mg/mg reactant at longer times (≥ 5 min), indicating that the initial reactant species are converted rapidly to coke, consistent with reactions and molecular adsorption at highly reactive surface acid sites. At intermediate reaction times, toluene methylation is the dominant reaction mechanism, indicating that the most reactive surface sites on the zeolite USY materials are passivated by coke deposition and not accessible to

further cracking reactions. At long reaction times (9 min), toluene disproportionation reactions dominate, likely because oligomerized coke species block the zeolite nanopore entrances, inhibiting further zeolite-catalyzed reactions. The coke deposits in the post-reaction zeolite catalysts are predominantly aromatic, with small quantities of alkyl moieties (*ca*. 5%), as established by quantitative solid-state ^{13}C MAS NMR analyses. The toluene-methylation catalytic reaction analyses indicate that coke formation occurs most rapidly at early reaction times, and so the molecular interactions of zeolite surface sites with the carbonaceous deactivation products at early stages are expected to be of high importance. However, establishing the atomic-scale interactions of deactivation products and reactive surface adsorption sites has until now been entirely infeasible, due to the dilute quantities of deactivation products at the earliest stages of deactivation and the complicated non-ordered distributions of the adsorption/reaction sites.

5.3.4 Types and interactions of deactivation products in post-reaction USY zeolite catalysts

The carbonaceous deactivation products on post-reaction H^+-USY are predominantly aromatic, with small quantities of $-CH_3$ and $-CH_2-$ environments. The types of carbonaceous deactivation products adsorbed on H^+-USY zeolite catalysts after exposure to toluene methylation reaction conditions for 0.9 minutes are determined by the 2D $^{13}C\{^1H\}$ DNP-HETCOR spectra in Figure 5.8. For the very short $^{13}C\{^1H\}$ cross-polarization contact time used to acquire the 2D spectrum in Figure 5.8a, correlated signal intensity arises from coupled ^{13}C and ^1H nuclear spin pairs over distances of <0.5 nm, such that the spectrum manifests primarily signals from directly-bonded C-H species. The spectrum is dominated by broad correlated signal intensity at 70 ppm in the ^{13}C dimension and 6.5 ppm in the ^1H

dimension which arises from frozen tetrachloroethane DNP solvent molecules. A weak well-resolved ^{13}C signal at a ^{13}C shift of 37 ppm is correlated with a ^{1}H signal at 4.0 ppm, consistent with the expected ^{1}H and ^{13}C chemical shift positions of -CH_2- environments. Similarly, ^{13}C signals at 21 ppm from -CH_3 environments are correlated with ^{1}H signals at 1.8 and 3.2 ppm, indicating that the alkyl species in the adsorbed carbonaceous reaction byproducts include short-chain alkanes. Additional ^{13}C signals in the aromatic region are resolved at ^{13}C chemical shifts of 152, 145, 132, and 130 ppm, which are each correlated with ^{1}H signals in the 8.7 to 12.7 ppm, consistent with aromatic carbonaceous reaction byproducts. On the basis of past solid-state ^{13}C NMR analyses of post-reaction zeolites, the ^{13}C NMR signals in the frequency region 130-140 ppm are assigned to partially alkylated aromatic species, while the ^{13}C signals at 140-155 ppm are assigned to partially graphitized ^{13}C species or bridging carbon atoms between aromatic rings.[45,46]

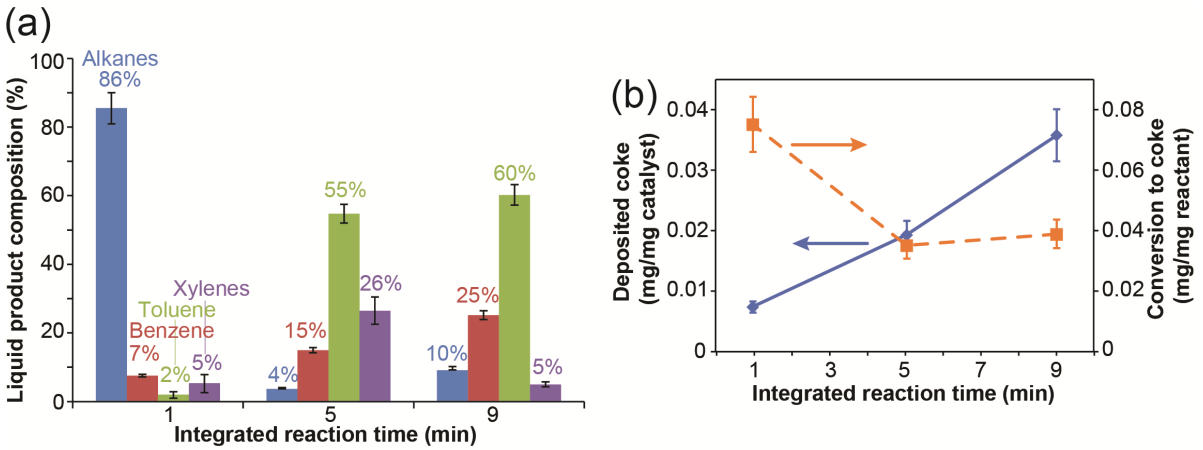

Figure 5.7. (a) Toluene methylation product distributions as a function of integrated reaction time for toluene methylation over H^+-USY zeolite at 500 °C in flowing argon at 1 atm. (b) Quantity of deposited coke (blue) and conversion to coke (orange), as functions of reaction time for toluene methylation over H^+-USY zeolite at 500 °C in flowing argon.

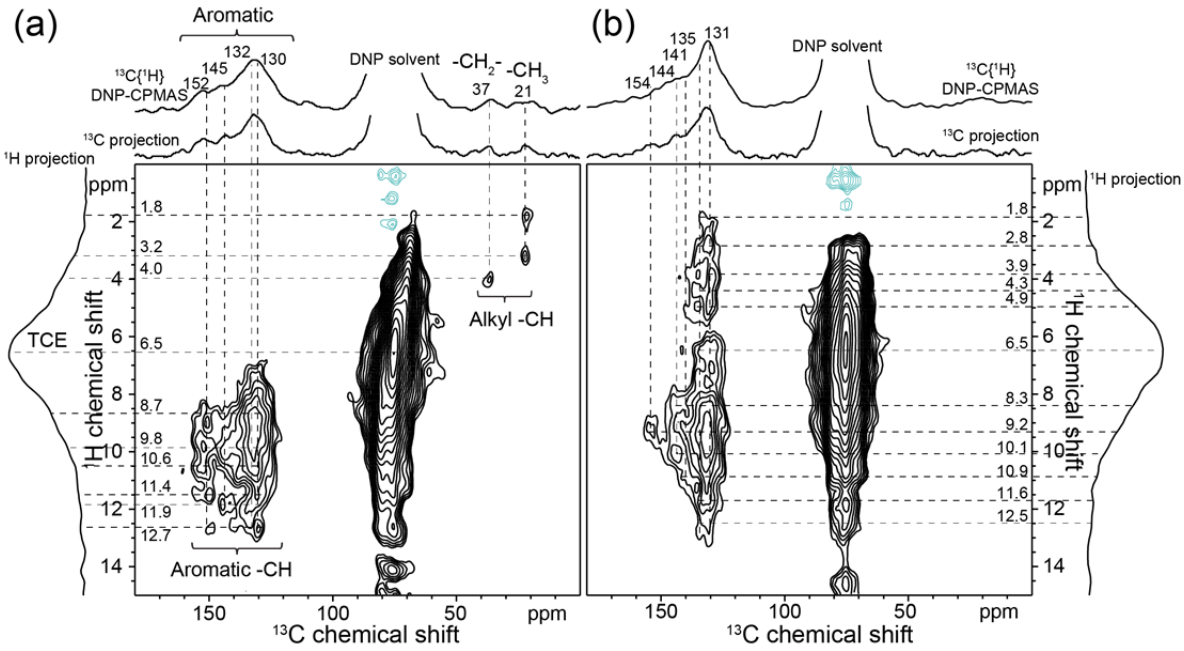

Figure 5.8. Solid-state 2D $^{13}C\{^{1}H\}$ DNP-HETCOR spectra acquired with (A) short (0.2 ms) and (B) longer (4 ms) $^{13}C\{^{1}H\}$contact times of reacted H^{+}-USY zeolite catalyst following toluene methylation at 500 °C and subsequent deactivation (1 min). The spectra were acquired at 9.4 T, 100 K, 12.5 kHz MAS, in the presence of 16 mM TEKPOL biradical in frozen TCE, with microwave irradiation at 263 GHz. 1D $^{13}C\{^{1}H\}$ DNP-CPMAS spectra acquired under the same conditions are shown along the horizontal axes for comparison with the 1D projections of the 2D spectra. The green contour lines indicate regions of negative signal intensity, which are spectral artifacts that arise from truncation of the ^{1}H signal from the DNP solvent.

These insights into the types of adsorbed carbonaceous species are confirmed and extended by the 2D $^{13}C\{^{1}H\}$ DNP-HETCOR spectra acquired at a longer contact time of 4 ms (Fig. 5.8b), which manifests longer-range intermolecular interactions, being principally limited to ^{13}C-^{1}H through-space couplings over distances of < 1 nm. As with the corresponding spectrum acquired at short contact times, ^{13}C signals in the frequency range 131-154 ppm from aromatic carbon species are correlated with ^{1}H signals in the range 8.3-12.5 ppm from covalently-bonded carbons. The ^{13}C signals at 131-135 ppm are also correlated with ^{1}H signals at 1.8-4.9 ppm from alkyl moieties and at 6.5-7.5 ppm from the frozen TCE solvent molecules. These correlated signals indicate that the corresponding ^{13}C

signals arise from alkylated aromatic species that are in close proximity to TCE solvent molecules, establishing that alkylated aromatic carbonaceous reaction byproducts are adsorbed at the surfaces of the zeolite catalyst particles. By contrast, the ^{13}C signals at 141-154 ppm are not correlated with the ^{1}H signals from the DNP solvent molecules, suggesting that the signals in this frequency region arise from sub-surface aromatic molecules that are not accessible to the DNP solvent molecules.

5.3.5 Direct identification of H^+-USY deactivation sites

Crucially, dilute partially-crosslinked particle exterior and mesopore surface -O-Al-OH-Si-OH moieties act as adsorption sites for complicated carbonaceous reaction products that are associated with zeolite catalyst deactivation. The site-specific interactions of the adsorbed carbonaceous side products at framework ^{29}Si sites are established by the 2D $^{13}C\{^{29}Si\}$ dipolar-mediated DNP-enhanced spectrum of H^+-USY zeolite after toluene methylation at 500 °C for 1 min. The DNP-enhanced 2D $^{13}C\{^{29}Si\}$ NMR correlation spectrum in Fig. 5.9 selectively detect ^{13}C and ^{29}Si species that are in molecular (< 1 nm) mutual proximities and yields correlated signal intensity that corresponds to only narrow subsets of the adsorbed ^{13}C species that are adsorbed and interacting with framework ^{29}Si sites. Specifically, the ^{13}C signals at 129 and 126 ppm from aromatic coke products are correlated with ^{29}Si signals in the region 88-93 ppm, which arise from partially-crosslinked surface Q^3(1Al) silicate moieties. Additional strong intensity correlations are observed for the ^{13}C signals at 22 and 20 ppm from alkyl moieties and the same ^{29}Si signals, which establish unambiguously that the coke deposits most intimately associated with the zeolite framework are alkylated aromatic species at early reaction times. An additional weak correlated signal is detected at

142 ppm and -95 ppm in the ^{13}C and ^{29}Si dimensions, respectively, that likely arises from residual toluene or xylene molecules adsorbed within the zeolite nanopores in close proximity to Q^4(2Al) silicate species. The interactions of ^{13}C coke molecules with framework- and extraframework ^{27}Al sites are directly evidenced by the 2D $^{27}Al\{^{13}C\}$ dipolar-mediated NMR correlation spectrum in Figure 5.9b, which selectively detects dipole-dipole coupled ^{27}Al-^{13}C spin pairs over sub-nanometer distances. The spectrum shows ^{27}Al signals at 58 ppm from four-coordinated ^{27}Al species, which are correlated to two well-resolved ^{13}C signals at 142 and 128 ppm from aromatic coke moieties. The spectrum corroborates that adsorbed ^{13}C molecules occupy near-surface adsorption sites at framework ^{27}Al species within the USY zeolite framework as depicted schematically in Fig. 5.9c. The combined DNP-NMR results and analyses collectively establish that surface exterior or mesopore -Si-OH-Al-O-Si-OH moieties, act as the predominant adsorption sites for bulky molecular reaction byproducts.

5.4 Conclusions

The results and analyses presented provide direct spectroscopic evidence for different surface mesopore and nanopore adsorption and reaction sites in ultrastable H^+-Y zeolite catalysts. Surface mesopore acid species act as preferential adsorption sites for carbonaceous reaction byproducts, which oligomerize and graphitize over short reaction times, consistent with pore-mouth blocking that has been hypothesized to inhibit diffusion to the zeolite nanopores, thereby leading to deactivation of the catalyst. Targeted surface modification of the H^+-USY zeolite catalysts to passivate the mesopore adsorption/deactivation sites is expected to improve catalyst conversion, selectivity, and stability, and correspondingly

decrease selectivity for coke. The analyses here on the technologically important zeolite H^+-USY, which is a component of many industrial FCC catalysts, are expected to be applicable generally to zeolite catalysts and other materials where similar organic-inorganic surface interactions influence the macroscopic adsorption and reaction properties.

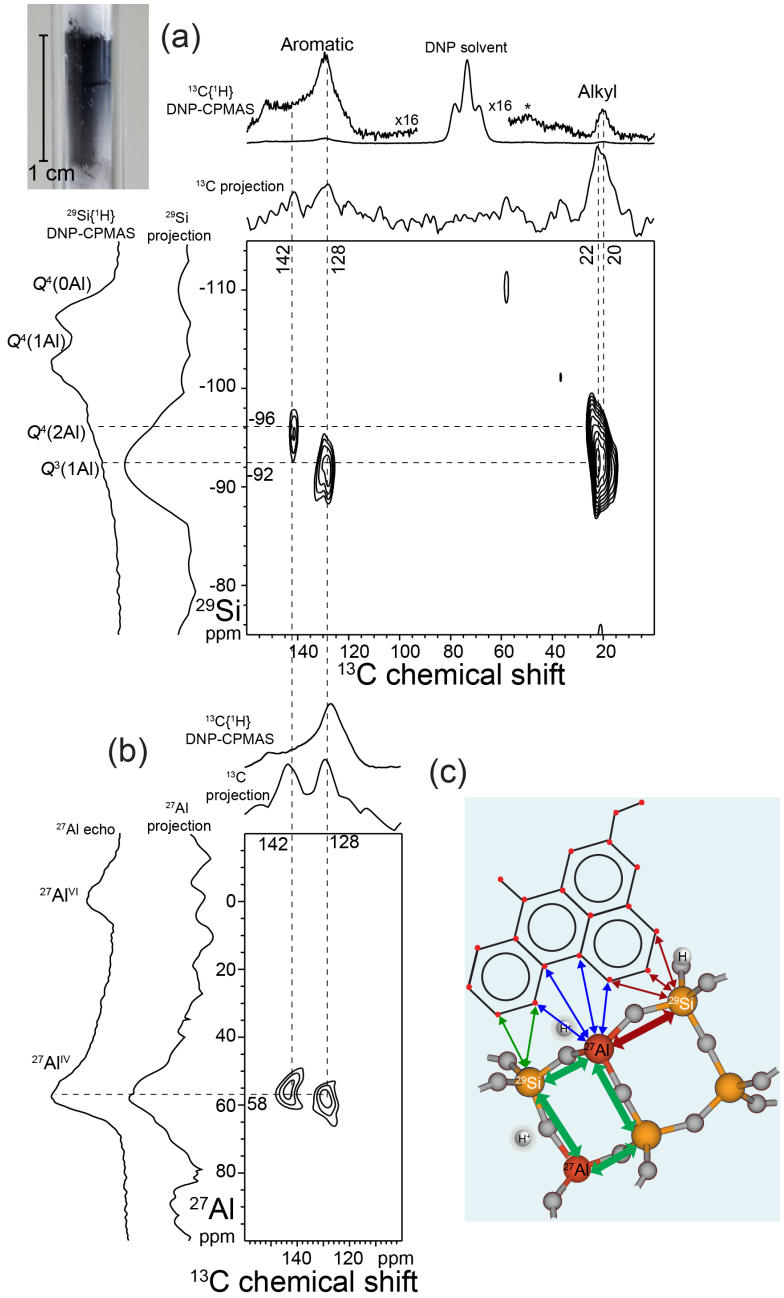

Figure 5.9. Solid-state DNP-enhanced 2D (a) $^{13}C\{^{29}Si\}$ and (b) $^{27}Al\{^{13}C\}$ dipolar-mediated NMR correlation spectra of H^+-USY zeolite after exposure to toluene methylation reaction

conditions at 500 °C for 1 min, with reactants isotopically labeled to 99.9% abundance of ^{13}C. The spectra were acquired at 9.4 T, 89 K, 8 kHz MAS, in the presence of 16 mM TEKPol biradical polarizing agent in frozen TCE, and under microwave irradiation at 263 GHz. Solid-state 1D $^{13}C\{^{1}H\}$ and $^{29}Si\{^{1}H\}$ DNP-CPMAS or ^{27}Al echo spectra acquired under the same conditions are shown along the corresponding ^{13}C, ^{29}Si, or ^{27}Al axesfor comparison with the 1D projections of the 2D spectra. The inset in (a) shows the microcolumn containing the inhomogeneously-coked post-reaction coked zeolite materials. (c) Structural schematic showing the interactions of a coke molecule with a surface Q^3(1Al) adsorption site, consistent with the 2D DNP-NMR spectra and analyses.

5.5 Materials and Methods

USY zeolite catalyst materials and preparation

NH_4^+-USY steam aged at 500 °C and H^+-USY steam aged at 600 °C were procured from Zeolyst. NH_4^+-USY was converted to the H^+ form by calcination at 500 °C overnight in flowing air.

Toluene-methylation reaction tests

For the toluene methylation reaction tests, 50 mg of zeolite powder was held in a quartz microreactor by using quartz wool. The zeolite powder was dried in flowing argon for at least 30 minutes at 450 °C until no water release was observed in the effluent gas by on-line mass spectrometer. The reactor was then heated to the reaction temperature, after which the toluene/methanol reactant mixture was injected into the flowing argon. Heavy reaction products were trapped in d_6-acetone in a cold bath for subsequent quantification by solution-state NMR while light reaction products were measured by on-line mass spectrometry.

X-ray diffraction

The powder XRD measurements were conducted under ambient conditions on a Panalytical Empyrean Powder X-Ray Diffractometer in θ-2θ mode using Cu Kα radiation

with a wavelength of 1.5405 Å and equipped with a rotating sample stage rotating at two turns per minute.

Electron microscopy

Scanning electron microscopy (SEM) images were acquired on a FEI Nova Nano 650 FEG SEM. The scanning transmission electron microscopy (STEM) image in Figure 5.1c and the Al elemental map were provided by Dr. Subramanian Prasad of the BASF corporation.

Solid-state NMR measurements

Solid-state 1D and 2D MAS NMR spectroscopy was used to analyze the ^{1}H, ^{13}C, ^{27}Al, and ^{29}Si environments in USY zeolites catalysts before and after exposure to catalytic reaction conditions. The ^{1}H, ^{13}C, and ^{29}Si chemical shifts were referenced to trimethylsilane (TMS) at 0.0 ppm, using tetrakis(trimethylsilyl)silane as a secondary external chemical shift reference. The ^{27}Al shifts were referenced to a 0.5 M solution of $Al(NO_3)_3$ as a secondary external shift reference. The conventional quantitative 1D single-pulse ^{29}Si spectra were acquired on an 11.7 T Bruker AVANCE-II NMR spectrometer operating at frequencies of 499.84 MHz for ^{1}H and 99.31 for ^{29}Si. The quantitative 1D ^{29}Si spectra were acquired with recycle delay times of 120 s to allow for spin-lattice relaxation of the ^{29}Si nuclei. Low temperature MAS NMR conditions (95 K) were used to improve NMR signal sensitivity and thereby enable the acquisition of 2D $^{27}Al\{^{29}Si\}$ heteronuclear multiple quantum correlation (HMQC) NMR spectra for materials with natural abundance ^{29}Si (4.7%). The 2D $^{27}Al\{^{29}Si\}$ HMQC NMR spectra in Figure 5.3 were acquired on a Bruker ASCEND 800 MHz (18.8 T) DNP NMR spectrometer operating at Larmor frequencies of 208.387 and 158.864 for ^{27}Al and ^{29}Si, respectively, and equipped with a 3.2 mm triple-resonance HXY low-temperature

MAS probehead. The *J*-mediated HMQC spectrum was acquired with an experimentally-optimized τ delay of 20 ms to refocus the weak (ca. 15 Hz) ^{27}Al-O-^{29}Si scalar *J* couplings while the dipolar-mediated mediated HMQC spectra were acquired with 36 rotor periods of $SR4_2^{11}$ dipolar recoupling to reintroduce the ^{27}Al-^{29}Si nuclear dipole-dipole couplings.[34,35]

DNP-enhanced NMR measurements

The solid-state DNP-enhanced 1D and 2D ^{29}Si{^{1}H}, ^{13}C{^{1}H}, ^{13}C{^{29}Si}, and ^{27}Al{^{13}C} NMR experiments were carried out on a Bruker ASCEND 400 DNP-NMR spectrometer with a 9.4 Tesla superconducting magnet operating at 399.95, 104.21, 101.63, and 79.46 MHz for ^{1}H, ^{27}Al, ^{13}C, and ^{29}Si nuclei, respectively, and equipped with a gyrotron and microwave transmission line capable of providing 263 GHz microwave irradiation at the sample and a low-temperature 3.2 mm MAS probe. The DNP-enhanced ^{13}C{^{29}Si} correlation spectra of toluene-adsorbed, methanol-adsorbed, and post-reaction H^+-USY were acquired at 89 K, 8 kHz MAS, under continuous microwave irradiation at 263 GHz, and in the presence of 16 mM TEKPol biradical[38] in frozen 1,1,2,2-tetrachloroethane (DNP solvent), which do not influence the structure or surface properties of the materials.[26] The ^{13}C DNP-NMR signal enhancements, quantified as the ratio of the fully-relaxed ^{13}C{^{1}H} CPMAS signal intensities obtained with and without microwave irradiation, were ~10, approximately the same enhancement as estimated for ^{29}Si. Thus, the carbonaceous side products in the reacted H^+-USY zeolite catalysts remained predominantly adsorbed to the surface of the zeolite particles on exposure to the DNP solvent, TCE. The 2D ^{13}C{^{29}Si} correlation spectra were acquired using an HMQC sequence with 11 rotor periods of TEDOR[47,48] recoupling to reintroduce the ^{13}C-^{29}Si nuclear dipole-dipole couplings, while the 1D and 2D ^{27}Al{^{13}C} correlation spectra were acquired using an HMQC sequence with 12 rotor periods of $SR4_2^{11}$ recoupling to

reintroduce the ^{13}C-^{27}Al dipolar couplings. The 2D $^{13}C\{^{1}H\}$ HETCOR spectra were acquired using homonuclear ^{1}H-^{1}H eDUMBO-1_{22} decoupling[49] during the ^{1}H evolution periods to improve resolution in the ^{1}H dimensions. The 2D $^{27}Al\{^{13}C\}$ dipolar-mediated correlation spectrum was acquired using an HMQC sequence with 48 rotor periods of $SR4_2$[11] dipolar recoupling to reintroduce the ^{27}Al-^{13}C nuclear dipole-dipole couplings and one rotor period (8 kHz) sweep width in the indirect ^{13}C dimension. To improve spectral resolution in the indirect ^{13}C dimension, 16 points were added to the indirectly-detected ^{13}C FID using forward interpolation. All of the 1D and 2D DNP-NMR spectra were acquired with 100 kHz heteronuclear SPINAL-64 ^{1}H decoupling[50] during the acquisition period.

5.6 References

(1) Gounder, R.; Iglesia, E. *Chem. Commun.* **2013**, *49* (34), 3491.
(2) Gallego, E. M.; Portilla, M. T.; Paris, C.; León-Escamilla, A.; Boronat, M.; Moliner, M.; Corma, A. *Science.* **2017**, *355* (6329), 1051.
(3) Nugent, P.; Belmabkhout, Y.; Burd, S. D.; Cairns, A. J.; Luebke, R.; Forrest, K.; Pham, T.; Ma, S.; Space, B.; Wojtas, L.; Eddaoudi, M.; Zaworotko, M. J. *Nature* **2013**, *495* (7439), 80.
(4) Davis, M. E. *Nature* **2002**, *417*, 813.
(5) Kwak, J. H.; Tonkyn, R. G.; Kim, D. H.; Szanyi, J.; Peden, C. H. F. *J. Catal.* **2010**, *275* (2), 187.
(6) Brändle, M.; Sauer, J. *J. Am. Chem. Soc.* **1998**, *120* (7), 1556.
(7) Vogt, E. T. C.; Weckhuysen, B. M. *Chem. Soc. Rev.* **2015**, *44* (20), 7342.
(8) Chang, C. D. *Catal. Rev.* **1983**, *25* (1), 1.
(9) Liu, B.; Slocombe, D.; AlKinany, M.; AlMegren, H.; Wang, J.; Arden, J.; Vai, A.; Gonzalez-Cortes, S.; Xiao, T.; Kuznetsov, V.; Edwards, P. P. *Appl. Petrochemical Res.* **2016**, *6* (3), 209.
(10) Al-Khattaf, S.; Rabiu, S.; Tukur, N. M.; Alnaizy, R. *Chem. Eng. J.* **2008**, *139* (3), 622.
(11) Ristanović, Z.; Hofmann, J. P.; Richard, M. I.; Jiang, T.; Chahine, G. A.; Schülli, T. U.; Meirer, F.; Weckhuysen, B. M. *Angew. Chemie - Int. Ed.* **2016**, 7496.
(12) Meirer, F.; Kalirai, S.; Morris, D.; Soparawalla, S.; Liu, Y.; Mesu, G.; Andrews, J. C.; Weckhuysen, B. M. *Sci. Adv.* **2015**, *1* (3), e1400199.
(13) Goetze, J.; Meirer, F.; Yarulina, I.; Gascon, J.; Kapteijn, F.; Ruiz-mart, J.; Weckhuysen, B. M. **2017**.
(14) Meirer, F.; Kalirai, S.; Weker, J. N.; Liu, Y.; Andrews, J. C.; Weckhuysen, B. M. *Chem. Commun.* **2015**, *51* (38), 8097.
(15) Ding, W.; Meitzner, G. D.; Iglesia, E. *J. Catal.* **2002**, *206* (1), 14.
(16) Altwasser, S.; Jiao, J.; Steuernagel, S.; Weitkamp, J.; Hunger, M. *Stud. Surf. Sci. Catal.* **2004**, *154B* (Recent Advances in the Science and Technology of Zeolites and Related Materials), 1212.
(17) Li, S.; Zheng, A.; Su, Y.; Zhang, H.; Chen, L.; Yang, J.; Ye, C.; Deng, F. *J. Am. Chem. Soc.* **2007**, *129* (12), 11161.
(18) Wouters, B. H.; Chen, T.; Grobet, P. J. *J. Phys. Chem. B* **2001**, *105* (6), 1135.

(19) Van Donk, S.; Janssen, A. H.; Bitter, J. H.; De Jong, K. P. *Catal. Rev. - Sci. Eng.* **2003**, *45* (2), 297.
(20) Silaghi, M. C.; Chizallet, C.; Sauer, J.; Raybaud, P. *J. Catal.* **2016**, *339*, 242.
(21) Baerlocher, C.; McCusker, L. B. Database of Zeolite Structures.
(22) Beyerlein, R. A.; Choi-feng, C.; Hall, J. B.; Huggins, B. J.; Ray, G. J. **1997**, *4*, 27.
(23) Lesage, A.; Lelli, M.; Gajan, D.; Caporini, M. A.; Vitzthum, V.; Mieville, P.; Alauzun, J.; Roussey, A.; Thieuleux, C.; Mehdi, A.; Bodenhausen, G.; Coperet, C.; Emsley, L. *J. Am. Chem. Soc.* **2010**, *132*, 15459.
(24) Rossini, A. J.; Zagdoun, A.; Lelli, M.; Canivet, J.; Aguado, S.; Ouari, O.; Tordo, P.; Rosay, M.; Maas, W. E.; Copéret, C.; Farrusseng, D.; Emsley, L.; Lesage, A. *Angew. Chemie - Int. Ed.* **2012**, *51* (1), 123.
(25) Ni, Q. Z.; Daviso, E.; Can, T. V.; Markhasin, E.; Jawla, S. K.; Swager, T. M.; Temkin, R. J.; Herzfeld, J.; Griffin, R. G. *Acc. Chem. Res.* **2013**, *46* (9), 1933.
(26) Sangodkar, R. P.; Smith, B. J.; Gajan, D.; Rossini, A. J.; Roberts, L. R.; Funkhouser, G. P.; Lesage, A.; Emsley, L.; Chmelka, B. F. *J. Am. Chem. Soc.* **2015**, *137* (25), 8096.
(27) Mance, D.; van der Zwan, J.; Velthoen, M. E. Z.; Meirer, F.; Weckhuysen, B. M.; Baldus, M.; Vogt, E. T. C. C. *Chem. Commun.* **2017**, *53* (28), 3933.
(28) Berkson, Z. J.; Messinger, R. J.; Na, K.; Seo, Y.; Ryoo, R.; Chmelka, B. F. *Angew. Chemie - Int. Ed.* **2017**, No. 2, 2.
(29) Wolf, P.; Valla, M.; Núñez-Zarur, F.; Comas-Vives, A.; Rossini, A. J.; Firth, C.; Kallas, H.; Lesage, A.; Emsley, L.; Copéret, C.; Hermans, I. *ACS Catal.* **2016**, *6* (7), 4047.
(30) Wolf, P.; Valla, M.; Rossini, A. J.; Comas-Vives, A.; Núñez-Zarur, F.; Malaman, B.; Lesage, A.; Emsley, L.; Copéret, C.; Hermans, I. *Angew. Chemie - Int. Ed.* **2014**, *53* (38), 10179.
(31) Mouat, A. R.; George, C.; Kobayashi, T.; Pruski, M.; Van Duyne, R. P.; Marks, T. J.; Stair, P. C. *Angew. Chemie - Int. Ed.* **2015**, *54* (45), 13346.
(32) Smeets, S.; Berkson, Z. J.; Xie, D.; Zones, S. I.; Wan, W.; Zou, X.; Hsieh, M. F.; Chmelka, B. F.; McCusker, L. B.; Baerlocher, C. *J. Am. Chem. Soc.* **2017**, *139* (46), 16803.
(33) Lesage, A.; Sakellariou, D.; Steuernagel, S.; Emsley, L. *J. Am. Chem. Soc.* **1998**, *120* (7), 13194.
(34) Hu, B.; Trébosc, J.; Amoureux, J. P. *J. Magn. Reson.* **2008**, *192* (1), 112.
(35) Garaga, M. N.; Hsieh, M.-F.; Nour, Z.; Deschamps, M.; Massiot, D.; Chmelka, B. F.; Cadars, S. *Phys. Chem. Chem. Phys.* **2015**, *17* (33), 21664.
(36) Li, S.; Zheng, A.; Su, Y.; Zhang, H.; Chen, L.; Yang, J.; Ye, C.; Deng, F. *J. Am. Chem. Soc.* **2007**, *129* (36), 11161.
(37) Yu, Z.; Zheng, A.; Wang, Q.; Chen, L.; Xu, J.; Amoureux, J.-P. P.; Deng, F. *Angew. Chemie - Int. Ed.* **2010**, *49* (46), 8657.
(38) Zagdoun, A.; Casano, G.; Ouari, O.; Schwarzwälder, M.; Rossini, A. J.; Aussenac, F.; Yulikov, M.; Jeschke, G.; Copéret, C.; Lesage, A.; Tordo, P.; Emsley, L. *J. Am. Chem. Soc.* **2013**, *135* (34), 12790.
(39) Anderson, M. W.; Barrie, P. J.; Klinowski, J. *J. Phys. Chem* **1991**, *95* (10), 235.
(40) Pourpoint, F.; Trébosc, J.; Gauvin, R. M.; Wang, Q.; Lafon, O.; Deng, F.; Amoureux, J. P. *ChemPhysChem* **2012**, *13* (16), 3605.
(41) Li, S.; Pourpoint, F.; Trébosc, J.; Zhou, L.; Lafon, O.; Shen, M.; Zheng, A.; Wang, Q.; Amoureux, J.-P.; Deng, F. *J. Phys. Chem. Lett.* **2014**, *5* (17), 3068.
(42) Perras, F. A.; Padmos, J. D.; Johnson, R. L.; Wang, L.-L. L.; Schwartz, T. J.; Kobayashi, T.; Horton, J. H.; Dumesic, J. A.; Shanks, B. H.; Johnson, D. D.; Pruski, M. *J. Am. Chem. Soc.* **2017**, *139* (7), 2702.
(43) Mikkelsen, Ø.; Rønning, P. O.; Kolboe, S.; Rùnning, P. O.; Kolboe, S.; Mikkelsen, Ø.; Rønning, P. O.; Kolboe, S. *Microporous Mesoporous Mater.* **2000**, *40* (1–3), 95.
(44) Runnebaum, R. C.; Ouyang, X.; Edsinga, J. A.; Rea, T.; Arslan, I.; Hwang, S. J.; Zones, S. I.; Katz, A. *ACS Catal.* **2014**, *4* (7), 2364.

(45) Rozwadowski, M.; Lezanska, M.; Wloch, J.; Erdmann, K.; Golembiewski, R.; Kornatowski, J. *Chem. Mater.* **2001**, *13* (5), 1609.
(46) Pradhan, A. R.; Wu, J. F.; Jong, S. J.; Chen, W. H.; Tsai, T. C.; Liu, S. B. *Appl. Catal. A Gen.* **1997**, *159* (1–2), 187.
(47) Fyfe, C. A.; Mueller, K. T.; Grondey, H.; Wong-Moon, K. C. *Chem. Phys. Lett.* **1992**, *199* (1–2), 198.
(48) Fu, R.; Smith, S. A.; Bodenhausen, G. *Chem. Phys. Lett.* **1997**, *272* (5–6), 361.
(49) Elena, B.; de Paëpe, G.; Emsley, L. *Chem. Phys. Lett.* **2004**, *398* (4–6), 532.
(50) Fung, B. M.; Khitrin, A. K.; Ermolaev, K. **2000**, *101*, 97.

Chapter 6

Network formation and strength development in alkali-activated aluminosilica cements

Adapted from: Z. J. Berkson, H. A. Dobbs, G. Degen, K. Kristiansen, B. F. Chmelka, J. N. Israelachvili, *in preparation*

6.1 Abstract

The initial formation and development of molecular-scale structure, as well as the influence of such structures on macroscopic physical properties, are largely unknown for many aluminosilica materials including inorganic polymer binders (IPBs), which are attractive as low-CO_2 cement materials. Here, we determine the molecular-level structures and compositions during early formation of aluminosilica networks under strong alkaline (pH >14) conditions using amorphous silica and alumina colloidal microparticle precursors as SiO_2 and Al_2O_3 sources, respectively. Specifically, the transient evolution of local ^{23}Na, ^{27}Al, ^{29}Si, and ^{1}H environments at early stages of network formation and condensation is determined using dynamic nuclear polarization surface-enhanced solid-state NMR spectroscopy (DNP-SENS) techniques, with complementary X-ray diffraction and electron microscopy analyses. One- and two-dimensional DNP-enhanced heteronuclear correlation spectra establish the hydration environments and ^{27}Al-O-^{29}Si network connectivities of the aluminosilica network, which forms at the surfaces of the alumina particles. As network formation time increases, the aluminosilica networks become locally-ordered and more condensed, which correlates with development of macroscopic strength of the aluminosilica material. The results demonstrate the ability of DNP-enhanced NMR techniques to measure and characterize local transient structures in aluminosilica networks, which provides

important insights into the influences of impurities and solution chemistry in developing inorganic networks with desirable macroscopic properties, which is crucial for the formulation of new IPB cement materials .

6.2 Introduction

Aluminum, silicon, and oxygen are three of the most earth-abundant elements and comprise a wide variety of natural and technological systems with diverse industrial applications in catalysis, structural materials, and separations.[1–4] The physiochemical and mechanical properties of aluminosilicate materials vary dramatically depending on their local structures and compositions, even for materials with similar bulk chemical compositions. By adjusting the synthesis conditions of aluminosilicate materials, different structures and properties can be achieved for different applications. For example, aluminosilicate zeolites and aluminosilica inorganic polymer binders (IPBs) are two types of highly condensed aluminosilicate materials composed of non-stoichiometric corner-sharing AlO_4^- and SiO_4^{2-} tetrahedra and charge-balancing cationic species (e.g., H^+, Na^+, Ca^{2+}, etc.), exhibit very different degrees of local order and long-range order. While both zeolites and IPBs are formed by condensation of solid- or solution-phase aluminate and silicate species in aqueous media (e.g., gels or colloidal suspensions), they differ in their density and corresponding mechanical properties. Zeolites are generally formed under elevated pressures and temperatures and mildly alkaline solution conditions over intermediate time scales (hours-days), yielding well-defined nanoporous framework structures with high extents of long-range periodic ordering.[5–7] By comparison, IPBs are formed from partial dissolution, reprecipitation, and gradual condensation under highly alkaline conditions (*ca*. 16 M NaOH)

of dense inorganic oxides such as fly ash, a waste product of coal combustion, or natural clays.[3] Under these reaction conditions, a network of polymerized aluminate and silicate tetrahedra forms and condenses between the metal oxide particles, requiring long timescales to fully condense (days-months).

The condensation of the aluminosilica network is concomitant with development of macroscopic compressive strength in IPBs,[8] leading to interest in their application as new structural materials. Conventional structural materials (e.g., ordinary Portland cement, OPC) are produced through high-temperature calcination of lime ($CaCO_3$), resulting in the release of 0.9 ton CO_2 per ton of cement produced and accounting for 8-10% of global anthropogenic CO_2 emissions. By comparison, IPB-based cements can be produced using common waste products (fly ash), releasing little to no CO_2 in their production and making them attractive as new sustainable cement materials. However, the current methods of IPB cement production are commercially untenable because of the very slow reaction kinetics and highly alkaline reaction conditions needed to for the development of macroscopic strength. Minor variations in IPB precursor composition and crystallinity can yield materials with compressive strengths ranging from very poor to almost three times greater than that of OPC.[9] In general, aluminosilicate networks, including those present in IPBs, are poorly understood because they are difficult to characterize.[10] The difficulty in preparing IPBs with desirable structural properties arises from a lack of molecular-level understanding of the formation and condensation processes of aluminosilica networks, as well as the relations between IPB structures, compositions, and the development of micro- and macroscopic compressive strength.[11]

The generally accepted mechanism for formation of IPBs includes distinct steps: dissolution of the solid-state precursors, oligimerization of solution phase species, nucleation of discrete particles of the new phase, and growth of the aluminosilica network.[12] The formation of IPBs is depicted schematically in Figure 6.1 for SiO_2 and Al_2O_3 materials. At early reaction times, aluminosilica networks can form dense, locally-ordered structures that evolve over time, though may lack long-range or crystalline order.[13–15] Determining the local structures and interactions of aluminosilica networks that correspond to the development of macroscopic strength properties has been exceptionally challenging,[10] and formulation of new IPB cement materials has been largely empirical.[9] This is because IPB materials can contain diverse components that lack long-range order, have different solubilities, and different non-stoichiometric surface compositions, especially at early times in the formation of the IPB networks. These challenges have limited understanding of the development of specific microstructures and macroscopic mechanical properties of the materials.[7] To advance the technological applications of aluminosilica networks in IPBs, a more detailed understanding of the early stages of network formation is required in relation to changes in the micro- and macroscopic strength properties of the materials.

In this work, the early network formation of aluminosilica networks formed from amorphous silica and alumina sources in strongly alkaline (6 M NaOH) reaction conditions is elucidated to obtain a detailed understanding of IPB network formation and evolution during the initial condensation and growth of the aluminosilica network. Tracking the evolution of such aluminosilica networks and the corresponding development of interparticle adhesion and macroscopic material strength has been challenging due to the heterogeneous surface compositions and small (~nm) particle-particle distances under realistic reaction conditions.

Newly developed solid-state NMR techniques and advances in the surfaces forces apparatus (SFA) enable detection and correlation of atomic bonding and hydration environments in aluminosilica networks formed at different reaction times (hours to weeks) as well as elucidation of the nanoscopic interparticle adhesion energies and strength properties. Specifically, *ex-situ* solid-state dynamic nuclear polarization (DNP) enhanced NMR techniques yield drastic improvements in NMR signal intensity from particle surfaces. Notably, solid-state 2D DNP NMR correlation spectra establish the ^{29}Si-O-^{27}Al connectivities within the dilute aluminosilica networks formed at different stages of the network formation and evolution, providing detailed information on the structures that development and transform over the course of the reaction. The detailed molecular-level insights into network evolution during early aluminosilica formation provides new understanding of the development of micro- and macroscopic structures and properties, bridging the gap between initial molecular-level network formation and the development of desirable properties in IPBs.

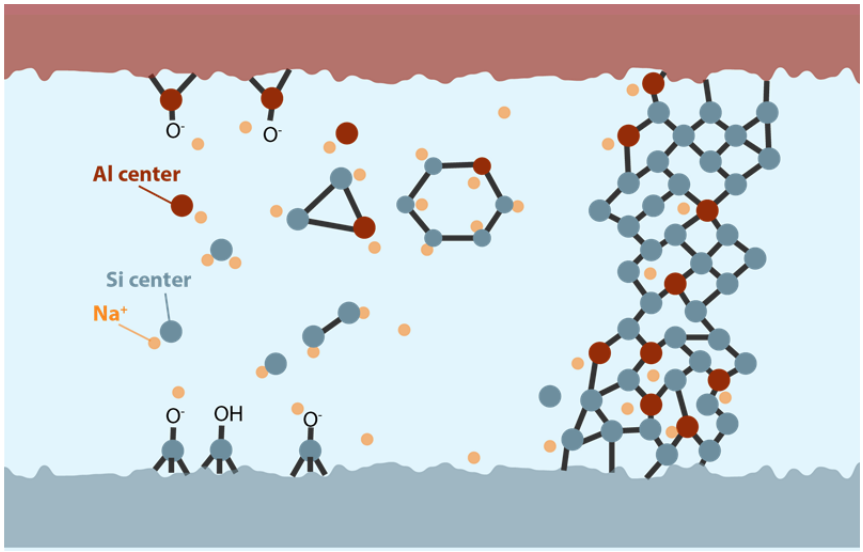

Figure 6.1. Schematic diagram showing the complex coupled and transient processes involved in dissolution and formation of inorganic polymer binders for silica (blue) and alumina (red) surfaces in highly alkaline conditions, including monomer detachment from the

surfaces, solution-phase speciation and oligomerization, and reprecipitation of the condensed network.

6.3 Results and discussion

6.3.1 Morphology and long-range order in alkali-activated IPBs

Aluminosilica networks form between colloidal Al_2O_3 and SiO_2 particles reacted under alkaline conditions (6 M NaOH), which are tracked as a function of reaction time using wide-angle X-ray diffraction (XRD) and scanning electron microscopy (SEM), shown in Figure 6.2. The XRD patterns of a mixture of amorphous Al_2O_3 and SiO_2 particles (atomic Si/Al ratio ~ 2) after reaction at 295 K in 6 M NaOH solution (water/solids ratio ~ 2) do not change significantly after reaction times of 24, 72, or 384 h (Fig. 6.2a,b,c), indicating that there is no detectable change in the long-range periodic ordering of the reaction products. The XRD patterns exhibit relatively narrow reflections that are indexed to crystalline NaCl species (red dots) formed upon acid neutralization of the reaction mixture with HCl to arrest the reaction progress at the end of each time point. Additional reflections are indexed to an aluminum hydroxide phase (blue dots), likely present as an impurity in the alumina source. The positions and widths of the XRD reflections from the crystalline NaCl and AlO(OH) phases are the same for the materials reacted for 24, 72, and 384 h, indicating that the AlO(OH) phase does not participate to a detectable extent in the development of the aluminosilica network and that the formation of NaCl on quenching the reaction occurs for all of the different time points. Each of the XRD patterns also exhibit a broad, featureless reflection at 22° 2θ, which arises from regions of the material that lack long-range order, such as the aluminosilica networks formed by the reaction of SiO_2 and Al_2O_3 in highly alkaline aqueous media. Due to the similar electron densities of Al and Si atoms,[16] as well as the inability of

scattering techniques to resolve regions of the material that lack long-range order, the XRD patterns are unable to provide further insights into the development of aluminosilica network formed under alkaline reaction conditions.

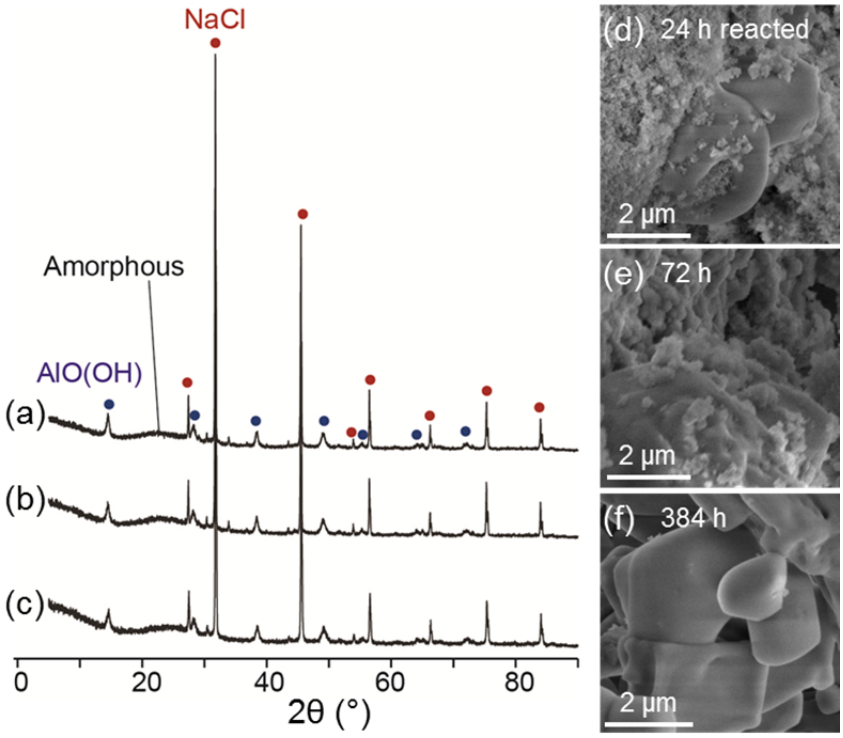

Figure 6.2. (a,b,c) XRD patterns and (d,e,f) representative SEM images of amorphous Al_2O_3 and SiO_2 particles reacted at 295 K in 6 M NaOH solution for (a,d) 24 h, (b,e) 72 h, and (c,f) 384 h. Reflections indexable to crystalline NaCl (JCPDS card no. 05-0628) and AlO(OH) (JCPDS card no. 00-021-1307) are indicated with red and blue dots, respectively.

Despite their similar XRD patterns, the morphology of the Al_2O_3 and SiO_2 particle mixture changes significantly after reaction in 6 M NaOH for 24, 72, or 384 h, as shown by the representative SEM images in Fig. 6.2c,d,e. After 24 h reaction time, the particules aggregate to form a low density network of 50 nm particles, indicating that the colloidal Al_2O_3 and SiO_2 particles (~50 nm mean diameter) do not change significantly in size after 24 h reaction. After 72 h reaction, the aggregated particles range in diameter from 100-500 nm, indicating that the colloidal Al_2O_3 and SiO_2 particles have partially dissolved and reacted to

form larger amorphous particles. Additional large (~3 μm), irregular particles are also observed in the SEM images, which are attributed to the AlO(OH) phase that is also manifested in the XRD patterns. Large, cubic crystals are also observed in some of the SEM images of the reacted Al_2O_3 and SiO_2 particles. These are attributed to crystalline NaCl particles formed during the neutralization of the reaction mixture, corroborating the macroscopic phase segregation of the NaCl and aluminosilica regions of the material. After reaction for 384 h, the material is composed predominantly of aggregated 2-10 μm particles, indicating that the small colloidal SiO_2 and Al_2O_3 particles have almost completely dissolved and reprecipitated in the form of an aluminosilica IPB material after the long reaction time.

6.3.2 Local ^{1}H, ^{27}Al, and ^{29}Si environments in alkali-activated IPB networks formed at early reaction times

The atomic-scale ^{1}H, ^{29}Si, ^{27}Al, and ^{23}Na environments and interactions in the aluminosilica IPB materials are established by one-dimensional (1D) and two-dimensional (2D) solid-state nuclear magnetic resonance (NMR) spectroscopy, which provides element-specific insights into the chemical environments, covalent bonding configurations, and nanoscale interactions of the atomic species of interest. For example, the 1D single-pulse ^{27}Al magic-angle-spinning (MAS) NMR spectra of amorphous Al_2O_3 and SiO_2 particles reacted in aqueous 6 M NaOH for 24, 72, and 384 h, Fig. 6.3, exhibit different ^{27}Al signals from ^{27}Al species in four- and six-coordinated environments, denoted $^{27}Al^{IV}$ and $^{27}Al^{VI}$, respectively. The 1D ^{27}Al MAS NMR spectra are dominated by a ^{27}Al signal at 11 ppm, which is assigned to $^{27}Al^{VI}$ environments in the Al_2O_3 and AlO(OH) particles. A weak signal at 55 ppm accounts for 1-2% of the total integrated ^{27}Al signal intensity and is assigned to

$^{27}Al^{IV}$ environments at the surfaces of the Al_2O_3 particles and within the nascent aluminosilica network. Previously, the formation of $^{27}Al^{IV}$ environments in IPB materials has been correlated to the development of macroscopic compressive strength.[8] The very small overall quantity of four-coordinated ^{27}Al species detected in the Al_2O_3 and SiO_2 materials reacted for 24 h indicates that only a very small fraction of the total Al in the material has participated in the formation of the aluminosilica network at this early stage. The total percentage of $^{27}Al^{IV}$ species detected in the ^{27}Al MAS NMR spectra increases to 1.5% after 72 h reaction and 2.0% after 384 h reaction, which indicates a gradual increase in the quantity of $^{27}Al^{IV}$ species that are expected to be incorporated into an aluminosilica network.

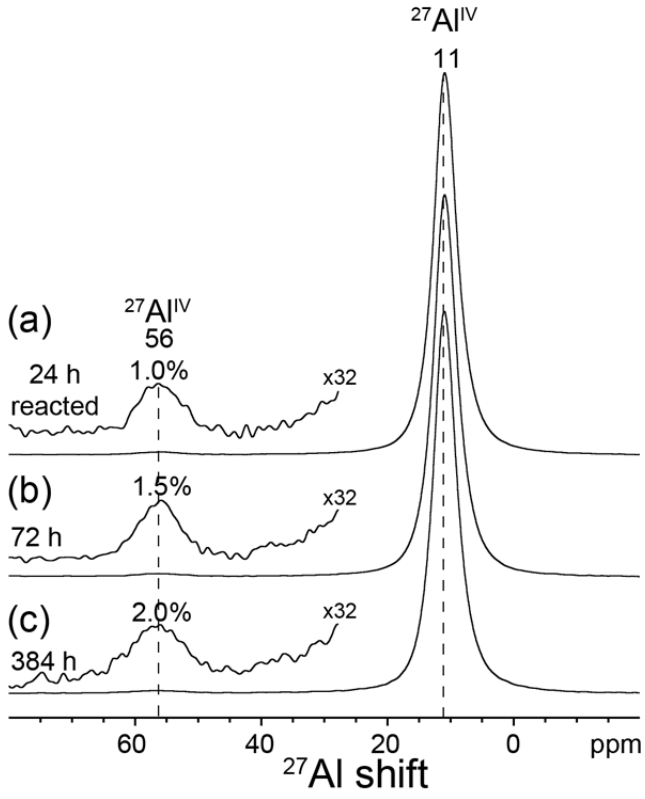

Figure 6.3. Solid-state 1D single-pulse ^{27}Al MAS NMR spectra of amorphous Al_2O_3 and SiO_2 particles reacted at 295 K in 6 M NaOH solution for (a) 24 h, (b) 72 h, and (c) 384 h. The spectra were acquired at 295 K, 18.8 T, and 20 kHz MAS.

The development of tensile and compressive strength in IPB materials is hypothesized to arise from molecular-level changes in the compositions and structures of the aluminosilica network that occur gradually over the course of the reaction period.[8] However, distinguishing the local chemical environments of ^{27}Al and ^{29}Si species in the aluminosilica networks in IPB materials is exceptionally challenging due in part to their non-stoichiometric compositions, dilute overall quantities (especially for early reaction times), and broad and overlapping NMR signals from different phases within the complex and heterogeneous IPB materials. However, recent advances in solid-state NMR spectroscopy, most notably dynamic-nuclear-polarization surface-enhanced MAS NMR (DNP-SENS) techniques at low temperatures (<100 K), provide significantly enhanced NMR signal sensitivity that enables the detection and correlation of ^{27}Al and ^{29}Si environments in dilute aluminosilica materials, even at natural isotopic abundance (4.7%) ^{29}Si.[15,17,18] For the alkali-activated aluminosilica IPB materials studied here, DNP-SENS techniques provides high signal enhancements (*ca.* x100), which enables enables the measurement of 2D heteronuclear correlation spectra of dilute surface species in the aluminosilica networks. Such spectra have until now been challenging or infeasible to characterize without expensive isotopic enrichment in ^{29}Si. With DNP-SENS techniques, powerful 2D NMR correlation analyses can be applied to establish the molecular-level structures and compositions of aluminosilica networks, which are hypothesized to correlate directly to the development of macroscopic strength in the materials.

Specifically, DNP-SENS heteronuclear correlation spectra correspond to the hydration environments, ^{27}Al-O-^{29}Si bonding configurations, and the interactions and environments of Na^+ cations in aluminosilica networks formed by reaction of Al_2O_3 and SiO_2 particles in highly alkaline conditions after different reaction times. These insights are provided by two-

dimensional (2D) $^{29}Si\{^{1}H\}$, $^{27}Al\{^{29}Si\}$, and $^{23}Na\{^{29}Si\}$ DNP-SENS heteronuclear correlation spectra, which result from through-space internuclear dipole-dipole couplings that operate over distances of < 1 nm. The 2D spectra are plotted as 2D contour plots with ^{1}H, ^{29}Si, ^{27}Al, or ^{23}Na frequency axes plotted with normalized units of Hz/MHz = ppm. Correlated signals in the 2D spectra manifest the site-specific interactions and nanoscale proximities of the dipole-dipole coupled ^{1}H, ^{29}Si, ^{27}Al, or ^{23}Na nuclei with the corresponding NMR signals. The 2D DNP-SENS spectra thus selectively detect and resolve signals from dilute species within the aluminosilica networks, including directly-bonded ^{27}Al-O-^{29}Si moieties and charge-balancing Na^{+} cations situated near AlO_4^{-} tetrahedral within the IPB networks.

Strong hydrogen-bonding interactions of adsorbed water at the surfaces of the SiO_2 particles and within the aluminosilica networks are established by the 2D $^{29}Si\{^{1}H\}$ DNP-SENS HETeronuclear CORrelation (HETCOR) spectra in Figure 6.4. The 2D $^{29}Si\{^{1}H\}$ spectrum of the particle mixture after 24 h of reaction in 6 M NaOH shows broad, overlapping ^{29}Si signals at -92, -100, and -108 ppm, which result from overlapping signal contributions from $Q^3(1Al)/Q^2(0Al)$, $Q^4(1Al)/Q^3(0Al)$, and $Q^4(0Al)$ silicate species, respectively. All of these signals are correlated with a broad distribution ^{1}H signals from 5.2 to 20 ppm, which arise from -OH moieties participating to different extents in hydrogen bonding at the different ^{29}Si sites. The ^{1}H signals at 5.2 ppm are consistent with physisorbed water,[19] while the signals at higher ^{1}H chemical shift values arise from -OH moieties which form strong hydrogen bonds with incompletely condensed Si-OH, Al-OH, and H_2O species at particle surfaces and in the crosslinking aluminosilica network. Well-established semi-empirical correlations relate the ^{1}H chemical shift to the -OH···O- hydrogen bond distances.[20,21] Using these correlations, the broad ^{1}H signals from 6-20 ppm correspond to -

OH···O- distances ranging from 0.23-0.29 nm, establishing the presence of distributions of hydrogen bond lengths at partially and completely crosslinked silicate sites at the surfaces of the SiO_2 particles and the aluminosilica networks. The ^{29}Si signal at -100 ppm from Q^3(0Al) and Q^4(1Al) silicate species shows an additional weak intensity correlation with the ^1H signal at 2.5 ppm, which is assigned to dilute isolated Si-OH moieties associated with the surfaces of the SiO_2 particles. The 2D DNP-SENS $^{29}Si\{^1H\}$ HETCOR spectrum of the same material after 72 h reaction shows similar ^{29}Si-^1H intensity correlations between ^{29}Si signals at -92, -100, and -106 ppm and ^1H signals at 5.7 ppm from adsorbed water, and 8.7-15 ppm from strongly H-bonded -OH groups with -OH···O- distances of 0.24-0.28 nm. Previous analyses of cementitious IPB materials have suggested that macroscopic compressive strength development coincides with expulsion of water from the IPB into mesopores formed as the material condenses.[22] The reduced extent of hydrogen bonding detected after 72 h reaction compared to 24 h is consistent with exclusion of water from between the SiO_2 particles and from within the aluminosilica network during condensation of the material. All ^{29}Si signals in the 2D $^{29}Si\{^1H\}$ HETCOR spectrum in Fig. 4b are also correlated with ^1H signals at 2.0 and -0.5 ppm, which are assigned to isolated -Si-OH and Na-OH moieties, respectively. The stronger correlated signal intensities from isolated -Si-OH species after 72 h reaction compared to 24 h suggests that longer reaction times lead to greater densities of relatively isolated (as opposed to strongly H-bonded) hydroxyl groups, which is also consistent with the reduced extent of hydrogen bonding for the material reacted for 72 h. Furthermore, the correlated signals from Na-OH species establish that a subset of the alkaline NaOH species present in the reaction media are adsorbed (within 1 nm) at the surfaces of the partially-crosslinked SiO_2 particles.

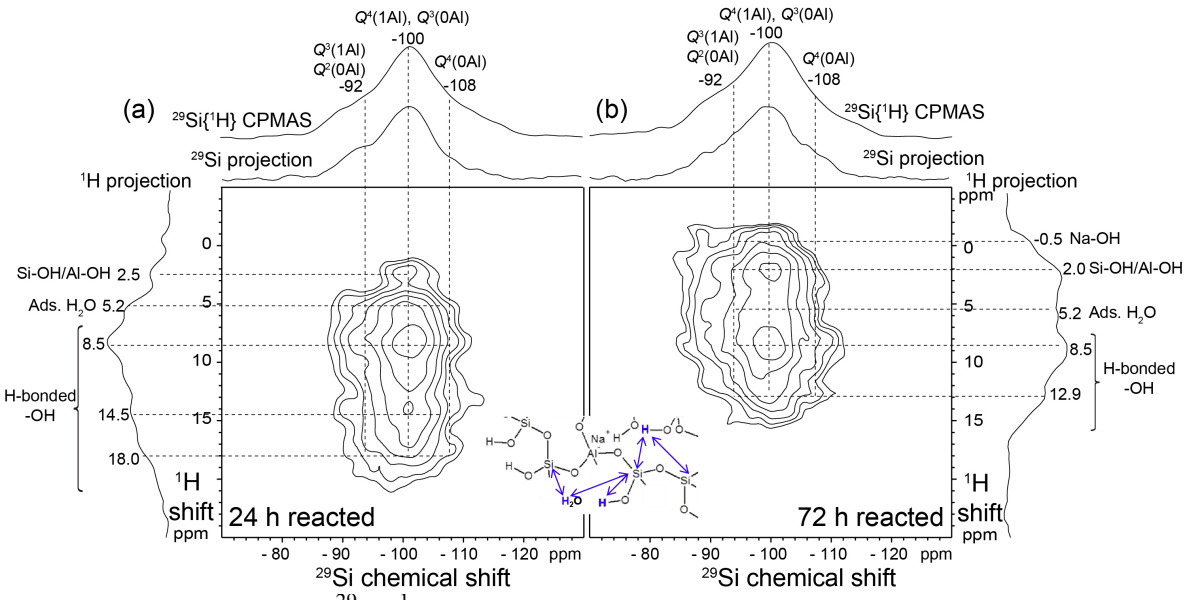

Figure 6.4. Solid-state 2D ^{29}Si{^{1}H} DNP-CP-HETCOR spectra of amorphous Al_2O_3 and SiO_2 particles reacted at 295 K in 6 M NaOH solution for (a) 24 h and (b) 72 h. The spectra were acquired at 95 K, 9.4 T, 8 kHz MAS, in the presence of 8 mM TEKPol biradical polarizing agent in 1,1,2,2-tetrachloroethane (DNP solvent), and using ^{29}Si{^{1}H} CP contact times of 0.5 ms. Solid-state 1D ^{29}Si{^{1}H} DNP-CPMAS spectra are shown along the horizontal axes for comparison with the 1D ^{29}Si projections of the 2D spectra, and the ^{1}H projections are shown along the vertical axes. The inset shows interactions of hydroxyl moieties and occluded water molecules with ^{29}Si atoms in the aluminosilica network.

6.3.3 Atomic-scale rearrangements of the aluminosilica network

As reaction time increases, the ^{27}Al and ^{29}Si species within the dilute aluminosilica IPB network gradually condense, as established by the 2D ^{27}Al{^{29}Si} dipolar-mediated heteronuclear multi-quantum coherence (*D*-HMQC) NMR spectra (Fig. 6.5). The 2D ^{27}Al{^{29}Si} HMQC spectra selectively detect and correlate ^{27}Al species that are dipole-dipole-coupled to, and within nanoscale proximity of, ^{29}Si nuclei, being principally sensitive to interactions of directly-bonded ^{27}Al-O-^{29}Si spin pairs.[18] The 2D spectra establish the types, distributions, and covalent bonding of ^{29}Si and ^{27}Al species within the aluminosilica networks, which contain only ca. 1-2% of the Al in the IPB materials based on the ^{27}Al single-pulse spectra discussed above. The 2D ^{29}Si{^{27}Al} HMQC spectrum of the Al_2O_3 and

SiO_2 particles after 24 h reaction (Fig. 6.5a) shows broad partially-resolved ^{27}Al signals at 53 and 48 ppm that arise from different $^{27}Al^{IV}$. By comparison to the ^{27}Al signal at 48 ppm, the ^{27}Al signal at 53 ppm is substantially broader, indicating that it arises from $^{27}Al^{IV}$ species in distorted tetrahedral environments likely associated with Al-OH species. The signal is correlated to ^{29}Si signals centered at -85 ppm from Q^2(1Al) species (blue shaded region), indicating that the corresponding ^{27}Al-O-^{29}Si moieties are in regions of the aluminosilica network that are incompletely-crosslinked, likely at the edges and surfaces of the nascent IPB network. The narrower $^{27}Al^{IV}$ signal at 48 ppm is predominantly correlated to a ^{29}Si signal at -96 (red shaded region), indicating that the corresponding $^{27}Al^{IV}$ species in the aluminosilica network are bonded (through bridging oxygen atoms) to partially-crosslinked Q^3(1Al). At this early stage in the formation of the IPB network, none of the correlated ^{27}Al-^{29}Si signal intensities are detected in spectral regions associated with fully-crosslinked Q^4(1Al) species.

Increasing reaction times are associated with further gradual condensation and rearrangement of the aluminosilica IPB network, as evidenced by the correlated signal intensities in the 2D $^{27}Al\{^{29}Si\}$ *D*-HMQC spectrum of Al_2O_3 and SiO_2 particles reacted in 6 M NaOH for 72 h (Fig. 6.5b). The spectrum shows a broad continuous distribution of signal intensity with partially-resolved maxima at 62 and 40 ppm in the ^{27}Al dimension, which is correlated to a relatively narrow ^{29}Si signal at -94 ppm from Q^3(1Al) silicate species. The ^{27}Al signals arise from a distribution of $^{27}Al^{IV}$ environments, though the low sensitivity and dilute quantities of the $^{27}Al^{IV}$ species preclude determining if the broad signal linewidth arises from a distribution of chemical environments or a distribution of quadrupolar interactions. The change in the position of the correlated signal in the ^{29}Si dimension from -84 ppm after 24 h reaction to -94 ppm after 72 h reaction establishes the gradual

condensation of the majority of the ^{29}Si species in the aluminosilica network from Q^2(1Al) to Q^3(1Al).

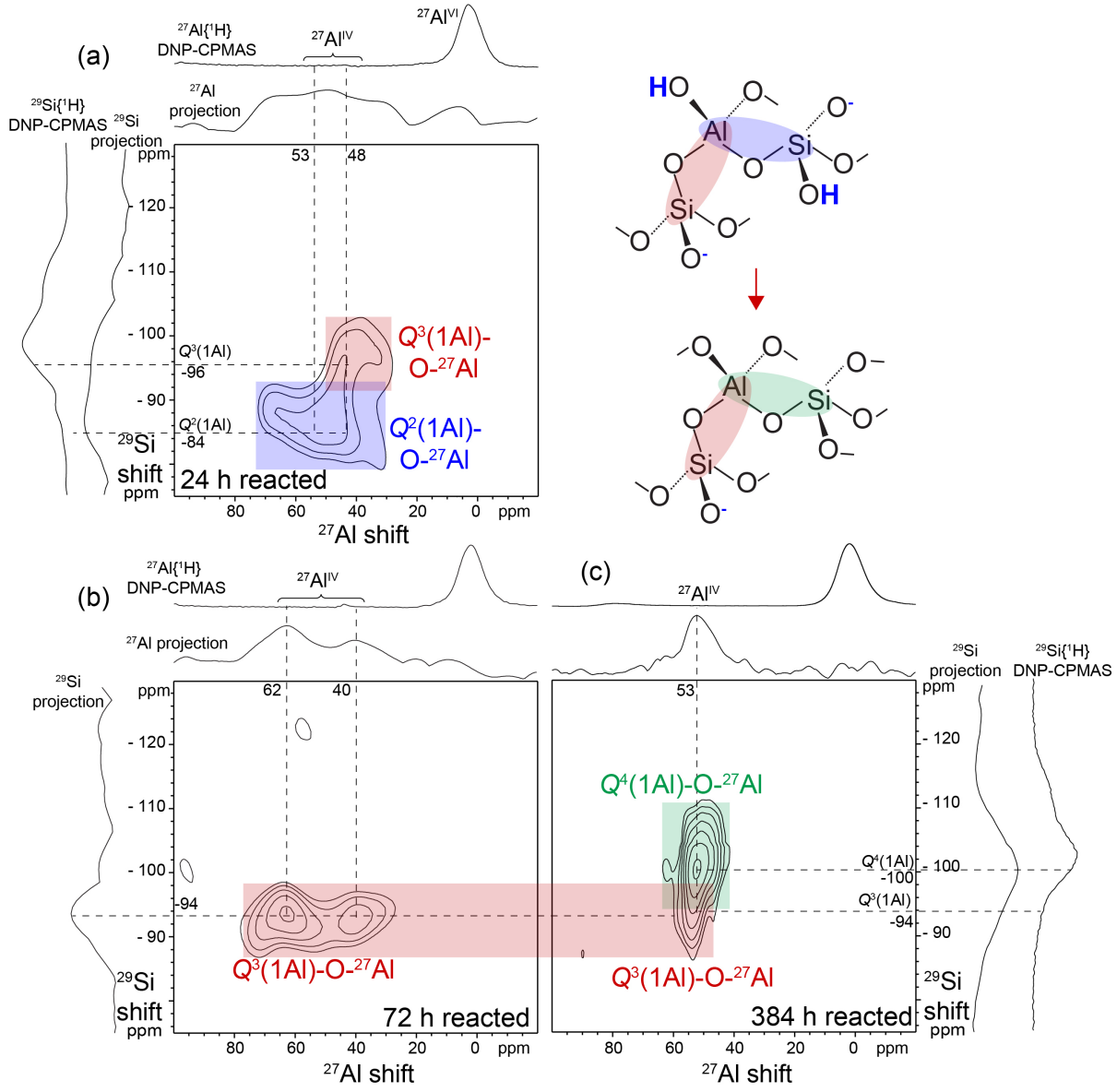

Figure 6.5. Solid-state 2D ^{27}Al{^{29}Si} DNP-*D*-HMQC spectra of amorphous Al_2O_3 and SiO_2 particles reacted at 295 K in 6 M NaOH solution for (a) 24 h, (b) 72 h, and (c) 384 h. The spectra were acquired at 95 K, 9.4 T, 8 kHz MAS, and in the presence of 8 mM TEKPol biradical polarizing agent in 1,1,2,2-tetrachloroethane (DNP solvent). Solid-state 1D ^{27}Al{^{1}H} or ^{29}Si{^{1}H} DNP-CPMAS spectra are shown along the horizontal axes for comparison with the 1D projections of the 2D spectra. The schematic insets show the partially-condensed aluminosilica network at early reaction times (top) and a more completely condensed network (bottom), consistent with the 2D NMR spectra.

After even longer reaction times (384 h), the aluminosilica network condenses further to form completely-crosslinked Q^4(1Al) species with a concomitant increase in the local order of the ^{27}Al species. This is evidenced by the correlated signal intensities in the 2D ^{27}Al{^{29}Si} *D*-HMQC spectrum of the 384 h reacted material (Fig. 6.5c), which shows a relatively narrow ^{27}Al signal at 53 ppm that is correlated to ^{29}Si signals in the -94 to -100 ppm region. The reduction in the ^{27}Al linewidth after 384 h compared to after 72 h indicates an increase in the local order of the corresponding $^{27}Al^{IV}$ species as the aluminosilica network condenses. The ^{29}Si signals around -100 ppm (green shaded region) are assigned to completely-crosslinked Q^4(1Al) silicate species,[23,24] confirming that after 384 h reaction time a dense network of linked SiO_4^{4-} and AlO_4^{3-} tetrahedra has formed, with Na^+ cations presumably incorporated to charge-balance the AlO_4^{3-} tetrahedra. However, the tail of ^{29}Si signal intensity at -94 ppm (red shaded region) indicates that a detectable fraction of Q^3(1Al) species remain uncondensed, even after this relatively long reaction time. The combined 2D ^{27}Al{^{29}Si} DNP-*D*-HMQC spectra and analyses establish that the reaction of Al_2O_3 and SiO_2 particles in 6 M NaOH is accompanied by the formation and gradual condensation of an aluminosilica network at the particle surfaces and between the particles, which densifies slowly over long time periods (~weeks).

The comprehensive 1D and 2D ^{27}Al{^{1}H}, ^{29}Si{^{1}H}, and ^{27}Al{^{29}Si}, DNP-SENS spectra and analyses together provide detailed information on the compositions and structures of the surface species in alkali-activated aluminosilica cements and their evolution over time A schematic diagram of the types and distributions of surface ^{23}Na, ^{27}Al, and ^{29}Si species that compose the aluminosilica network is shown in Fig. 6.6 that is consistent with the solid-state NMR analyses. Specifically, the aqueous 6 M NaOH reaction mixture equilibrates rapidly as

solution-phase species saturate. Less than 2% of all of the aluminum atoms present in the material are incorporated into the aluminosilica network formed after 24-384 h. Nevertheless, the structure and composition of the aluminosilica IPB network change dramatically over that same time period. Water is excluded from the interparticle networks as silicate species in the aluminosilica network condense. Over the reaction period studied, the aluminosilica network condenses from partially-crosslinked Q^2(1Al) and Q^3(1Al) silicate moieties and hydroxyated ^{27}Al species to form completely-crosslinked Q^4(1Al) silicate species and relatively ordered $^{27}Al^{IV}$ environments. The gradual condensation and rearrangement processes of the aluminosilica network are expected to be correlated to the development of macroscopic strength of the IPB network. Complementary measurements of the nanoscopic tensile strength of aluminosilica networks formed between extended surfaces are ongoing using the surface forces apparatus (SFA).[25,26] These measurements are expected to elucidate the nanoscopic interparticle adhesion energies and strength properties of aluminosilica IPB networks formed in highly alkaline conditions after different reaction times.

6.4 Conclusions

The local atomic environments and distributions of ^{1}H, ^{27}Al, and ^{29}Si species in aluminosilica IPB materials have been established for colloidal SiO_2 and Al_2O_3 particles reacted in highly alkaline (6 M NaOH) aqueous media by using state-of-the-art 1D and 2D DNP-enhanced solid-state NMR techniques, with complementary X-ray diffraction and electron microscopy analyses. The results establish the covalent bonding configurations and hydration environments within the aluminosilica IPB network that evolve over time, corresponding to the development of the macroscopic strength of the material. The

aluminosilica network forms from reaction of surface and near-surface species and incorporates <2% of all of the ^{27}Al species in the bulk material after reaction times of 24-384 h. The aluminosilica network is comprised of four- ^{27}Al and ^{29}Si species that are partially-crosslinked at early reaction times (24-72 h) but condense over time. After 384 h reaction time, the aluminosilica network is predominantly composed of completely-crosslinked Q^4(1Al) silicate moieties and relatively ordered $^{27}Al^{IV}$ environments, with a substantial fraction of partially-crosslinked Q^3(1Al) species. The results and analyses presented here provide an atomic-level view of the molecular rearrangement processes that corresponds with "setting" of the bulk cement material, and are expected to assist in screening of initial precursor (fly ash) selection in the development of new IPB materials with applications as low-CO_2 cements.

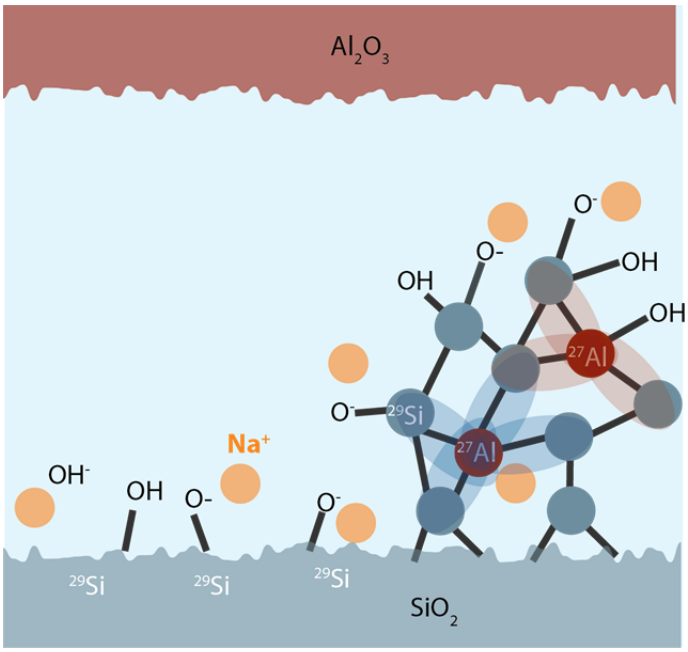

Figure 6.6. Schematic diagram of the partially-condensed aluminosilica network formed on reaction of colloidal alumina and silica particles in aqueous 6 M NaOH for short reaction periods (24-72 h). Silicon, aluminum, and sodium atoms are represented by blue, red, and yellow circles, respectively, and the ^{27}Al-^{29}Si interactions manifested by the 2D ^{27}Al{^{29}Si} DNP-*D*-HMQC spectra in Fig. 6.5 are represented by the blue and red colored regions.

6.5 Materials and methods

Materials synthesis

An aluminosilica network analogous to fly ash-based IPB formulations was synthesized using a mixture of amorphous, 50 nm alumina (US Research Nanomaterials, Inc.) and silica (PPG *Hi-Sil*) colloidal nanoparticles in an Si/Al atomic ratio of 2. The composition was chosen to be similar to many standard fly ash materials.[9] The colloidal particles were suspended in a 6 M NaOH (Sigma-Aldrich) solution with a water/solids (w/s) ratio of 2 and allowed to react for 2 h to X days at 295 K while shaking, after which the mixture was neutralized with equimolar, equivolume HCl and freeze-dried to completely halt the network formation reaction at each timepoint.

X-ray diffraction

The powder XRD measurements were conducted under ambient conditions on a Panalytical Empyrean Powder X-Ray Diffractometer in θ-2θ mode using Cu Kα radiation with a wavelength of 1.5405 Å and equipped with a rotating sample stage rotating at two turns per minute.

Electron microscopy

Scanning electron microscopy (SEM) images were acquired on a FEI Nova Nano 650 FEG SEM.

Solid-state NMR spectroscopy

The conventional 1D single-pulse ^{27}Al spectra were acquired on an 18.8 T narrow-bore Bruker AVANCE-III NMR spectrometer operating at frequencies of 208.526 for ^{27}Al and equipped with a Bruker Tri-Gamma triple-resonance H/X/Y 3.2 mm MAS NMR probehead. The spectra were acquired at 20 kHz MAS, 295 K, and using a 0.42 μs π/12 pulse and

relaxation delays of 7-9 s for adequate relaxation of the ^{27}Al nuclei. The 1D and 2D DNP-enhanced ^{27}Al{^{29}Si}, ^{27}Al{^{1}H}, and ^{29}Si{^{1}H} NMR experiments were carried out on a Bruker ASCEND 400 DNP-NMR spectrometer with a 9.4 Tesla superconducting magnet operating at 399.95, 104.28, and 79.46 MHz for ^{1}H, ^{27}Al, and ^{29}Si nuclei, respectively, and equipped with a gyrotron and microwave transmission line capable of providing 263 GHz microwave irradiation at the sample and a variable-temperature 3.2 mm triple-resonance H/X/Y MAS probe. The 1D and 2D DNP-enhanced ^{29}Si{^{1}H}, ^{27}Al{^{1}H}, and ^{29}Si{^{27}Al} spectra were acquired at 95 K, 8 kHz MAS, under continuous microwave irradiation at 263 GHz, with 100 kHz SPINAL-64 proton decoupling,[17] and in the presence of 8 mM TEKPol biradical[16] in frozen 1,1,2,2-tetrachloroethane (DNP solvent), which do not influence the structure of the material.[18] Experimentally-optimized repetition times of 2-10 s were used for maximum signal sensitivity. The solid-state 2D DNP-enhanced dipolar-mediated ^{27}Al{^{29}Si} spectra were acquired using a dipolar-mediated Heteronuclear Multiple Quantum Correlation (HMQC) experiment based on $SR4_2^{11}$ recoupling.[27] A 1 ms ^{27}Al double-frequency sweep pulse[28] was applied to invert the satellite transitions of quadrupolar ^{27}Al nuclei (I = 5/2) and improve sensitivity. Experimentally optimized recoupling times of 4.5 ms were used for best overall efficiency. The 2D ^{29}Si{^{1}H} HETCOR spectra were acquired using homonuclear ^{1}H-^{1}H eDUMBO-1_{22} decoupling[29] during the ^{1}H evolution periods to improve resolution in the ^{1}H dimensions. All of the 1D and 2D DNP-NMR spectra were acquired with 100 kHz heteronuclear SPINAL-64 ^{1}H decoupling[30] during the acquisition period.

6.6 References

(1) Sherman, J. D. *Proc. Natl. Acad. Sci.* **1999**, *96* (7), 3471.
(2) Taguchi, A.; Schüth, F. *Ordered mesoporous materials in catalysis*; 2005; Vol. 77.
(3) Duxson, P.; Fernández-Jiménez, A.; Provis, J. L.; Lukey, G. C.; Palomo, A.; Van Deventer, J. S. J. *J. Mater. Sci.* **2007**, *42* (9), 2917.
(4) Davis, M. E. *Nature* **2002**, *417*, 813.

(5) Cundy, C. S.; Cox, P. A. *Chem. Rev.* **2003**, *103* (3), 663.
(6) Cundy, C. S.; Cox, P. A. *Microporous Mesoporous Mater.* **2005**, *82* (1–2), 1.
(7) Grand, J.; Awala, H.; Mintova, S. *CrystEngComm* **2016**, *18* (5), 650.
(8) Fernández-Jiménez, A.; Palomo, A.; Sobrados, I.; Sanz, J. *Microporous Mesoporous Mater.* **2006**, *91* (1–3), 111.
(9) Aughenbaugh, K. L.; Williamson, T.; Juenger, M. C. G. *Mater. Struct.* **2015**, *48* (3), 607.
(10) Khale, D.; Chaudhary, R. *J. Mater. Sci.* **2007**, *42* (3), 729.
(11) Duxson, P.; Provis, J. L.; Lukey, G. C.; Mallicoat, S. W.; Kriven, W. M.; Van Deventer, J. S. J. *Colloids Surfaces A Physicochem. Eng. Asp.* **2005**, *269* (1–3), 47.
(12) Hellmut, G. K.; Weitkamp, J. *Synthesis (Molecular Sieves)*; Springer, 1998.
(13) Yang, P.; Zhao, D.; Margolese, D. I.; Chmelka, B. F.; Stucky, G. D. *Nature* **1998**, *396*, 152.
(14) Messinger, R. J.; Na, K.; Seo, Y.; Ryoo, R.; Chmelka, B. F. *Angew. Chemie - Int. Ed.* **2014**, *54* (3), 927.
(15) Berkson, Z. J.; Messinger, R. J.; Na, K.; Seo, Y.; Ryoo, R.; Chmelka, B. F. *Angew. Chemie - Int. Ed.* **2017**, No. 2, 2.
(16) Dědeček, J.; Sobalík, Z.; Wichterlová, B. *Catal. Rev. - Sci. Eng.* **2012**, *54* (2), 135.
(17) Smeets, S.; Berkson, Z. J.; Xie, D.; Zones, S. I.; Wan, W.; Zou, X.; Hsieh, M. F.; Chmelka, B. F.; McCusker, L. B.; Baerlocher, C. *J. Am. Chem. Soc.* **2017**, *139* (46), 16803.
(18) Kobayashi, T.; Singappuli-Arachchige, D.; Wang, Z.; I. Slowing, I.; Pruski, M. *Phys. Chem. Chem. Phys.* **2017**, *19* (3), 1781.
(19) Malfait, W. J.; Xue, X. *Geochim. Cosmochim. Acta* **2010**, *74* (2), 719.
(20) Yesinowski, J. P.; Eckert, H.; Rossman, G. R. *J. Am. Chem. Soc.* **1988**, *110* (5), 1367.
(21) Xue, X.; Kanzaki, M. *J. Am. Ceram. Soc.* **2009**, *92* (12), 2803.
(22) Collins, F.; Sanjayan, J. . *Cem. Concr. Res.* **2000**, *30* (9), 1401.
(23) Kodakari, N.; Tomita, K.; Iwata, K.; Katada, N.; Niwa, M. *Langmuir* **1998**, *14* (16), 4623.
(24) Greiser, S.; Hunger, M.; J??ger, C. *Solid State Nucl. Magn. Reson.* **2016**, *79* (May), 6.
(25) Israelachvili, J.; Min, Y.; Akbulut, M.; Alig, A.; Carver, G.; Greene, W.; Kristiansen, K.; Meyer, E.; Pesika, N.; Rosenberg, K.; Zeng, H. *Reports Prog. Phys.* **2010**, *73* (3).
(26) Dobbs, H. A.; Kaufman, Y.; Scott, J.; Kristiansen, K.; Schrader, A. M.; Chen, S. Y.; Duda, P.; Israelachvili, J. N. *Adv. Eng. Mater.* **2018**, *20* (2), 1.
(27) Hu, B.; Trébosc, J.; Amoureux, J. P. *J. Magn. Reson.* **2008**, *192* (1), 112.
(28) Iuga, D.; Schäfer, H.; Verhagen, R.; Kentgens, A. P. M. *J. Magn. Reson.* **2000**, *147* (2), 192.
(29) Elena, B.; de Paëpe, G.; Emsley, L. *Chem. Phys. Lett.* **2004**, *398* (4–6), 532.
(30) Fung, B. M.; Khitrin, A. K.; Ermolaev, K. **2000**, *101*, 97.

Chapter 7

Atomic-scale origins of oxygen reduction activity in non-precious-metal mesoporous Fe,N-carbon electrocatalysts with high N contents

Adapted from: Z. J. Berkson, S. Becwar, N. P. Zussblatt, N. A. Prisco, N. Fechler, C. Hunt, G. Menard, B. F. Chmelka, *in preparation*

7.1 Abstract

Detailed atomic-level analyses of the physical and chemical properties of conductive, high-N-content (10-30 wt%) carbons show significant differences for materials prepared without and with silica or mixed-salt mesoporous templating agents, which influence their macroscopic electrochemical properties. The materials were synthesized by condensation of cyclohexanehexone octahydrate and urea precursors, which form a low-temperature eutectic mixture above 341 K. *Ex-situ* X-ray diffraction, nuclear magnetic resonance (NMR) spectroscopy, Raman spectroscopy, and transmission electron microscopy analyses establish that, after condensation at temperatures of 1073 K, the materials exhibit graphitic properties. Solid-state two-dimensional (2D) $^{13}C\{^{15}N\}$ NMR analyses enable distinct types, distributions, and covalent bonding environments of nitrogen heteroatoms to be identified in the N-containing mesoporous carbon materials. Quantitative solid-state ^{13}C and ^{15}N NMR spectra and X-ray photoelectron spectroscopy (XPS) reveal that the quantities and types of heteroatom environments in the mesoporous carbon materials depend on the types of surface interactions with sacrificial templating agents during synthesis. Introduction of mesoporosity with either mesoporous silica or a mixture of NaCl-$ZnCl_2$ salts results in different

distributions of nitrogen environments, as determined by solid-state ^{15}N NMR spectroscopy. Notably, materials prepared by condensation in the presence of NaCl-$ZnCl_2$ mixtures as templating agents possess greater quantities of pyrazinic and pyridinic nitrogen environments that are associated with exposed edges of graphitic domains. The high-surface-area mesoporous materials also exhibit significant oxygen reduction electrocatalytic activities, exceeding the activity of Pt/C when 1.1 wt% Fe is also incorporated into the synthesis mixture. The electrocatalytic activities are correlated with the proportion of isolated pyridinic N sites and Fe_2N moieties, which are identified in the mesoporous Fe,N-carbon material by solid-state ^{15}N NMR and Mössbauer spectroscopy. Collectively, the analyses provide new insights into the compositions and properties of N-containing mesoporous carbon materials and the roles of surface interactions during synthesis on their macroscopic physical and catalytic properties.

7.2 Introduction

Carbon materials containing heteroatoms such as Fe and N have received significant attention in recent years as inexpensive and environmentally-inert materials for catalytic and electrochemical applications, such as electrodes,[1–3] electrocatalysts,[4–9] and catalyst supports.[10–13] These include materials for the electrochemical reduction of oxygen, which have been proposed as replacements for Pt-based catalysts at the cathode of fuel cells.[14–17] Due to the sluggish kinetics of the oxygen reduction reaction (ORR), high Pt loadings are typically required, which significantly increases the overall costs of fuel cells and have limited their applications.[18] N-containing carbon catalysts have been generally prepared by high-temperature condensation of macrocycles or small molecule precursors.[19,20] Although

inexpensive and scalable, such reactions are difficult to control and tend to result in materials with distributions of graphitic domain sizes[21] and distributions of the types, quantities, and locations of nitrogen moieties.[22] In addition, high-temperature condensation-based methods generally lead to low quantities of retained heteroatoms, such as nitrogen, that often introduce desired functional properties to the carbonized product materials.[23] Nevertheless, we recently reported the preparation of a high-N-content (28 wt% N) carbon material, which also exhibited a moderately high conductivity of 2.0 S/cm.[24] The molecular precursors used to synthesize this material, urea and cyclohexanehexone octahydrate, were shown to form a low-melting eutectic phase and cross-link into materials with N moieties that resist volatilization during condensation at elevated temperatures. These features allowed facile preparation of high-surface-area high-N-content porous carbon compared to previous templating approaches,[24] although the material compositions, structures, and electrocatalytic properties were not reported.

While the high N contents, high electrical conductivities, and high surface areas of the high-N-content carbon materials are expected to make them attractive for use as fuel cell electrocatalysts, much remains unknown regarding the active moieties that catalyze oxygen reduction. For example, in different N-containing carbon materials, pyrrolic nitrogen,[25] pyridinic nitrogen,[21,25,26] and/or graphitic nitrogen[27,28] species have been proposed as ORR active sites. In carbon-based electrocatalyst materials prepared with both Fe- and N-containing precursors, the role of Fe has also been widely debated, with some proposing that Fe atoms serve as catalysts for the formation of active nitrogen moieties,[29] or that Fe-containing moieties such as $Fe_2N_xC_y$[30] or porphyrinic planar FeN_4[17,31] species serve as electrocatalytic active sites. Overall, the disorder in heteroatom-containing carbon materials

has left the types and structures of the ORR active sites open to debate. Indeed, different active moieties may be present in different Fe,N-carbon materials as a result of different synthesis conditions and precursor compositions. Elucidating the types of heteroatom species in such materials is challenging, in part because scattering techniques such as wide-angle X-ray scattering and Raman spectroscopy provide limited insights into bonding environments of Fe and N heteroatoms, which tend to occupy distributions of local environments. X-ray absorption near-edge spectroscopy (XANES), is sensitive to the valence electron environment of transition metal ions, and has proven valuable in elucidating different Fe moieties in Fe,N-carbon materials when paired with density functional theory calculations,[31] though it is not able to resolve structural details for lighter elements like N and C. X-ray photoelectron spectroscopy (XPS), in principle, is sensitive to differences in the types of Fe and N environments that are present in N-containing carbon materials, but the small differences in binding energy associated with different nitrogen-containing moieties limit spectral resolution and reduce the confidence of assignments.[32] By contrast, solid-state nuclear magnetic resonance (NMR) spectroscopy is capable of distinguishing and quantifying molecular environments within complicated heterogeneous materials,[33–35] including materials with electrical conductivity,[36–38] and porous carbon materials.[39] For N-containing carbons prepared by high-temperature condensation, one-dimensional (1D) solid-state NMR has previously been used to monitor differences resulting from high-temperature syntheses and to identify potential ORR active sites,[40–43] but the generally low nitrogen contents and broad distributions of ^{15}N environments have resulted in low sensitivity and low resolution, even with isotopic enrichment in ^{15}N. The challenge of characterizing such

materials with solid-state NMR is further exacerbated by the presence of unpaired electrons, which can broaden and displace NMR signals.[44]

Here, we report the local environments of Fe and N active sites in high-surface-area mesoporous Fe,N-carbon materials with high heteroatom contents with combined Mössbauer spectroscopy, X-ray diffraction, electron microscopy, and solid-state one- (1D) and two-dimensional (2D) ^{15}N and $^{13}C\{^{15}N\}$ NMR spectroscopy. The combined analyses elucidate the macroscopic electrocatalytic properties of the material, and show that in the absence of Fe heteroatoms, the material possessing the greatest proportion of isolated pyridinic N sites exhibits the highest ORR activity. In the mesoporous materials containing both Fe and N heteroatoms, electrocatalytic activity correlates both to the presence of isolated pyridinic N sites as well as square-planar iron porphyrrinic environments, showing overall ORR activity may be improved by preparation of materials with a diversity of catalytically-active sites.

7.3 Results and discussion

7.3.1 Synthesis, surface compositions, and long-range order of mesoporous high-N-content carbon electrocatalysts

The mesoporous carbon materials containing N and Fe heteroatoms are prepared through high-temperature condensation at 1073 K of molecular precursors cyclohexanehexone, urea, and 1.1 wt% $FeCl_2$ in the presence of a mesopore directing agent, either SBA-15 mesoporous silica or a mixture of structure-directing salts, as depicted schematically in Fig. 7.1. Successful removal of the template materials to produce high-surface area mesoporous materials was confirmed by N_2 sorption measurements, transmission electron microscopy (TEM), and near-surface elemental analysis. The surface compositions of the mesoporous

Fe,N-containing carbon materials determined from XPS analyses are provided in Table 7.1. To investigate the types and distributions of N-containing moieties and their influences on ORR activity, carbon materials were prepared with and without Fe additive templated with NaCl-$ZnCl_2$ salt mixtures or SBA-15 mesoporous silica. After condensation at 1073 K, the mesoporous N-carbon materials without Fe consist of graphitic-like layers that are partially ordered, as evidenced by wide-angle X-ray diffraction (WAXS), Raman spectroscopy, and transmission electron microscopy (TEM) analyses (Fig. 7.2). The WAXS patterns of the mesoporous N-carbon materials exhibit broad reflections at 26° 2θ (*d*-spacings of 0.34 nm) that are indexable to the (*002*) stacking of aromatic moieties of graphitic carbon materials.[45] A second weaker reflection at 43° 2θ (*d*-spacing of 0.21 nm) corresponds to the superposition of the (*100*) and (*101*) graphitic planes.

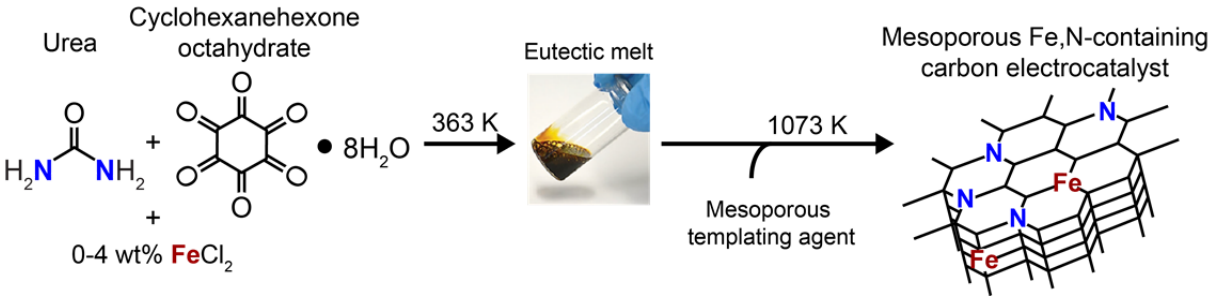

Figure 7.1. Schematic diagram of the synthesis of the mesoporous Fe,N-containing electrocatalysts.

Table 7.1. Near-surface elemental compositions of the high-N-content mesoporous carbon electrocatalysts materials, determined from XPS.

Material	*Near-Surface elemental composition [atom%]*					*N/C Ratio*
	C	N	O	Zn	Fe	
No template	73	23	4	-	0	0.32
SBA-15 silica template	74	16	11	-	0	0.22
NaCl/$ZnCl_2$ template	82	8	10	0	0	0.10
Fe-containing NaCl/$ZnCl_2$ template	70	4	21	0	5	0.06

The relative extents of graphitic order in the mesoporous N- and Fe,N-carbon materials are quantified by Raman spectroscopy, which is sensitive to both ordered and disordered aromatic domains. The Raman spectra (Figure 1c,d) of the N-carbon materials with mesoporosity templated by mesoporous SBA-15 silica and $ZnCl_2$-NaCl salt mixture both show broad regions of intensity at 1000-1700 cm^{-1} that can be deconvoluted into three Lorentzian-shaped bands. The bands are centered at 1570 cm^{-1} (*G*), 1350 cm^{-1} (*D*), and 1210 cm^{-1}, and are attributed respectively to the characteristic lattice-vibration mode of graphite,[47] bond vibrations in locally distorted graphitic lattices associated with heteroatom or edge/surface environments,[47,48] and stretching vibrations in polyene-type structures.[49] The broad linewidths of the *G* and *D* bands (*ca.* 150 and 200 cm^{-1} full-width-half-maximum, FWHM, respectively) are a manifestation of the high extent of N incorporation and associated distributions of graphitic environments in the materials.[50,51] The integrated intensity ratios (*D/G*) of the dominant Raman bands are approximate measure of the relative extents of graphitic ordering within the materials, with lower values being generally desirable.[47,49] For the *D/G* ratios for the salt- and SBA-15 silica-templated materials are 3.1 and 3.4, respectively, which are not as low as values near unity reported for other highly-graphitic N-containing materials,[52] but are similar to or less than those of other high-heteroatom-content (≥15 wt% N, O, and/or S combined) carbon materials.[53,54]

General results from the N_2 sorption measurements were previously reported,[24] but in brief, the isotherms of the SBA-15-templated and NaCl-$ZnCl_2$ templated carbon materials, exhibit Type-IV isotherms with H4 hystereses, indicative of a mixture of micro- and mesopores.[55] Consequently, the pore-size distributions, indicate that the porous materials prepared by either templating method possess populations of pores with diameters of both

1.0-1.5 nm and 2.5-4.0 nm. Brunauer-Emmett-Teller (BET)[56] analyses yielded estimated specific surface areas of the SBA-15 and NaCl-$ZnCl_2$-templated materials of 540 m^2/g and 1500 m^2/g, respectively.[24] Representative TEM images of the templated materials (Fig. 1e,f) show that the SBA-15-templated material exhibits local regions of aligned mesopores between domains with disordered pore structures. By contrast, the NaCl-$ZnCl_2$-templated material shows unaligned pores of various sizes. Any mesoscale order in the materials exists only locally within the mesoporous particles, as evidenced by the lack of reflections in the small-angle X-ray diffraction patterns of the materials.[57] No XPS peak associated with the presence of silicon is observed in the XPS spectrum of the SBA-15-templated material, indicating complete removal of the template. A small quantity (*ca.* 2 atom%) of zinc is observed in the spectrum of the material templated by a NaCl-$ZnCl_2$ mixture following the removal of the salts, but no chlorine or sodium signals are observed, indicating that the zinc remaining in the material is not in the form of residual $ZnCl_2$, but as ZnO,[46] consistent with WAXS results. The results show that the N-containing carbon materials can be prepared with different porous structures with high surface areas, and with little to no retention of the templating materials after their removal by chemical means. The overall heteroatom contents of the materials are high (as measured by XPS, Table 7.1), with the N-carbon materials templated by NaCl-$ZnCl_2$ and SBA-15 silica exhibiting near-surface atomic percentages of 11 and 16% for N, respectively, and 7 and 11% for O.

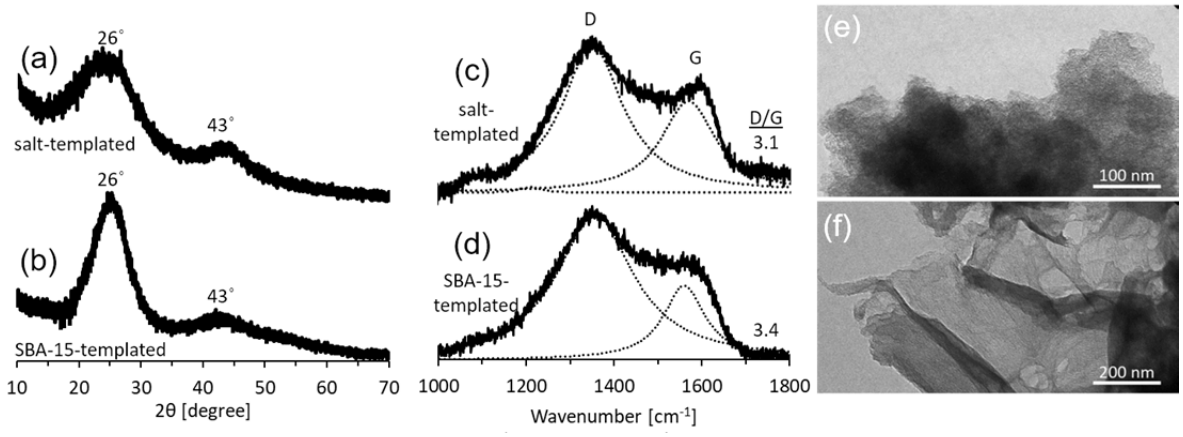

Figure 7.2. (a,b) Wide-angle X-ray diffraction patterns, (c,d) Raman spectra, and (e,f) representative TEM images of high-N-content mesoporous carbon materials synthesized with cyclohexanehexone and urea at a 1:3 molar ratio, templated with (a,c,e) a $ZnCl_2$-NaCl mixture and (b,d,f) SBA-15 mesoporous silica, and subsequently condensed at 1073 K. The asterisks in (a) indicate reflections indexed to a crystalline ZnO impurity.[46]

7.3.2 Electrocatalytic activities of mesoporous Fe,N-carbon electrocatalysts

Compositional and structural differences of the mesoporous high-N-content materials prepared using the two different templating materials yield very different electrocatalytic properties. The electrocatalytic ORR activities are manifested by polarization curves (Fig. 7.3) collected under alkaline conditions (0.1 M KOH) with oxygen saturation of the electrolyte. The silica-templated material delivers a higher current density than the NaCl-$ZnCl_2$ templated material at all examined potentials, with an onset potential of 0.85 V versus the reversible hydrogen electrode (RHE). The silica-templated material furthermore exhibits no saturated current-density plateau in the low potential region (i.e., no limiting current density), indicating an inefficient catalytic mechanism.[18] By comparison, the mesoporous N-containing carbon material templated with a NaCl-$ZnCl_2$ salt mixture exhibits a higher onset potential of 0.93 V versus RHE, manifesting its superior electrocatalytic ORR activity. At low potentials, the current density generated by the NaCl-$ZnCl_2$ templated material was greater in magnitude than the SBA-15 templated material and reached a limit imposed by

diffusion of oxygen atoms through the electrolyte,[58] indicating that this material has different and more effective catalytic sites. The different onset potentials and trends in currents at low potentials suggest that the SBA-15 templated N-carbon material is not a lower-performing catalyst material due solely to its somewhat lower specific surface area, but rather because of inherent differences in the electrocatalytic activity of the surface sites of the different materials. The performance of the mesoporous salt-templated N-carbon material approaches that of a Pt/C electrode material measured under the same conditions, which displays an onset potential of 1.0 V versus RHE and a limiting current of -4.0 mA/cm^2. A mesoporous salt-templated Fe,N-containing carbon material, prepared using 1.1 wt% $FeCl_2$ in the synthesis mixture, exhibits improved electrocatalytic properties compared to the analogous material prepared without Fe, with an onset potential of 1.0 V versus RHE and a limiting current of -4.9 mA/cm^2. The mesoporous salt-templated Fe,N-containing carbon material outperforms Pt/C for all potentials <0.9 V versus the RHE, indicating that this material is an exceptionally promising ORR electrocatalyst material.

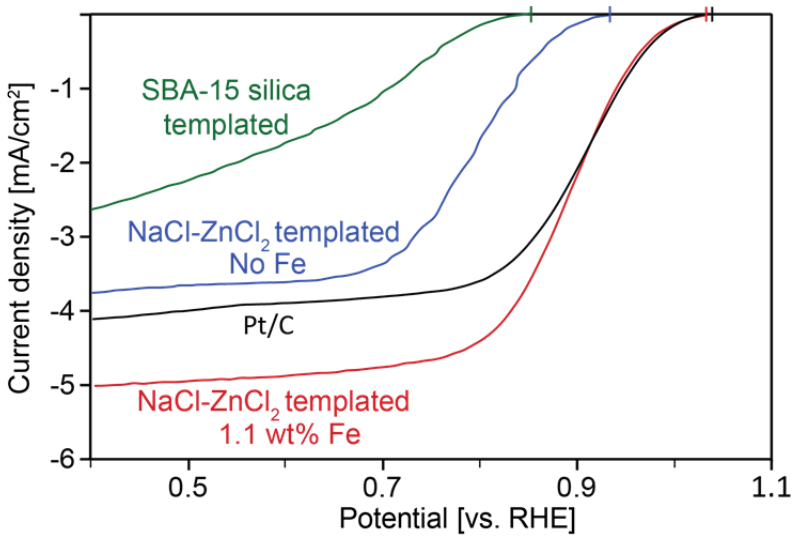

Figure 7.3. Polarization curves for the electrocatalytic reduction of oxygen (O_2) by cyclohexanehexone-urea-derived carbon materials condensed at 1073 K with mesoporosity templated by SBA-15 mesoporous silica (green) or a NaCl-$ZnCl_2$ mixture without (blue) or

with Fe (red). The performance of a conventional Pt/C catalyst (black) is shown for comparison. Curves were collected by staircase voltammetry with the materials placed on a rotating disk electrode within a 0.1 M KOH solution saturated with O_2 gas, and currents normalized by the geometric electrode area. Onset potentials are indicated by vertical bars along the upper axis.

While the Raman and WAXS results discussed above show that the N-containing carbon materials exhibit significant extents of graphitic order, more detailed molecular-level information is limited by the relatively low resolution of these analyses. By comparison, solid-state 1D and 2D ^{15}N, ^{13}C, and $^{13}C\{^{15}N\}$ MAS NMR analyses can detect, resolve, and correlate different types and distributions of ^{15}N and ^{13}C moieties in mesoporous high-N-content carbon materials. Previous solid-state NMR analyses of N-containing carbon materials have primarily relied on 1D NMR spectra,[40–43] the sensitivity and resolution of which are severely limited by low ^{15}N contents (even with isotopic enrichment), large inhomogeneous distributions of local ^{13}C and ^{15}N environments, and spectral broadening associated with the electrical conductivity of graphitic materials.[44] Nevertheless, 2D $^{13}C\{^{15}N\}$ NMR correlation spectra can provide dramatically improved spectral resolution by correlating the isotropic chemical shifts of different ^{13}C and ^{15}N nuclei via heteronuclear ^{13}C-^{15}N dipole-dipole couplings.

7.3.3 Local ^{15}N heteroatom environments in mesoporous high-N-content carbon electrocatalysts

The macroscopic electrocatalytic properties of high-N-content carbon materials are expected to be strongly influenced by the specific types and distributions of N-sites. To distinguish the different N heteroatom environments, powerful solid-state 2D $^{13}C\{^{15}N\}$ correlation NMR spectra are applied, which detect pairs of dipole-dipole ^{13}C and ^{15}N nuclei

in the mesoporous N-carbon materials and enable ^{13}C and ^{15}N environments to be resolved and correlated. The heteronuclear ^{13}C-^{15}N dipole-dipole couplings scale as the cube of the distance between the two nuclear spins, making these measurements principally sensitive to ^{13}C and ^{15}N nuclei that are directly bonded, with next-nearest neighbor interactions contributing negligible fractions of the overall signal intensity for the very short ^{13}C-^{15}N recoupling times used here (0.6 ms).[59] The 2D $^{13}C\{^{15}N\}$ *H*eteronuclear *M*ulti-*Q*uantum *C*orrelation (HMQC) MAS NMR spectra (Fig. 7.4) of the SBA-15 and NaCl-$ZnCl_2$ templated N-carbon materials selectively detect and correlate ^{13}C species which are dipole-dipole coupled to proximate (<0.5 nm) ^{15}N nuclei. The 2D NMR spectra are presented as 2D contour maps with ^{13}C and ^{15}N frequencies (Hz/MHz or ppm) on the horizontal and vertical axes, respectively, where correlated signal intensities manifest the interactions and proximities of dipole-dipole coupled ^{13}C-^{15}N spin pairs, enabling the ^{15}N NMR signals from different N-containing moieties in the materials to be resolved and assigned.

The choice of mesoporous templating agent crucially influences the types and distributions of heteroatom species in the mesoporous N-containing carbon materials, as shown by comparison of the 2D $^{13}C\{^{15}N\}$ HMQC spectra of the N-carbon materials prepared with different templating agents. The 2D $^{13}C\{^{15}N\}$ HMQC spectrum of the NaCl-$ZnCl_2$ templated N-carbon material shows broad correlated signal intensities at 140-180 ppm in the ^{15}N dimension and 110-145 ppm in the ^{13}C dimension (Fig. 7.4a, blue shaded region) that are assigned to ^{15}N atoms in graphitic environments.[60] Correlated signals at 230-250 ppm in the ^{15}N dimension and 135-155 ppm in the ^{13}C dimension (yellow shaded region) arise from ^{15}N species in pyridinic moieties that are relatively isolated.[61] These isolated pyridinic sites are expected to be associated with surfaces and edges of the mesoporous carbon material,

consistent with the materials higher surface area and lower N content relative to the SBA-15-silica templated N-carbon material. The correlated signal at 260-290 ppm in the ^{15}N dimension and 135-145 ppm in the ^{13}C dimension (red shaded region) is assigned to pyridinic or pyrazinic moieties containing ^{15}N atoms that are relatively close (within 2 bond distances) to other ^{15}N atoms.[60,62] Interestingly, the ^{15}N signals at 260-290 ppm from pyridinic/pyrazinic ^{15}N species are also correlated to ^{13}C signals at 120-130 ppm (green shaded region) from graphitic ^{13}C species, which establishes that a subset of the pyridinic/pyrazinic ^{15}N species are bonded to graphitic ^{13}C atoms that are also bonded to ^{15}N atoms in graphitic environments. In general, the ^{15}N signals in the 2D spectrum are broader (30-50 ppm FWHM) relative to the correlated ^{13}C signals (15-25 ppm FWHM), reflecting the sensitivity of ^{15}N nuclei to their local chemical and electronic environments. The different types of ^{15}N species in the NaCl-$ZnCl_2$ salt-templated material are quantified by integration of the relative signal intensities in the quantitative single-pulse ^{15}N MAS NMR spectrum (Fig. 7.4b), which shows that 41% of the ^{15}N heteroatoms are in pyridinic/pyrazinic environments, 29% in isolated pyridinic environments, and 30% in graphitic environments. The different types and bonding environments of the mesoporous salt-templated N-carbon material are shown in the schematic cartoon below Fig. 7.4a, consistent with the correlated signal intensities in the 2D spectrum.

By comparison to the NaCl-$ZnCl_2$-templated material, the SBA-15 silica material exhibits fewer isolated pyridinic ^{15}N sites, with broader distributions of graphitic ^{15}N environments. The 2D $^{13}C\{^{15}N\}$ HMQC spectrum (Fig. 7.4c) of the silica-templated N-containing carbon material shows a broad distribution of correlated signal intensity with partially-resolved intensity maxima at 160 ppm in the ^{15}N dimension and 115 and 130 ppm in

the ^{13}C dimension, which are assigned respectively to pyrrolic (purple shaded region) and graphitic (blue shaded region) nitrogen-containing moieties. A region of correlated signal intensity at 230-270 ppm in the ^{15}N dimension and 140-160 ppm in the ^{13}C dimension is assigned to pyridinic nitrogen-containing moieties (red shaded region). Though there are correlated signals with ^{15}N shifts in the 230-250 ppm frequency region associated with isolated pyridinic ^{15}N species, no signals in this region are resolved for the SBA-15-silica templated N-carbon material. Therefore, the pyridinic species in this material occupy broad distributions, with only small quantities of isolated pyridinic species that cannot be resolved. A correlated signal intensity at 250-280 ppm in the ^{15}N dimension and 125-135 ppm in the ^{13}C dimension (lower green shaded region) arises from pyridinic/pyrazinic ^{15}N atoms that are additionally bonded to ^{13}C atoms in graphitic moieties. Similarly, a correlated signal intensity at 140-190 ppm in the ^{15}N dimension and 145-160 ppm in the ^{13}C dimension (upper green shaded region) indicates that a subset of the ^{15}N atoms in pyrrolic and/or graphitic moieties are also within sub-nanometer proximity to ^{13}C atoms in pyrazinic/pyridinic moieties. Integration of the quantitative 1D single-pulse ^{15}N spectrum of the SBA-15-silica templated N-carbon material (Fig. 7.4d) shows that 39% of the ^{15}N heteroatoms are in pyridinic or pyrazinic moieties and 53% in graphitic or pyrrolic moieties, with 8% in isolated pyridinic environments. Overall, the solid-state 1D and 2D $^{13}C\{^{15}N\}$ and ^{15}N NMR analyses resolve, identify, and quantify the different types of ^{15}N heteroatoms present in mesoporous high-N-content carbon materials, and clearly show that interactions between the carbonaceous materials and the template during high-temperature condensation can significantly alter both the overall compositions and heteroatom distributions of the resultant heteroatom-containing carbon materials.

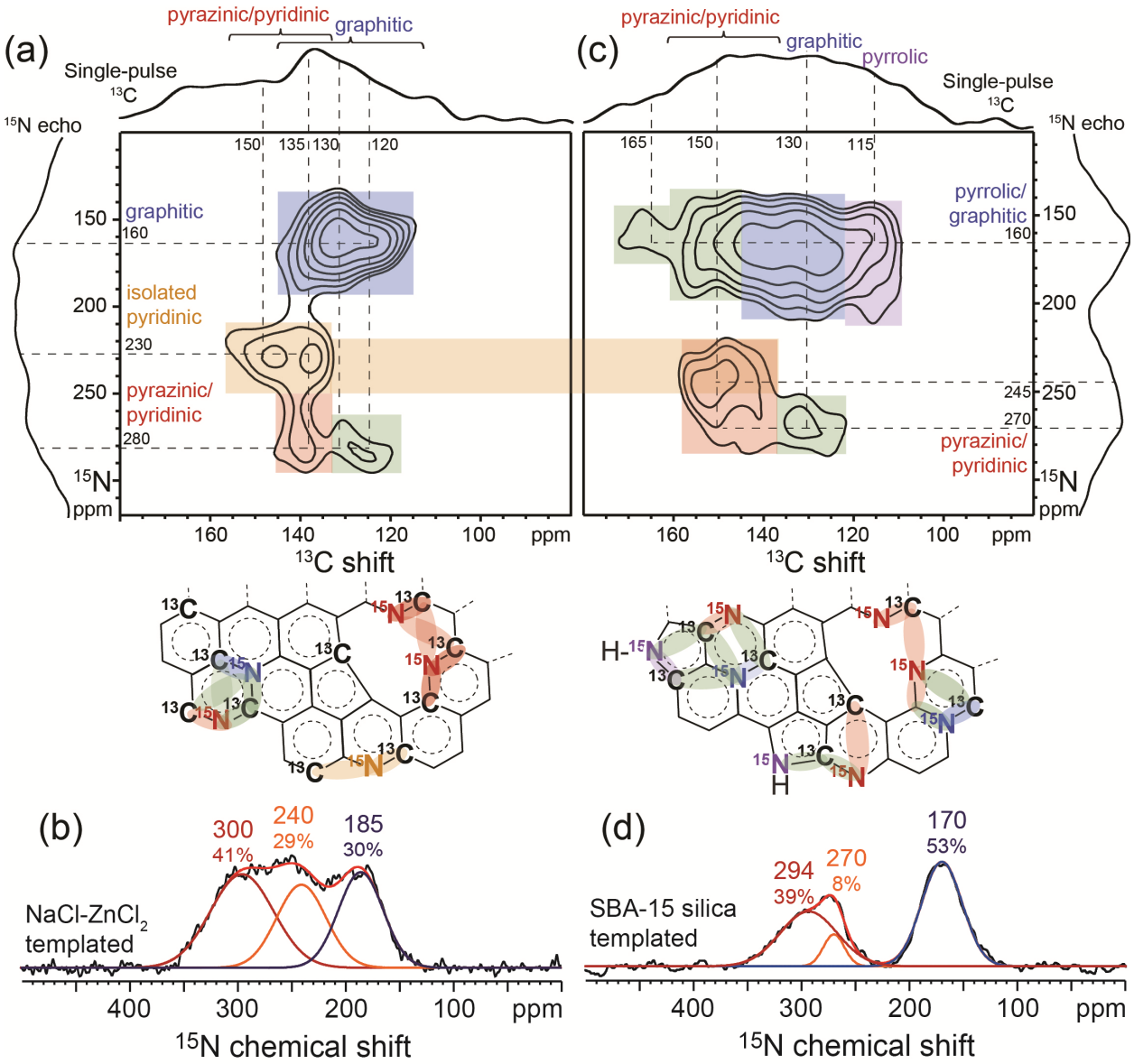

Figure 7.4. Solid-state (a,b) 2D $^{13}C\{^{15}N\}$ NMR correlation spectra and (c,d) quantitative 1D single-pulse ^{15}N MAS NMR spectra of high-N-content carbon materials synthesized with cyclohexanehexone and ^{13}C,^{15}N-enriched urea at a 1:3 molar ratio and subsequently condensed in a Nitrogen atmosphere at 1073 K with mesoporosity templated by (a,c) a $ZnCl_2$-NaCl salt mixture or (b,d) SBA-15 mesoporous silica. The 2D NMR spectra in (a,b) were acquired at 9.4 T, 95 K, and 8 kHz MAS. 1D ^{13}C and ^{15}N spectra acquired under the same conditions are shown along the horizontal and vertical axes, respectively. The red, blue, and purple shaded regions indicate correlated signals arising respectively from pyrazinic/pyridinic, graphitic, and pyrrolic moieties present in the high-N-content mesoporous carbon materials as shown in the corresponding schematic cartoons below the 2D spectra, while the green shaded regions indicate correlated signals arising from proximate pyrazinic or pyridinic and pyrrolic or graphitic moieties. The 1D ^{15}N spectra in (c,d) were acquired at 295 K, 11.7 T, and 10 kHz MAS. For all of the solid-state NMR measurements the materials were diluted by a 1:3 ratio with KBr.

From the solid-state NMR analyses, the primary compositional difference between the SBA-15 and NaCl-$ZnCl_2$ templated N-carbon materials is the presence of significant quantities of isolated (edge) pyridinic nitrogen atoms in the NaCl-$ZnCl_2$ templated material. This result, along with the electrocatalytic performance tests in Fig. 7.3, suggests that isolated pyridinic N species are likely the primary active site for the oxygen reduction reaction in N-containing carbon materials, as had been suggested by recent work using model materials.[21]

7.3.4 Structure and ^{15}N and ^{57}Fe heteroatom environments of mesoporous Fe,N-carbon electrocatalysts

In addition to exhibiting improved electrocatalytic properties, the mesoporous salt-templated Fe,N-carbon material exhibits a higher overall extent of graphitization. Fe heteroatoms are introduced into the salt-templated N-containing mesoporous carbon material by addition of $FeCl_2$ salt into the molecular precursor mixture prior to melting at 90 °C, addition of the NaCl-$ZnCl_2$ template mixture, and subsequent high-temperature pyrolysis. Comparison of materials prepared with different Fe contents shows that the best electrocatalytic properties are obtained for 1.1 wt% $FeCl_2$ in the synthesis mixture,[57] which yields *ca.* 0.1 wt% Fe in the final material from XPS elemental analysis. The WAXS pattern of the Fe,N-containing salt templated material (Fig. 7.5a) shows overlapping narrow and broad reflections at 26° 2θ (*d* spacing of 0.34 nm) from long-range ordering of the (002) plane of graphitic-like carbon sheets in the mesoporous Fe,N-carbon material, indicating that the material contains coexisting domains with different extents of long-range ordering. Similarly to the mesoporous N-carbon materials prepared without Fe discussed above, the

WAXS pattern of the mesoporous Fe,N-carbon material also exhibits a weak second reflection at 43° (*d*-spacing of 0.21 nm) from the superposition of the (*100*) and (*101*) graphitic planes,[45] corroborating a greater extent of graphitization. However, signals from ZnO and graphitic oxide moieties are no longer distinguishable as they were in the non-Fe containing material, consistent with the graphitizing property of Fe reducing the extent of impurities within the material. The Raman spectrum of the same material (Fig. 7.5b) is deconvoluted into two Lorentzian lines at 1360 and 1580 cm^{-1}, assigned to the *D* and *G* Raman bands, respectively. The *D*/*G* intensity ratio for the mesoporous salt-templated Fe,N-carbon material is ~2.7, corroborating the higher extent of graphitization in this material compared to the analogous material prepared without Fe, consistent with Fe acting as a graphitization agent during the high-temperature condensation of the molecular precursors.

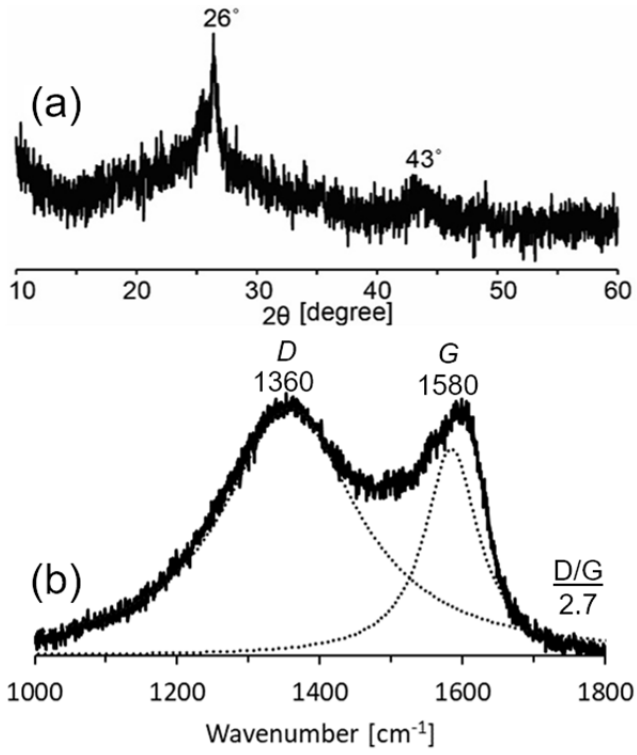

Figure 7.5. (a) X-ray diffraction pattern and (b) Raman spectrum of the mesoporous Fe,N-containing carbon material synthesized with cyclohexanehexone and urea at a 1:3 molar ratio

with 1.1 wt% Fe in the synthesis mixture, templated with a $ZnCl_2$-NaCl mixture and subsequently condensed at 1073 K.

Information on the local environments of the ^{57}Fe and ^{15}N heteroatoms in mesoporous Fe,N-containing carbon materials is accessed directly by solid-state ^{15}N NMR spectroscopy and ^{57}Fe Mössbauer spectroscopy. Solid-state NMR analyses of Fe-containing carbon materials are exceptionally rare due to the complicating influences of paramagnetic Fe^{3+} species on proximate ^{13}C or ^{15}N species, which introduce unpaired electrons into the material that couple with nearby nuclear spins. Such electron-nuclear couplings may substantially broaden and/or displace the ^{13}C or ^{15}N NMR signals associated with the ^{13}C or ^{15}N environments near the unpaired electrons.[63,64] Resolving NMR signals from these environments is challenging, but may be enabled through paramagnetic-NMR techniques including very fast sample rotation and relaxation-resolved NMR spectroscopy.[65–67] Relaxation-resolved NMR measurements exploit the very rapid spin-lattice (T_1) relaxation of nuclear spins experiencing paramagnetic interactions, which are often orders-of-magnitude shorter than the diamagnetic analogue. The paramagnetic relaxation enhancement (PRE) effect enables the NMR signals associated with species undergoing very rapid paramagnetic relaxation to be resolved.[64]

The mesoporous salt-templated Fe,N-carbon material contains different types of ^{15}N environments that are near and far from paramagnetic Fe species. The fully relaxed solid-state 1D ^{15}N NMR spectrum of mesoporous salt-templated Fe,N-carbon (Fig. 7.6a, top) shows overlapping ^{15}N signals with partially-resolved maxima at 300, 250, and 180 ppm, which are assigned respectively to pyridinic/pyrazinic, isolated pyridinic, and graphitic ^{15}N environments on the basis of their shift positions and the 2D $^{13}C\{^{15}N\}$ NMR correlation

spectrum of the analogous material without Fe discussed above. The 1D ^{15}N NMR spectrum shows that the types and distributions of ^{15}N environments in the mesoporous salt-templated Fe,N-carbon material are largely unaffected by the incorporation of Fe heteroatoms compared to the analogous material containing no Fe. However, the relaxation-resolved 1D ^{15}N NMR spectrum acquired with a very short relaxation delay (0.01 s) selectively enhances and resolves a narrow (10 ppm FWHM) ^{15}N signal at 300 ppm. This signal is assigned on the basis of its shift position, analyses of the ^{15}N T_1 relaxation times, and comparison to theoretical equations for paramagnetic relaxation to ^{15}N atoms that are directly bonded to Fe atoms in highly ordered Fe-N environments.

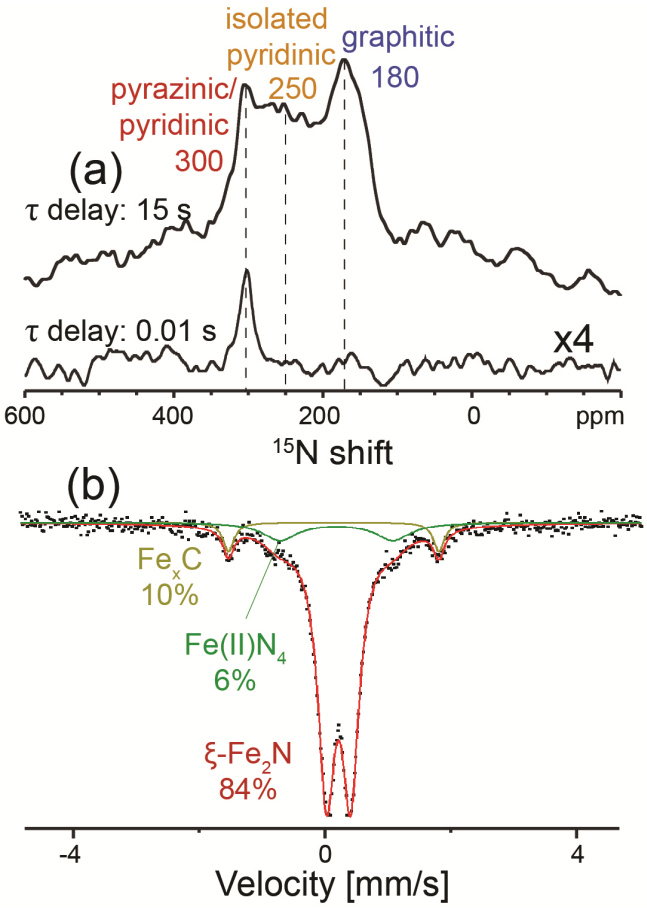

Figure 7.6. (a) Solid state 1D ^{15}N echo spectra of acquired with different relaxation τ delay times of 15 s (top) and 0.01 s (bottom) and (b) ^{57}Fe Mössbauer spectrum (black points) of Fe,N-containing mesoporous carbon material synthesized with 1.1 wt% $FeCl_2$ and

cyclohexanehexone and urea at a 1:3 molar ratio, templated with a $ZnCl_2$-NaCl mixture and subsequently condensed at 1073 K. The solid-state ^{15}N NMR spectra were acquired at 9.4 T, 95 K, and 8 kHz MAS, and the ^{57}Fe Mössbauer spectrum was acquired at 298 K.

The presence of Fe-N bonds in the mesoporous Fe,N-carbon material is corroborated by complementary ^{57}Fe Mössbauer spectroscopy (Fig. 7.6b), which is sensitive to the covalent bonding environments of ^{57}Fe nuclei. The ^{57}Fe Mössbauer spectrum of the mesoporous Fe,N-carbon material is deconvoluted into three doublets arising from three distinct ^{57}Fe environments, which are assigned on the basis of their isotropic shifts and quadrupolar splitting parameters. Specifically, the majority (84%) of detected ^{57}Fe species are in ξ-Fe_2N environments,[68] which have also been recently identified in similar Fe-N-carbon electrocatalyst materials materials by high-resolution TEM analyses.[17] The weaker doublet signals are attributed to Fe_xC (orange, 10%)[68] and square-planar porphyrinic $Fe(II)N_4$ (green, 6%)[31] species. Overall, the solid-state ^{15}N NMR and ^{57}Fe Mössbauer spectroscopy analyses of the mesoporous salt-templated Fe,N-carbon material elucidate the presence of different types of Fe and N heteroatom active sites that are expected to contribute to the catalytic activity of the material. Specifically, the solid-state ^{15}N NMR analyses show that isolated pyridinic ^{15}N moieties are present in both the mesoporous salt-templated N- and Fe,N-carbon materials, which both exhibit high electrocatalytic performance for ORR, while the mesoporous SBA-15-silica-templated N-carbon material possesses few isolated pyridinic species and exhibits poor electrocatalytic performance. The solid-state ^{15}N NMR and ^{57}Fe Mössbauer spectra of the mesoporous salt-templated Fe,N-containing material furthermore each provide direct and complementary evidence for Fe-N covalent bonds. The high performance of the mesoporous salt-templated Fe,N-carbon material is therefore explained by the diversity of heteroatom sites, and specifically isolated pyridinic nitrogen, ξ-Fe_2N, and

$Fe(II)N_4$ environments, each of which is expected to be associated with active sites for the oxygen reduction reaction.

7.4 Conclusions

High-nitrogen-content carbon materials have been synthesized through high-temperature condensation of molecular precursors with mesoscale porosity introduced by sacrificial templating materials. The materials exhibit high N contents, high electrical conductivities, and high electrocatalytic activities which make them promising for uses in electrochemical devices and as electrocatalysts. Solid-state ^{13}C and ^{15}N NMR analyses of the materials, with complementary XPS, Raman spectroscopy, WAXS diffraction, and ^{57}Fe Mössbauer spectroscopy reveal the compositions and structures of the mesoporous Fe,N-carbon materials. Notably, by correlating electrocatalytic oxygen reduction activities with molecular compositions determined by advanced solid-state 2D $^{13}C\{^{15}N\}$ heteronuclear correlation NMR analyses show that isolated edge pyridinic nitrogen sites are the likely promoters of ORR activity of these N-containing carbon catalysts. The quantity of these catalytically-relevant nitrogen sites is influenced by surface interactions during synthesis associated with the different surface compositions of the mesoporous silica or mixed-salt templating agents. Selection of templating agent is therefore a means to influence the surface composition and corresponding macroscopic properties of mesoporous N-containing carbon electrocatalysts. Incorporation of Fe heteroatoms further improves the electrocatalytic properties of the material, to the point where they are equivalent to or exceed standard Pt/C electrode materials under the conditions studied here. Analyses of ^{57}Fe Mössbauer and relaxation-resolved solid-state ^{15}N NMR spectroscopy indicate that the high electrocatalytic activities of

the mesoporous Fe,N-carbon material arise from the high quantities of square planar Fe-N porphyrin structures in addition to isolated edge pyridinic nitrogen sites. These insights into the types of nitrogen sites in ORR catalysts are expected to aid in the further development of non-precious-metal-containing catalysts, by providing new criteria for the rational design of new heteroatom-containing carbon materials.

7.5 Materials and methods

Materials syntheses

Mesostructured silica (SBA-15) was prepared according to a previously reported procedure.[69] Briefly, 8.0 g of poly(ethyleneoxide)$_{20}$-poly(propylene-oxide)$_{70}$-poly(ethyleneoxide)$_{20}$ triblock copolymer (Pluronic® P123, Sigma-Aldrich) were dissolved in 60 ml of deionized water. To this solution was added 17 g of tetraethoxysilane and 240 ml of 3 M HCl, and the combined solution was stirred vigorously at room temperature for 10 min. The solution was then stirred for 20 h at 313 K, placed in a 363 K oven without stirring for 2 days, vacuum-filtered, and then calcined in air at 823 K to remove the structure-directing surfactant species to obtain the mesoporous silica powder.

Mesoporous N- and Fe,N-carbon materials were synthesized from urea and cyclohexanehexone as described previously.[24] Briefly, urea (99%, Sigma-Aldrich) and cyclohexanehexone octahydrate (97%, Sigma-Aldrich) were mixed in a 3:1 stoichiometric ratio, such that the total numbers of carbonyl groups on the cyclohexanehexone octahydrate molecules and amine groups on the urea molecules were equal. The mixture of urea and cyclohexanehexone octahydrate was heated to 341 K to form the eutectic melt, and then to 363 K to promote cross-linking. The cross-linked solid was then condensed by heating at a

ramp rate of 2.5 K/min to 1073 K under flowing N_2 gas and held at the target temperature for 60 min. Mesoporosity was introduced according to the templating method originally reported by Ryoo, *et al*.,[70,71] modified for use with the eutectic precursor melt. In this method, previously prepared SBA-15 mesoporous silica powder was mixed into the urea and cyclohexanehexone octahydrate mixture (in a ratio 0.85 g SBA-15 per gram of mixture) after it had been heated to form a eutectic melt, but before subsequent heating to promote cross-linking. The composite silica and cross-linked solid material was then condensed as previously described. Silica was dissolved from the composite by stirring overnight in 1 M NaOH, resulting in N-containing mesoporous carbon solids with an inverse structure of the mesoporous silica template (e.g., SBA-15). Alternatively, mesoporous N-containing carbon materials were prepared by using a "salt-templating" method, where a mixture of sodium chloride and zinc chloride salts serves as the sacrificial templating material.[72] After the organic precursors were heated to form a eutectic melt at 341 K, but before cross-linking at 363 K, a physical mixture of ground 35 mol% NaCl and 65 mol% $ZnCl_2$ was added with a 1:3 weight ratio of organic precursors to salts. Following heat treatment, the composite products were ground into a powder, and the salts removed by washing overnight in distilled water. Following the removal of either template material, the resultant mesoporous high-N-content carbon products were dried in a vacuum oven at 323 K. Versions of the materials were also prepared by using ^{13}C,^{15}N-enriched urea (99 atom% ^{13}C, 99 atom% ^{15}N, Sigma Aldrich) under otherwise identical conditions to improve ^{13}C and ^{15}N signal sensitivity for solid-state nuclear magnetic resonance (NMR) spectroscopy.

X-ray Powder Diffraction

Graphitic ordering in the materials was assessed by using wide-angle X-ray diffraction (XRD) and Raman spectroscopy. XRD patterns were recorded over a 2θ range of 10° to 70° in increments of 0.02° using a Bruker D8 ADVANCE diffractometer with Cu K_α radiation.

Raman spectroscopy

Raman measurements were made using a Horiba Jobin Yvon T64000 confocal microscope 100X operating in single mono mode with 1800 groove/mm grating and LN2-cooled CCD detector, 488 nm excitation, and 20 s acquisition time. Raman data were processed with linear baseline subtraction and deconvoluted into Lorentzian lineshapes.

Electron Microscopy

To assess mesostructural order, high-resolution transmission electron micrograms were acquired on a double Cs corrected JEOL ARM 200F instrument operating at 200 kV. TEM samples were prepared by dispersing material in ethanol and drop-casting the solution onto a carbon-coated copper grid.

Mössbauer spectroscopy

The atomic environments of ^{57}Fe species in mesoporous Fe,N-carbon materials were established by ^{57}Fe Mössbauer measurements. Measurements were performed on a MS6 Mössbauer Spectroscopy System from SEE CO with a ^{57}Co(Rh) source. Measurements were acquired at 298 K under a nitrogen atmosphere using 50 mg of sample in HDPE sample cups. Run time for each measurement was 24 h. The isomer shift and Doppler velocity were calibrated against iron foil.

Solid-state NMR spectroscopy

Solid-state ^{13}C and ^{15}N magic-angle-spinning (MAS) NMR spectroscopy was used to analyze the local environments of ^{13}C and ^{15}N moieties in the N- and Fe,N-carbon materials synthesized from a 1:3 molar ratio of cyclohexanehexone octahydrate and uniformly ^{13}C,^{15}N-enriched urea. Single-pulse ^{15}N MAS NMR spectra were acquired on a Bruker AVANCE III spectrometer with an 18.8 T narrow-bore superconducting magnet using a Bruker 3.2 mm Tri-Gamma HXY triple-resonance MAS probehead. Unless otherwise specified, all of the ^{13}C and ^{15}N experiments were performed at room temperature with 100 kHz ^{1}H decoupling, using zirconia rotors, Kel-F® caps, and under MAS conditions of 10 kHz. Chemical shifts were referenced to their respective values in uniformly ^{13}C,^{15}N-enriched glycine powder, with ^{13}C chemical shifts referenced to the carboxyl carbon at 172.7 ppm (tetramethylsilane at 0 ppm) and ^{15}N chemical shifts referenced to 33.4 ppm (liquid ammonia at 0 ppm).[73] The conductive materials were diluted with KBr at a sample:KBr ratio of 1:3 w/w. The KBr served as both an internal temperature probe[74] and to reduce undesirable sample heating that may arise from rapid rotation of conductive samples in the high magnetic field required for the NMR measurements.[75] The ^{15}N recycle delay times were optimized to ensure full spin-lattice relaxation of the ^{15}N nuclei for the quantitative 1D single-pulse ^{15}N spectra.

Solid-state two-dimensional (2D) $^{13}C\{^{15}N\}$ *H*eteronuclear *M*ultiple *Q*uantum *C*oherence (HMQC) experiments[76,77] were used to correlate isotropic ^{13}C and ^{15}N chemical shifts of ^{13}C and ^{15}N nuclei that are dipolar-coupled through space over sub-nanometer distances. The 2D *J*-mediated $^{13}C\{^{15}N\}$ HMQC NMR spectra in Figures 7.3.4 were acquired at 8 kHz MAS on a Bruker ASCEND 400 DNP-NMR spectrometer with a 9.4 T superconducting magnet operating at 400.20, 100.64, and 40.56 MHz for ^{1}H, ^{13}C, and ^{15}N nuclei, respectively, and

equipped with a variable-temperature 3.2 mm HXY MAS probehead. The temperature measured in the MAS gas stream nearest to the stator was 95 K, and the actual sample temperature was estimated from ^{79}Br T_1 relaxation measurements to be *ca*. 99 K. The 2D ^{13}C{^{15}N} HMQC spectra were acquired using 512 transients, with 16-22 t_1 increments in the indirect dimension, 0.6 ms of $SR4_2^{11}$ dipolar recoupling to reintroduce the ^{13}C-^{15}N dipole-dipole couplings,[77,78] and experimentally-optimized recycle times of 7-10 s for maximum signal sensitivity.

Electrocatalytic activity tests

Oxygen reduction activities of the porous high-N-content carbon materials were determined by conducting staircase voltammetry measurements with a BioLogic VSP potentiostat. A three-electrode configuration was used with a rotating-disk electrode with a 5.61 mm diameter glassy carbon disk used as the working electrode, and with a graphite rod and an Ag/AgCl (3 M NaCl) electrode as the counter and reference electrodes, respectively. Catalyst inks were prepared by dispersing 7.4 mg of high-N-content carbon into a mixture composed of 250 μL of milli-Q-water, 750 μL of isopropanol, and 60 μL of 5 wt% Nafion™ solution. The suspension was sonicated for 60 min to form a homogeneous ink, and then 20 μL of catalyst ink were deposited dropwise onto the glassy carbon electrode and dried at 40 °C to yield a catalyst loading of 600 μg/cm^2. Staircase voltammetry tests were conducted within an O_2-saturated 0.1 M KOH solution. During the tests, the working electrode was rotated at a rate of 900 rpm using a Modulated Speed Rotator (Pine Research Instrumentation) to promote mixing of the electrolyte and reduce concentration gradients in the bulk fluid in contact with the catalyst layer. Following the measurements, the oxygen

reduction currents were scaled by the area of the glassy carbon electrode to obtain current densities, and the potentials were converted to the reversible hydrogen electrode (RHE) scale.

7.6 References

(1) Zhang, L. L.; Zhao, X. S. *Chem. Soc. Rev.* **2009**, *38*, 2520.
(2) Zhao, Y.; Hu, C.; Hu, Y.; Cheng, H.; Shi, G.; Qu, L. *Angew. Chemie - Int. Ed.* **2012**, *51* (45), 11371.
(3) Xu, Y.; Lin, Z.; Zhong, X.; Huang, X.; Weiss, N. O.; Huang, Y.; Duan, X. *Nat. Commun.* **2014**, *5*.
(4) Gong, K.; Du, F.; Xia, Z.; Durstock, M.; Dai, L. *Science* **2009**, *323* (5915), 760.
(5) Zhao, Y.; Nakamura, R.; Kamiya, K.; Nakanishi, S.; Hashimoto, K. *Nat. Commun.* **2013**, *4*, 1.
(6) Liang, H.-W.; Zhuang, X.; Brüller, S.; Feng, X.; Müllen, K. *Nat. Commun.* **2014**, *5*, 4973.
(7) Shao, M.; Chang, Q.; Dodelet, J.-P.; Chenitz, R. *Chem. Rev.* **2016**, *116* (6), 3594.
(8) Seh, Z. W.; Kibsgaard, J.; Dickens, C. F.; Chorkendorff, I.; Nørskov, J. K.; Jaramillo, T. F. *Science.* **2017**, *355* (6321).
(9) Lu, Z.; Chen, G.; Siahrostami, S.; Chen, Z.; Liu, K.; Xie, J.; Liao, L.; Wu, T.; Lin, D.; Liu, Y.; Jaramillo, T. F.; Nørskov, J. K.; Cui, Y. *Nat. Catal.* **2018**, *1*, 156.
(10) Joo, S. H.; Choi, S. J.; Oh, I.; Kwak, J.; Liu, Z.; Terasaki, O.; Ryoo, R. *Nature* **2001**, *412* (6843), 169.
(11) Lefèvre, M.; Proietti, E.; Jaouen, F.; Dodelet, J. P. *Science.* **2009**, *324* (5923), 71.
(12) He, L.; Weniger, F.; Neumann, H.; Beller, M. *Angew. Chemie - Int. Ed.* **2016**, *55* (41), 12582.
(13) Sahoo, B.; Surkus, A. E.; Pohl, M. M.; Radnik, J.; Schneider, M.; Bachmann, S.; Scalone, M.; Junge, K.; Beller, M. *Angew. Chemie - Int. Ed.* **2017**, *56* (37), 11242.
(14) Yang, W.; Fellinger, T.-P.; Antonietti, M. *J. Am. Chem. Soc.* **2011**, *133* (2), 206.
(15) Li, Y.; Zhou, W.; Wang, H.; Xie, L.; Liang, Y.; Wei, F.; Idrobo, J.-C.; Pennycook, S. J.; Dai, H. *Nat. Nanotechnol.* **2012**, *7* (6), 394.
(16) Chung, H. T.; Won, J. H.; Zelenay, P. *Nat. Commun.* **2013**, *4*, 1922.
(17) Chung, H. T.; Cullen, D. A.; Higgins, D.; Sneed, B. T.; Holby, E. F.; More, K. L.; Zelenay, P. *Science.* **2017**, *357* (6350), 479.
(18) Othman, R.; Dicks, A. L.; Zhu, Z. *Int. J. Hydrogen Energy* **2012**, *37* (1), 357.
(19) Zhu, Y. P.; Guo, C.; Zheng, Y.; Qiao, S.-Z. *Acc. Chem. Res.* **2017**, *50*, 915−923.
(20) Dombrovskis, J. K.; Palmqvist, A. E. C. *J. Power Sources* **2017**, *357*, 87.
(21) Guo, D.; Shibuya, R.; Akiba, C.; Saji, S.; Kondo, T.; Nakamura, J. *Science* **2016**, *351* (6271), 361.
(22) Wang, D.-W.; Su, D. *Energy Environ. Sci.* **2014**, *7* (2), 576.
(23) Wang, X.; He, Z.; Shi, Y.; Li, B. *J. Electrochem. Soc.* **2017**, *164* (6), F620.
(24) Fechler, N.; Zussblatt, N. P.; Rothe, R.; Schl??gl, R.; Willinger, M.-G. G.; Chmelka, B. F.; Antonietti, M.; Schlögl, R.; Willinger, M.-G. G.; Chmelka, B. F.; Antonietti, M. *Adv. Mater.* **2016**, *28* (6), 1287.
(25) Ding, W.; Wei, Z.; Chen, S.; Qi, X.; Yang, T.; Hu, J.; Wang, D.; Wan, L.-J.; Alvi, S. F.; Li, L. *Angew. Chemie - Int. Ed.* **2013**, *52* (45), 11755.
(26) Wu, J.; Ma, L.; Yadav, R. M.; Yang, Y.; Zhang, X.; Vajtai, R.; Lou, J.; Ajayan, P. M. *ACS Appl. Mater. Interfaces* **2015**, *7* (27), 14763.
(27) Liu, G.; Li, X.; Ganesan, P.; Popov, B. N. *Electrochim. Acta* **2010**, *55* (8), 2853.
(28) Lai, L.; Potts, J. R.; Zhan, D.; Wang, L.; Poh, C. K.; Tang, C.; Gong, H.; Shen, Z.; Lin, J.; Ruoff, R. S. *Energy Environ. Sci.* **2012**, *5* (7), 7936.

(29) Subramanian, N. P.; Li, X.; Nallathambi, V.; Kumaraguru, S. P.; Colon-Mercado, H.; Wu, G.; Lee, J. W.; Popov, B. N. *J. Power Sources* **2009**, *188* (1), 38.
(30) Tributsch, H.; Koslowski, U. I.; Dorbandt, I. *Electrochim. Acta* **2008**, *53* (5), 2198.
(31) Zitolo, A.; Goellner, V.; Armel, V.; Sougrati, M. T.; Mineva, T.; Stievano, L.; Fonda, E.; Jaouen, F. *Nat. Mater.* **2015**, *14* (9), 937.
(32) Dorjgotov, A.; Ok, J.; Jeon, Y.; Yoon, S. H.; Shul, Y. G. *J. Appl. Electrochem.* **2013**, *43* (4), 387.
(33) Zujovic, Z.; Webber, A. L.; Travas-Sejdic, J.; Brown, S. P. *Macromolecules* **2015**, *48* (24), 8838.
(34) Mao, K.; Kennedy, G. J.; Althaus, S. M.; Pruski, M. *Energy and Fuels* **2013**, *27* (2), 760.
(35) Wang, Z.; Opembe, N.; Kobayashi, T.; Nelson, N. C.; Slowing, I. I.; Pruski, M. *Carbon* **2018**.
(36) Leskes, M.; Kim, G.; Liu, T.; Michan, A. L.; Aussenac, F.; Dorffer, P.; Paul, S.; Grey, C. P. *J. Phys. Chem. Lett.* **2017**, *8* (5), 1078.
(37) Halat, D. M.; Dervişoğlu, R.; Kim, G.; Dunstan, M. T.; Blanc, F.; Middlemiss, D. S.; Grey, C. P. *J. Am. Chem. Soc.* **2016**, *138* (36), 11958.
(38) Yesinowski, J. P.; Berkson, Z. J.; Cadars, S.; Purdy, A. P.; Chmelka, B. F. *Phys. Rev. B* **2017**, *95* (23), 1.
(39) Pham, H. N.; Anderson, A. E.; Johnson, R. L.; Schwartz, T. J.; O'Neill, B. J.; Duan, P.; Schmidt-Rohr, K.; Dumesic, J. A.; Datye, A. K. *ACS Catal.* **2015**, *5* (8), 4546.
(40) Kuroki, S.; Nabae, Y.; Chokai, M.; Kakimoto, M. A.; Miyata, S. *Carbon* **2012**, *50* (1), 153.
(41) Baccile, N.; Laurent, G.; Coelho, C.; Babonneau, F.; Zhao, L.; Titirici, M.-M. *J. Phys. Chem. C* **2011**, *115*, 8976.
(42) Zhao, L.; Baccile, N.; Gross, S.; Zhang, Y.; Wei, W.; Sun, Y.; Antonietti, M.; Titirici, M. M. *Carbon* **2010**, *48* (13), 3778.
(43) Falco, C.; Sevilla, M.; White, R. J.; Rothe, R.; Titirici, M. M. *ChemSusChem* **2012**, *5* (9), 1834.
(44) Carrasco, P. M.; Grande, H. J.; Cortazar, M.; Alberdi, J. M.; Areizaga, J.; Pomposo, J. A. *Synth. Met.* **2006**, *156* (5–6), 420.
(45) Gierszal, K. P.; Jaroniec, M.; Kim, T.-W.; Kim, J.; Ryoo, R. *New J. Chem.* **2008**, *32*, 981.
(46) Yu, Z.-L. L.; Li, G.-C. C.; Fechler, N.; Yang, N.; Ma, Z.-Y. Y.; Wang, X.; Antonietti, M.; Yu, S.-H. H. *Angew. Chemie - Int. Ed.* **2016**, *55* (47), 14623.
(47) Tuinstra, F.; Koenig, L. *J. Chem. Phys.* **1970**, *53* (3), 1126.
(48) Herrmann, I.; Kramm, U. I.; Radnik, J.; Fiechter, S.; Bogdanoff, P. *J. Electrochem. Soc.* **2009**, *156* (10), B1283.
(49) Dippel, B.; Jander, H.; Heintzenberg, J. *Phys. Chem. Chem. Phys.* **1999**, *1* (20), 4707.
(50) Yang, Q.-H.; Hou, P.-X.; Unno, M.; Yamauchi, S.; Saito, R.; Kyotani, T. *Nano Lett.* **2005**, *5* (12), 2465.
(51) Podyacheva, O. Y.; Cherepanova, S. V.; Romanenko, A. I.; Kibis, L. S.; Svintsitskiy, D. A.; Boronin, A. I.; Stonkus, O. A.; Suboch, A. N.; Puzynin, A. V.; Ismagilov, Z. R. *Carbon* **2017**, *122*, 475.
(52) Lee, S.; Kwak, D.-H.; Han, S.-B.; Lee, Y.-W.; Lee, J.-Y.; Choi, I.-A.; Park, H.-S.; Park, J.-Y.; Park, K.-W. *ACS Catal.* **2016**, *6* (8), 5095.
(53) Wu, M.; Tang, Q.; Dong, F.; Bai, Z.; Zhang, L.; Qiao, J. *J. Catal.* **2017**, *352*, 208.
(54) Zhu, J.; Xu, Y.; Zhang, Y.; Feng, T.; Wang, J.; Mao, S.; Xiong, L. *Carbon* **2016**, *107*, 638.
(55) Sing, K. S. W. S. W.; Everett, D. H. H.; Haul, R. A. W. A. W.; Moscou, L.; Pierotti, R. A. A.; Rouquérol, J.; Siemieniewska, T.; Rouquerol, J.; Siemieniewska, T. *Pure Appl. Chem.* **1985**, *57* (4), 603.
(56) Brunauer, S.; Emmett, P. H.; Teller, E. *J. Am. Chem. Soc.* **1938**, *60* (2), 309.
(57) Berkson, Z. J.; Becwar, S.; Zussblatt, N. P.; Prisco, N. A.; Fechler, N.; Hunt, C.; Ménard, G.; Chmelka, B. F. *In preparation*; 2018.
(58) Xia, W.; Mahmood, A.; Liang, Z.; Zou, R.; Guo, S. *Angew. Chemie - Int. Ed.* **2016**, *55* (8), 2650.

(59) Kobayashi, T.; Singappuli-Arachchige, D.; Wang, Z.; I. Slowing, I.; Pruski, M. *Phys. Chem. Chem. Phys.* **2017**, *19* (3), 1781.
(60) Martin, G. J. .; Martin, M. L. .; Gouesnard, J.-P. *15N-NMR Spectroscopy*; Diehl, P., Fluck, E., Kosfeld, R., Eds.; Springer-Verlag: Heidelburg, New York, 1981.
(61) Wang, X.; Hou, Z.; Ikeda, T.; Terakura, K. *J. Phys. Chem. C* **2014**, *118*, 13929.
(62) Gammon, W. J.; Hoatson, G. L.; Holloway, B. C.; Vold, R. L.; Reilly, A. C. *Phys. Rev. B* **2003**, *68* (19), 195401.
(63) Koehler, J.; Meiler, J. *Prog. Nucl. Magn. Reson. Spectrosc.* **2011**, *59* (4), 360.
(64) Bakhmutov, V. I. *Chem. Rev.* **2011**, *111* (2), 530.
(65) Clément, R. J.; Pell, A. J.; Middlemiss, D. S.; Strobridge, F. C.; Miller, J. K.; Whittingham, M. S.; Emsley, L.; Grey, C. P.; Pintacuda, G. *J. Am. Chem. Soc.* **2013**, *134*, 17178.
(66) George, N. C.; Pell, A. J.; Dantelle, G.; Page, K.; Llobet, A.; Balasubramanian, M.; Pintacuda, G.; Chmelka, B. F.; Seshadri, R. *Chem. Mater.* **2013**, *25* (20), 3979.
(67) George, N. C.; Brgoch, J.; Pell, A. J.; Cozzan, C.; Jaffe, A.; Dantelle, G.; Llobet, A.; Pintacuda, G.; Seshadri, R.; Chmelka, B. F. *Chem. Mater.* **2017**, *29* (8), 3538.
(68) Strickland, K.; Miner, E.; Jia, Q.; Tylus, U.; Ramaswamy, N.; Liang, W.; Sougrati, M. T.; Jaouen, F.; Mukerjee, S. *Nat. Commun.* **2015**, *6*, 1.
(69) Zhao, D.; Feng, J.; Huo, Q.; Melosh, N.; Fredrickson, G. H.; Chmelka, B. F.; Stucky, G. D. *Science* **1998**, *279* (5350), 548.
(70) Ryoo, R.; Joo, S. H.; Jun, S. *J. Phys. Chem. B* **1999**, *103* (37), 7743.
(71) Jun, S.; Sang Hoon Joo; Ryoo, R.; Kruk, M.; Jaroniec, M.; Liu, Z.; Ohsuna, T.; Terasaki, O. *J. Am. Chem. Soc.* **2000**, *122* (43), 10712.
(72) Fechler, N.; Fellinger, T. P.; Antonietti, M. *Adv. Mater.* **2013**, *25* (1), 75.
(73) Bertani, P.; Raya, J.; Bechinger, B. *Solid State Nucl. Magn. Reson.* **2014**, *61–62*, 15.
(74) Thurber, K. R.; Tycko, R. *J. Magn. Reson.* **2009**, *196* (1), 84.
(75) Yesinowski, J. P.; Ladouceur, H. D.; Purdy, A. P.; Miller, J. B. *J. Chem. Phys.* **2010**, *133* (23), 234509.
(76) Lesage, A.; Sakellariou, D.; Steuernagel, S.; Emsley, L. *J. Am. Chem. Soc.* **1998**, *120* (7), 13194.
(77) Hu, B.; Trébosc, J.; Amoureux, J. P. *J. Magn. Reson.* **2008**, *192* (1), 112.
(78) Garaga, M. N.; Hsieh, M.-F.; Nour, Z.; Deschamps, M.; Massiot, D.; Chmelka, B. F.; Cadars, S. *Phys. Chem. Chem. Phys.* **2015**, *17* (33), 21664.

Chapter 8

Atomic-scale compositions and structures that account for the stability of the historic pigment Maya Blue

Adapted from: Z. J. Berkson, D. Lalli, M. S. Beeson, N. A. Prisco, E. H. Poniatowski, M. Sanchez del Rio, F. Sánchez-Ochoa, A. Lesage, G. Pintacuda, B. F. Chmelka, *in preparation.*

8.1 Abstract

The historic pigment Maya Blue is an organic-inorganic hybrid material composed of the natural nanoporous phyllosilicate clay palygorskite and dilute quantities (1 wt%) of the organic dye indigo. Remarkably, the pigment retains its vibrant blue-turquoise color even when exposed to aging, weathering, thermal degradation, concentrated acid, or chemical solvents. As a result, many Mesoamerican murals, artifacts, and sculptures that incorporate Maya Blue still retain their coloration, long after pigments of other hues have faded due to weathering. Despite extensive previous research efforts focused on Maya Blue pigments, the interactions and distributions of organic molecules within the material and the atomic-level origins of the long-term stability have long been elusive. Here, the stability of the indigo-palygorskite complex is elucidated by solid-state 2D $^{1}H\{^{1}H\}$, $^{13}C\{^{1}H\}$, $^{27}Al\{^{1}H\}$, and $^{29}Si\{^{1}H\}$ NMR spectroscopy, with sensitivity enhanced by very high magnetic field strengths (23.5 T) or dynamic nuclear polarization (DNP). During the synthesis of Maya Blue, indigo is shown to form dehydroindigo as well as decompose to form indoxyl species. The hydrophilic indoxyl species diffuse deep (~10 nm) into the palygorskite nanopores. The indigo and dehydroindigo molecules are stabilized by strong hydrogen bonding interactions with structural water molecules at near surface (~2 nm) nanopore locations. The

comprehensive analyses presented here demonstrate that complicated distributions and interactions of dilute (< 1 wt%) organic molecules in porous inorganic solids may be elucidated, with relevance to diverse other material systems of broad catalytic, optical, and cultural significance.

8.2 Introduction

Organic-inorganic interactions at nanostructured surfaces often account for the macroscopic properties of diverse solid-state materials, including heterogeneous catalysts,[1,2] battery materials,[3] optoelectronic devices,[4,5] and biominerals.[6] An example of cultural and historical significance is the pigment Maya Blue, an organic-inorganic hybrid material prepared from the natural clay palygorskite (or attapulgite) and organic dyes derived from indigo that was developed and used by Mesoamerican civilizations between the 6th and 16th century.[7–9] Remarkably, the pigment retains its vibrant blue-turquoise color even when exposed to aging, weathering, thermal degradation, concentrated acid, or chemical solvents.[9,10] As a result, many Mesoamerican murals, artifacts, and sculptures that incorporate Maya Blue still retain their coloration, long after pigments of other hues have faded due to weathering.[11] These exceptional properties have prompted theoretical and experimental studies to investigate the composition, structure, and stability of the organic-inorganic complex of indigo and palygorskite,[12–20] but the nature and molecular origins of the interactions that account for the stability of Maya Blue are still unknown.

Despite extensive previous research efforts focused on Maya Blue pigments, the interactions and distributions of organic molecules (e.g., indigo and dehydroindigo) within the material and the atomic-level origins of the long-term stability have long been elusive.

This is due in part to the dilute quantities (< 1 wt%) and complex distributions of the organic species, heterogeneities in the natural palygorskite framework, and the difficulties associated with identifying and distinguishing organic-inorganic interactions in porous frameworks. The stability of the indigo-palygorskite complex has been attributed variously to: (1) adsorption of indigo/dehydroindigo at surface sites on the palygorskite particles with interactions of the carbonyl groups on indigo molecules and surface silanol species;[7] (2) preferential adsorption at the tips or ends of the bundles of palygorskite fibers with organic molecules partially blocking the openings of the palygorskite nanochannels;[12,16] (3) competitive adsorption of the organic species with structural water molecules to coordinate to Mg^{2+}, Al^{3+}, or Fe^{3+} cations at the octahedral sites within the palygorskite framework;[21] and (4) stabilization of the organic molecules within the nanopores by hydrogen bonding interactions with occluded water molecules.[17,20] The palygorskite framework in Maya Blue has been evidenced to partially and irreversibly dehydrate during the synthesis process, with indigo incorporation linked to inhibited rehydration of the palygorskite framework,[17,22] indicating the partial blockage of the palygorskite nanochannels by organic molecules. Recent DFT calculations suggest shallow insertion of indigo and dehydroindigo molecules into the palygorskite nanochannels stabilized by strong hydrogen bonds of both the amine and carbonyl groups to structural water molecules,[20] though until now there has been no direct experimental evidence of such hydrogen bonding interactions.

8.3 Results and discussion

8.3.1 Synthesis, long-range order, and morphology of Maya Blue

The exact procedure used historically to prepare Maya Blue has been lost,[11] though pigments with analogous optical properties and stability may be prepared by thermal treatment of macroscopic mixtures of indigo and palygorskite at temperatures greater than 130˚C,[16] (Fig. 8.1a). In pre-Columbian Mesoamerica, Maya Blue was prepared by maceration and heat treatment of mixtures of palygorskite and the leaves of the plant *Indigofera suffruticosa*.[11,18]

Maya Blue is characterized by it's acid stability, as shown in Figure 8.1b. Neat indigo (left column) discolors almost instantly on exposure to concentrated HNO_3. Indigo also forms a complex with the clay sepiolite, which is similar in structure to palygorskite but with slightly larger nanopore diameters.[12] However, the indigo-sepiolite hybrid material discolors on extended exposure to concentrated HNO_3 (middle column). By comparison, the Maya Blue material (indigo-palygorskite) does not discolor after long-term exposure to concentrated HNO_3 (right column), evidencing the remarkable acid-stability of the pigment.

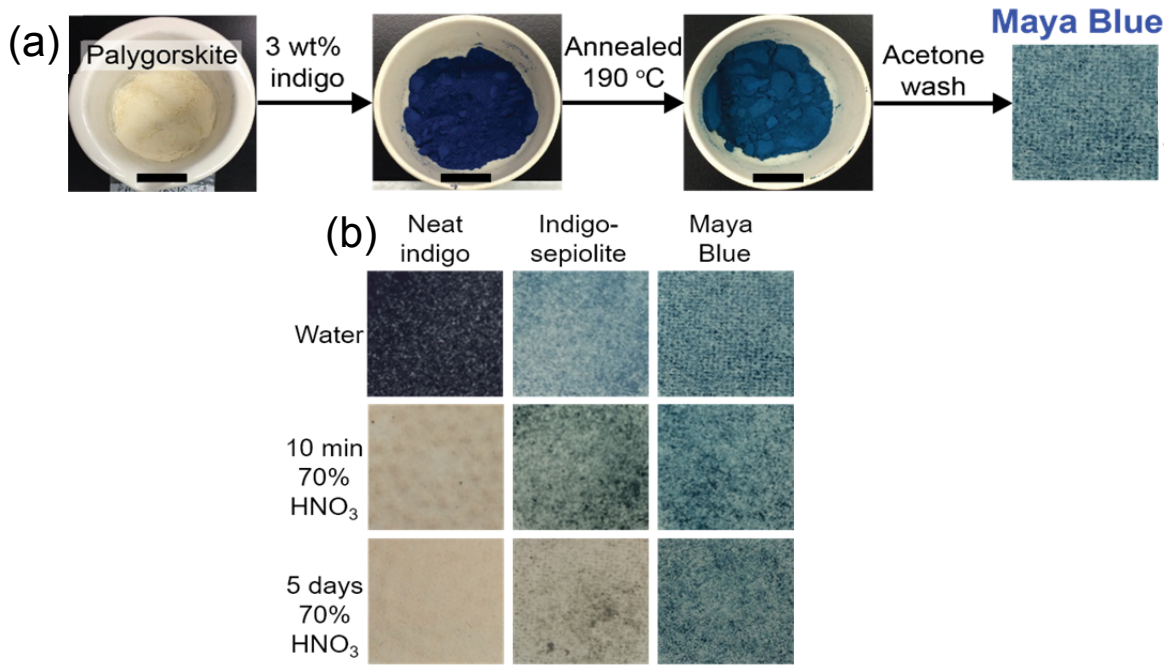

Figure 8.1. (a) Synthesis of Maya blue: ground palygorskite powder is mixed with 3 wt% indigo, annealed at 190 °C, and washed to remove excess indigo. Scale bars are 1 cm. (b)

Images of neat indigo (left column), indigo-sepiolite (middle column), and indigo-palygorskite (right column) dispersed on filter paper after exposure to water (top row), 70% HNO_3 for ten minutes (middle row), and 70% HNO_3 for five days (bottom row).

The annealing process and incorporation of indigo into the pigment does not influence significantly the periodic structure of palygorskite, as established by the X-ray diffraction (XRD) patterns of palygorskite and Maya Blue in Figure 8.2a,b. All of the X-ray reflections in both XRD patterns are indexable to the palygorskite structure, indicating that the palygorskite framework is retained during the synthesis of Maya Blue, consistent with past studies.[16,23] Palygorskite is a nanoporous 2:1 phyllosilicate clay that forms long, narrow fibers ranging in length from 100-1200 nm and in width from 5-30 nm,[23] which are shown in the representative transmission (TEM) and scanning electron micrographs (SEM) in Figure 8.2c. Elemental analyses of the palygorskite (obtained from Ticul, Mexico) and Maya Blue materials studied here yield Si/Al and Si/Mg ratios of ~4 and an Al/Mg ratio of ~1. The palygorskite nanopores are linear channels with effective cross sectional areas of 3.7 x 6.4 □,[24] that run parallel to the length of the fibers[22] (Fig. 8.3a). Structural water molecules within the palygorskite nanochannels coordinate to magnesium, iron, or aluminum atoms that occupy the octahedrally-coordinated sites, and a network of physisorbed hydrogen-bonded water fills the nanochannels under atmospheric conditions.[17] Previous electrochemical and spectroscopic studies[13,15,19] have identified the organic components of Maya Blue as indigo and dehydroindigo, which together account for the green-blue hue of the Maya Blue pigments. Indigo and dehydroindigo are typically present in dilute quantities in Maya Blue, estimated at ~0.75 wt% by TGA for the materials studied here. Indigo and dehydroindigo are incorporated into Maya Blue to different relative extents depending on the synthesis conditions and precursor compositions,[18] which yield different hues in different samples of

archaelogical Maya Blue that likely arise from variations in historical preparation methods and precursor material compositions from region to region.[18]

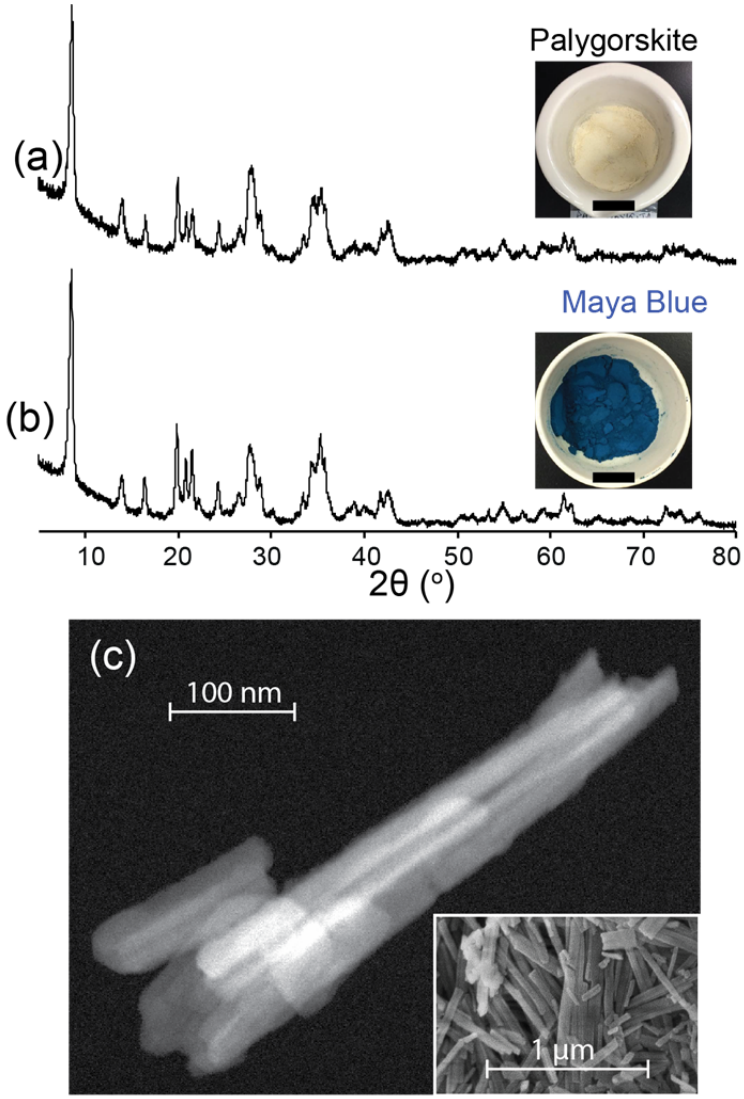

Figure 8.2. X-ray diffraction patterns of (a) palygorskite and (b) Maya Blue (middle). The insets show optical images of the palygorskite or Maya Blue powders; scale bars are 1 cm. All reflections are indexable to the palygorskite structure. No significant changes are observed in the XRD pattern between palygorskite and Maya Blue. (c) Representative dark field TEM image of palygorskite, showing the long nanofibrils that compose the palygorskite particles. The inset shows a representative SEM image of palygorskite.

8.3.2 Framework-indigo interactions in Maya Blue

In Maya Blue, indigo molecules and their derivatives are intercalated inside the palygorskite nanochannels, where they interact with structural water molecules and hydroxyl

groups. This is established unambiguously by the solid-state two-dimensional (2D) magic angle spinning (MAS) nuclear magnetic resonance (NMR) correlation spectra shown in Fig. 8.3 and 8.4, which are mediated by internuclear dipole-dipole interactions that operate through space over distances of less than 1 nm. The 2D NMR correlation spectra establish the mutual proximities of ^{1}H or ^{13}C moieties on organic molecules and ^{1}H, ^{29}Si, or ^{27}Al species in the palygorskite framework, elucidating the distrubutions of organic molecules and the organic-inorganic interactions in Maya Blue. Such insights have been inaccessible in the past for materials like Maya Blue because of the dilute concentrations of occluded organic molecules and correspondingly low NMR signal sensitivity, as well as broad distributions of framework and organic species, which yield inhomogeneously-broadened NMR signals that are challenging to resolve. Here, NMR signal sensitivity is improved by utilizing either very high magnetic field strengths (23.5 T, 1.5 GHz for ^{1}H) and/or dynamic-nuclear-polarization (DNP) NMR techniques at low temperatures, which provide dramatic enhancements in NMR signal sensitivity. These techniques enable the acquisition of highly-resolved 2D $^{1}H\{^{1}H\}$, $^{29}Si\{^{1}H\}$, and $^{13}C\{^{1}H\}$ NMR correlation spectra (Fig. 2 and 3), which have two ^{1}H, ^{13}C, ^{27}Al, or ^{29}Si frequency axes with normalized frequency units of Hz/MHz or ppm. Correlated signal intensities in such 2D dipolar-mediated solid-state NMR correlation spectra establish the mutual nanoscale (<1 nm) proximities of the corresponding ^{1}H, ^{13}C, ^{27}Al, or ^{29}Si species. The solid-state 2D NMR correlation spectra and analyses elucidate the site-specific interactions and distributions of dilute organic indigo/dehydroindigo molecules in palygorskite that account for the stability of the Maya Blue pigment.

For example, ^{1}H signals from different organic and inorganic ^{1}H environments in Maya Blue are resolved and correlated by 1D and 2D ^{1}H NMR spectra acquired at high magnetic

field strengths (23.5 T) and under fast MAS conditions (60 kHz). The fast MAS conditions partially average the strong ^{1}H-^{1}H nuclear dipole-dipole couplings and yield 1D ^{1}H MAS NMR spectra that show resolved ^{1}H signals at -1.1, 0.9, 3.4, 4.0, 17.5, and 25.5 ppm for both palygorskite and Maya Blue materials (Figure 8.3b). The ^{1}H signals at 4.0 and 3.4 ppm are assigned respectively to loosely-bound water molecules and water molecules that are coordinated to Mg and Al atoms at octahedrally-coordinated sites. The relatively narrow ^{1}H signal at 0.9 ppm is assigned to structural Al-OH or Mg-OH groups on the basis of its shift position and complementary 2D ^{27}Al{^{1}H} NMR correlation spectra of palygorskite and Maya Blue. The ^{1}H signals at 4.0, 3.4, and 0.9 ppm are modestly broadened in the ^{1}H NMR spectrum of Maya Blue compared to that of palygorskite, indicating that the synthesis procedure increases the disorder of the ^{1}H species within the palygorskite nanochannels. Notably, Maya Blue exhibits additional ^{1}H signals at 5.8, 6.4, and 7.7 ppm, which are not present in the spectrum of neat palygorskite and are assigned to indigo and/or dehydroindigo molecules. While the ^{1}H signals from very similar molecules such as indigo, dehydroindigo, and other indigo derivates like indoxyl cannot be resolved in the solid state, the ^{1}H specra confirm the presence of organic molecules in Maya Blue.

The incorporation of indigo/dehydroindigo molecules into the palygorskite nanochannels is established by the nanoscale proximities of their -CH moieties with structural water molecules and -OH moieties in palygorskite, which yield correlated ^{1}H{^{1}H} signal intensities in the solid-state 2D ^{1}H{^{1}H} correlation spectrum in Figure 8.3c. In this spectrum, the ^{1}H NMR signals are spread into a 2D contour plot with single quantum (SQ) and double quantum (DQ) shift dimensions. On-diagonal ^{1}H signals at SQ 0.9 ppm, 3.4 ppm, and 6.0-6.4 ppm arise respectively from hydroxyl groups, water molecules, and -CH moieties on the

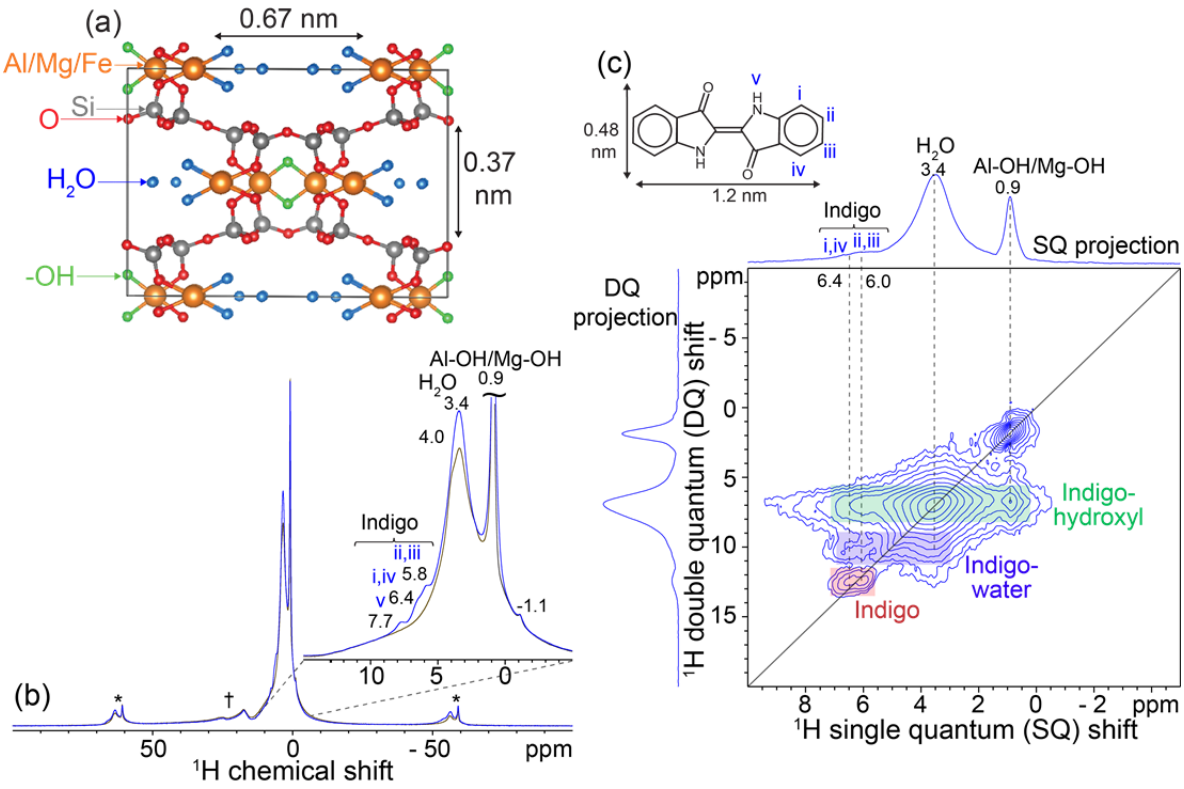

Figure 8.3. ^{1}H environments and indigo-framework interactions in Maya Blue. (a) Palygorskite unit cell viewed along the c axis. (b) Overlay of the solid-state 1D ^{1}H echo NMR spectra of palygorskite (black) and Maya Blue (blue). The boxed insets show enlargements of the corresponding spectral features. Both spectra show ^{1}H signals from structural Al-OH or Mg-OH moieties and adsorbed H_2O and broad ^{1}H signals from paramagnetically-displaced ^{1}H species. Asterisks indicate spinning sidebands and the cross symbol indicates signals from a probe background.. (c) Solid-state 2D ^{1}H{^{1}H} SQ-DQ NMR correlation spectrum of Maya Blue, showing off-diagonal correlated signal intensities that establish the mutual nanoscale proximities of indigo molecules and framework hydroxyl groups (green shaded region), indigo molecules and coadsorbed nanopore water molecules (blue shaded region), and intramolecular indigo interactions (red shaded region). The schematic inset shows the molecular structure and approximate dimensions of indigo, with the different ^{1}H moieties labeled. The 1D SQ and DQ projections of the 2D spectrum are shown along the horizontal and vertical axes, respectively. The NMR spectra in (b) and (c) were acquired at 23.5 T, 255 K, and under MAS conditions of 60 kHz. The combined ultra high field and fast-MAS ^{1}H NMR measurements unambiguously establish the presence and interactions of indigo molecules within the palygorskite nanopores.

indigo/dehydroindigo molecules. The off-diagonal ^{1}H signal intensities at SQ shifts of 0.9 and 6.0-6.4 ppm and a DQ shift of 7.1 ppm (green shaded region) arise from interactions of indigo molecules and structural hydroxyl groups that are in nanoscale proximities,

establishing that the organic molecules are within the palygorskite framework. Furthermore, the broad off-diagonal signal intensities at SQ shifts of 3.4 ppm and 6.0-6.4 ppm and a DQ shift of 9.6 ppm (blue shaded region) arise from interactions of indigo/dehydroindigo molecules and adsorbed water within the palygorskite framework. These correlated intensities show that indigo/dehydroindigo molecules do not significantly displace structural water molecules within Maya Blue, which are instead associated directly with the indigo adsorption sites. The ^{1}H signals in the red shaded region of the 2D spectrum arise from intramolecular interactions among the different ^{1}H moieties in the indigo molecules. Together, the correlated ^{1}H signal intensities are consistent with the complete or partial inclusion of indigo molecules into the palygorskite framework. The absence of correlated ^{1}H signal intensities from -NH moieties on indigo molecules (expected around 8-10 ppm) suggests that the majority of the occluded indigo molecules in the Maya Blue samples studied here are predominantly in the dehydroindigo form.

Further insights into the distributions and site-specific framework interactions of dilute organic molecules in Maya Blue are established by analysis of 2D $^{13}C\{^{1}H\}$ and $^{29}Si\{^{1}H\}$ DNP-enhanced HETeronuclear CORrelation (HETCOR) NMR spectra (Fig. 8.4), which show correlated $^{29}Si\{^{1}H\}$ or $^{13}C\{^{1}H\}$ signals from ^{29}Si or ^{13}C nuclei that are dipole-dipole coupled to nearby (<1 nm) ^{1}H nuclei in the organic molecules or palygorskite framework. The sensitivity of such 2D HETCOR measurements is limited by the low natural isotopic abundances of ^{13}C (1.1%) and ^{29}Si (4.7%) nuclei, making them previously infeasible for materials containing dilute organic molecules such as Maya Blue. Recently-developed DNP-NMR techniques[25–31] provide dramatic enhancements in NMR signal sensitivity that enable

acquisition of 2D NMR correlation spectra for materials at natural isotopic abundance ^{29}Si[32–34] or ^{13}C[35,36] such as Maya Blue.

The different types of structural hydroxyl groups, water molecules, and hydrogen bonded -OH species within the palygorskite framework are resolved and identified on the basis of their interactions with framework ^{29}Si atoms. These interactions yield correlated $^{29}Si\{^{1}H\}$ signals in the 2D $^{29}Si\{^{1}H\}$ DNP-HETCOR spectrum in Figure 8.4a, which shows three resolved ^{29}Si signals at -92, -94, and -98 ppm. The ^{29}Si signals at -92 and -98 ppm are correlated with ^{1}H signals at 0.9 ppm from framework -Al-OH or -Mg-OH moieties, 3.6-5.7 ppm from nanopore water molecules, and 8.2-10.4 ppm from H-bonded -OH species. The broad correlated signal intensities at 8.2 ppm in the ^{1}H dimension likely contain signal contributions from the ^{1}H moieties on nanopore-adsorbed indigo molecules, which overlap with signals from weakly H-bonded water molecules and cannot be distinguished. The ^{29}Si signals at -92 and -98 ppm are assigned to ^{29}Si atoms at the two different tetrahedral sites in the palygorskite framework.[22] By comparison, the ^{29}Si signal at -94 ppm is correlated only with the ^{1}H signal at 0.9 ppm from Al-OH/Mg-OH moieties, but not to water molecules or H-bonded species. This confirms that the ^{29}Si signal at -94 ppm is associated with dehydrated regions of the palygorskite material, which contain few structural or physisorbed water molecules.

The $^{13}C\{^{1}H\}$ DNP-NMR analyses of Maya Blue resolve signals from three different types of organic molecules (indigo, dehydroindigo, and indoxyl), which have different relative distributions and framework interactions within the pigment. Indoxyl is a decomposition product of indigo and has been previously observed in Maya Blue materials by ^{13}C MAS NMR, where it was hypothesized to oxidize over time to indigo.[19] Different ^{13}C

signals from indigo, dehydroindigo, and indoxyl are resolved in the 1D and 2D $^{13}C\{^{1}H\}$ DNP-NMR spectra of Maya Blue (Fig. 8.4b), which are assigned on the basis of simulations of the NMR parameters of the different organic molecules shown in Fig. 8.4c and previous NMR studies of Maya Blue materials.[19,37] The spectral complexity of the $^{13}C\{^{1}H\}$ DNP-NMR spectra in Fig. 4b arises from overlapping ^{13}C signals from indigo, dehydroindigo, and indoxyl molecules adsorbed at different surface and near-surface framework sites in palygorskite. Specifically, the ^{13}C signals in the 112-156 ppm frequency region arise from carbon atoms 1-8 on indigo and dehydroindigo, as well as carbon atoms 2-6 and 8 on indoxyl, as indicated by the colored numbers in Figure 4b. Additional ^{13}C signals are detected in the 99-106 ppm region, which are assigned to carbon atoms 1 and 7 on indoxyl molecules.

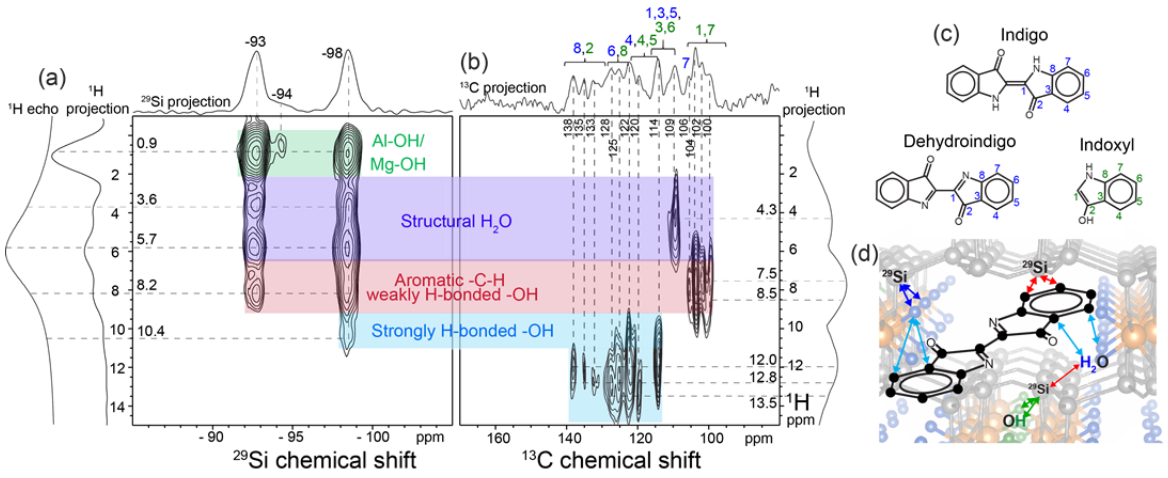

Figure 8.4. Solid-state 2D (a) $^{29}Si\{^{1}H\}$ and (b) $^{13}C\{^{1}H\}$ DNP-HETCOR spectra of Maya Blue, with shaded regions indicating interactions of ^{29}Si atoms in the palygorskite framework or ^{13}C atoms in adsorbed indigo or indoxyl molecules with (green) structural hydroxyl groups, (blue) adsorbed water molecules, (red) aromatic C-H or weakly H-bonded -OH, and (light blue) very strongly H-bonded -OH species. Solid-state 1D $^{29}Si\{^{1}H\}$ or $^{13}C\{^{1}H\}$ DNP-CPMAS and ^{1}H DNP-echo spectra are shown along the horizontal and vertical axes, respectively, for comparison with the 1D projections of the 2D spectra. The DNP-NMR spectra were acquired at 95 K, 10 kHz MAS, 9.4 T, in the presence of 16 mM AMUPol biradical in 60 ^{12}C-enriched d_8-glycerol: 40 D_2O, under continuous-wave microwave irradiation at 263 GHz, and with $^{29}Si\{^{1}H\}$ or $^{13}C\{^{1}H\}$ cross-polarization contact times of 7 ms and 0.2 ms, respectively. (c) Structures of indigo, dehydroindigo, and indoxyl molecules.

(d) Schematic showing the interactions of adsorbed indigo molecules and the palygorskite framework, with colored arrows indicating the interactions consistent with the corresponding signal intensities in the solid-state 2D DNP-NMR spectra.

The different types of organic molecules in Maya Blue occupy different near-surface or subsurface adsorption sites and exhibit different interactions with framework ^{1}H environments in palygorskite, which enables them to be resolved in the 2D $^{13}C\{^{1}H\}$ DNP-HETCOR spectrum in Fig. 8.4b. Specifically, the ^{13}C signals in the 114 to 136 ppm region, which arise predominately from indigo and dehydroindigo molecules, are all correlated with ^{1}H signals in the 10.4 to 13.5 ppm region from strongly H-bonded -OH moieties. The correlated signal intensities unambiguously establish that indigo/dehydroindigo molecules participate in strong hydrogen bonds in Maya Blue, likely involving the carbonyl oxygen atoms and structural water molecules coordinated to magnesium or aluminum atoms within the palygorskite framework. Such strong hydrogen bonding interactions have been previously suggested on the basis of synchrotron powder X-ray analyses, infrared spectroscopy, and molecular dynamics simulations, but are here directly established experimentally for the first time. The ^{1}H chemical shift correlates directly to the -O···HO- hydrogen bond distance and, correspondingly, the strength of the hydrogen bond interaction. Using well-established semi-empirical relations for this correlation,[38,39] the -C=O···HOH distance between the carbonyl moieties and structural water molecules is 0.25-0.27 nm. The hydrogen bond lengths estimated from the DNP-NMR results are in excellent agreement with recent molecular dynamics simulations of indigo and dehydroindigo molecules in palygorskite nanochannels,[20] which predicted -C=O···HOH distances of 0.26-0.27 nm for both dehydroindigo and indigo. Complementary 2D DNP-HETCOR NMR analyses of Maya Blue samples using different DNP solvent formulations indicate that the

indigo/dehydroindigo molecules occupy sites that are relatively near to the palygorskite particle surface (results not shown). Due to the relatively large molecular dimensions of indigo and dehydroindigo, as well as their hydrophobic character, they do not penetrate deep into the palygorskite nanopores and are instead stabilized by H-bonds at near-surface adsorption sites.

By comparison to the indigo/dehydroindigo molecules, the indoxyl molecules occupy sub-surface environments within the palygorskite particles, consistent with molecular diffusion of indoxyl into the palygorskite nanopores. In the 2D $^{13}C\{^{1}H\}$ DNP-NMR spectrum in Figure 3b, the ^{13}C signals in the 99-106 ppm region, which are assigned to indoxyl molecules, are correlated with ^{1}H signals at 4.6 and 7.5 ppm. The ^{1}H signal at 4.6 ppm arises from water within the palygorskite nanopores, while the signals at 7.5-8.5 ppm contains overlapping contributions from ^{1}H aromatic moieties on the organic molecules and weakly H-bonded -OH species (-O···HO- distance ~ 0.28 nm). The correlated signals thus establish that the indoxyl molecules interact with weakly H-bonded water molecules that fill the nanopore interior volume of the palygorskite nanochannels. The correlated $^{13}C\{^{1}H\}$ signal intensities associated with the indoxyl molecules are the same for Maya Blue materials measured under the same conditions excpt using different partially- or fully-deuterated DNP solvents (results not shown), indicating that the indoxyl molecules are inaccessible to DNP solvent molecules and are therefore predominately sub-surface.

Further insights into the mesoscale distributions of indigo/dehydroindigo and indoxyl molecules in Maya Blue are provided by DNP-NMR polarization buildup curves (Fig. 8.5), which depend on the distance of the different organic molecules from the palygorskite particle surfaces. The NMR signal intensities for the ^{13}C signals at 114 ppm

(indigo/dehydroindigo) and 100 ppm (indoxyl) were measured by $^{13}C\{^{1}H\}$ DNP-CPMAS experiments is shown as a function of parameterized buildup time (Figure 8.5a). The different ^{13}C signals exhibit different buildup behaviors manifested by the T_{DNP} buildup times extracted from monoexponential fits to the experimental data (dotted lines). The ^{13}C signals at 114 ppm and 100 ppm have T_{DNP} times of 1.8 ± 0.3 s and 4.8 ± 0.5 s, respectively. The much faster buildup time of the ^{13}C signal at 114 ppm from indigo/dehydroindigo indicates that the corresponding indigo/dehydroindigo molecules are predominantly near-surface, as the indigo/dehydroindigo molecules receive polarization rapidly via spin diffusion from the DNP solvent molecules at the palygorskite particle surfaces. By comparison, the ^{13}C signal at 100 ppm from indoxyl moieties builds up relatively slowly as polarization must be relayed from the particle surfaces into the nanopore interiors. Efforts are currently underway to model the spin diffusion behavior and quantify the spatial distribution of indigo, dehydroindigo, and indoxyl molecules in Maya Blue. Nevertheless, the DNP-NMR spin diffusion analyses confirm qualitatively that the indigo/dehydroindigo molecules occupy adsorption sites near the surfaces of the palygorskite nanofibrils while the indoxyl molecules are diffused deeper into the palygorskite nanopores, as depicted schematically in Figure 8.5b.

8.4 Conclusions

The types and distributions of organic molecules in the organic-palygorskite pigment Maya Blue have been elucidated by state-of-the-art solid-state NMR analyses, with complementary electron microscopy, X-ray diffraction, and surface forces measurements. Indigo and dehydroindigo molecules occupy near-surface environments within the palygorskite nanopores and are stabilized by strong hydrogen bonds between the carbonyl

moieties on the organic molecules and structural water molecules. During the preparation of the pigment, indigo molecules partially decompose to indoxyl molecules, which diffuse into the palygorskite nanopores and occupy sub-surface adsorption sites. By comparison, the bulky and hydrophobic indigo and dehydroindigo molecules occupy near-surface adsorption sites, where they are stabilized by strong hydrogen bonding interactions.

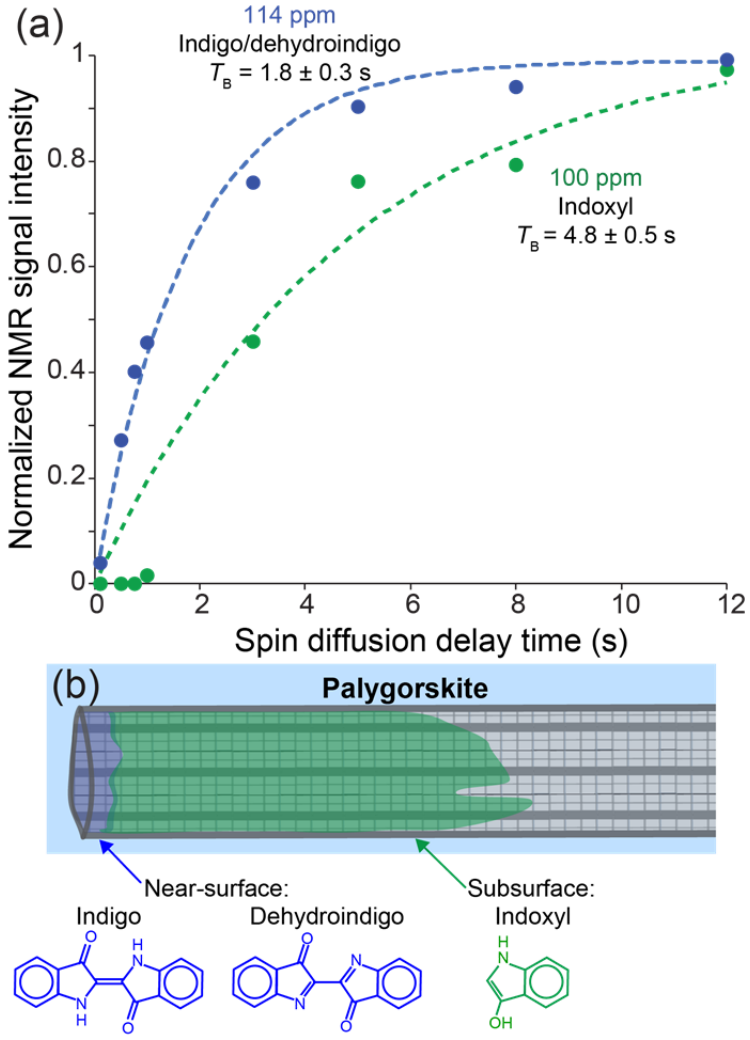

Figure 8.5. (a) DNP-NMR signal intensity detected using $^{13}C\{^1H\}$ DNP-CPMAS experiments as a function of parameterized spin delay time for the ^{13}C signals at 114 and 100 ppm, which correspond to indigo/dehydroindigo and indoxyl species, respectively. The faster NMR signal intensity buildup of the DNP-NMR signal at 114 ppm indicates near-surface locations of indigo/dehydroindigo molecules relative to indoxyl molecules, as depicted schematically in (b).

Elucidating the stability of the Maya Blue pigment has been a long-standing historical challenge. The organic-inorganic hydrogen bonding interactions established here to correlate to the remarkable durability of Maya Blue are expected to be broadly relevant to diverse nanostructured organic-inorganic materials, where similar interactions play important roles in governing macroscopic properties of interest. The study of the Maya Blue pigment has already generated interest in indigo incorporation in other nanoporous metal oxide materials such as zeolites and layered silicates to form new, highly stable pigments with controllable hues. More broadly, the comprehensive analyses presented here demonstrate that complicated distributions and interactions of dilute (< 1 wt%) organic molecules in porous inorganic solids may be elucidated. These analyses are expected to be fully extendable to diverse porous inorganic-organic hybrid materials of technological importance, including optoelectronic materials and heterogenous catalysts. By developing detailed understanding of the origins of the macroscopic optical, electronic, or catalytic properties of interest, new principles for the design of future materials may be established.

8.5 Materials and methods

Preparation of Maya Blue

There is no historical or archeological record of how the Maya Blue pigment was prepared historically, and the original formulation of Maya Blue has been lost.[11] To prepare a palygorskite-indigo hybrid material with the same properties as historic Maya Blue pigments, palygorskite and indigo were ground and heated following previously-reported methods previously reported.[10] For a typical synthesis, palygorskite (Ticul, Mexico) was ground into a fine powder using a mortar and pestle. Indigo (3 wt%) was added to the

palygorskite and ground for an additional 10 minutes to create a homogeneous bright blue powder. The macroscopic mixture of indigo and palygorskite was annealed at 190 ˚C in air for 5 hours and cooled in air, producing a turquoise-blue powder. Once cooled, the palygorskite-indigo composite was washed thoroughly with acetone to remove residual indigo. Residual acetone was removed by drying at 50 ˚C for 1 hr.

X-ray powder diffraction

The powder XRD measurements on the Maya Blue and palygorskite materials were conducted at room temperature on a Panalytical Empyrean Powder X-Ray Diffractometer in θ-2θ mode using Cu Kα radiation with a wavelength of 1.5405 Å and equipped with a rotating sample stage rotating at two rotations per minute.

Electron microscopy

SEM images of palygorskite were obtained using FEI Nova Nano 650 FEG SEM using a voltage of 3.00 kV and a working distance of 3.6 mm. TEM images were obtained in dark-field imaging mode using a FEI Titan 300 kV FEG TEM/STEM system.

Solid-state NMR spectroscopy

The fast-MAS 1D and 2D ^{1}H, ^{1}H{^{1}H}, ^{1}H{^{13}C}, and ^{1}H{^{15}N} solid-state NMR experiments of Maya Blue, palygorskite, and neat indigo (Figures 2, S4-S6) were carried out on a Bruker Avance III 1 GHz standard bore spectrometer operating at a static field of 23.4 T, equipped with a triple channel H, C, N, 0.7 mm probe, at a MAS rate of 100 kHz. Sample temperature was maintained at about 305 K using a Bruker cooling unit with regulated N2 gas directed at the rotor. The temperature of this gas measured just before reaching the sample was 280 K. Chemical shifts were referenced to adamantane (^{1}H signal at 1.87 ppm). The nonselective pulses were set to 2.4 μs at 104 kHz rf-field amplitude for ^{1}H.

DNP-enhanced NMR spectroscopy

DNP-enhanced MAS NMR techniques at low temperatures (*ca.* 100 K)[25–31] provide significantly enhanced NMR signal sensitivity that allows for detection and analysis of ^{13}C, ^{27}Al, and ^{29}Si environments in Maya Blue and palygorskite materials at natural isotopic abundance ^{29}Si (4.7%) and ^{13}C. All solid-state DNP-enhanced $^{13}C\{^1H\}$, $^{27}Al\{^1H\}$, and $^{29}Si\{^1H\}$ NMR experiments were carried out on a Bruker ASCEND 400 DNP-NMR spectrometer with a 9.4 Tesla superconducting magnet operating at 400.197, 104.280, 100.637, and 79.46 MHz for ^1H, ^{27}Al, ^{13}C, and ^{29}Si nuclei, respectively, and equipped with a gyrotron and microwave transmission line capable of providing 263 GHz microwave irradiation at the sample and a low-temperature 3.2 mm triple-resonance MAS probehead. The DNP-enhanced spectra were acquired at temperatures of 89-95 K, 8-10 kHz MAS, under continuous microwave irradiation at 263 GHz, and in the presence of 16-32 mM AMUPol biradical[40] in frozen DNP solvent (60 d_8-glycerol : 40 D_2O). For the DNP-NMR measurements on Maya Blue, ^{13}C-depleted glycerol (Cortecnet) was used to mitigate the overlap of ^{13}C signals from the DNP solvent and ^{13}C signals from the dilute organic molecules in Maya Blue. The ^{29}Si and ^{13}C DNP-NMR signal enhancements were quantified as the ratio of the fully-relaxed $^{13}C\{^1H\}$ and $^{29}Si\{^1H\}$ CPMAS signal intensities obtained with and without continuous microwave irradiation, and were measured to be ca. 8 and 5 for ^{13}C and ^{29}Si, respectively. The DNP-enhanced 2D $^{29}Si\{^1H\}$ HETCOR spectra of Maya Blue and palygorskite were acquired using 0.2 ms contact times, 32 t_1 increments, an incremental step size of 64 μs, 128 transients, and repetition times of 3 s for total acquisition times of 4 h. The 2D $^{13}C\{^1H\}$ DNP-HETCOR spectrum of Maya Blue was acquired using 0.2 ms contact times, 32 t_1 increments, an incremental step size of 64 μs, 512 transients, and a repetition

time of 6 s for a total acquisition times of 27 h. All of the 2D $^{13}C\{^{1}H\}$, $^{27}Al\{^{1}H\}$, $^{29}Si\{^{1}H\}$ DNP-HETCOR spectra were acquired using eDUMBO-1_{22} homonuclear coupling during the ^{1}H evolution period to improve resolution in the ^{1}H dimension.[41] All of the DNP-NMR spectra were acquired using 100 kHz SPINAL-64 ^{1}H decoupling during the acquisition period.[42]

8.6 References

(1) Meirer, F.; Kalirai, S.; Morris, D.; Soparawalla, S.; Liu, Y.; Mesu, G.; Andrews, J. C.; Weckhuysen, B. M. *Sci. Adv.* **2015**, *1* (3), e1400199.
(2) Gallego, E. M.; Portilla, M. T.; Paris, C.; León-Escamilla, A.; Boronat, M.; Moliner, M.; Corma, A. *Science.* **2017**, *355* (6329), 1051.
(3) Goodenough, J. B.; Park, K. S. *J. Am. Chem. Soc.* **2013**, *135* (4), 1167.
(4) Shirasaki, Y.; Supran, G. J.; Bawendi, M. G.; Bulović, V. *Nat. Photonics* **2013**, *7* (1), 13.
(5) Osterloh, F. E. *Chem. Soc. Rev.* **2013**, *42* (6), 2294.
(6) Gebbie, M. A.; Wei, W.; Schrader, A. M.; Cristiani, T. R.; Dobbs, H. A.; Idso, M.; Chmelka, B. F.; Herbert Waite, J.; Israelachvili, J. N. *Nat. Chem.* **2017**, *9* (5), 473.
(7) Van Olphen, H. *Science* **1966**, *154* (3749), 645.
(8) Puche, S.; Carmen, M. *Science. 273* **1996**, 223
(9) Del Río, M. S.; Doménech, A.; Doménech-Carbó, M. T.; De Agredos Pascual, M. L. V.; Suárez, M.; García-Romero, E. *Dev. Clay Sci.* **2011**, *3* (1962), 453.
(10) Del Río, M. S.; Martinetto, P. **2006**, *1* (May 2005), 115.
(11) Reyes-Valerio, C. *De Bonampak al Templo Mayor : el azul maya en Mesoamérica*, 1st ed.; México, D.F. : Siglo Veintiuno Editores : Agro Asemex, 1993.
(12) Hubbard, B.; Kuang, W.; Moser, A.; Facey, G. A.; Detellier, C. *Clays Clay Miner.* **2003**, *51* (3), 318.
(13) Doménech, A.; Doménech-Carbó, M. T.; De Agredos Pascual, M. L. V. *J. Phys. Chem. C* **2007**, *111* (12), 4585.
(14) Del Río, M. S.; Gutiérrez-León, A.; Castro, G. R.; Rubio-Zuazo, J.; Solís, C.; Sánchez-Hernández, R.; Robles-Camacho, J.; Rojas-Gaytán, J. *Appl. Phys. A Mater. Sci. Process.* **2008**, *90* (1), 55.
(15) Domenech, A.; Domenech-Carbo, M. T.; Ŕo, M. S. Del; Goberna, S.; Lima, E. *J. Phys. Chem. C* **2009**, *113* (28), 12118.
(16) Del Río, M. S.; Boccaleri, E.; Milanesio, M.; Croce, G.; Van Beek, W.; Tsiantos, C.; Chyssikos, G. D.; Gionis, V.; Kacandes, G. H.; Suárez, M.; García-Romero, E. *J. Mater. Sci.* **2009**, *44* (20), 5524.
(17) Giustetto, R.; Levy, D.; Wahyudi, O.; Ricchiardi, G.; Vitillo, J. G. *Eur. J. Mineral.* **2011**, *23* (3), 449.
(18) Doménech, A.; Doménech-Carbõ, M. T.; Vidal-Lorenzo, C.; De Agredos-Pascual, M. L. V. *Angew. Chemie - Int. Ed.* **2012**, *51* (3), 700.
(19) Lima, E.; Guzman, A.; Vera, M.; Rivera, J. L.; Fraissard, J. *J. Phys. Chem. C* **2012**, *116* (7), 4556.
(20) Sánchez-Ochoa, F.; Cocoletzi, G. H.; Canto, G. *Microporous Mesoporous Mater.* **2017**, *249*, 111.

(21) Tilocca, A.; Fois, E. *J. Phys. Chem. C* **2009**, *113* (20), 8683.
(22) Kuang, W.; Facey, G. A.; Detellier, C. *Clays Clay Miner.* **2004**, *52* (5), 635.
(23) Polette-Niewold, L. A.; Manciu, F. S.; Torres, B.; Alvarado, M.; Chianelli, R. R. *J. Inorg. Biochem.* **2007**, *101* (11–12), 1958.
(24) Frost, R. L.; Ding, Z. *Thermochim. Acta* **2003**, *397* (1–2), 119.
(25) Maly, T.; Debelouchina, G. T.; Bajaj, V. S.; Hu, K.-N.; Joo, C.-G.; Mak–Jurkauskas, M. L.; Sirigiri, J. R.; van der Wel, P. C. A.; Herzfeld, J.; Temkin, R. J.; Griffin, R. G. *J. Chem. Phys.* **2008**, *128* (5), 052211.
(26) Lesage, A.; Lelli, M.; Gajan, D.; Caporini, M. A.; Vitzthum, V.; Mieville, P.; Alauzun, J.; Roussey, A.; Thieuleux, C.; Mehdi, A.; Bodenhausen, G.; Coperet, C.; Emsley, L. *J. Am. Chem. Soc.* **2010**, *132*, 15459.
(27) Ni, Q. Z.; Daviso, E.; Can, T. V.; Markhasin, E.; Jawla, S. K.; Swager, T. M.; Temkin, R. J.; Herzfeld, J.; Griffin, R. G. *Acc. Chem. Res.* **2013**, *46* (9), 1933.
(28) Rossini, A. J.; Zagdoun, A.; Lelli, M.; Lesage, A.; Copéret, C.; Emsley, L. *Acc. Chem. Res.* **2013**, *46* (9), 1942.
(29) Perras, F. A.; Kobayashi, T.; Pruski, M. *J. Am. Chem. Soc.* **2015**, *137* (26), 8336.
(30) Perras, F. A.; Padmos, J. D.; Johnson, R. L.; Wang, L.-L. L.; Schwartz, T. J.; Kobayashi, T.; Horton, J. H.; Dumesic, J. A.; Shanks, B. H.; Johnson, D. D.; Pruski, M. *J. Am. Chem. Soc.* **2017**, *139* (7), 2702.
(31) Copéret, C.; Liao, W.-C.; Gordon, C. P.; Ong, T.-C. *J. Am. Chem. Soc.* **2017**, *139* (31), 10588.
(32) Lee, D.; Monin, G.; Duong, N. T.; Lopez, I. Z.; Bardet, M.; Mareau, V.; Gonon, L.; De Paëpe, G. *J. Am. Chem. Soc.* **2014**, *136* (39), 13781.
(33) Smeets, S.; Berkson, Z. J.; Xie, D.; Zones, S. I.; Wan, W.; Zou, X.; Hsieh, M. F.; Chmelka, B. F.; McCusker, L. B.; Baerlocher, C. *J. Am. Chem. Soc.* **2017**, *139* (46), 16803.
(34) Berkson, Z. J.; Messinger, R. J.; Na, K.; Seo, Y.; Ryoo, R.; Chmelka, B. F. *Angew. Chemie - Int. Ed.* **2017**, No. 2, 2.
(35) Johnson, R. L.; Perras, F. A.; Kobayashi, T.; Schwartz, T. J.; Dumesic, J. A.; Shanks, B. H.; Pruski, M. *Chem. Commun.* **2016**, *52* (9), 1859.
(36) Leskes, M.; Kim, G.; Liu, T.; Michan, A. L.; Aussenac, F.; Dorffer, P.; Paul, S.; Grey, C. P. *J. Phys. Chem. Lett.* **2017**, *8* (5), 1078.
(37) Holmes, S. T.; Dybowski, C. *Solid State Nucl. Magn. Reson.* **2015**, *72*, 90.
(38) Yesinowski, J. P.; Eckert, H.; Rossman, G. R. *J. Am. Chem. Soc.* **1988**, *110* (5), 1367.
(39) Xue, X.; Kanzaki, M. *J. Am. Ceram. Soc.* **2009**, *92* (12), 2803.
(40) Sauvée, C.; Rosay, M.; Casano, G.; Aussenac, F.; Weber, R. T.; Ouari, O.; Tordo, P. *Angew. Chemie - Int. Ed.* **2013**, *52* (41), 10858.
(41) Elena, B.; de Paëpe, G.; Emsley, L. *Chem. Phys. Lett.* **2004**, *398* (4–6), 532.
(42) Fung, B. M.; Khitrin, A. K.; Ermolaev, K. **2000**, *101*, 97.

Chapter 9

Spatially correlated distributions of local metallic properties in bulk and nanocrystalline GaN

Adapted from:

J. P. Yesinowski, Z. J. Berkson, S. Cadars, A. P. Purdy, B. F. Chmelka, *Physical Review B* **2017**, *95* (23), 235201

Z. J. Berkson, J. P. Yesinowski, U. Werner-Zwanziger, A. P. Purdy, B. F. Chmelka, *in preparation*

9.1 Abstract

The local electronic structures at different atom types of a metallic semiconductor are compared for bulk and nanocrystalline forms. Multinuclear magic-angle-spinning nuclear magnetic resonance (MAS NMR) establishes that GaN synthesized as an intentionally-doped bulk powder or as annealed nanocrystalline particles exhibits metallic behavior and a wide distribution of differing electronic environments in both forms as manifested by ^{71}Ga, ^{69}Ga, ^{15}N, and ^{14}N Knight shifts arising from coupling of the nuclei to delocalized electron charge carriers in the GaN conduction band. Bulk polycrystalline wurtzite GaN doped with 0.13% Ge as a shallow donor exhibits a temperature-independent distribution of ^{71}Ga Knight shifts over the temperature range 123–473 K. Each Knight shift frequency in the inhomogeneously broadened spectrum is characterized by a ^{71}Ga spin-lattice relaxation time T_1 that is in good agreement with the value predicted by the theoretical Knight-Korringa relation across the broad range of temperatures. Similarly, annealed nanocrystalline wurtzite GaN (50–100 nm, and without Ge) exhibits a ^{71}Ga Knight shift distribution and T_1 values (at 295 K) that follow

the same Knight-Korringa behavior. Thus, both bulk and nanocrystalline forms of GaN are n type and well above the metal-insulator transition (MIT), the nanocrystals most likely as a result of incorporation of shallow donor oxygen atoms during synthesis. Carriers in both forms of samples exhibit the near-ideal characteristics of a degenerate Fermi gas of noninteracting spins. The observation of NMR signals from both atom types, Ga and N, allows for the direct spatial correlation of the local electronic structure at the two sites in the lattice, specifically the *s*-orbital character of the electronic wave function of conduction band electrons at the Fermi edge. The relative values of these carrier wave-function probabilities (nearly twice as great for the N atom as for the Ga) are in line with theoretical predictions. Analyses of ^{71}Ga, ^{69}Ga, ^{14}N, and ^{15}N NMR results, including double-resonance 2D ^{15}N{^{71}Ga} measurements, reveal electronic disorder in the form of broad distributions of local metallic properties (Knight shifts) that are shown to be spatially correlated on a subnanometer scale.

9.2 Introduction

Semiconductors heavily doped with shallow donors become metallic, acquiring useful electronic and photonic properties. Mott provided a quantitative estimate of the donor concentration required to induce such a transition,[1] known as the metal-insulator transition (MIT) or Mott transition. Physically, this corresponds to a transition between two extrema: (1) dilute isolated and independent shallow donors, that at low temperatures are un-ionized and have weakly bound electrons whose wave functions[2] typically extend over several lattice constants; and (2) concentrated and interacting shallow donors, whose overlapping wave functions form an impurity band that can lie below the conduction band or, at higher

concentrations, enter into it. Magnetic resonance techniques based upon observing either the electron spin, e.g., electron paramagnetic resonance (EPR) or the nuclear spin via the electron spin, e.g., electron-nuclear double resonance (ENDOR) have provided very detailed insights on local electronic structures in the first regime,[3–5] but not the second. Detailed experimental and theoretical understanding of the spatially varying electronic structures of heavily doped semiconductors is challenging because of the electronic disorder arising from the assumed random substitutions of shallow donors in the lattice.[6]

One of the few means of observing such electronic disorder over the atomic scale is provided by magnetic resonance techniques that exploit well-understood interactions between electron and nuclear spins. Extensive magnetic resonance studies on doped Si around the MIT, including nuclear magnetic resonance (NMR) studies,[7–11] have yielded important insights into local electronic structure. However, an unambiguous interpretation of the NMR results has proven difficult because of complications due to formation of impurity bands distinct from the conduction band.[9,10] Furthermore, no direct experimental evidence has yet been obtained for spatial variations in the electronic structure about individual atoms in metallic doped materials.

By working with the compound semiconductor hexagonal (or wurtzite) gallium nitride (h-GaN), which has technologically important applications in solid-state lighting and power electronics,[12,13] we have directly correlated spatial variations in the electronic structures of constituent atoms in semiconductor samples well above the MIT. The insights come from two main sources. There are frequency displacements, called Knight shifts (K), of the ^{71}Ga, ^{14}N, and ^{15}N NMR signals that arise here from nuclear hyperfine interactions with electrons

in the conduction band having *s*-orbital character.[14] There are also associated contributions to the overall spin-lattice relaxation rate T^{-1} from the Korringa relaxation term $T_K{}^{-1}$.[14]

Here, we show that both bulk polycrystalline GaN prepared from an alkali-metal flux containing Ga and Ge under N_2 pressure and containing 0.13 wt% Ge as a substitutional n-type dopant (GaN:Ge),[15] as well as annealed nanocrystalline GaN powders, are highly metallic, i.e. are well above the MIT. The results and analyses resolve widely differing interpretations of the electronic structure of nanocrystalline GaN powders manifested by their ^{69}Ga, ^{71}Ga, and ^{15}N NMR spectra.[11,16–21] The results also represent a detailed electronic structural characterization of a degenerately doped semiconductor in bulk and nanocrystalline forms. While both GaN:Ge and nanocrystalline GaN materials exhibit properties that are characteristic of degenerate Fermi gases of noninter- acting spins, the local metallic properties, as reflected by the Knight shifts and Korringa relaxation rates, vary widely over subnanometer length scales. We determine the ratio of *s*-orbital carrier wave-function probabilities at the Fermi edge, with the N atoms having significantly more *s* character than the Ga atoms regardless of the local metallic property. Furthermore, the spatial correlation of local metallic properties at different neighboring spin pairs (in this case ^{71}Ga and ^{15}N or ^{14}N) provides a strong indication that the Knight shift distributions are due to electronic disorder related to the proximities to randomly located shallow donors.

9.3 Results and discussion

9.3.1 Bulk polycrystalline GaN:Ge

Both ^{71}Ga and ^{14}N magic-angle spinning (MAS) NMR spectra of GaN:Ge show broad Knight-shifted signals arising from distributions of ^{71}Ga and ^{14}N electronic environments.

Figure 9.1a shows the central transitions (+1/2 to −1/2) of six overlaid ^{71}Ga MAS NMR spectra acquired at temperatures from 123 to 473 K. The small narrow peak at ca. 332 ppm corresponds to undoped h-GaN[22] and is assigned to regions of the sample that experience no Knight shift. The considerably broader ^{71}Ga signals dominating the spectra arise from regions of the sample having different Knight shifts.[15] Unlike doped Si above the MIT,[23] the distribution of Knight-shifted intensity is essentially temperature independent when the weak temperature-dependence of the GaN lattice parameters[24] are taken into account.[25] The temperature-independence of the Knight shift K over the temperature range 123–473 K was used to estimate a lower bound for the Fermi level in GaN:Ge, which yielded a Fermi temperature of ~4500 K and a corresponding Fermi energy for the conduction-band electrons of ca. 400 meV above the bottom of the conduction band.

The ^{14}N spectrum of GaN:Ge in Fig. 9.1b corroborates and extends these conclusions. It has a centerband region showing a weak narrow signal at −302 ppm, the same shift as observed for undoped h-GaN.[22] A dominant inhomogeneously broadened peak is also present at −202 ppm, reflecting a distribution of Knight shifts. In addition to the centerband, a set of spinning sidebands spaced at integer multiples of the spinning rate (12 kHz) manifest the ^{14}N nuclear quadrupole coupling constant (NQCC) arising from (first-order) interactions between the nuclear electric quadrupole moments and the electric field gradients at the nuclei. The NQCC is axially symmetric (asymmetry parameter η = 0), with a quadrupole coupling constant Cq (=$e2\ Qq\ /h$) of 24.14 kHz at 296 K.[26]

The inset in Fig. 9.1b shows a region centered on the +1 sideband superimposed upon an equivalent region of the centerband and normalized to the same peak height. The greater intensity on the left side of the sideband spectrum indicates that those regions of GaN:Ge

having larger Knight shifts also have significantly altered anisotropic interactions that cause their sideband intensities to increase relative to the centerband. In principle these altered interactions could result from changes in the electric field gradients at the ^{14}N sites that change the NQCC or from an increase in the ^{14}N chemical shift anisotropy from its value of zero in an undoped GaN film.[26] Although the latter cause seems less likely, the corresponding increase in intensity of Knight-shifted regions seen for the −1 sideband is somewhat less than that for the +1 sideband, an asymmetric behavior that is not expected for alterations of the NQCC alone. This correlation between the charge (NQCC, or possibly chemical shift as well) and the spin (Knight shift) effects of dopants has been seen in ^{71}Ga spectra of GaN films[27] and suggests that the most Knight-shifted ^{14}N and ^{71}Ga nuclei are closest to the dopants.

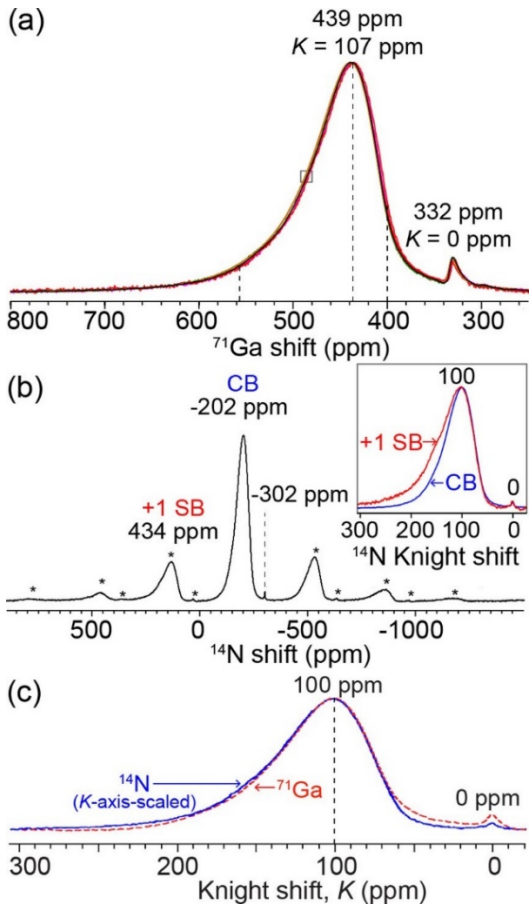

Figure 9.1. MAS-NMR spectra of bulk GaN:Ge powder at 11.7 T. (a) Overlaid ^{71}Ga spectra (5-kHz MAS, 15-s delay) at different temperatures from 123 to 473 K; (b) ^{14}N rotor-

synchronized Hahn-echo NMR spectrum (12-kHz MAS, 20-s delay) acquired at 295 K. Spinning sidebands (SB) are indicated by asterisks. (c) Comparison of the Knight shift distributions of ^{71}Ga and ^{14}N (obtained by summing the center band and three pairs of side bands), with normalized peak heights and with an *x* axis corresponding to the ^{71}Ga Knight shift and the ^{14}N Knight shift scaled by a factor of 1.059 to give the best overlap.

Complementary analyses of the ^{71}Ga and ^{14}N Knight-shift distributions directly relate the conduction electron density at Ga and N lattice sites. The Knight shift K due to the contact interaction in a Fermi gas of noninteracting electron spins, after replacing the spin contribution to the susceptibility χ_e^s by $\gamma_e^2\hbar^2\rho_0(E_f)/2$, is described by[14]

$$K = \frac{4\pi}{3}\gamma_e^2\hbar^2|u_k(0)|^2E_f\rho_f(E_f) \quad (1)$$

Here, $|u_k(0)|^2E_f$ is the probability of an electron at the Fermi level in an s-orbital being at the nucleus, $\rho_0(E_f)$ is the density of states (DOS) of this s-orbital at the Fermi level, γ_e is the electron gyromagnetic ratio, and $\hbar$ is Planck's constant. Interestingly, after scaling the ^{14}N frequency axis by a factor of 1.059, the shapes of the ^{71}Ga and ^{14}N intensity distributions are nearly identical, as shown in Figure 9.1c. This suggests that each ^{71}Ga nucleus associated with a particular ^{71}Ga Knight shift isochromat has neighboring ^{14}N nuclei with correlated Knight shifts. The scaling factor provides a direct experimental means of comparing, at both atomic sites, the relative s-orbital characters of the conduction band electrons at the Fermi edge, which may be calculated from density functional theory. A more detailed discussion of this comparison is provided in ref. 25.

9.3.2 Korringa T_1 relaxation of ^{71}Ga and ^{14}N

Associated with Knight shifts is the Korringa spin-lattice relaxation time $T_{1,K}$, which for the Fermi gas of non-interacting electrons assumed in Eq.1 is given by[14]

$$\frac{1}{T_{1,K}} = \left(\frac{\gamma_n}{\gamma_e}\right)^2 \frac{4\pi k_B T}{\hbar} K^2 \qquad (2)$$

where k_B is Boltzmann's constant and γ_n is the nuclear gyromagnetic ratio. Figure 9.2 summarizes ^{71}Ga $T_{1,K}$ measurements on GaN:Ge over the temperature range 123 K to 473 K. The inset to Fig. 9.2a depicts the two rate constants W_1 and W_2 characterizing the single- and double-quantum quadrupolar relaxation processes, respectively, and the single rate constant W characterizing the magnetic (Korringa) relaxation process. Since $W_1 = W_2$ in GaN,[28] the single-exponential time constant T_1 obtained from fitting the saturation-recovery intensities (with complete saturation of all three transitions, a condition that was shown to be necessary to obtain physically-meaningful ^{71}Ga relaxation results[21]) at each frequency in the spectrum obeys the equation[28] $1/T_1 = 2W_1 + 2W$. Thus, subtracting the quadrupolar relaxation term, measured at the zero-Knight shift peak, from the measured $1/T_1$ at any given frequency position in the spectrum yields $1/T_{1,K}$ (= 2W), the Korringa relaxation rate[15] (making the reasonable assumption that the quadrupolar relaxation term is constant across the Knight-shifted spectrum). By Eq. 2, this rate is proportional to K^2 and $T_{1,K}$ is expected to depend linearly upon $1/T$ with a zero intercept for all K.

Using a reduced variable for the ordinate, $T_{1,K}K^2$, the relaxation data is shown in Fig. 9.2a for six different temperatures from 123 to 473 K for three representative Knight shifts to a single theoretical dashed line obtained from Eq. 2. The linearity, slope, and zero intercept of the data for the various K values agree very well with the theoretical prediction, which involves no adjustable parameters. Temperature-dependent Korringa relaxation in n-type GaN has been previously observed under conditions where a Knight shift measurement was not possible.[29] Figure 9.2b shows the square root of $T_{1,K}^{-1}$ plotted against K for three representative temperatures, along with theoretical predictions based upon Eq. 2 (shown as

dashed lines, and again involving no adjustable parameters). The deviations shown in the inset for small Knight shifts (< 60 ppm) at low temperature (173 K) may represent the effects of freezing out and localization of donor electrons onto Ge sites, leading to more rapid relaxation at lower temperatures than predicted by the Korringa relation. The ^{14}N Knight shifted signals in bulk GaN:Ge have also been shown to exhibit Korringa-type relaxation.[25]

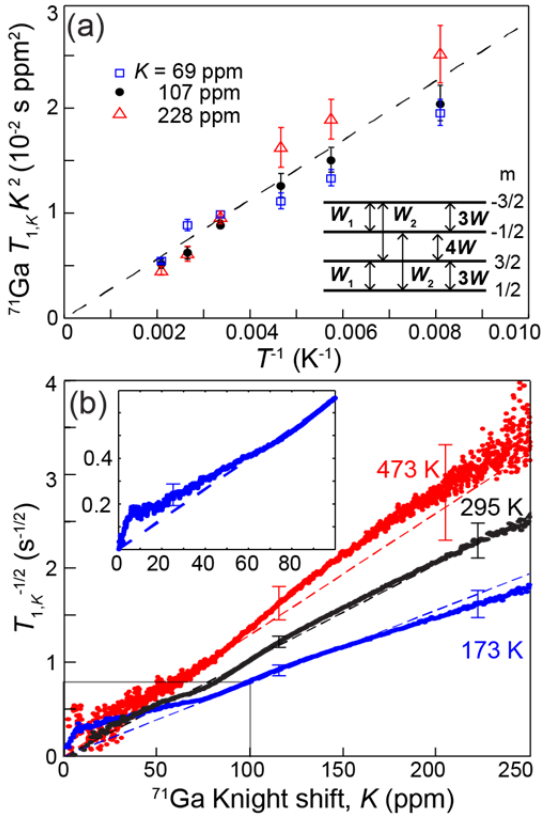

Figure 9.2. Plots of ^{71}Ga MAS-NMR spin-lattice relaxation times due to Korringa relaxation $T_{1,K}$ for different temperatures and Knight shifts K in GaN:Ge. (a) $T_{1,K}K^2$ versus inverse temperature for three representative Knight-shifted signals indicated by dashed lines in Fig. 9.1a. The dashed line is the theoretical prediction from Eq. 2. The inset shows transition rates between the ^{71}Ga (I = 3/2) Zeeman sublevels due to quadrupolar (W_1 and W_2) and magnetic (W) relaxation processes. (b) $T_{1,K}^{-1/2}$ plotted as a function of the ^{71}Ga Knight shift K at three temperatures; dashed lines are theoretical predictions from Eq. 2.

9.3.3 Photoluminescence properties, ^{71}Ga Knight shifts and Korringa-type T_1 relaxation in nanocrystalline GaN

Annealed nanocrystalline GaN materials manifest evidence for similar distributions of local metallic environments. The nanocrystalline GaN materials were produced by ammonolysis of GaO(OH) at 900-1100 °C with NH_3 and are crystalline h-GaN, as evidenced by the XRD patterns in Fig. 9.3a,b. Debye-Scherrer analyses of the nanocrystalline GaN yield mean crystallite sizes of 11 ± 4 nm and 66 ± 16 nm after ammonolysis at 900 °C and 1100 °C, respectively. The larger crystallite sizes formed at higher annealing temperatures are corroborated by the TEM images of the materials (Fig. 9.3c,d), which show that the particles are highly aggregated. Interestingly, the different nanocrystalline GaN materials yield markedly different photoluminescence properties (Fig. 9.3e), with the material annealed at higher temperature exhibiting *ca*. 4x greater photoluminescence intensity at somewhat lower energy (3.1 eV compared to 2.9 eV for the material annealed at 900 °C). The much improved photoluminescence intensity of the nanocrystalline GaN annealed at 1100 °C may be due in part to the greater degree of crystallinity, however, the shift in the position of the photoluminescence emission spectrum suggests that the different optoelectronic properties of the materials arise from differences in their electronic structures.

The ^{71}Ga NMR spectra (Fig. 9.4) of the nanocrystalline GaN show that the local ^{71}Ga environments depend strongly on the annealing temperature. The material annealed at 900 °C shows a single broad (25 ppm FWHM) ^{71}Ga signal at 331 ppm, which is the shift position of undoped bulk h-GaN.[22] By comparison, the nanocrystalline GaN material annealed at 1100 °C exhibits ^{71}Ga spectral features similar to bulk GaN:Ge are observed in the NMR spectra: a broad signal around 417 ppm and a relatively narrow peak (11 ppm FWHM) at the shift position of undoped bulk h-GaN at 331 ppm.[22] The ^{71}Ga spin-lattice relaxation times were obtained (using single-exponential fits) and analyzed as discussed above to obtain a plot of

$(T_{1,K})^{-1/2}$ versus K, Fig. 9.5, which is in excellent agreement with the theoretical line from Eq. 2. Similar distributions of ^{71}Ga Knight shifts, but affecting a smaller proportion of Ga atoms, are observed for the nanocrystalline GaN prepared at lower ammonolysis temperatures.[18,19] The ^{71}Ga NMR relaxation analyses establish conclusively that the nanocrystalline GaN is heavily doped above the MIT when annealed at 1100 °C, and demonstrate that synthesis of nanocrystalline GaN by ammonolysis is an effective way to introduce electrically-active dopants into a semiconductor nanomaterial, which can otherwise be difficult.[30] Such NMR techniques provide a promising tool for understanding heavily doped semiconductor nanomaterials, which have interesting plasmonic properties for optoelectronic applications[31] but for which bulk electrical characterization methods are often infeasible due to the difficulties associated with making electrical contacts.

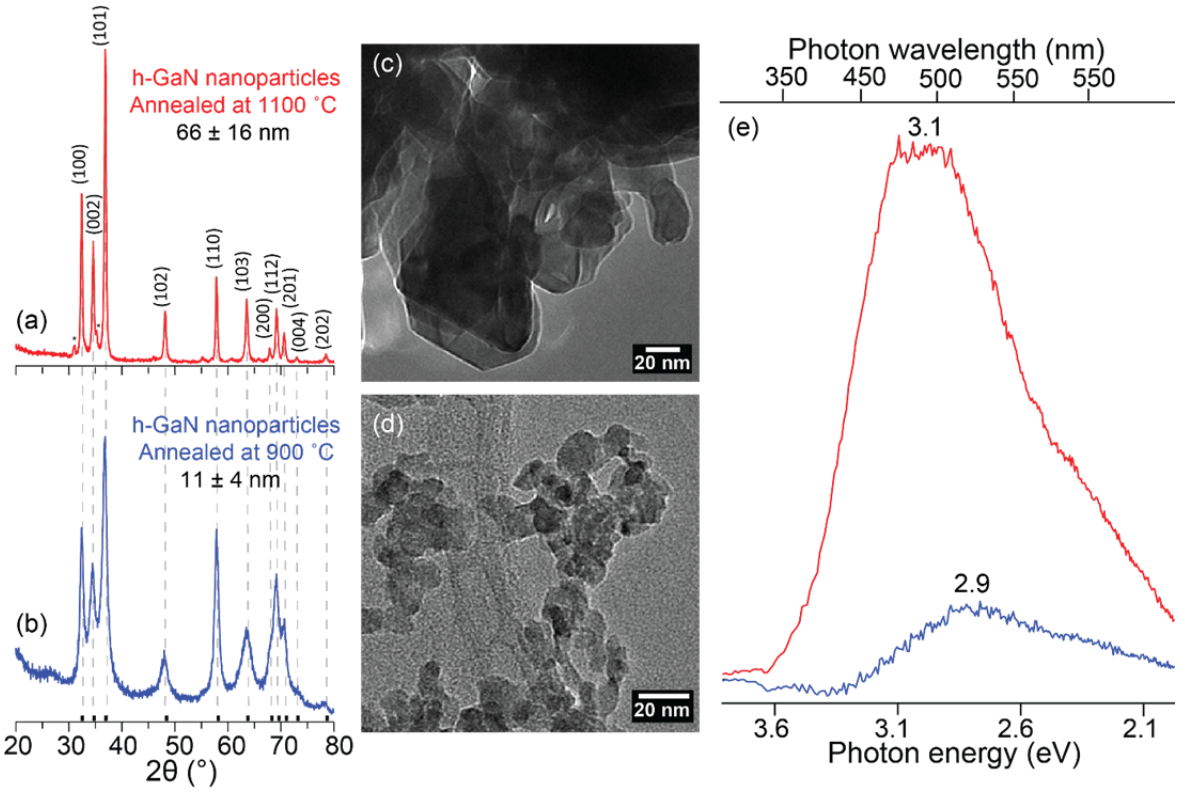

Figure 9.3. (a, b) Powder XRD patterns, (c, d) TEM images, and (e) photoluminescence spectra of nanocrystalline GaN prepared by ammonolysis at temperatures of (a,c, red)

1100 °C or (b,d, blue) 900 °C. The XRD reflections indexable to hexagonal h-GaN are indicated by dotted black lines in (a,b) and asterisks indicate reflections indexable to a minor β-Ga_2O_3 impurity. The nanocrystalline GaN synthesized at 900 ˚C display a broad, weak photoluminescence emission spectrum peaking at 2.9 eV. The nanocrystalline GaN synthesized at 1100 ˚C display a photoluminescence emission spectrum approximately four times as intense as those synthesized at a lower temperature, and shifted slightly to lower energies (3.1 eV).

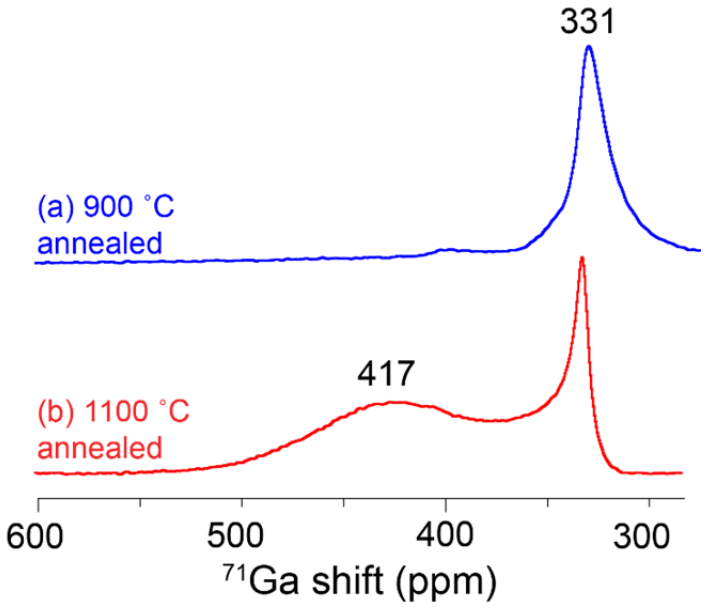

Figure 9.4. Solid-state ^{71}Ga Hahn-echo NMR spectra of nanocrystalline GaN prepared by ammonolysis at temperatures of (a) 900 °C or (b) 1100 °C, acquired at 18.8 T, 298 K, 18 kHz MAS.

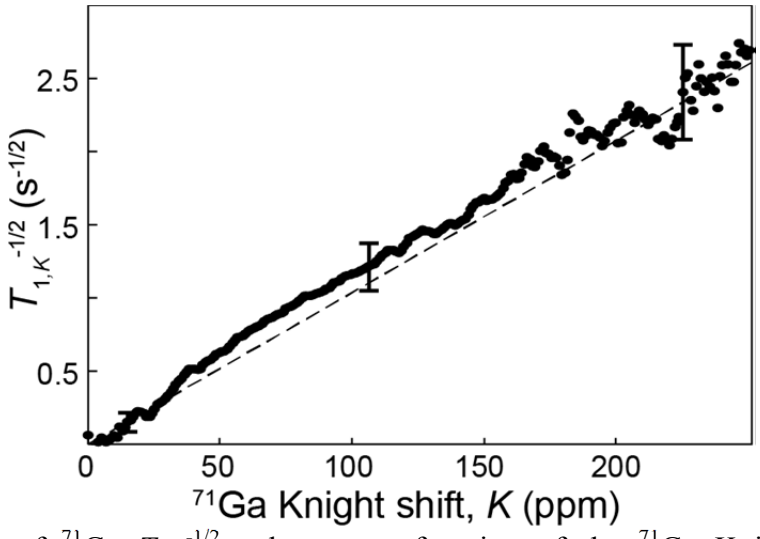

Figure 9.5. Plot of ^{71}Ga $T_{1,K}^{-1/2}$ values as a function of the ^{71}Ga Knight shift K for nanocrystalline GaN prepared by ammonolysis at 1100 °C. Data were acquired at 18.8 T, 298 K, and 5 kHz MAS. The dashed line is the theoretical prediction from Eq. 2.

9.3.4. Spatial correlation of ^{71}Ga and ^{15}N Knight shifts

The ^{71}Ga and ^{15}N Knight shifts in nanocrystalline GaN are spatially correlated over atomic length scales. This is established by the 2D ^{15}N{^{71}Ga} transferred-echo double resonance (TEDOR) spectrum in Fig. 9.6 of a ^{15}N-labelled nanocrystalline GaN (Ga^{15}N) sample. The TEDOR pulse sequence is used for transferring polarization from one type of nucleus to another type via relatively weak dipolar couplings.[32,33] The two-dimensional version, which has been developed and applied to polarization transfer from quadrupolar nuclei to spin-1/2 nuclei,[34,35] yields a 2D spectrum showing correlated signal intensity from spatially-proximate nuclear spin pairs that are dipole-dipole coupled. Here, the result is a 2D contour plot with ^{71}Ga and ^{15}N shift axes, and a 1D projection spectrum for ^{15}N. The relative intensity at each ^{15}N shift position reects the number of ^{15}N nuclei at a given ^{15}N shift that are dipole-coupled (through space, <1 nm) to ^{71}Ga nuclei having the range of ^{71}Ga shifts depicted in the 2D contour plot. Perfectly correlated ^{71}Ga and ^{15}N shifts would yield a contour plot consisting of a narrow diagonal ridge, which resembles what is experimentally observed in Fig. 9.6a.

The slope of the best-fit diagonal in Fig. 9.6a is 1.052±0.007 (^{71}Ga/^{15}N), the same (within experimental uncertainty) as the scaling factor of 1.059 (^{71}Ga/ ^{14}N) determined above for bulk GaN:Ge, Fig. 9.1c. This equivalence for the two different approaches indicates that the relative s-orbital characters of the conduction band electrons at the Ga and N sites are very similar in bulk Ge-doped and nanocrystalline GaN. Representative vertical slices extracted from the TEDOR spectrum, Fig. 9.6b, have widths that are considerably smaller than the over-all 1D ^{71}Ga spectrum, again indicating that the respective ^{71}Ga and ^{15}N Knight shifts from neighboring atoms in the nanocrystals are correlated.

There is an increasing spread in the frequency range of the ^{71}Ga nuclei in cross-peaks associated with a given ^{15}N frequency as one moves to larger Knight shifts in Fig. 9.6, a spread which reaches its maximum of about 60 ppm (^{71}Ga) width in the asymmetric high-frequency tail of the distribution. *A priori* this spread could arise from three possible sources involving either chemical shifts, NQCCs, or Knight shifts. Differential chemical shift changes of the two types of nuclei (e.g. from defects or surface effects) are ruled out as the explanation because of the near-linear correlation between the ^{71}Ga and ^{15}N, as expected for a distribution arising solely from Knight shifts.[25] NQCC effects could arise due to Ga atoms in the direct vicinity of defects such as O_N substitutions (or N vacancies) having strongly asymmetric environments resulting in much larger ^{71}Ga quadrupolar interactions and associated spectral broadening (so-called second-order quadrupolar broadening). However, such NQCC effects are ruled out on two grounds. First, previous ^{71}Ga MAS NMR results on similar GaN nanoparticle materials found little or no evidence for anisotropic second-order quadrupolar broadening effects across the Knight shift distribution.[19] Second, if such effects were responsible, then one would not expect Korringa-type relaxation behavior across the entire distribution of ^{71}Ga Knight shifts, as observed in Fig. 9.5.

We conclude that each ^{15}N Knight shift isochromat is correlated with a distribution of ^{71}Ga Knight shifts whose width increases for the larger ^{15}N Knight shifts. To understand how this might happen, consider the inset to Fig. 9.6a, which depicts a particular ^{15}N nucleus and the associated distances and calculated dipolar couplings to both a directly- bonded ^{71}Ga nucleus as well as to next-nearest-neighbor ^{71}Ga nuclei. There are 4 closest sites for ^{71}Ga nuclei, and 24 sites for ^{71}Ga nuclei separated by a gallium and a nitrogen atom (having dipolar couplings to ^{15}N that are 19% or 8% of the directly-bonded value). Thus, both

directly-bonded ^{71}Ga nuclei as well as next-nearest-neighbor ^{71}Ga nuclei will contribute to the observed signal intensity in the dipolar-coupling mediated ^{15}N{^{71}G} TEDOR spectrum shown in Figure 9.6a.

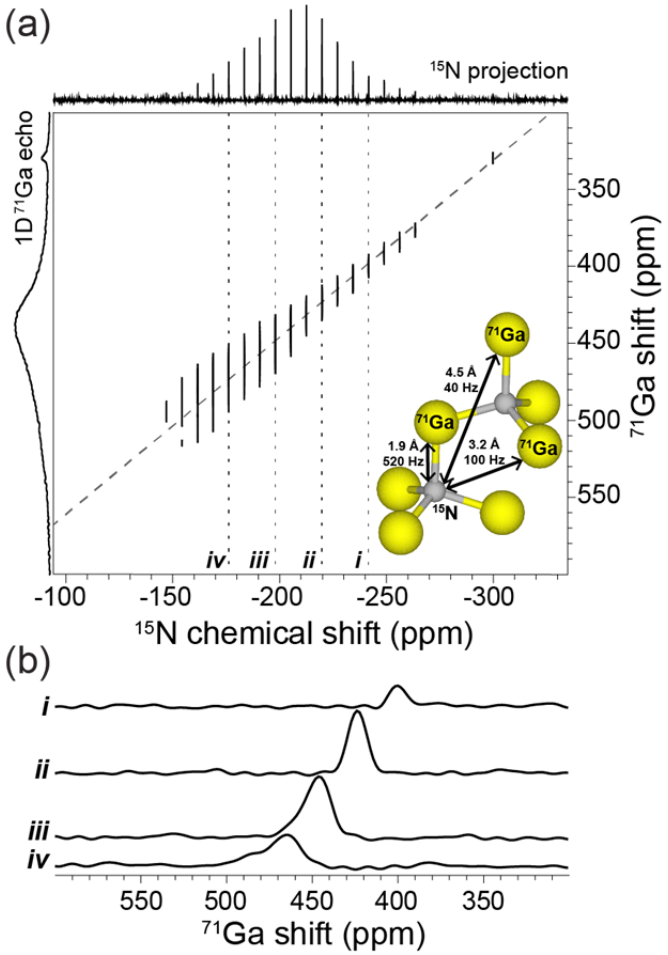

Figure 9.6. (a) Two-dimensional ^{15}N{^{71}G} dipolar-mediated TEDOR correlation spectrum (20 kHz MAS, 298 K, 18.8 T) of ^{15}N-enriched nanocrystalline GaN prepared by ammonolysis at 1100 °C. CPMG pulse sequence was used for detection to maximize the ^{15}N signal intensity, which yields a manifold of narrow peaks (spikelets) whose envelope reflects the ^{15}N shift distribution. A 1D ^{71}Ga echo spectrum acquired under the same conditions is shown along the vertical axis for comparison. (b) Slices extracted from the 2D spectrum at positions indicated by the Roman numerals.

The increasing spread in the frequency range of the ^{71}Ga nuclei in cross peaks associated with the most Knight-shifted ^{15}N nuclei can then be explained if those ^{15}N nuclei, such as depicted in the inset to Fig. 9.6a, 8 are close to the shallow donors, and thus experience the largest Knight shifts due to peaking of the wavefunction near donor sites.[36] Their 4 closest

sites for ^{71}Ga nuclei, and their 24 sites for next-nearest-neighbor ^{71}Ga nuclei would then have significantly different nanoscale proximities to the same shallow donor, and hence different ^{71}Ga Knight shifts.

This interpretation in terms of varying local metallic properties is consistent with the larger ^{14}N Knight shifts associated with N atoms closer to (Ge) shallow donors in GaN:Ge (Fig 9.1b). A rough estimate of the magnitude of this spatial variation of ^{71}Ga Knight shifts can be made by assuming that the 60 ppm ^{71}Ga linewidth described above is due to a 60 ppm difference in Knight shifts between two ^{71}Ga nuclei attached to the same N atom with a 3.20 □ separation (from the crystal structure of hexagonal GaN), and with the internuclear vector aligned with the dopant atom for maximal effect. This yields a Knight shift spatial variation in the regions nearest the dopant of ca. 20 ppm/□. The sensitivity of 2D NMR techniques to nanoscale variations of electronic structure thus provides a basis for spatially correlating the electronic properties of two atom types in compound semiconductors (bulk or nanocrystalline) doped above the MIT for comparison with theoretical calculations of such properties. The attribution of at least some part of the observed distribution of Knight shifts to nanoscale variations in electronic structure, based upon these experimental results, has significant implications. It indicates that interpreting observed Knight shift distributions in terms of macroscopic (rather than nanoscopic) probability distributions of carrier densities is not justifiable in the way originally proposed.[11,15]

9.3.5. Likely shallow donors in nanocrystalline GaN

Oxygen substitution on an N site (O_N) is likely to be present in the nanocrystalline GaN materials, which were prepared from an oxygen-containing precursor, GaO(OH). The XRD

pattern (Fig. 5(a)) of the nanocrystalline natural abundance GaN shows weak reflections that are indexable to β-Ga_2O_3 (< 3%), consistent with oxygen being present in the sample. This impurity is not visible in the ^{71}Ga NMR spectrum in Fig. 9.3b due to its dilute quantity and inhomogeneously broadened signals. Oxygen doping in GaN is usually associated with Ga vacancies (V_{Ga}), which act as triple acceptors and partially compensate the ON shallow donors. Typically, V_{Ga} and O_N are assumed to form a complex which acts as a deep level, and only the uncompensated O_N will act as shallow donors.[37] Nitrogen vacancies could also be present, given that the synthesis temperature is high enough to dissociate GaN under vacuum.[38] However, nitrogen vacancies are reported to be energetically unfavorable under n-type conditions, with a formation energy that depends greatly on Fermi level.[37]

The most energetically favorable shallow donors in n-type material are O_N, Si_{Ga}, and Ge_{Ga},[37] of which O_N is the most physically reasonable for the nanocrystalline GaN materials given the presence of oxygen in the starting material. The GaN wurtzite lattice can accommodate large concentrations of O atoms while maintaining tetrahedral coordination of Ga atoms.[39] However, Si_{Ga} cannot be completed ruled out since the nanocrystalline GaN was prepared by ammonolysis was in alumina crucibles, and typical alumina ceramics use silica-based sintering aids in their manufacture. A recent modeling study based on hybrid functional calculations[40] predicted similar shallow-donor electronic behaviors for O_N and Ge_{Ga} substitution defects in GaN, which is fully consistent with our analyses of the similar NMR spectral features and corresponding electronic structures observed here for nanocrystalline GaN and bulk GaN:Ge. These results are also consistent with previous results[19] for nanocrystalline GaN synthesized differently, which exhibited a broad distribution of Knight-shifted intensities.

9.4 Conclusions

In summary, ^{71}Ga, ^{14}N, and ^{15}N MAS-NMR experiments have provided detailed new insights on the similar local electronic structures of nanocrystalline and doped bulk GaN. They reveal the highly metallic character of both bulk GaN heavily doped n-type with Ge and nanocrystalline GaN made by high temperature ammonolysis, and conclusively demonstrate the origin of the shifts observed in the latter material to be conduction band electrons. Such high carrier concentrations in nanocrystalline GaN are most likely due to oxygen atoms from the GaO(OH) precursor, which are known to give rise to n-type GaN in bulk.

Measurements of Korringa spin-lattice relaxation times for differing Knight shifts across the spectra prove that both forms of GaN are well above their MIT, with carriers exhibiting the near-ideal characteristics of a degenerate Fermi gas of non-interacting spins. This close approach to ideal behavior, which contrasts with deviations from ideal Korringa behavior often observed for true metals,[41] can be attributed to the orders of magnitude lower carrier concentration in the degenerately-doped semiconductor.

Although the magnitude and character of the conduction electron wavefunction at the Group III and Group V nuclear sites have been measured in other bulk metallic semiconductors,[42] this is the first determination of the Group V/III ratio of s-orbital carrier wavefunction probabilities at the Fermi edge across the entire distribution of Knight shifts in both bulk doped and nanocrystalline materials, with the N to Ga ratios equal to ca. 1.7 for both forms.

Two-dimensional ^{15}N{^{71}Ga} NMR results establish that the local metallic properties (Knight shifts) at Ga and N sites are spatially correlated on a sub-nanometer scale. They

provide additional evidence that distributions of Knight shifts are due to electronic disorder arising from differing proximities to randomly located shallow donors. This conclusion has been reached more indirectly by a theoretical model accounting for ^{29}Si Knight shift distributions in doped silicon.[43] Such detailed insights on atomic-level electronic structures are expected to be relevant generally to Group III-V and other technologically important semiconducting solids. The present approach to observing spatial correlations in electronic structure between different atom types should thus prove valuable in future investigations of nanocrystalline semiconductors, where the effects of interfaces and randomly-substituted dopants on the MIT are not well understood, and in comparisons of their properties to those in doped bulk analogs.

9.5 Materials and methods

Materials Synthesis

Nanocrystalline gallium nitride was synthesized by ammonolysis of micron-sized gallium oxide hydroxide (GaO(OH)) particles as previously reported.[19] Micron-sized GaO(OH) particles were prepared by placing 60 mL of 0.1 M aqueous gallium nitrate solution in a sealed container containing an excess amount (200 mL) of 1.2% NH_4OH solution. The gallium nitrate solution was stirred rapidly with a magnetic stir bar and allowed to react with the ammonia-containing atmosphere for 18 hours, after which the resulting white precipitate was collected by vacuum filtration, washed with deionized water, and dried under air. The product was identified as crystalline GaO(OH) by powder X-ray diffraction, with some amorphous component seen in the TEM, and characterized by ^{71}Ga MAS-NMR.

To prepare nanocrystalline GaN, the as-synthesized GaO(OH) powder was crushed to a powder, placed in an alumina crucible, and loaded into a quartz Schlenk tube. The tube was placed in a tube furnace and purged with nitrogen for 30 minutes prior to heating. The tube furnace was ramped to 750 ˚C at a rate of 15 ˚C/min under a flow of nitrogen gas. The nitrogen flow was turned off and was replaced by an ammonia flow of 20 standard cm^3/min. For the synthesis of ^{15}N-enriched nanocrystalline GaN, ammonia enriched to 99.9% in ^{15}N was used. The tube furnace was then ramped to the annealing temperature of 900 or 1100 ˚C. The reaction was allowed to proceed for 2 hours, after which the tube was cooled to room temperature under continued ammonia flow. The resultant light yellow GaN powders were stored in sealed vessels in a vacuum desiccator to prevent degradation due to hydrolysis or oxidation.

The bulk Ge-doped GaN sample was synthesized by a Na/K flux method and characterized as described previously.[15]

Materials characterization

The powder XRD measurements on the nanocrystalline GaN were conducted at room temperature on a Rigaku SmartLab High Resolution X-Ray Diffractometer or a Panalytical Empyrean Powder X-Ray Diffractometer in θ-2θ mode using Cu Kα radiation with a wavelength of 1.54 Å. TEM micrographs were acquired using an FEI Tecnai G2 Sphera microscope with an acceleration beam voltage of 200 kV and a Gatan UltraScan 1000P CCD camera for image recording. Nanocrystalline GaN was prepared for TEM measurements by dispersing 1 mg of the powdered sample in 1 mL of dry methanol, sonicating for 10 – 15 minutes, and dispensing one to two drops of the suspension on a lacey carbon TEM grid.

MAS-NMR measurements

For bulk Ge-doped GaN, ^{71}Ga (152.5 MHz) saturation-recovery data and the ^{14}N (36.1 MHz) Hahn echo spectrum in Fig. 1(b) were obtained on a Varian/Agilent DDRS 11.7 T NMR spectrometer using a variable-temperature 4.0 mm triple-resonance probe. The 90° pulse length for the central transition of ^{71}Ga was 1.7 μs, and for the non-selective ^{14}N transitions 10 μs. Chemical shifts for both nuclei were referenced to a 1M $Ga(NO_3)_3$ aqueous solution at zero ppm. A spectral width of 250 kHz (1.25 MHz) with 12800 (64000) data points were used for the ^{71}Ga, and ^{14}N spectra respectively. The ^{14}N spectrum was obtained with a rotor-synchronized π/2-τ-π-Acquire Hahn echo pulse sequence with the delay between the midpoint of the pulses set to 83.3 μs, the inverse of the 12 kHz MAS rate; the data were Fourier-transformed after shifting to the echo maximum. Both central and satellite ^{71}Ga transitions were saturated by applying a train of sixty 1.7 μs pulses at 74 kHz from the central transition frequency spaced 2016 μs apart and thus asynchronous with the 200 μs rotor period. An asynchronous saturation pulse train has been shown to yield more reliable T_1 values than alternative methods.[21] An array of 30 saturation-recovery delay times was used with 64 scans for each delay, with a recycle delay of 0.5 s. The saturation-recovery curves were fit in MATLAB to a single exponential recovery from zero. At the shortest recovery time (3.3 ms) the signal intensity at the Knight shift maximum was only about 2% of the fully-recovered intensity, consistent with good saturation of the transition, and the measured T_1 for the maximal intensity Knight-shifted peak at 295 K of 0.497 ± 0.003 s agrees well with the corresponding carefully-determined "true T_1" in the same sample at 294 K of 0.491±0.001 s.[21]

A recycle delay of 20 s was used to acquire 12056 scans (67 h) for the ^{14}N MAS-NMR spectrum of GaN:Ge. Based on the measured T_1 values, this results in a partial saturation of

the weak sharp zero Knight shift peak (3.0 ppm FWHM) as well as that portion of the spectrum with small Knight shifts. The smaller ^{14}N relative to ^{71}Ga intensity seen in this region in Fig. 9.1c is attributed to this partial saturation effect. In Fig. 9.1b the symmetrically situated peaks on either side of the centerbands of both the zero Knight shift peak and that of the Knight shift distribution are spinning sidebands arising primarily from the ^{14}N NQCC (= e2Qq/h), which in undoped GaN is 24.14 kHz.[44] A line-broadening apodization of 36 Hz (1.0 ppm) was used. The method of summing centerband and sidebands in Fig. 9.1c is essentially that of two-dimensional one-pulse (TOP) NMR, in the present case obtained by summing offset sections of the total spectra having spectral widths of the MAS rate.

The ^{71}Ga and ^{15}N MAS NMR measurements of the nanocrystalline GaN samples were performed on a Bruker AVANCE-III Ultrashield Plus 800 MHz (18.8 T) narrow-bore spectrometer operating at Larmor frequencies of 244.1 and 81.1 MHz for ^{71}Ga and ^{15}N, respectively, and using a Bruker 3.2 mm broadband Bruker Tri-Gamma H-X-Y probehead. The ^{71}Ga shifts were referenced to a 0.1 M gallium nitrate solution at 0.0 ppm. In order to provide a comparison to the ^{14}N shifts in GaN:Ge referenced to a 1 M gallium nitrate, the ^{15}N shifts were measured against ^{15}N-labeled glycine but then adjusted to the ^{15}N shift of a 1 M aqueous nitrate solution.

The ^{71}Ga spin-lattice (T_1) relaxation times of the nanocrystalline GaN sample were measured by using a saturation recovery pulse sequence with a rotor-asynchronous saturating pulse train with a ^{71}Ga $\pi/2$ pulse of 1.3 μs. The solid-state 2D ^{15}N{ ^{71}Ga} transferred-echo double resonance (TEDOR) spectrum of nanocrystalline Ga ^{15}N was acquired using a π pulse length of 10 μs on ^{71}Ga to reintroduce the heteronuclear ^{15}N- ^{71}Ga dipolar couplings. To maximize signal intensity in the direct dimension, the spectrum was acquired using the Carr-

Purcell-Meiboom-Gill (CPMG) acquisition method, by generating and acquiring series of echoes, accumulating the signal of all these echoes and co-adding for each transient. Signal enhancement is only obtained in favorable cases where the spectrum is broad relative to the inverse of the lifetime of transverse coherences (*i.e.* where the inhomogeneous linewidth is much larger than the homogeneous one). This is typically the case for ^{15}N nuclei in the nanocrystalline Ga ^{15}N, since the width of the one-dimensional ^{15}N spectrum is on the order of 10^2 ppm (*i.e.*, 8×10^3 Hz at 18.8 T) due to Knight shift distributions while the inverse transverse dephasing times measured here are on the order of 1 Hz. For each scan, 320 echoes were collected during the acquisition for a total acquisition time of 0.55 seconds. This yields a signal intensity increase by a factor of ca. 18 as compared to a spectrum collected without CPMG acquisition. Furthermore, in this experiment, the fast-relaxing ^{71}Ga nucleus is excited first and then transfers its magnetization to nearby ^{15}N nuclei using the TEDOR pulse sequence, which means that experiments can be repeated rapidly. As most of the ^{71}Ga magnetization is recovered during the 0.55 s during which the ^{15}N signal is collected, the experiment can be repeated immediately, and thus the recycle delay was set to 1 ms.

9.6 References

(1) Mott, N. F. *Adv. Phys.* **1972**, *21* (94), 785.
(2) Kohn, W.; Luttinger, J. M. *Phys. Rev.* **1955**, *98* (4), 915.
(3) Hale, E. B.; Mieher, R. L. *Phys. Rev.* **1969**, *184* (3), 739.
(4) Ivey, J. L.; Mieher, R. L. *Phys. Rev. B* **1975**, *11* (2), 849.
(5) Orlinskii, S. B.; Schmidt, J.; Groenen, E. J. J.; Baranov, P. G.; de Mello Donega, C.; Meijerink, A. *Phys. Rev. Lett.* **2005**, *94* (9), 97602.
(6) Belitz, D.; Kirkpatrick, T. R. *Rev. Mod. Phys.* **1994**, *66* (2), 261.
(7) Kobayashi, S. I.; Fukagawa, Y.; Ikehata, S.; Sasaki, W. *J. Phys. Soc. Jpn.* **1978**, *45* (4), 1276.
(8) Hirsch, M. J.; Holcomb, D. F. *Phys. Rev. B* **1986**, *33* (4), 2520.
(9) Meintjes, E.; Danielson, J.; Warren, W. *Phys. Rev. B* **2005**, *71* (3), 35114.
(10) Hoch, M. J. R.; Holcomb, D. F. *Phys. Rev. B* **2005**, *71* (3), 35115.
(11) Yesinowski, J. P. *"Solid State NMR of Inorganic Semiconductors";* Topics in Current Chemistry; Springer: Berlin, 2012; Vol. 306.
(12) Mishra, U. K.; Shen, L.; Kazior, T. E.; Wu, Y. F. *Proc. IEEE* **2007**, *96* (2), 287.
(13) Denbaars, S. P.; Feezell, D.; Kelchner, K.; Pimputkar, S.; Pan, C. C.; Yen, C. C.; Tanaka, S.;

Zhao, Y.; Pfaff, N.; Farrell, R.; Iza, M.; Keller, S.; Mishra, U.; Speck, J. S.; Nakamura, S. *Acta Mater.* **2013**, *61* (3), 945.
(14) Slichter, C. P. *Principles of Magnetic Resonance, Third Edition*; Springer-Verlag: Berlin, 1990.
(15) Yesinowski, J. P.; Purdy, A. P.; Wu, H. Q.; Spencer, M. G.; Hunting, J.; DiSalvo, F. J. *J. Am. Chem. Soc.* **2006**, *128* (15), 4952.
(16) Schwenzer, B.; Hu, J.; Wu, Y.; Mishra, U. K. *Solid State Sci.* **2006**, *8* (10), 1193.
(17) Jung, W. *Mater. Lett.* **2004**, *58* (24), 3058.
(18) Drygas, M.; Olejniczak, Z.; Grzanka, E.; Bucko, M. M.; Paine, R. T.; Janik, J. F. *Chem. Mat.* **2008**, *20* (21), 6816.
(19) Schwenzer, B.; Hu, J.; Morse, D. E. *Adv. Mater.* **2011**, *23* (20), 2278.
(20) Drygaś, M.; Jeleń, P.; Bućko, M. M.; Olejniczak, Z.; Janik, J. F. *RSC Adv.* **2015**, *5* (100), 82576.
(21) Yesinowski, J. P. *J. Magn. Reson.* **2015**, *252*, 135.
(22) Yesinowski, J. P.; Purdy, A. P. *J. Am. Chem. Soc.* **2004**, *126* (30), 9166.
(23) Meintjes, E. M.; Warren, J. W. W.; Yesinowski, J. P. *Solid State Nucl. Magn. Reson.* **2013**, *55–56* (0), 91.
(24) Minikayev, R.; Paszkowicz, W.; Piszora, P.; Knapp, M.; Bahtz, C.; Podsiadlo, S. *X-Ray Spectrom.* **2015**, *44* (5), 382.
(25) Yesinowski, J. P.; Berkson, Z. J.; Cadars, S.; Purdy, A. P.; Chmelka, B. F. *Phys. Rev. B* **2017**, *95* (23), 1.
(26) Purdy, A. P.; Yesinowski, J. P.; Hanbicki, A. T. *Phys. Status Solidi C Conf.* **2005**, *2* (7), 2437.
(27) Mahadik, N. A.; Qadri, S. B.; Rao, M. V; Yesinowski, J. P. *Appl. Phys. A* **2007**, *86* (1), 67.
(28) Yesinowski, J. P. *J. Magn. Reson.* **2006**, *180* (1), 147.
(29) Corti, M.; Gabetta, A.; Fanciulli, M.; Svane, A.; Christensen, N. *Phys. Rev. B* **2003**, *67* (6), 64416.
(30) Norris, D. J.; Efros, A. L.; Erwin, S. C. *Science.* **2008**, *319* (5871), 1776.
(31) Liu, X.; Swihart, M. T. *Chem. Soc. Rev.* **2014**, *43* (11), 3908.
(32) Hing, A. W.; Vega, S.; Schaefer, J. *J. Magn. Reson.* **1992**, *96* (1), 205.
(33) Hing, A. W.; Vega, S.; Schaefer, J. *J. Magn. Reson. Ser. A* **1993**, *103* (2), 151.
(34) Fyfe, C. A.; Mueller, K. T.; Grondey, H.; Wong-Moon, K. C. *Chem. Phys. Lett.* **1992**, *199* (1–2), 198.
(35) Amoureux, J. P.; Trebosc, J.; Tricot, G. *Magn. Reson. Chem.* **2007**, *45*, S187.
(36) Meyer, J. R.; Bartoli, F. J.; Mott, N. F. *Phil. Mag. B* **1985**, *52* (4), L51.
(37) de Walle, C. G. *J. Appl. Phys.* **2004**, *95* (8), 3851.
(38) Unland, J.; Onderka, B.; Davydov, A.; Schmid-Fetzer, R. *J. Cryst. Growth* **2003**, *256* (1–2), 33.
(39) Mishra, K.; Schmidt, P.; Laubach, S.; Johnson, K. *Phys. Rev. B* **2007**, *76* (3), 35127.
(40) Gordon, L.; Lyons, J. L.; Janotti, A.; de Walle, C. G. *Phys. Rev. B* **2014**, *89* (8), 6.
(41) Winter, J. *Magnetic Resonance in Metals*; The International Series of Monographs on Physics; Clarendon Press: Oxford, 1971.
(42) Tunstall, D. P. *J. Phys. C-Sol. State Phys.* **1988**, *21* (15), 2853.
(43) Kamimura, H. *Philos. Mag.* **1974**, *29* (1), 65.
(44) Yesinowski, J. P. *Phys. Status Solidi C - Conf. Crit. Rev. Vol 2, No 7* **2005**, *2* (7), 2399.

Chapter 10

Conclusions and outlook

The objective of this dissertation has been to elucidate the atomic-scale origins of macroscopic properties for diverse complicated and heterogeneous materials, focusing particularly on the influences of non-stoichiometric species at surfaces and interfaces. The goal has been to measure, understand, and correlate the atomic-scale surface structures, interactions, and properties of nanostructured inorganic materials with applications for the conversion, storage, and utilization of energy including zeolite catalysts, nanocrystalline semiconductors, and precious-metal-free electrocatalysts. Atomic-level insights are provided by state-of-the-art surface characterization techniques, most notably multidimensional solid-state nuclear magnetic resonance spectra (NMR) with sensitivity enhanced by high magnetic field strengths, low temperatures, and/or dynamic nuclear polarization (DNP). The solid-state NMR analyses, with complementary X-ray diffraction and electron microscopy measurements, yield detailed information on the local structures, compositions, and interactions of dilute heteroatom, defect, and/or surface species that determine the macroscopic adsorption, reaction, optical, or electronic properties of the materials. The atomic-level insights are correlated to bulk macroscopic material properties in order to develop new design rules for synthetic and post-synthetic treatment of the materials to improve the desired qualities. Though the materials here studied vary in composition, structure, and application, the overall unifying themes are: (1) analysis of order and disorder in semi-crystalline inorganic solids using state-of-the-art diffraction and spectroscopic characterization techniques; (2) determining the distributions and structures of non-

stoichiometric species, particularly at surfaces and interfaces; and (3) correlating atomic-level structures and compositions with macroscopic material properties.

For aluminosilicate zeolite catalysts with applications in hydrocarbon conversion and pollution removal, the results and analyses presented here provide new insights into the crystallization pathways, heteroatom distributions, and molecular interactions of different exterior and nanopore surface adsorption/reaction sites. Mesostructured zeolite nanosheets are shown to crystallize through non-topotactic rearrangement and condensation of layered silicate intermediates (Ch. 2). The layered molecular sieve SSZ-70 possesses different types of structural silanol groups in its interlayer regions, which are promising targets for future catalytic modification (Ch. 3). In aluminosilicate Al-SSZ-70, the types and distributions of Al heteroatoms are determined, with preferential siting of Al at the surfaces of the interlayer channels (Ch. 4). In such aluminosilicate zeolites, Al heteroatoms are associated with molecular adsorption and catalytic reaction sites and understanding their distributions is crucial in order to develop molecular level understanding of the catalytic properties. However, determining the Al distributions and occupancies at different sites in zeolite frameworks has been a long-standing challenge and is typically infeasible using conventional scattering techniques. Recently-developed solid-state NMR techniques, presented here, allow the positions of Al heteroatoms within zeolite frameworks to be determined and their occupancies quantified. These techniques are fully generalizable and will enable new insights into the distributions of Al heteroatoms in diverse other aluminosilicate zeolite materials.

For example, here the methods and analyses are extended to ultrastable Y (USY) zeolites catalysts, which are of high importance for fluidized catalytic cracking (FCC) processes that produce gasoline (Ch. 5). In USY zeolite catalysts, different types of Al heteroatom

environments within the zeolite nanopores and at surface exterior defect sites are resolved and identified. The different Al sites are shown to be associated with different molecular adsorption properties, with partially-crosslinked -Al-OH-Si-OH moieties at the zeolite particle exterior surfaces acting as adsorption sites for bulky carbonaceous deactivation products formed during catalytic reaction. The identification of specific molecular adsorption sites that are associated with zeolite deactivation processes is an important step in correlating the atomic compositions and structures with the macroscopic reaction/deactivation properties of zeolite catalysts. Future work will focus on developing synthetic- or post-synthetic methods to passivate the surface defect sites most prone to deactivation and thereby improve zeolite catalyst stability for FCC reactions.

Reaction of colloidal Al_2O_3 and SiO_2 particles in highly alkaline media (6 M NaOH) is shown to rapidly form a partially-crosslinked aluminosilica IPB network that contains only small quantities (<2%) of the total Al in the material. The aluminosilica network is shown to gradually rearrange over long reaction times (days-weeks) by condensation of Al-OH and Si-OH bonds to form a dense cementitious IPB, with concomitant release of water (Ch. 6). The formation of Al-O-Si and Si-O-Si bonds within the aluminosilica network correlates to the development of macroscopic material strength of the IPB, providing molecular-level insights that are expected to yield design rules for improving future IPB formulations.

Mesoporous carbon materials containing Fe and/or N heteroatoms are promising alternatives to Pt/carbon electrocatalysts for applications in fuel cells and battery materials. The local environments of Fe and N heteroatoms are elucidated for high-N-content Fe,N-carbon materials with electrocatalytic activities that approach or exceed conventional Pt/carbon catalysts (Ch. 7). In the absence of Fe, isolated pyridinic N sites are correlated to

improved macroscopic electrocatalytic activity. With Fe, directly-bonded Fe-N species are detected by solid-state ^{15}N NMR and ^{57}Fe Mössbauer spectroscopy. The Fe-N moieties coexist with isolated pyridinic sites, both of which are expected to act as active sites for electrocatalysis. The results and analyses identify the types and distributions of Fe and N active sites in non-precious-metal electrocatalysts, and furthermore suggest synthetic pathways for maximizing the activity of these promising materials for fuel cell applications.

The historic pigment Maya Blue is an inorganic/organic hybrid material of indigo and palygorskite that exhibits remarkable long-term durability, the molecular origins of which have long been elusive. Advanced solid-state NMR methods identify the types and distributions of organic molecules within the nanoporous clay and show that indigo/dehydroindigo molecules occupy near-surface adsorption sites within the palygorskite pores (Ch. 8). The indigo/dehydroindigo molecules are shown to participate in strong hydrogen bonding interactions with structural water molecules within the palygorskite framework that stabilize the organic component of the pigment, allowing Maya Blue to retain its hue over century timescales.

The III-V semiconductor GaN has important applications including LEDs and power electronics. In nanocrystalline GaN semiconductors, blue photoluminescence properties are improved by annealing at temperatures of 1373 K. The high-temperature annealing is shown to introduce electronically-active defects that yield local metallic properties of the nanocrystals established by analysis of solid-state ^{71}Ga NMR spectra and relaxation times (Ch. 9). Comparison to bulk GaN materials shows that the local electronic structures of ^{71}Ga and ^{15}N atoms of the annealed nanocrystals are comparable to those in heavily-doped bulk GaN:Ge. The techniques presented here provide new methods for understanding the

influences of dopant and/or defect species on electronic structure in nanocrystalline semiconductors, which have been previously challenging to characterize.

In conclusion, the detailed new molecular-level analyses presented in this dissertation demonstrate the importance of heteroatom and/or defect species at surfaces and interfaces in determining the macroscopic properties of diverse interesting and important nanostructured inorganic materials. Non-stoichiometric heteroatom, defect, and/or surface species have previously been exceptionally challenging to characterize in such detailed ways, but are here accessed by new advances in spectroscopy in combination with state-of-the-art scattering techniques. The analyses in this dissertation provide criteria for improved design of catalytic, structural, and optoelectronic materials of broad technological importance for energy conversion, storage, and utilization. Furthermore, the techniques and methods applied are expected to be completely generalizable to other systems where non-stoichiometric distributions of surface, heteroatom, and/or defect species in nanostructured materials crucially influence the macroscopic properties.

Appendix 1

Ultrathin mordenite crystals synthesized using cooperative organic structure-directing agents

Adapted from: M. Kumar, Z. J. Berkson, R. J. Clark, Y. Shen, N. A. Prisco, H. Zheng, L. B. McCusker, J. C. Palmer, B. F. Chmelka, and J. D. Rimer *in preparation.*

A1.1 Abstract

The role of organic structure-directing agents in microporous materials crystallization remains an area of active research owing to their ability to selectively tailor the physicochemical properties of zeolites for applications spanning separations to catalysis. The rational design of organics often entails the identification of molecules with a geometry that is commensurate with the channels and cages of the target zeolite structure. Syntheses tend to employ a single organic where only a few examples report the ability of two or more organics operating synergistically to yield a desired product. Using a combination of state-of-the-art characterization techniques and molecular modeling, we show that a combination of two organics, each yielding distinct zeolites, results in the cooperative direction of a third structure. These organics work in tandem to produce ultrathin mordenite crystals with a characteristic diffusion pathlength less than 100 nm, which enhances catalyst performance relative to micron-sized crystals prepared by conventional syntheses.

A1.2 Introduction

The demand for more efficient zeolite catalysts creates a need to develop new synthesis approaches capable of tailoring crystal properties for optimal performance. Among many

physicochemical properties of zeolites, crystal size plays a significant role in mediating internal mass transport[1, 2] wherein diffusion pathlengths less than 100 nm can markedly improve catalyst lifetime and alter product selectivity.[3, 4] Various approaches have been explored to precisely tune the anisotropic growth of zeolite crystals, including the alteration of synthesis conditions, introduction of growth modifiers,[5] designing new organic structure-directing agents (OSDAs),[6-8] and the use of crystalline seeds.[9, 10] Achieving materials with well-controlled properties is often challenging owing to the complex and poorly understood mechanisms of zeolite crystallization.[11, 12] Here, we use a combination of high resolution characterization and modeling to examine the role of OSDAs in the formation of mordenite (MOR), which is typically difficult to prepare with sub-micron dimensions.

Mordenite is a large pore zeolite (pore diameter *ca*. 0.7 nm) with unidirectional channels aligned along the c-axis that is used as a commercial catalyst in reactions such as dehydration of alcohols to olefins,[13] oxidation of methane to methanol,[14] (hydro)isomerization,[15] cracking,[16] alkylation,[17] and carbonylation.[18] Prior studies have attributed the catalytic activity of mordenite to the intersection of 12-membered ring (MR) channels comprised of 8-ring pockets that facilitate shape-selective reactions; however, mordenite is highly susceptible to deactivation owing to mass transport limitations imposed by 1-dimensional pores and large channels that accommodate the formation of polyaromatics (i.e., coke precursors). Reported syntheses of mordenite have typically yielded large crystallites with sizes that range 5 to 20 μm and with stacking faults that reduce the effective pore apertures,[19] requiring post-synthesis modification to mitigate internal diffusion limitations.[20] To this end, crystallites with sub-micron dimensions of the [001] facet are expected to extend catalyst lifetimes. Suib and coworkers have reported sizes as small as 40 - 60 nm using complicated

synthesis protocols that include the use of crystalline seeds,[21] alcohol additives, and/or microwave heating.[22] Mordenite nanorods (ca. 10 × 100 nm) have been synthesized using seeds or cationic gemini surfactants by Xiao[23] and Ryoo[24] and their coworkers, respectively. These syntheses have resulted in nanometer-sized domains within larger aggregates, which similarly involve highly-defective structures and stacking faults that limit internal mass transport.

Zeolite syntheses often employ a combination of inorganic and organic structure-directing agents (OSDAs) to regulate the kinetics of crystallization.[25] Preparation of the vast majority of zeolites requires the use of OSDA molecules with sizes and shapes that are commensurate with the cages/channels of zeolites, which thus facilitate the generation of porous structures.[7] OSDAs are occluded within the framework and must typically be removed by post-synthesis calcination. It is common practice to use a single OSDA for each zeolite synthesis. In select cases, OSDAs can form clusters (e.g., dimers or aggregates) to stabilize the framework.[26] Few syntheses employ two or more different OSDAs. Examples often involve scenarios where only one organic functions as the OSDA and the other alters properties such as crystal size or habit, but is a bystander for structure direction.[27] Combinations of OSDAs have been used to prevent polymorphism in order to improve product purity.[28] Wright and coworkers have demonstrated for zeotypes, such as STA-20, that two organics may be necessary to achieve a desired crystalline phase.[29] In such cases, the OSDAs act cooperatively to produce a product that otherwise could not be achieved with either individual organic.

A1.3 Results and discussion

A.1.3.1 Synthesis and morphology of mordenite crystallites prepared using cooperative OSDAs

Here, we show that a combination of two OSDAs, N, N, N-trimethyl-1-1-adamantammonium ($TMAda^+$) and 1,2-hexanediol ($D6_{1,2}$), work cooperatively to yield mordenite. $TMAda^+$ is a well-documented OSDA for commercial SSZ-13 (**CHA**) (Fig. A1.1a). The same synthesis using only $D6_{1,2}$ results in ZSM-5 (**MFI**) (Fig. A1.1b), whereas an organic-free synthesis with Na^+ as an inorganic SDA also yields ZSM-5. Interestingly, the combination of $D6_{1,2}$ and TMAda produces mordenite (Figs. A1.1c), denoted as HOU-4.[30, 31] We observe that individual OSDAs and their binary combination generate three different zeolites (Fig. A1.1d): ZSM-5 is a 3-dimensional medium-pore zeolite; SSZ-13 is a 3-dimensional small-pore zeolite; and mordenite is a 1-dimensional large-pore zeolite. The three zeolites have similar elemental compositions,[31] but differ with respect to crystal habit and quantity of occluded OSDA. SSZ-13 crystals have a spheroidal morphology with sizes of 1 – 2 μm and 10 wt% organic determined by TGA (ca. 1.3 TMAda per unit cell). ZSM-5 crystals exhibit an indistinct morphology with sub-micron dimensions, and contain 5 wt% organic (ca. 2.7 $D6_{1,2}$ per unit cell). By comparison, HOU-4 crystallizes as thin plate-like particles that retain ca. 2 $D6_{1,2}$ and 2 $TMAda^+$ molecules per unit cell, as determined by synchrotron PXRD and solid-state NMR analyses, discussed below. All of the $D6_{1,2}$ molecules are removed by post-synthetic washing with water, which establishes the that $D6_{1,2}$ molecules are able to diffuse without appreciable restrictions out of the mordenite nanochannels. Facile extraction of the diol molecules from zeolite frameworks without the

need for post-synthesis calcination is uncommon; therefore, the synthesis of HOU-4 offers a promising route to recover and potentially recycle the OSDAs.

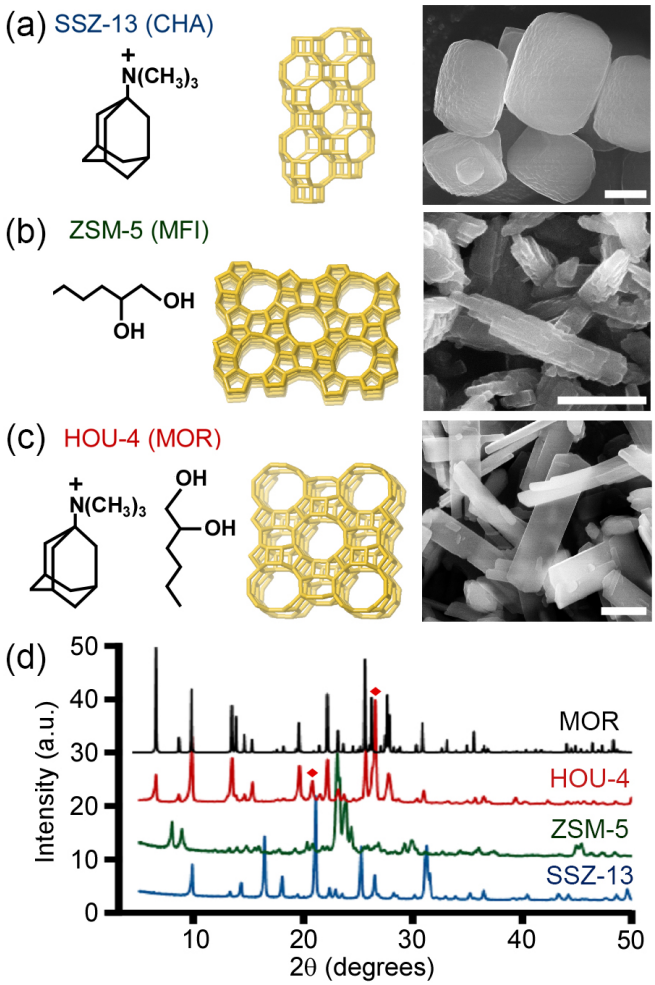

Figure A1.1. The OSDA(s) (left column), corresponding zeolite structure with composite building units (middle column), and representative scanning electron micrograph of zeolite crystals (right column) are shown for: (a) SSZ-13 (CHA) prepared with TMAda; (b) ZSM-5 (MFI) prepared with $D6_{1,2}$ or Na ions; and (c) HOU-4 (MOR) prepared with TMAda and $D6_{1,2}$. Scale bars are 1 μm. (d) Powder X-ray diffraction patterns of the solid precipitates obtained after 6 days of hydrothermal treatment at 180°C confirms the formation of SSZ-13 (blue), ZSM-5 (green), and HOU-4 (red). The structure of HOU-4 was confirmed using a reference pattern for MOR (black). Reflections corresponding to quartz are labelled with diamonds.

A substantial fraction of the HOU-4 crystallites have an ultrathin morphology that is expected to yield improved mass transport properties for catalysis. Transmission electron micrographs (Fig. A1.2a) show that the [100] width of the HOU-4 crystallites can reach 1 μm

with an average length-to-width (or [010]/[100]) aspect ratio of 4.0 ± 0.7. Selected-area electron diffraction (Fig. A1.2b) confirms the basal surface is the (001) face. Atomic force microscopy (AFM) topographical images of HOU-4 crystals (Fig. A1.2c) reveal an ultrathin habit wherein the analysis of multiple crystals shows a distribution of [001] around 80 nm.[31]

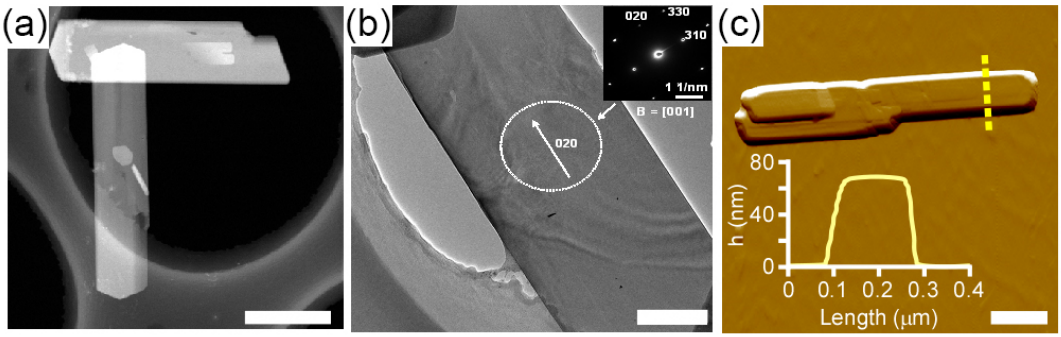

Figure A1.2. (a) Representative transmission electron micrograph of HOU-4 crystals. (b) TEM image with an SAED scattering pattern (inset) confirming the [001] orientation. (c) AFM amplitude mode image of a HOU-4 crystal in air. The inset shows a height profile measured along the dashed line. All scale bars are 0.5 μm.

A1.3.2 Quantifying and locating the organic structure-directing molecules

We hypothesize that the cooperativity of OSDAs leads to the ultrathin crystallite morphology. To ascertain the spatial arrangement of OSDAs within zeolite channels, we analyzed an unwashed HOU-4 sample (containing both diol and $TMAda^+$ molecules) by synchrotron PXRD and located the organic species by Rietveld refinement of the powder XRD pattern. The analyses confirm that TMAda resides within the 12-MR channels (Fig. 3a,b), while Na^+ and $D6_{1,2}$ are within the 8-ring side pockets (Fig. 3c). Rietveld refinement of the framework structure with occluded OSDAs indicates 2 Na^+, 2 $TMAda^+$, and 2 $D6_{1,2}$ per unit cell,[31] without detecting evidence for appreciable bulk crystallite shape anisotropy or stacking faults. The synchrotron PXRD analyses thus indicate an approximately 1:1 ratio of $TMAda^+$ and $D6_{1,2}$ molecules within the mordenite zeolite nanopores.

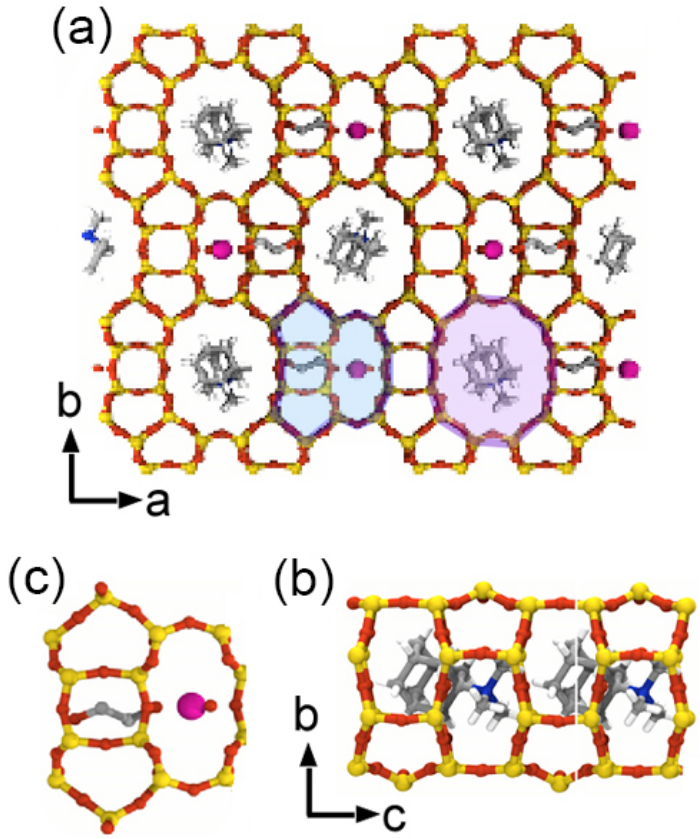

Figure A1.3. Results of synchrotron PXRD analysis of HOU-4. (a) Refined mordenite structure viewed axially in the c-direction showing $TMAda^+$ within the 12-ring channels, Na^+ in the oval 8-ring channels, and the diol headgroup in the 8-ring pockets. (b) Refined 8-ring pocket showing the stabilization of a framework Al atom by a Na^+ ion and a $D6_{1,2}$ molecule. (c) Orthogonal view of the 12-MR channel showing the arrangement of TMAda molecules. Additional details of the synchrotron PXRD analysis are provided in ref. 31.

However, a substantial fraction of diol molecules are surface-adsorbed adsorbed, as evidenced by quantitative solid-state one-dimensional (1D) single-pulse ^{13}C magic-angle-spinning (MAS) NMR analyses (Fig. A1.4). The 1D ^{13}C MAS NMR spectra of HOU-4 detect ^{13}C signals at 73, 67, 34, 29, 23, and 15 ppm from $D6_{1,2}$, as well as signals at 76, 49, 35, and 2 ppm, which are assigned to $TMAda^+$ molecules. Interestingly, weak signals are also detected at 58 and 46 ppm, which are assigned to dimethyl-adamantamine (DMAda) on the basis of prior literature.[32] The presence of dilute quantitities of DMAda in HOU-4 indicate that $TMAda^+$ undergoes partial decomposition via Hofmann elimination[32] during the hydrothermal synthesis. Due to the structural similarities of $TMAda^+$ and DMAda, the

synchrotron PXRD refinement is unable to distinguish between the two molecules, which likely both occupy positions within the 12-ring mordenite channels. Integration of the quantitative ^{13}C MAS NMR spectrum in Fig. A1.4 and use of TKS as an internal spin-counting reference yields an estimated ratio ($D6_{1,2}$ to $TMAda^{+}$+DMAda) of 6-13, which is much larger than the ratio of occluded organics established by synchrotron PXRD refinement. This suggests a substantial quantity of excess diol in unwashed HOU-4, which likely retains significant quantities of diol molecules on particle surfaces. This is corroborated by TGA of unwashed HOU-4, which shows 37 wt% mass loss consistent with desorption of surface-adsorbed diol molecules. After post-synthesis washing of HOU-4, only 10 wt% mass loss is observed by TGA, consistent with the removal of approximately all of the $D6_{1,2}$ molecules. Additional details of the TGA and quantification of the organic content are provided in ref. 31.

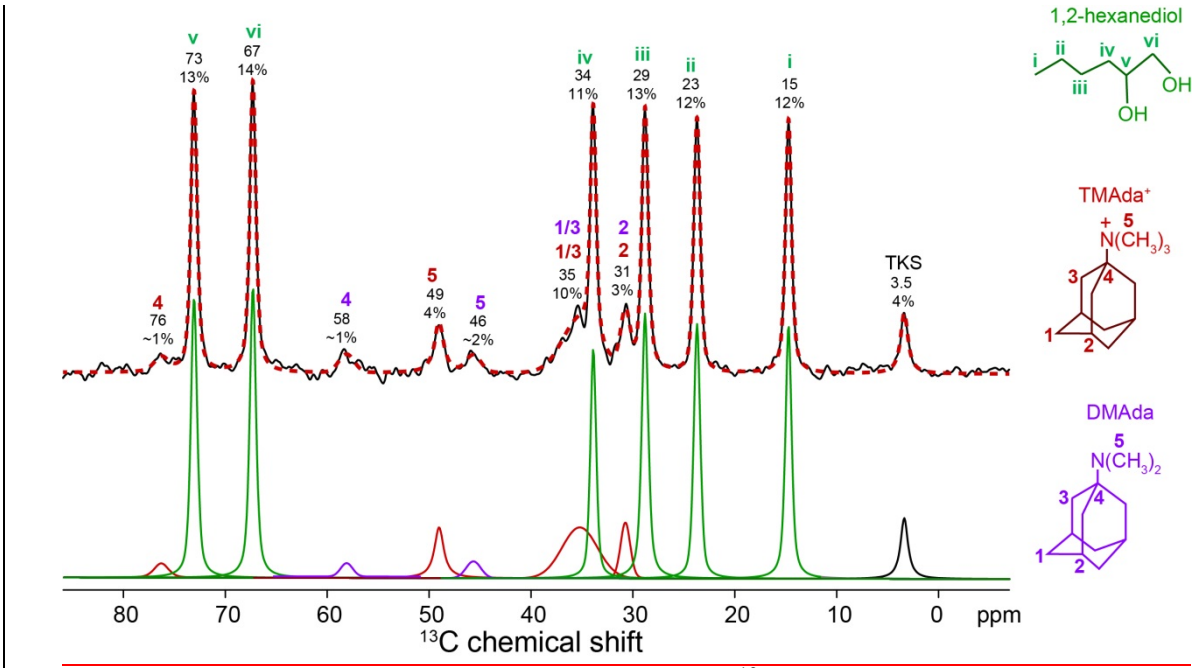

Figure A1.4. Solid-state quantitative 1D single-pulse ^{13}C MAS NMR spectrum of HOU-4, acquired at 11.7 T, 10 kHz MAS, 298 K, and with a repetition delay of 60 s. The simulated spectrum is shown offset below, and insets to the left show the molecular structures of $D6_{1,2}$, $TMAda^{+}$, and DMAda. Integration of the spectrum and comparison to TKS as an internal

spin-counting reference yields 1.2-1.3, 0.1-0.2, and 0.1 μmol/mg of $D6_{1,2}$, $TMAda^+$, and DMAda, respectively.

A1.3.3 Site-specific organic-inorganic interactions in mordenite prepared using cooperative OSDAs

The site-specific interactions of the different framework ^{27}Al species with OSDA molecules are established by solid-state two-dimensional (2D) HETeronuclear CORrelation (HETCOR) NMR spectra of HOU-4 (Fig. A1.5). The 2D NMR correlation spectra exploit internuclear dipole-dipole (through-space) or *J* (through-covalent-bond) couplings and are plotted as 2D contour plots where correlated signal intensities manifest the mutual proximities or covalent connectivities of the corresponding ^{1}H, ^{13}C, ^{27}Al, or ^{29}Si species.[33, 34] For example, covalent ^{27}Al-O-^{29}Si bonds within the HOU-4 frameworks are unambiguously established by the 2D $^{27}Al\{^{29}Si\}$ *J*-mediated NMR correlation spectrum (Fig. A1.5a), which shows a distribution of correlated signal intensity at 54 ppm in the ^{27}Al dimension and -109 to -99 ppm in the ^{29}Si dimension arising from framework aluminum atoms bonded to fully- or partially-crosslinked ^{29}Si atoms. Previously, such 2D $^{27}Al\{^{29}Si\}$ through-bond-mediated correlation spectra of aluminosilicate zeolites have been limited due in part to the low natural isotopic abundance of ^{29}Si (4.7%) and weak ^{27}Al-O-^{29}Si *J* couplings (<20 Hz), but are enabled here by the improved sensitivity of low-temperature measurement conditions. The ^{27}Al signals exhibit Czjzek lineshapes[35] that reflect a random distribution of ^{27}Al heteroatom environments within the mordenite framework and among the four distinct tetrahedral (T) sites. The relatively small percentage of partially-crosslinked ^{29}Si species are likely associated with defect sites at the exterior of the particle surfaces and are estimated to comprise *ca*. 2% of all ^{29}Si species by quantification of the single-pulse ^{29}Si NMR spectrum in Fig. A1.6. The Si/Al ratio of HOU-4 estimated by quantitative ^{29}Si MAS NMR is ca. 10,

which is consistent with values of ca. 10 and 13 measured by electron X-ray dispersive spectroscopy and estimated from synchrotron PXRD refinement, respectively.[31]

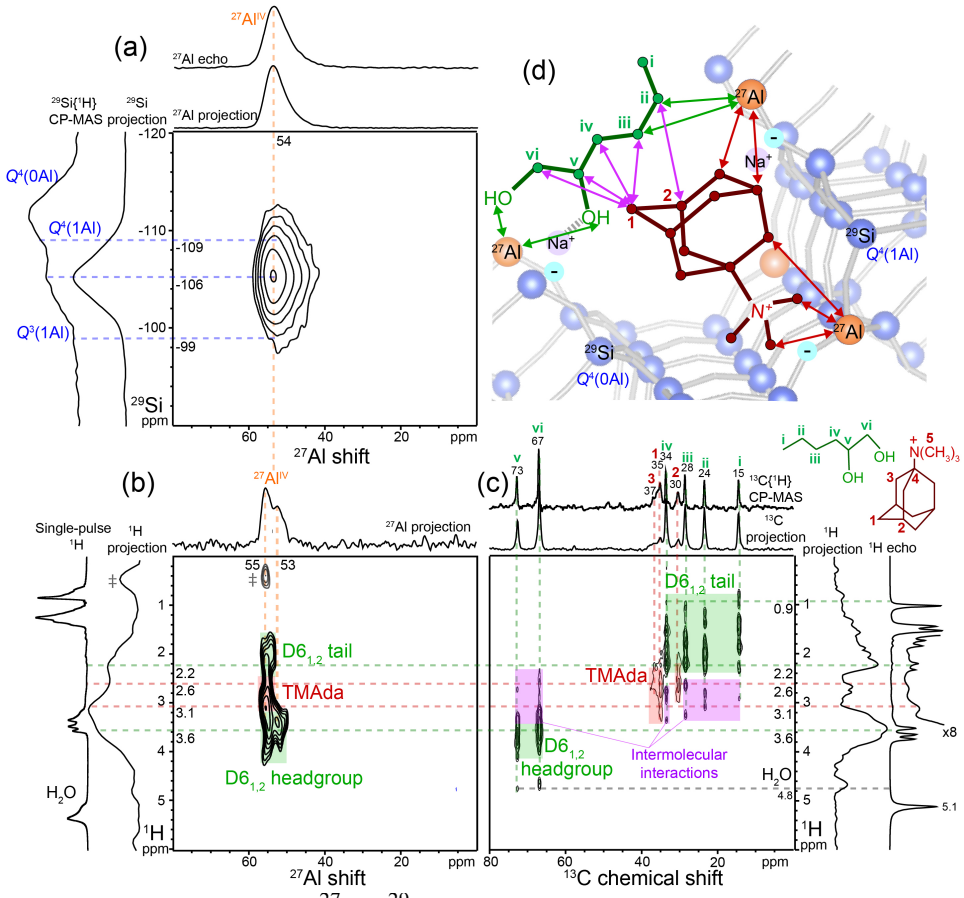

Figure A1.5. (A) Solid-state 2D ^{27}Al{^{29}Si} *J*-mediated NMR correlation spectrum acquired at 95 K, 9.4 T, and 10 kHz MAS. (B) Solid-state 2D ^{27}Al{^{1}H} HETCOR spectrum acquired at 263 K, 18.8 T, 12.5 kHz MAS, and a ^{27}Al{^{1}H} contact time of 0.5 ms. The ‡ symbol indicates a center-frequency artifact (see Supplementary Online Material). (C) Solid-state 2D ^{13}C{^{1}H} HETCOR spectrum acquired at 263 K, 11.7 T, 12.5 kHz MAS and with a ^{13}C{^{1}H} contact time of 5 ms. All of the ^{13}C signals are assigned to ^{13}C moieties on the TMAda$^+$ and D6$_{1,2}$ molecules, as indicated in the inset molecular structures. 1D ^{27}Al, ^{13}C{^{1}H}, or ^{1}H MAS NMR spectra acquired under the same conditions are shown along the corresponding ^{27}Al, ^{13}C, or ^{1}H axes for comparison with the 1D projections of the 2D spectra. (D) Idealized depiction of framework-OSDA and intermolecular interactions established by 2D NMR analyses. Green and red arrows indicate framework ^{27}Al interactions with D6$_{1,2}$ and TMAda$^+$ molecules, respectively; purple arrows indicate intermolecular interactions of commingled OSDA molecules.

Different types of framework aluminum sites in HOU-4 are distinguished on the basis of their site-specific interactions with different OSDA molecules, which are established by the

2D $^{27}Al\{^{1}H\}$ (Fig. A1.5b) and $^{13}C\{^{1}H\}$ HETCOR (Fig. A1.5c) NMR spectra. The HETCOR spectra yield correlated ^{13}C- or ^{27}Al-^{1}H signal intensities from ^{13}C-^{1}H or ^{27}Al-^{1}H nuclear spin pairs that are dipole-dipole-coupled through space over sub-nanometer distances. The different ^{1}H and ^{13}C signals are assigned to ^{1}H and ^{13}C moieties on $D6_{1,2}$ (green shaded regions) or $TMAda^{+}$ (red shaded regions) molecules by analyses of complementary solid-state 1D and 2D $^{13}C\{^{1}H\}$ NMR spectra.[31] The 2D $^{27}Al\{^{1}H\}$ HETCOR spectrum (Fig. A1.5b) resolves two ^{27}Al signals: one at 55 ppm, which is correlated to ^{1}H signals at 2.2 to 3.6 ppm from $TMAda^{+}$ and $D6_{1,2}$ ^{1}H moieties, and one at 53 ppm, which is correlated only to the ^{1}H signal at 3.6 ppm from $D6_{1,2}$ alcohol headgroups coordinated to Na cations.[36] These correlated signals evidence two different types of framework ^{27}Al species with either $TMAda^{+}$ or Na^{+} cations charge-balancing the associated framework negative charges. As the $TMAda^{+}$ molecules are sterically hindered from entering the oval 8-ring mordenite channels, the framework ^{27}Al species proximate to $TMAda^{+}$ cations must be within the linear 12-ring channels, while those associated with charge-balancing Na cations may be located within the 8-ring channels, as corroborated by the synchrotron PXRD analysis.

Furthermore, the different OSDA molecules are in close mutual proximities within the mordenite nanochannels, as established by the 2D $^{13}C\{^{1}H\}$ HETCOR spectrum of HOU-4 in Fig. A1.5c). This spectrum shows correlated signals at 2.2-3.1 ppm in the ^{1}H dimension and at ^{13}C shifts of 15, 24, 26, 34, 67, and 73 ppm (purple shaded regions) that arise from intermolecular interactions of ^{1}H environments in $TMAda^{+}$ molecules and the different ^{13}C environments in proximate (<1 nm) $D6_{1,2}$ molecules. We conclude that the different OSDA molecules are intimately commingled within the zeolite nanopores and act cooperatively (as

idealized in Fig. A1.5d) during the hydrothermal syntheses of HOU-4 to direct the formation of the linear 12-MR channels and the distribution of Al heteroatoms within the framework.

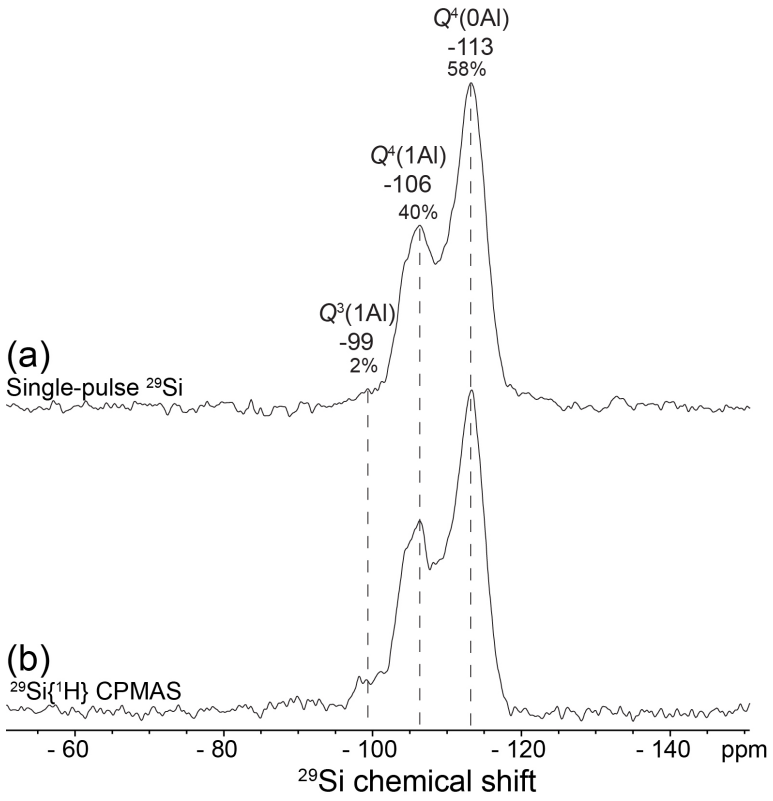

Figure A1.6. 1D ^{29}Si spectra of as-made HOU-4 acquired at 11.7 T and 298 K: (**a**) quantitative single-pulse ^{29}Si NMR spectrum, acquired at 10 kHz MAS and with a recycle delay of 120 s, and (**b**) ^{29}Si{^{1}H} CP MAS NMR spectrum, acquired with a contact time of 5 ms, a recycle delay of 1 s, and at 5 kHz MAS. The ^{29}Si signal at -99 ppm arises from dilute partially-crosslinked Q^3(1Al) moieties that are likely associated with defect sites at the HOU-4 particle surfaces.

A1.3.4 Catalytic properties of ultrathin mordenite

It is not fully understood how the ultrathin plate-like morphology of HOU-4 crystals is derived from the combined structure-directing influences of $TMAda^+$ and $D6_{1,2}$ molecules. Their role in zeolite crystallization is seemingly unrelated to that of a growth modifier that alters the crystal morphology in conventional mordenite synthesis, as neither organic solely produces thin crystals. The ability to prepare nanosized crystals has significant implications for catalytic applications. Zeolite catalysts with restricted mass transport, such as mordenite

and other one-dimensional framework types, are highly susceptible to rapid deactivation by coking; thus, a reduction in crystal dimension along the c-direction of mordenite (parallel to the large-pore channels) can have a substantial impact on catalyst performance. To illustrate this point, we prepared H-HOU-4 and conventional H-mordenite in their acid formsand compared their catalytic performance. The substantial difference in [001] facet thickness of H-HOU-4 (ca. 100 nm) and H-MOR (ca. 5 μm, Fig. A1.7a) imposes disparate limitations on internal mass transport. To quantify catalyst performance, we selected cumene cracking as a model reaction to evaluate time-on-stream lifetime (Fig. A1.7b. Tests in a packed bed reactor at 450°C reveal that the turnover number (evaluated in the shaded regions of Fig. A1.7b) is much larger for H-HOU-4 (38.7 mol cumene/mol H^+) compared to conventional mordenite (10.3 mol cumene/mol H^+) owing to the faster rate of H-MOR deactivation. These results are qualitatively consistent with studies of nanosized zeolite catalysts in literature that collectively report much longer lifetime owing to reduced mass transport limitations.

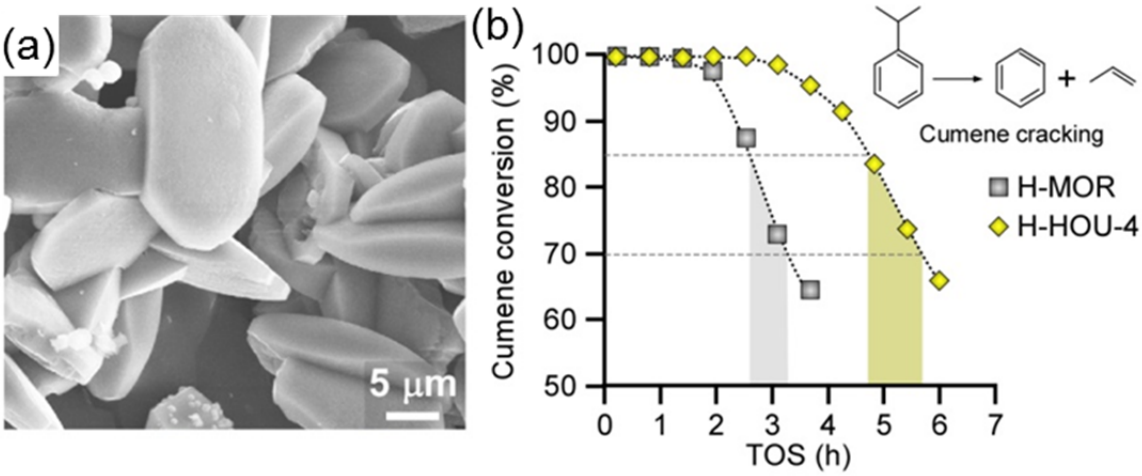

Figure A1.7. (a) representative scanning electron micrograph of conventional mordenite synthesized by a reported protocol.[21, 37]. (b) Comparative catalytic performance of H-mordenite crystals from a conventional synthesis and H-HOU-4 crystals. Cumene cracking was performed in a packed bed reactor at 450°C using a weight hourly space velocity (WHSV) of 2 h^{-1}.

A1.4 Conclusions

The generation of ultrathin HOU-4 crystallites using a combination of two organics is one of only a few reported cases where multiple OSDAs work in tandem to cooperatively direct zeolite crystallization and structure. Furthermore, syntheses of sub-micron mordenite crystals have been a significant challenge with implications for improving the design of commercial catalysts. It remains to be determined how multiple organic and inorganic structure-directing species function in a concerted manner to influence the physicochemical properties of zeolites or to control crystal polymorphism *a priori*. A unique aspect of HOU-4 crystallization is the role of diols, as non-ionic alcohols interact relatively weakly with crystalizing zeolite frameworks and are rarely employed as OSDAs in zeolite syntheses. Here, diol molecules work in tandem with cationic Na^+ and $TMAda^+$ species to stabilize the different linear nanopore systems in mordenite. Collectively, the findings in this study suggest that further exploration into the use of cooperative organics in zeolite syntheses holds considerable promise for engineering and optimization of microporous materials.

A1.5 Materials and methods

Synthesis of ultrathin mordenite

The following chemicals were used as reagents: Cab-O-Sil (M-5, Spectrum Chemical), sodium hydroxide (98% pellets, MACRON Fine Chemicals), N,N,N-trimethyl-1-1-adamantammonium hydroxide (25 wt % in water, SACHEM Inc.), 1,2-hexanediol ($D6_{1,2}$, 98%) and aluminum hydroxide (80.3 wt % $Al(OH)_3$, SPI0250 hydrogel). Deionized (DI) water used in all experiments was purified with an Aqua Solutions RODI-C-12A purification system (18.2 MΩ). All reagents were used as received without further purification.

Mordenite (HOU-4) was synthesized with the OSDA N,N,N-trimethyl-1-1-adamantammonium hydroxide (TMAda-OH) and 1,2-hexanediol (D61,2) using solutions with a molar composition of 0.052 $Al(OH)_3$:1.0 SiO_2:0.2 NaOH:44 H_2O:0.1 TMAda-OH:1.6 1,2-hexanediol. Sodium hydroxide (0.09 g, 0.0022 mol) was first dissolved in water (8.21 g, 0.4959 mol), followed by the addition of TMAda-OH (0.95 g, 0.0011 mol) and 1,2-hexanediol (2.17 g, 0.018 mol). This solution was stirred until clear (ca. 15 min). Aluminum hydroxide (0.06 g, 0.0005 mol) was added to the solution and left to stir for another 15 min at room temperature. To this clear solution was added the silica source (0.67 g, 0.0112 mol), and the resulting mixture was stirred (400 RPM) for 4 h at 80°C (mineral oil bath). Approximately 10 g of growth solution after 4 h of heated stirring was placed in a Teflon-lined stainless steel acid digestion bomb (Parr Instruments) and was heated under rotation (~30 rpm) and autogenous pressure in a Thermo-Fisher Precision Premium 3050 Series gravity oven. The nominal time and temperature for HOU-4 synthesis was 6 days at 180 °C. The products of all syntheses were isolated as white powder (ca. 600 mg) by centrifuging the mother liquor (13,000 rpm for 45 min) for three cycles with DI water washes. Samples for microscopy were prepared by first redispersing a small amount of powder (ca. 5 mg) in DI water. An aliquot of this solution was placed on a glass slide and dried overnight. Crystals were transferred to metal sample disks for microscopy studies by contacting the glass slide with carbon tape for SEM.

Synthesis of conventional mordenite

Conventional mordenite was synthesized using a growth solution with a molar composition of 1 Al_2O_3: 30 SiO_2:5 Na_2O:780 H_2O [21, 37]. Sodium hydroxide (0.25 g, 0.0061 mol) was first dissolved in water (8.437 g, 0.468 mol), followed by the addition of sodium

aluminate (0.1003 g, 0.00061 mol). The solution was stirred until clear (ca. 15 min) followed by the addition of silica gel (1.212 g, 0.0183 mol), and the resulting mixture was stirred at 400 RPM for 4 h. Approximately 10 g of the growth mixture was placed in a Teflon-lined stainless steel acid digestion bomb and was heated under static and autogenous pressure. The nominal time and temperature for synthesis was 4 days and 170°C, respectively. The products of all syntheses were isolated from mother liquor using vacuum filtration and 0.45 μm membrane filter with copious amount of DI water washes. Samples for microscopy were prepared as described below.

Solid-state Nuclear magnetic resonance (NMR)

Solid-state 1D and 2D ^{1}H, ^{13}C, ^{27}Al, and ^{29}Si MAS NMR spectroscopy was used to analyze the ^{1}H, ^{13}C, ^{27}Al, and ^{29}Si environments in as-made ultrathin mordenite crystallites. The 2D ^{27}Al{^{29}Si} *J*-mediated NMR correlation spectrum was acquired on a Bruker ASCEND 400 MHz (9.4 T) DNP NMR spectrometer operating at Larmor frequencies of 400.203, 104.283, and 79.501 MHz for ^{1}H, ^{27}Al, and ^{29}Si nuclei, respectively and equipped with a 3.2 mm triple-resonance HXY low-temperature MAS probehead. Low-temperature measurement conditions of 95 K were used for improved signal sensitivity. The spectrum was acquired using a 2D *H*eteronuclear *M*ultiple *Q*uantum *C*orrelation (HMQC) pulse sequence[38, 39] with an experimentally-optimized half-echo tau delay of 20 ms used to refocus the weak (*ca*. $1/(4\tau)$ = 12.5 Hz) through-bond ^{27}Al-O-^{29}Si *J*-couplings. The signal sensitivity was enhanced by applying a 1 ms ^{27}Al adiabatic double-frequency sweep pulse during the preparation period to invert the ^{27}Al satellite transitions. [40] During the rotor-synchronized tau delay periods, 100 kHz of continuous wave ^{1}H decoupling was applied. A recycle delay time of 1 s was used with a rotor-synchronized t_1 increment step size of 100 μs, 96 t_1 increments,

and 256 transients for a total acquisition time of 7 h. The 2D $^{13}C\{^{1}H\}$ spectra were acquired on a Bruker AVANCE 500 MHz (11.7 T) wide-bore spectrometer operating at Larmor frequencies of 500.222, 125.789, and 99.369 MHz for ^{1}H, ^{13}C, and ^{29}Si, respectively. Recycle delay times of 0.75 s were used with t_1 increment step sizes of 128 μs. The 2D $^{13}C\{^{1}H\}$ HETCOR spectrum was acquired respectively with 430 t_1 increments and 128 transients for atotal acquisition time of 11.5 h. The 2D $^{27}Al\{^{1}H\}$ HETCOR spectrum was acquired on a Bruker AVANCE-III Ultrashield Plus 800 MHz (18.8 T) narrow-bore spectrometer operating at Larmor frequencies of 208.527 and 800.242 MHz for ^{27}Al and ^{1}H, respectively, and a Bruker 3.2 mm broadband double-resonance HX probehead was used. The 2D $^{27}Al\{^{1}H\}$ HETCOR spectrum was acquired with a repetition time of 1 s, 50 t_1 increments and 512 transients for a total acquisition time of 7 h. All of the 2D HETCOR spectra were acquired using homonuclear ^{1}H-^{1}H eDUMBO-1_{22} decoupling[41] during the ^{1}H evolution periods to improve resolution in the ^{1}H dimensions. For the 2D $^{29}Si\{^{1}H\}$, $^{13}C\{^{1}H\}$, and $^{27}Al\{^{1}H\}$ HECTOR experiments, a variable-temperature chiller unit was to cool the sample temperature to approximately 263 K to reduce the mobility of the OSDA species and improve cross-polarization signal sensitivity. All of the 1D and 2D NMR spectra were acquired with 100 kHz heteronuclear SPINAL-64 [42] ^{1}H decoupling during the acquisition period.

Atomic force microscopy (AFM)

AFM measurements were performed in air using an Asylum Research MFP-3D-SA instrument (Santa Barbara, CA). An aliquot of HOU-4 dispersed in water was placed on silicon wafer and was allowed to dry at room temperature. The silicon wafer was calcined at 500°C for 5 h, followed by cleaning under inert Ar gas flow to remove loosely-bound

crystals. AFM images were collected using a Cr/Au-coated silicon nitride cantilever (Olympus RC800PB) with a spring constant of 0.82 N/m. AFM images were collected in contact mode at a scan rate of 1.2 Hz and 256 lines/scan.

Electron microscopy

Scanning electron microscopy (SEM) was performed with a FEI 235 dual-beam (focused ion-beam) system operated at 15 kV and a 5 mm working distance. All SEM samples were coated with a thin carbon layer (ca. 20 nm) prior to imaging.

X-ray analysis

Energy-dispersive X-ray spectroscopy (EDX) was performed using a JEOL JSM 6330F field emission scanning electron microscope (SEM) at working distance of 15 mm and voltage of 15 kV and 12 mA. Powder X-ray diffraction (XRD) patterns of as-made zeolite samples were collected on a Siemens D5000 X-ray diffractometer using a Cu Kα source (40 kV, 30 mA). For reference intensity ratio (RIR) analysis using mordenite-quartz mixtures, a Rigaku SmartLab diffractometer (40 kV, 44 mA) was used. The LTA framework was confirmed using a reference pattern provided by the International Zeolite Association Structure Database.

To discern experimentally the arrangement of the sodium and organic species within the pores of the mordenite framework structure, synchrotron powder diffraction data were collected on the Materials Science beamline at the Swiss Light Source. Analysis of the data revealed the presence of quartz impurity, thus a 2-phase refinement using the program Topas was undertaken. Idealized structures for the two OSDA species were generated using the program Avogadro.

For the quartz phase, the published structure was used and only the peakshape parameters and scale factor were refined. For the mordenite phase, structure analysis was initiated using the known MOR-type framework structure in the highest symmetry space group (*Cmcm*). The pattern was scaled using only the high-angle data and then a difference electron density (DED) map was generated using the complete pattern. This showed a significant column of electron density in the middle of the 12-ring channel. As the width of this column had a diameter consistent with that of the TMAda molecule, the simulated annealing (SA) global optimization procedure described by Smeets et al.[43] was applied to find the best location and orientation of a rigid TMAda molecule within this electron density. A second DED map then revealed the positions of the Na ions in the center of the oval 8-ring channels running parallel to the 12-ring channel, where they were coordinated to six framework oxygen atoms. The next DED map showed electron density in the 8-ring side pocket of the 12-ring channel; therefore, the SA procedure was applied once again, this time searching for the best position of the head group (C_2O_2) of the $D6_{1,2}$ molecule. The final DED map showed a peak within bonding distance of the Na ion, which was interpreted as a water molecule.

Catalyst preparation and testing

Samples for catalysis were calcined in a Thermo Fisher Lindberg Blue furnace under constant flow of 100 sccm dried air (Matheson Tri-Gas) at 550°C for 5 h with a temperature ramping/cooling rate of 1°C/min. These samples were converted to an acid form (Brønsted acids) by ion exchange wherein calcined zeolite was mixed with 1.0 M ammonium nitrate solution to obtain a 2 wt% suspension. This mixture was heated to 80°C for 2 h to allow the exchange of Na^+ with NH_4^+. This process was performed three times with centrifugation/washing between each ion exchange cycle. The final NH_4-zeolite samples

were washed three times with DI water before they were calcined once again with the same conditions stated above, thus becoming H-form zeolite.

Cumene cracking over H-form catalysts was carried out in a ¼ inch stainless steel tube installed in a Thermo Scientific Lindberg Blue M furnace. The catalyst bed was supported between two plugs of quartz wool, and a K-type thermocouple (Omega Engineering) was inserted into the stainless tube to measure the temperature of the catalyst bed. Prior to the reaction, the catalyst bed was pretreated *in situ* at 550°C for 3 h under flow of dried air (6 cm^3/min of O_2, 24 cm^3/min of N_2). After this pretreatment, the catalyst bed was cooled down to the reaction temperature, *i.e.* 450°C. Cumene (98%, Sigma Aldrich) was fed by a syringe pump (Harvard Apparatus) at 2 μl/min into a heated inert gas stream of Ar (50 cm^3/min), which resulted in a reactant flow with a weight hourly space velocity (WHSV) of 2 h^{-1}. The cumene conversion is defined as the percentage of cumene reacted at the effluent of catalyst bed. To compare the deactivation rate between different catalyst samples, turnover number (TON) is calculated for a selected span of time-on-stream (TOS) using a modified form of the equation reported by Bhan and coworkers,[44]

$$\mathrm{TON}(t) = \frac{1}{[\mathrm{H}^+]_0} \int_{t_1}^{t_2} F(\tau) d\tau$$

where $[H^+]_0$ is the total number of Brønsted acid sites (obtained from the NH_3-TPD data in Table S3), F(τ) is the molar flow rate of converted carbon (reacted cumene), and *t* is TOS selected between times t_1 and t_2 corresponding to 85 and 70% methanol conversion (i.e., regions of nearly linear deactivation in Figure A1.7b).

A1.6 References

(1) Corma, A., State of the art and future challenges of zeolites as catalysts. *J. Catal.* **2003,** *216* (1-2), 298-312.

(2) Pérez-Ramírez, J.; Abelló, S.; Villaescusa, L. A.; Bonilla, A., Toward Functional Clathrasils: Size- and Composition-Controlled Octadecasil Nanocrystals by Desilication. *Angewandte Chemie International Edition* **2008,** *47* (41), 7913-7917.
(3) Choi, M.; Na, K.; Kim, J.; Sakamoto, Y.; Terasaki, O.; Ryoo, R., Stable single-unit-cell nanosheets of zeolite MFI as active and long-lived catalysts. *Nature* **2009,** *461* (7261), 246-9.
(4) Olsbye, U.; Svelle, S.; Bjorgen, M.; Beato, P.; Janssens, T. V. W.; Joensen, F.; Bordiga, S.; Lillerud, K. P., Conversion of Methanol to Hydrocarbons: How Zeolite Cavity and Pore Size Controls Product Selectivity. *Angew. Chem.-Int. Edit.* **2012,** *51* (24), 5810-5831.
(5) Rimer, J. D.; Kumar, M.; Li, R.; Lupulescu, A. I.; Oleksiak, M. D., Tailoring the physicochemical properties of zeolite catalysts. *Catalysis Science & Technology* **2014,** *4* (11), 3762-3771.
(6) Brand, S. K.; Schmidt, J. E.; Deem, M. W.; Daeyaert, F.; Ma, Y. H.; Terasaki, O.; Orazov, M.; Davis, M. E., Enantiomerically enriched, polycrystalline molecular sieves. *Proceedings of the National Academy of Sciences of the United States of America* **2017,** *114* (20), 5101-5106.
(7) Gallego, E. M.; Portilla, M. T.; Paris, C.; León-Escamilla, A.; Boronat, M.; Moliner, M.; Corma, A., "Ab initio" synthesis of zeolites for preestablished catalytic reactions. *Science* **2017,** *355* (6329), 1051.
(8) Li, C.; Paris, C.; Martínez-Triguero, J.; Boronat, M.; Moliner, M.; Corma, A., Synthesis of reaction-adapted zeolites as methanol-to-olefins catalysts with mimics of reaction intermediates as organic structure-directing agents. *Nat. Catal.* **2018,** *1*, 547-555.
(9) Lai, Z. P.; Tsapatsis, M.; Nicolich, J. R., Siliceous ZSM-5 membranes by secondary growth of b-oriented seed layers. *Adv. Funct. Mater.* **2004,** *14* (7), 716-729.
(10) Majano, G.; Darwiche, A.; Mintova, S.; Valtchev, V., Seed-Induced Crystallization of Nanosized Na-ZSM-5 Crystals. *Ind. Eng. Chem. Res.* **2009,** *48* (15), 7084-7091.
(11) De Yoreo, J. J.; Gilbert, P.; Sommerdijk, N.; Penn, R. L.; Whitelam, S.; Joester, D.; Zhang, H. Z.; Rimer, J. D.; Navrotsky, A.; Banfield, J. F.; Wallace, A. F.; Michel, F. M.; Meldrum, F. C.; Colfen, H.; Dove, P. M., Crystallization by particle attachment in synthetic, biogenic, and geologic environments. *Science* **2015,** *349* (6247), aaa6760-1/9.
(12) Olafson, K. N.; Li, R.; Alamani, B. G.; Rirner, J. D., Engineering Crystal Modifiers: Bridging Classical and Nonclassical Crystallization. *Chem. Mat.* **2016,** *28* (23), 8453-8465.
(13) Chiang, H.; Bhan, A., Catalytic consequences of hydroxyl group location on the rate and mechanism of parallel dehydration reactions of ethanol over acidic zeolites. *J. Catal.* **2010,** *271* (2), 251-261.
(14) Grundner, S.; Markovits, M. A. C.; Li, G.; Tromp, M.; Pidko, E. A.; Hensen, E. J. M.; Jentys, A.; Sanchez-Sanchez, M.; Lercher, J. A., Single-site trinuclear copper oxygen clusters in mordenite for selective conversion of methane to methanol. *Nat. Commun.* **2015,** *6*, 7546 (1-9).
(15) Rozanska, X.; van Santen, R. A.; Hutschka, F.; Hafner, J., A periodic DFT study of intramolecular isomerization reactions of toluene and xylenes catalyzed by acidic mordenite. *J. Am. Chem. Soc.* **2001,** *123* (31), 7655-7667.
(16) Gora-Marek, K.; Tarach, K.; Tekla, J.; Olejniczak, Z.; Kustrowski, P.; Liu, L. C.; Martinez-Triguero, J.; Rey, F., Hierarchical Mordenite Dedicated to the Fluid Catalytic Cracking Process: Catalytic Performance Regarding Textural and Acidic Properties. *J. Phys. Chem. C* **2014,** *118* (48), 28043-28054.
(17) Bhan, A.; Allian, A. D.; Sunley, G. J.; Law, D. J.; Iglesia, E., Specificity of sites within eight-membered ring zeolite channels for carbonylation of methyls to acetyls. *J. Am. Chem. Soc.* **2007,** *129* (16), 4919-4924.
(18) Boronat, M.; Martinez-Sanchez, C.; Law, D.; Corma, A., Enzyme-like Specificity in Zeolites: A Unique Site Position in Mordenite for Selective Carbonylation of Methanol and Dimethyl Ether with CO. *J. Am. Chem. Soc.* **2008,** *130* (48), 16316-16323.

(19) Raatz, F.; Freund, E.; Marcilly, C., STUDY OF SMALL-PORT AND LARGE-PORT MORDENITE MODIFICATIONS .1. PREPARATION OF THE HM FORMS. *Journal of the Chemical Society-Faraday Transactions I* **1983,** *79*, 2299-2309.
(20) van Laak, A. N. C.; Sagala, S. L.; Zecevic, J.; Friedrich, H.; de Jongh, P. E.; de Jong, K. P., Mesoporous mordenites obtained by sequential acid and alkaline treatments - Catalysts for cumene production with enhanced accessibility. *J. Catal.* **2010,** *276* (1), 170-180.
(21) Hincapie, B. O.; Garces, L. J.; Zhang, Q. H.; Sacco, A.; Suib, S. L., Synthesis of mordenite nanocrystals. *Microporous and Mesoporous Materials* **2004,** *67* (1), 19-26.
(22) Nosheen, S.; Galasso, F.; Suib, S. L., Synthesis of Mordenite Aggregates of Nanometer-Sized Crystallites. *Science of Advanced Materials* **2009,** *1* (1), 31-37.
(23) Ren, L. M.; Guo, Q.; Zhang, H. Y.; Zhu, L. F.; Yang, C. G.; Wang, L.; Meng, X. J.; Feng, Z. C.; Li, C.; Xiao, F. S., Organotemplate-free and one-pot fabrication of nano-rod assembled plate-like micro-sized mordenite crystals. *J. Mater. Chem.* **2012,** *22* (14), 6564-6567.
(24) Jo, C.; Jung, J.; Shin, H. S.; Kim, J.; Ryoo, R., Capping with multivalent surfactants for zeolite nanocrystal synthesis. *Angew. Chem.-Int. Edit.* **2013,** *52* (38), 10014-10017.
(25) Lobo, R. F.; Zones, S. I.; Davis, M. E., Structure-Direction in Zeolite Synthesis. *J. Incl. Phenom. Mol. Recogn. Chem.* **1995,** *21* (1-4), 47-78.
(26) Corma, A.; Rey, F.; Rius, J.; Sabater, M. J.; Valencia, S., Supramolecular self-assembled molecules as organic directing agent for synthesis of zeolites. *Nature* **2004,** *431* (7006), 287-290.
(27) Zones, S. I.; Hwang, S. J., Synthesis of high silica zeolites using a mixed quaternary ammonium cation, amine approach: Discovery of zeolite SSZ-47. *Chem. Mat.* **2002,** *14* (1), 313-320.
(28) Camblor, M. A.; Corma, A.; Diaz-Cabanas, M. J.; Baerlocher, C., Synthesis and structural characterization of MWW type zeolite ITQ-1, the pure silica analog of MCM-22 and SSZ-25. *J. Phys. Chem. B* **1998,** *102* (1), 44-51.
(29) Turrina, A.; Garcia, R.; Watts, A. E.; Greer, H. F.; Bradley, J.; Zhou, W. Z.; Cox, P. A.; Shannon, M. D.; Mayoral, A.; Casci, J. L.; Wright, P. A., STA-20: An ABC-6 Zeotype Structure Prepared by Co-Templating and Solved via a Hypothetical Structure Database and STEM-ADF Imaging. *Chem. Mat.* **2017,** *29* (5), 2180-2190.
(30) Excess silica in the HOU-4 reaction mixture results in the formation of a dense and inert quartz phase and a minor unidentified aluminosilicate phase as detected by synchrotron PXRD. Details of quartz characterization are provided in ref. 31.
(31) Kumar, M.; Berkson, Z. J.; Clark, R. J.; Shen, Y.; Prisco, N. A.; Zheng, H.; McCusker, L. B.; Palmer, J. C.; Chmelka, B. F.; Rimer, J. D., Ultrathin mordenite crystals synthesized using cooperative organic structure-directing agents. *In preparation*, 2019.
(32) Adams, B. L.; Kovacic, P., HOFMANN ELIMINATION AND STEVENS REARRANGEMENT WITH N,N,N-TRIMETHYL-3-HOMOADAMANTYLAMMONIUM HYDROXIDE - EVIDENCE FOR 3-HOMOADAMANTENE. *Journal of Organic Chemistry* **1974,** *39* (21), 3090-3094.
(33) Berkson, Z. J.; Messinger, R. J.; Na, K.; Seo, Y.; Ryoo, R.; Chmelka, B. F., Non-Topotactic Transformation of Silicate Nanolayers into Mesostructured MFI Zeolite Frameworks During Crystallization. *Angew. Chem.-Int. Edit.* **2017,** *56* (19), 5164-5169.
(34) Smeets, S.; Berkson, Z. J.; Xie, D.; Zones, S. I.; Wan, W.; Zou, X. D.; Hsieh, M. F.; Chmelka, B. F.; McCusker, L. B.; Baerlocher, C., Well-Defined Silanols in the Structure of the Calcined High-Silica Zeolite SSZ-70: New Understanding of a Successful Catalytic Material. *J. Am. Chem. Soc.* **2017,** *139* (46), 16803-16812.
(35) d'Espinose de la Caillerie, J. B.; Fretigny, C.; Massiot, D., MAS NMR spectra of quadrupolar nuclei in disordered solids: The Czjzek model. *J. Magn. Reson.* **2008,** *192* (2), 244-251.
(36) Anderson, M. W.; Barrie, P. J.; Klinowski, J., H-1 Magic-Angle-Spinning NMR-Studies of the Adsorption of Alcohols on Molecular-Sieve Catalysts. *J. Phys. Chem.* **1991,** *95* (1), 235-239.
(37) Li, X. F.; Prins, R.; van Bokhoven, J. A., Synthesis and characterization of mesoporous mordenite. *J. Catal.* **2009,** *262* (2), 257-265.

(38) Garaga, M. N.; Hsieh, M. F.; Nour, Z.; Deschamps, M.; Massiot, D.; Chmelka, B. F.; Cadars, S., Local environments of boron heteroatoms in non-crystalline layered borosilicates. *Phys. Chem. Chem. Phys.* **2015,** *17* (33), 21664-21682.
(39) Lesage, A.; Sakellariou, D.; Steuernagel, S.; Emsley, L., Carbon-proton chemical shift correlation in solid-state NMR by through-bond multiple-quantum spectroscopy. *J. Am. Chem. Soc.* **1998,** *120* (50), 13194-13201.
(40) Van Veenendaal, E.; Meier, B. H.; Kentgens, A. P. M., Frequency stepped adiabatic passage excitation of half-integer quadrupolar spin systems. *Mol. Phys.* **1998,** *93* (2), 195-213.
(41) Elena, B.; de Paepe, G.; Emsley, L., Direct spectral optimisation of proton-proton homonuclear dipolar decoupling in solid-state NMR. *Chem. Phys. Lett.* **2004,** *398* (4-6), 532-538.
(42) Fung, B. M.; Khitrin, A. K.; Ermolaev, K., An improved broadband decoupling sequence for liquid crystals and solids. *J. Magn. Reson.* **2000,** *142* (1), 97-101.
(43) Smeets, S.; McCusker, L. B.; Baerlocher, C.; Elomari, S.; Xie, D.; Zones, S. I., Locating Organic Guests in Inorganic Host Materials from X-ray Powder Diffraction Data. *Journal of the American Chemical Society* **2016,** *138* (22), 7099-7106.
(44) Hwang, A.; Prieto-Centurion, D.; Bhan, A., Isotopic tracer studies of methanol-to-olefins conversion over HSAPO-34: The role of the olefins-based catalytic cycle. *J. Catal.* **2016,** *337*, 52-56.

Appendix 2

Colloidal F:In_2O_3 cubes: Fluorine-induced faceting and infrared plasmonic response

Adapted from: S.-H. Cho*, S. Gosh*, Z. J. Berkson*, J. Hachtel, J. Shi, L. Gilbert, Y. Ho, A. Yang, B. F. Chmelka, D. Milliron. *Equally-contributing authors. Submitted to *Journal of the American Chemical Society*. Preprint available on *ChemRxiv* under DOI: 10.26434/chemrxiv.7355042.v1.

A2.1 Abstract

Cube-shaped nanocrystals (NCs) of conventional metals like gold and silver generally exhibit localized surface plasmon resonance (LSPR) properties in the visible spectrum with spectral modes determined by their faceted shapes. Here, we describe the colloidal synthesis of nanoscale fluorine-doped indium oxide (F:In_2O_3) cubes with LSPR responses in the infrared (IR) region. Single crystalline 160 nm sized F:In_2O_3 cubes and 270 nm concave cubes were synthesized using a colloidal heat-up method. Fluorine is an anionic aliovalent dopant with an ionic radius (1.19 Å) that is similar to oxygen (1.24 Å) in the cubic bixbyite phase of In_2O_3, inducing free carriers leading to LSPR. The free carriers induce ^{19}F and ^{115}In Knight shifts, as established by solid-state ^{19}F and ^{115}In NMR , indicating that the F:In_2O_3 cubes are heavily doped beyond the metal-insulator transition. Fluorine simultaneously influences the morphology of cubic NCs by functioning as a surface-passivating agent on the {100} facets, determined by solid-state $^{1}H\{^{19}F\}$ NMR analyses and complementary DFT calculations. Crystallite shape is modulated from cubes to concave cubes, with the growth of protrusions at the corners at lower InF_3 concentrations. Cube-shaped F:In_2O_3 NCs exhibit narrow, shape-

dependent multimodal LSPR extinction peaks due to corner- and edge-centered modes that are visualized by electron energy loss spectroscopy in a scanning transmission electron microscope.

A2.2 Introduction

Colloidal syntheses of doped metal oxide NCs have emerged recently as new means for expanding localized surface plasmon resonance (LSPR) to the infrared (IR) range,[1] although shape control has yet to be broadly established. A wide range of morphologies have been reported for colloidal gold and silver NCs,[2] including cubes[3,4] and octopods,[5] leading to the observation of shape-dependent LSPR and strongly enhanced electromagnetic near-fields around corners and edges. Yet, metal NCs intrinsically possess high free-carrier concentrations exceeding 10^{23} cm^{-3}, so the optical response of isotropic NCs tends to be restricted to the visible region of the electromagnetic spectrum.[6,7] On the other hand, controlled doping of semiconductor NCs allows carrier concentrations below 10^{21} cm^{-3}, resulting in IR-range LSPR.[8,9] In this study, we demonstrate shape-controlled colloidal syntheses of highly-faceted fluorine-doped indium oxide ($F:In_2O_3$) cubes with an LSPR response in the IR range.

Typically, doping strategies in plasmonic metal oxide NCs (e.g., $Sn:In_2O_3$,[10] Al:ZnO,[11] and In:CdO[12] NCs) have focused on aliovalent cation substitution. Halogen anions, meanwhile, are capping agents[13] that have been used for shape control of metal,[14] metal oxide,[15] and metal chalcogenide[16,17] NCs. In some metal oxide NCs, fluorine has been incorporated as an anionic co-dopant (e.g., F,In:CdO,[18] $F,Sn:In_2O_3$[19]). Very little has been reported regarding fluorine doping alone to induce LSPR, as in fluorinated TiO_2 NCs.[20]

Furthermore, while anionic doping in nanocrystalline F:SnO_2 has been demonstrated, the effects of fluorine on NC faceting or LSPR properties have not been explored.[21]

Faceted nanoparticles provide shape-dependent LSPR properties not observed for spherical particles, including highly enhanced near-field hot spots around corners and edges[22] that, in conventional metals, have been leveraged for plasmonic nanoantennae[23,24] and surface-enhanced Raman spectroscopy (SERS).[25,26] Disks and elongated NCs of copper chalcogenide NCs have been reported, but reports are conflicting regarding shape effects on their LSPR properties, which are likely to be strongly influenced by crystalline anisotropy as well. Shape-dependent studies of LSPR in doped oxide NCs are few,[12,27] motivating the development of new strategies for synthetic shape control.

We succeed in modulating the shape of F:In_2O_3 NCs by varying the ratio of InF_3 to $In(acac)_3$ precursors and observe multimodal shape-dependent LSPR extinction features. The defining role of fluorine in shaping NC facets and inducing LSPR spectral response is attributed to the presence of fluorine on the external surfaces and internally within the NCs, respectively. Through X-ray photoelectron spectroscopy (XPS) and solid-state ^{19}F magic-angle-spinning (MAS) nuclear magnetic resonance (NMR) spectroscopy correlated with DFT calculations, fluorine is found to occupy surface sites on dominantly exposed {100} facets. Fluorine dopant species internal to the NCs are probed by X-ray diffraction (XRD), energy dispersive X-ray spectroscopy (EDX), time of flight-secondary ion mass spectrometry (TOF-SIMS), and ^{19}F MAS-NMR spectroscopy. Aliovalent substitutional fluorine doping on oxygen lattice sites allows free-carrier compensation, inducing free-electrons for LSPR. The local metallic environments of the sub-surface fluorine and indium atoms in the NC lattices are established by analyses of ^{19}F spin-lattice T_1 relaxation times and wideline ^{115}In NMR

spectra, which are shown to exhibit temperature- and frequency-dependencies that are characteristic of coupling to free (metallic) electron carriers. Arising from the free-carriers and highly-faceted NC shape, single particle LSPR spatial modes are directly visualized by monochromated electron energy loss spectroscopy (EELS) performed in a scanning transmission electron microscope (STEM) to verify the observed multimodal features.

A2.3 Results and discussion

A2.3.1. Synthesis and shape behavior of F:In_2O_3 cubes

The shapes of the F:In_2O_3 NCs were controlled by varying the molar ratio of InF_3 to $In(acac)_3$ precursors during synthesis, which also determined the extent of fluorine incorporation in the resulting NCs. F:In_2O_3 NCs with well-defined morphology were produced for 1–3% InF_3 in the growth solution, as shown in Fig. A2.1. SEM images showed that monodisperse NCs (edge length 162.1 ± 9.2 nm) with cubic morphology were obtained exclusively in the presence of InF_3 (3% in molar ratio to $In(acac)_3$) (Fig. A2.1a, rightmost panel). By comparison, in the absence of InF_3 during the synthesis, NCs with pseudospherical morphology were observed (Fig. A2.1a, leftmost panel), with no cubic-shaped NCs observed. Intermediate amounts of InF_3 led to variations in the NC morphology, specifically forming concave cubes with edges protruding outwards for 2% InF_3 (Fig. A2.1a, second from right) and 1% InF_3 (Fig. 2.1a, second from left).

The TEM images in Fig. 2.1b-g show that the as-synthesized F:In_2O_3 cubes exhibit well-defined crystalline facets. Selected-area electron diffraction (SAED) confirms that the F:In_2O_3 cubes are each single crystals and allows indexing of their surface facets. A TEM image of an F:In_2O_3 cube (3% InF_3) is shown in Fig. A2.1b, which exhibits a flat (100) face

and a well-defined edge. The cube is terminated with (100) facets of the In_2O_3 cubic bixbyite structure, corroborated by the position of the (400) reflections in the SAED pattern (Fig. A2.1b, right). A cube on <110> zone axis edge orientation exhibits (422) reflections in the SAED pattern (Fig. A2.1c, right), corresponding to the (422) spacings observed by HRTEM (Fig. A2.1f). Concave F:In_2O_3 cubes (1 and 2% InF_3) are also single crystalline as observed in SAED patterns collected down the <100> zone axis (Fig. A2.1d,e right). An HRTEM image of the elongated tip on a concave cube (1% InF_3) shows (022) lattice spacing (3.56 Å), along with (400) lattice spacing parallel to the facets (Fig. A2.1g). Together, these observations indicate that the as-synthesized F:In_2O_3 cubes have cubic bixbyite {100}-dominant surface facets. Additional details of the synthesis of the F:In_2O_3 cubes, including parametric analyses of the synthesis conditions, are provided in ref. 28.

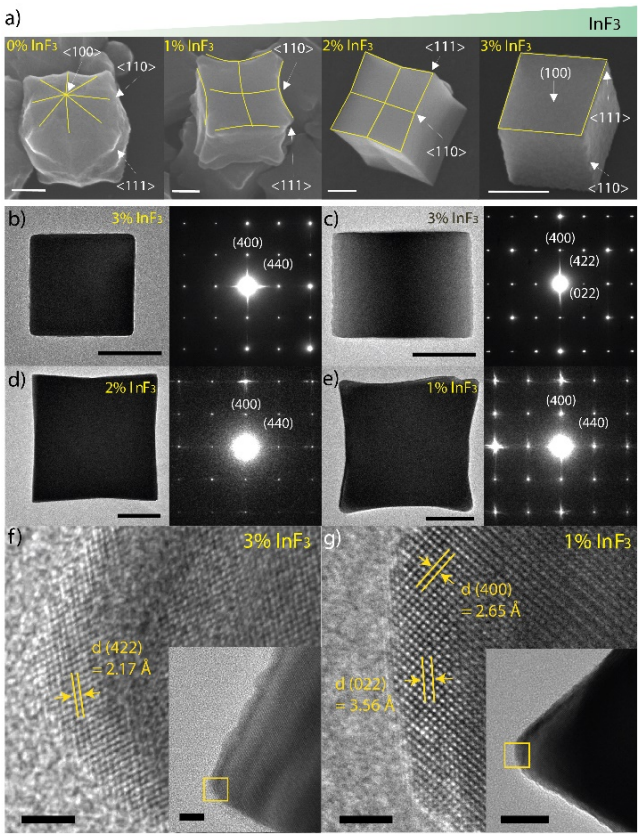

Figure A2.1. (a) SEM images showing the progressive effect of F on In_2O_3 NC morphology. Outlines are shown as guides to visualize the indicated facets. TEM images (left panels) and

the corresponding SAED patterns (right panels) of (b) cube, (c) edge-oriented cube, (d) sharp concave cube, and (e) concave cube F:In_2O_3 NCs. Scale bars are 100 nm for a-e. (f) HRTEM image of a single F:In_2O_3 cube corner with NC oriented on its edge (inset). (g) Extended corner of concave cube F:In_2O_3 NC (inset). Scale bars are 2 nm in f and g, and 20 nm in the insets.

A2.3.2. Influences of fluorine on F:In_2O_3 nanocrystal shape

SEM and HRTEM analyses indicate that fluorine has a facet-directing function in the growth of F:In_2O_3 NCs. The cube-shaped NCs were produced only in the presence of fluorine (Figure A2.1a, right), while the cubic shape is not observed in its absence (Figure A2.1a, left), or in the presence of $InCl_3$ or $InBr_3$.[28] This is because the bond dissociation energy is 439 kJ/mol for the In-Cl bond and 418 kJ/mol for the In-Br bond, which are lower than for In-F at 506 kJ/mol.[29] In-F bonds, being stronger than In-O bonds (at 360 kJ/mol), are hypothesized to be highly stable at In_2O_3 NC surfaces, while weaker In-Cl or In-Br bonds are less favorable.[13,30]

Since fluorine plays an important role in the faceting of the In_2O_3 NCs, XPS was used to probe the presence of fluorine on their surfaces. XPS is sensitive to surface composition, as the escape depth of photoelectrons is only a few nanometers. The existence of fluorine on the F:In_2O_3 NC surfaces was revealed by XPS spectra acquired for the In 3d (Fig. A2.2a) and F 1s (Fig. A2.3b) regions. As shown in Fig. A2.3a, the In $3d_{5/2}$ signal was deconvoluted into components that are assignable to lattice In-O (444.3 eV), In-OH (445.0 eV), and In-F (445.8 eV) species,[31] with the peak due to the In-F species becoming more dominant as the InF_3 precursor concentration is increased. Furthermore, the F 1s peak at 684.6 eV, flanked by the In 3p doublet peaks, also exhibited a similar increase in relative intensity as the InF_3 precursor concentration is increased (Fig. A2.2b). Overall, the undoped In_2O_3 NCs are

observed to have more surface-adsorbed hydroxyl and carbonyl species as compared to F:In_2O_3 NCs, which corroborates the incorporation of F species as surface-capping agents. XPS characterization thus suggests that fluorine adsorbs on the In_2O_3 NC surfaces, linked to the stability and prevalence of {100} facets in cube-shaped NCs.

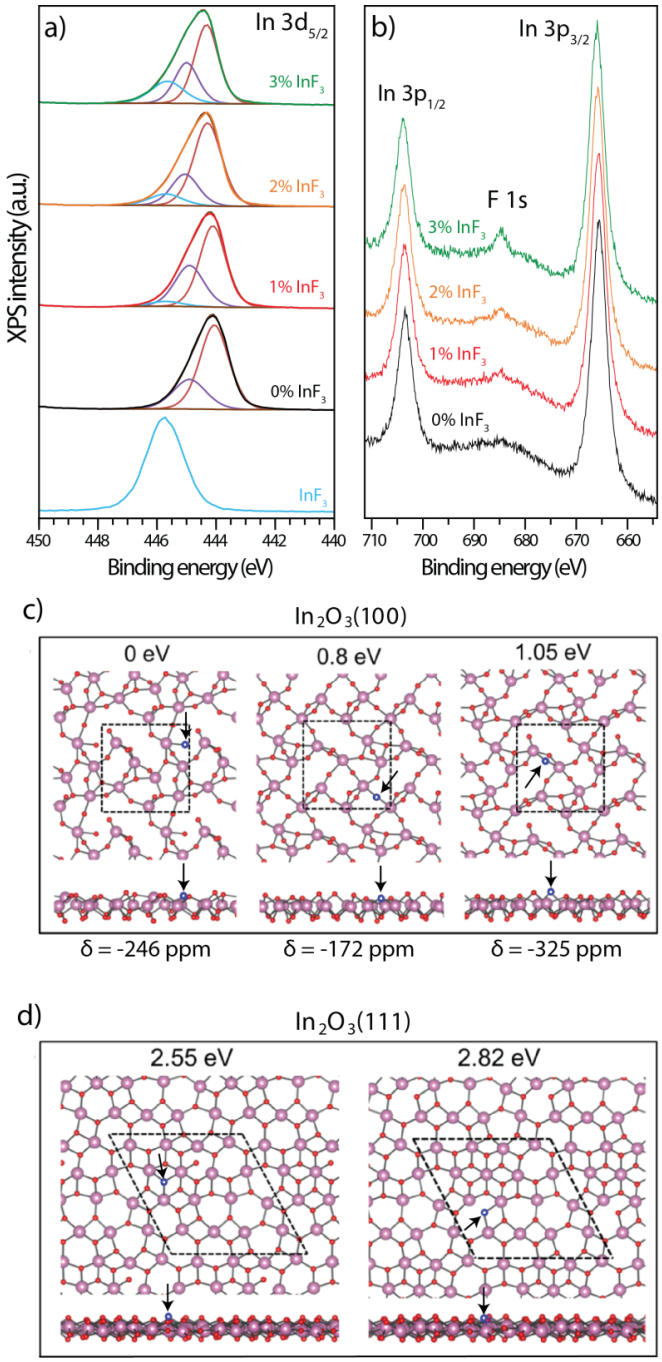

Figure A2.2. Tracking F incorporation in the F:In_2O_3 NCs by XPS. (a) In $3d_{5/2}$ region showing the contributions of various components (red = In-O, purple = In-OH and blue = In-

F), and (b) F 1s region (along with In 3p region) for undoped In_2O_3 NCs (black curve), concave cubes (red curve), sharp concave cubes (orange curve), and cubes (green curve). Note that the In-F component (blue curve in panel a) increases in intensity as the InF_3 concentration used during synthesis is increased. In $3d_{5/2}$ spectrum for InF_3 is shown for reference (blue curve, bottom). DFT calculated top and side views of an F atom substituting O on (c) In_2O_3(100) surface, and (d) In_2O_3(111) surface. Red: O; Purple: In; Blue: F (marked with arrow). For clarity, only the top In layer and the coordinated O and F are shown. The number on top of each panel shows the corresponding formation energy of the F/O substitution (see SI) with respect to the most stable configuration (c, left). δ_{iso} is the calculated NMR isotropic chemical shift. Only low-energy structures for each surface are shown.

Fluoride anions have been described as facet-directing agents in metal oxide NCs,[13] such as in the fluorinated synthesis of TiO_2 NCs[20,30] and may also have played this role in the synthesis of F and Sn co-doped In_2O_3 NCs.[19] Metal fluoride precursors, such as InF_3, decompose into HF in the presence of oleic acid during the reaction, releasing fluoride anions and passivating the In-O surfaces with In-F bonds.[20] Walsh et al.[32] determined through density functional theory (DFT) calculations that for bixbyite In_2O_3, relaxed {111} facets are energetically preferred over oxygen terminated {100} facets ($\gamma_{(111)} < \gamma_{(100)}$). However, surface-passivation by F^- in metal oxide NCs can be expected to alter the energetic sequence of the facets: F^- passivation of the {100} facets results in surface energy inversion ($\gamma_{(111)} > \gamma_{(100)}$).[30] Correspondingly, F^- functions as a favorable {100} facet capping agent over {111} in the bixbyite In_2O_3 NCs, hindering In atomic layer growth at the F^- terminated {100} surface due to fewer O sites available for In-OH monomer condensation to occur. This directs the synthesis of well-defined F:In_2O_3 cube NCs (3% InF_3) when sufficient F^- passivation occurs at the {100} facet.

To understand the surface effects of fluorine on the morphology of In_2O_3, density-functional theory (DFT) calculations were conducted[28] by calculating relative formation energies of F substituting at surface O atomic sites on (100) and (111) surfaces. The (111)

surface was selected for comparison with (100) as it has been reported to have the lowest surface energy in In_2O_3 without F doping.[32] All possible F substitution sites were considered, and only the low formation energy surface configurations are shown in Fig. A2.2c,d. F substitution is more energetically favorable on the (100) surfaces than the (111) surfaces, with F substitution at (111) surfaces yielding formation energies (2.55 eV, 2.82 eV) that are higher than the (100) surface configurations. Since growth through monomer deposition requires addition of new In/O atoms on oxygen terminated sites,[33] it can be expected that this process is more difficult for fluorine capped (100) surface than on (111). This explains why the (100) has a passivated growth rate and becomes the dominant NC surface. NMR chemical shifts of ^{19}F atoms in different configurations on the (100) surface are calculated, with the most stable structure (Fig. A2.2c, left) corresponding to a chemical shift of -246 ppm, to be compared below to experimental solid-state ^{19}F NMR spectra.

The complex concave cube shape of moderately passivated F:In_2O_3 NCs (1% InF_3) can be rationalized through the shape control model previously described for other halide-passivated NCs.[13,14] Colloidal syntheses of NCs involve both thermodynamic and kinetic effects that impact NC shape. The conceptual framework involves two monomer addition processes: deposition on facets with high surface energy (kinetic) and monomer surface diffusion to minimize total surface energy of NC facets (thermodynamic).[2] The high rate of In-OA precursor decomposition, driven by aminolysis, leads to a high rate of monomer deposition onto growth-favorable NC facets at a short reaction time (5 min). During fluorine-free synthesis, undoped In_2O_3 NCs exhibit growth in all <100>, <110>, and <111> directions into irregularly shaped NCs (Fig. A2.1a, leftmost panel). With intermediate InF_3 concentrations (1-2% InF_3), the {100} facet is partially capped by F^-, and In monomer

deposition becomes unfavorable on {100} facets with more F^- capped sites. Instead, the reaction conditions are favorable for selective monomer deposition on the less F^- surface occupied {111} facets. Thus, F^- passivated {100} facets have slower growth and monomers preferentially deposit on {111} facets during NC growth.[34] Through this process, elongated <111> direction tips are seen in F:In_2O_3 concave cube NCs (1% InF_3), with concave {100} facets (Fig. A2.1a, second from left). Well-defined concave cube F:In_2O_3 NCs of 290.4 ± 17.9 nm size with sharp elongated <111> corners result when using a 2% InF_3 precursor content, showing distinct high-index quadrant boundaries on the {100} facets (Fig. A2.1a, second from right). With higher InF_3 concentration (3% InF_3), the {100} facets become increasingly passivated by F^- capping. Fluorine terminated {100} surface exposure is favored for minimizing total surface energy, and well-defined cube-shaped NCs result.

Although the electron microscopy images and electron diffraction patterns indicate substantial long- and short-range lattice order in the F:In_2O_3 NCs, the non-stoichiometric distributions of fluorine species introduce significant and important complexity to the NC structures that govern their growth and optical properties. The types, distributions, and electronic environments of ^{19}F atoms in F:In_2O_3 NCs are established by solid-state ^{19}F MAS NMR analyses. The solid-state 1D ^{19}F MAS NMR spectrum of F:In_2O_3 NCs (3% InF_3) in Fig. A2.3a reveals four resolved ^{19}F signals at 50, -50, -208, and -234 ppm, which are assigned on the basis of the 2D $^1H\{^{19}F\}$ NMR correlation spectrum and ^{19}F spin-lattice relaxation time analyses discussed below to ^{19}F nuclei in different types of chemical and/or electronic environments in the F:In_2O_3 NCs.

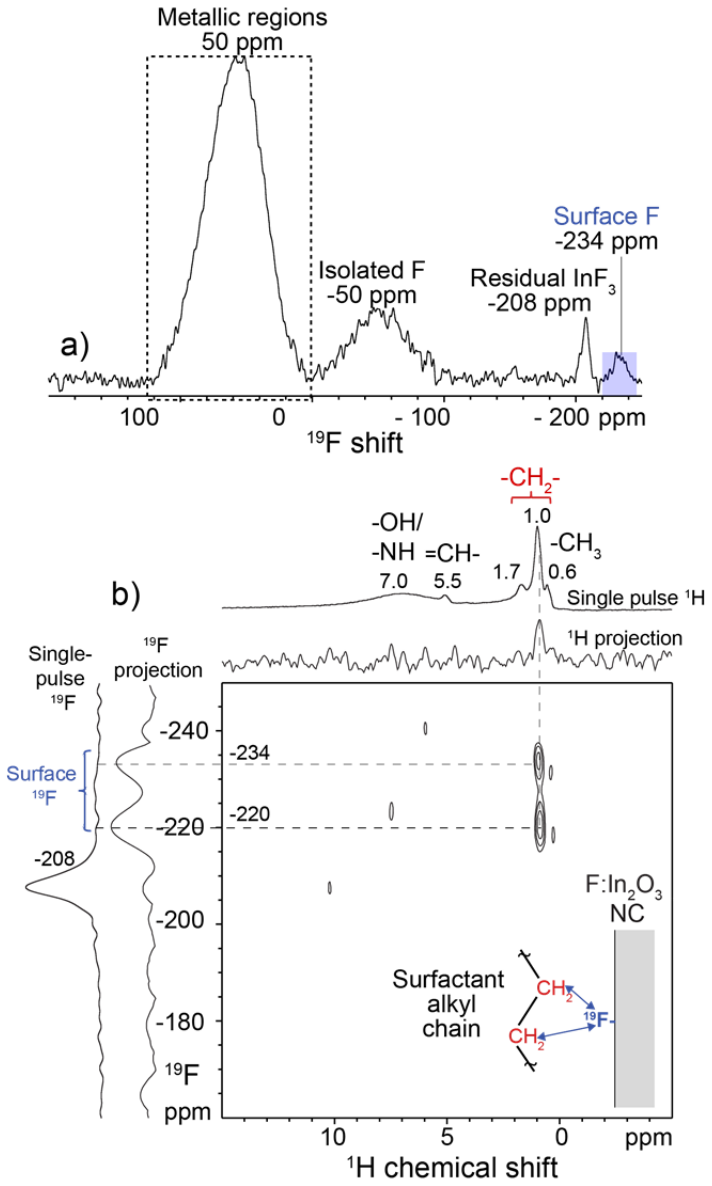

Figure A2.3. Solid-state (a) 1D ^{19}F echo and (b) 2D ^{1}H{^{19}F} correlation MAS NMR spectra of F:In_2O_3 NCs (3% InF_3) diluted in 1:1 ratio by mass with KBr. Solid-state 1D single-pulse ^{1}H and ^{19}F spectra acquired under the same conditions are shown along the horizontal and vertical axes of the 2D spectrum in (b) for comparison with the 1D projections. The inset shows a schematic diagram of a surface ^{19}F moiety interacting with the alkyl chain of a surface-bound organic ligand, as indicated by arrows. The spectra were acquired at 9.4 T, (a) 35 kHz MAS and 395 K or (b) 25 kHz MAS and 327 K.

Importantly, dilute surface fluorine moieties are detected and identified in the solid-state two-dimensional (2D) ^{1}H{^{19}F} correlation NMR spectrum in Fig. A2.3b. The spectrum is shown as a 2D contour plot, having ^{1}H and ^{19}F frequency axes (with units of Hz/MHz or

ppm) on the abscissa and ordinate, respectively. Correlated signal intensities in the 2D spectrum arise only from ^{1}H species that are dipole-dipole-coupled with ^{19}F atoms over nanoscale distances (<0.5 nm for the short dipolar recoupling time, 0.96 ms, used here), thereby establishing the mutual proximities of the ^{1}H and ^{19}F species with associated signals. For comparison, a standard 1D ^{1}H MAS NMR spectrum is shown above the ^{1}H axis of the 2D spectrum, which exhibits signals at 0.6, 1.0, 1.7, 5.5, and 7.0 ppm that are all assigned to ^{1}H moieties on the octylamine, trioctylamine, or oleate organic surfactant molecules as indicated by the labels above the respective ^{1}H signals. The 2D $^{1}H\{^{19}F\}$ correlation spectrum resolves two ^{19}F signals at -234 and -220 ppm that are correlated to ^{1}H signals at 1.0 ppm from $-CH_2-$ moieties on the organic surfactant molecules, unambiguously establishing the interactions and proximities of the corresponding ^{1}H and ^{19}F species at the $F:In_2O_3$ particle surfaces. Notably, no correlated signal intensity is observed for the relatively narrow ^{19}F signal at -208 ppm (6 ppm full-width-half-maximum, FWHM), which is assigned to residual InF_3 precursor species.[35] Furthermore, while ^{1}H signal intensity is detected in 1D $^{1}H\{^{19}F\}$ NMR spectra acquired with ^{19}F excitation at -210 ppm, the same excitation frequency used to acquire the 2D spectrum in Figure 4b, no ^{1}H signal intensity is detected for ^{19}F excitation at different frequencies.[28] These results indicate that only the ^{19}F signals in the -220 to -234 ppm frequency range correspond to ^{19}F surface species, and that the other types of ^{19}F environments detected in the 1D ^{19}F MAS NMR spectra in Fig. A2.3a are located in sub-surface environments, within the detection limits of the NMR measurements.

From the quantitative single-pulse 1D ^{19}F MAS NMR spectrum in Fig. A2.4, the ^{19}F signals in the frequency range from -220 to -234 ppm account for only 1-2% of all the ^{19}F signal intensity, indicating that <2% of all of the ^{19}F species in the $F:In_2O_3$ NCs are in surface

environments. These surface-related ^{19}F signals in the range of -220 to -234 ppm are close to the shift values predicted by DFT calculations for the most energetically stable ^{19}F structure on the (100) surface (-246 ppm, Fig. A2.2c, left). While the DFT models neglect other possible adsorbates for computational simplicity and represent an idealized subset of numerous possible surface configurations, this agreement suggests that the DFT calculations capture the main effects of fluorine on the (100) surface. The combined solid-state 1D ^{19}F and 2D $^{1}H\{^{19}F\}$ NMR analyses and DFT calculations thus identify and quantify the small fraction of ^{19}F species at the surfaces of the $F:In_2O_3$ NCs that are hypothesized to direct the NC morphology by adsorbing on {100} facet surface sites.

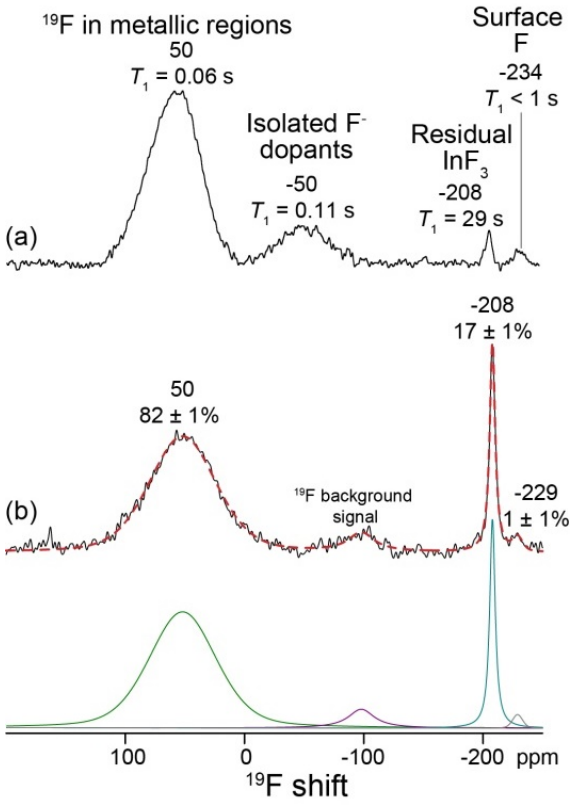

Figure A2.4. Solid state 1D (a) ^{19}F echo (same as Figure A2.3a) and (b) quantitative single-pulse ^{19}F MAS NMR spectra of $F:In_2O_3$ (3% InF_3) diluted with KBr in a 1:1 ratio by mass. The spectra were acquired at 9.4 T, 35 kHz MAS, and sample temperatures of 395 K. The ^{19}F spin-lattice T_1 relaxation times, measured under the same conditions, are given under the respective signal labels in (a). The dotted red line in (b) is the simulated ^{19}F spectrum, with the deconvolution shown offset below. The relative integrated signal intensities are shown

above the corresponding signals. The ^{19}F signal at -50 ppm from isolated F^- dopant species is not detected or resolved in the quantitative 1D single-pulse ^{19}F spectrum in (b), indicating that the corresponding ^{19}F species comprise <1% of the total amount of fluorine atoms in the material. The relatively weak ^{19}F signal at ca. -100 ppm in (b) is a ^{19}F background signal from Teflon in the MAS NMR probehead, and was not included in the quantification of the ^{19}F NMR signals from the $F:In_2O_3$ NCs.

A2.3.3. Fluorine as an anionic dopant

Substitutional fluorine dopants incorporated in the NCs can be charge-compensated by free electrons. Fluorine is well-established as anionic n-type dopant that induces high free electron concentrations in fluorine-doped tin oxide ($F:SnO_2$) transparent conductive oxide films.[21,36] The Kröger-Vink equation[37] for oxygen vacancy formation demonstrates that such defects in the In_2O_3 lattice can be charge compensated by two electrons (Eqn. A2.1).[38] Oxygen substitution by F induces one free electron per fluorine ion (Eqn. A2.2).[39,40]

$$In_{In}^{x} + O_{O}^{x} \rightarrow In_{In}^{x} + V_{O}^{\bullet\bullet} + 2e' + \frac{1}{2}O_{2\,(g)} \quad , \quad \text{(A2.1)}$$

$$In_{In}^{x} + 3O_{O}^{x} \xrightarrow[InF_3]{} 2In_{In}^{x} + 3F_{O}^{\bullet} + 3e' + \frac{3}{2}O_{2\,(g)} \quad , \quad \text{(A2.2)}$$

Kröger-Vink notation suggests halogen dopants with the same valency as F, should contribute to free-electron compensation. However, the large ionic radii of chloride (Cl^-) or bromide (Br^-) suggests that they are not suitable dopants to incorporate in In_2O_3 NCs. Doping of Cl or Br atoms into In_2O_3 NCs was attempted to check the viability of other halogen dopants in NCs. EDX quantification showed very low halide incorporation for these NCs, as compared to $F:In_2O_3$ NCs synthesized at the same dopant precursor concentration (3% InX_3, X= F, Cl, Br).[28] $Cl:In_2O_3$ NCs show only Cl/In = 0.32 ± 0.11 % atomic composition ratio and $Br:In_2O_3$ NCs had Br/In = 2.62 ± 0.06 %, whereas $F:In_2O_3$ cubes show higher F/In = 11.76 ± 2.70 %.[28] The low anionic dopant concentration observed can be attributed to Cl^- (1.81 Å) having a much larger ionic radius than F^- (1.19 Å), which would yield a correspondingly

large ionic radius mismatch (46.0%) with O^{2-} (1.24 Å) and cause significant lattice strain in the host lattice.[41] Similarly, Br^- (1.96 Å) is not incorporated within the In_2O_3 NC lattice, consistent with similar straining (58.1 %).[41]

Based on quantitative 1D ^{19}F MAS NMR and ^{19}F spin-lattice relaxation time analyses, the majority of ^{19}F atoms in the F:In_2O_3 NCs are located in metallic sub-surface environments. The 1D ^{19}F MAS NMR spectra in Fig. A2.3a and A2.4 show two broad ^{19}F signals at 50 ppm and -50 ppm with FWHM signal linewidths of 66 ppm and 26 ppm, respectively. The ^{19}F signal at -50 ppm is similar to ^{19}F signals observed for some other metal oxyfluorides[42–44] and is assigned to isolated F^- anionic dopant species in the F:In_2O_3 NCs. By comparison, based on temperature-dependent analyses of ^{19}F spin-lattice (T_1) relaxation times, the ^{19}F signal at 50 ppm is confidently assigned to a distribution of ^{19}F species in metallic environments in the F:In_2O_3 NCs. In metallic materials, including degenerately doped semiconductors,[45] nuclear spins and conduction band electrons in *s*-like orbitals couple through Fermi contact interactions. These interactions give rise to two characteristic effects that are manifested in the ^{19}F NMR spectra of F:In_2O_3 NCs: a frequency displacement of the ^{19}F NMR signals called the Knight shift,[45–47] and a Korringa-type temperature-dependence of the rate of ^{19}F nuclear spin-lattice relaxation.[46,48,49] For the ideal case of isolated nuclear spins coupled to a degenerate gas of electron spins, the Korringa contribution to the relaxation rate, $T_{1,K}^{-1}$, is related to the Knight shift, K, by the well-known Knight-Korringa relation:[46,48]

$$T_{1,K}^{-1}(K,T) = \left(\frac{\gamma_n}{\gamma_e}\right)^2 \frac{4\pi k_B T}{\hbar} K^2 \quad , \qquad \text{(A2.3)}$$

where γ_n and γ_e are the gyromagnetic ratios of the nuclear and electron spins, respectively, k_B and $\hbar$ are the Boltzmann and Planck constants, and T is the absolute temperature. The Knight-Korringa relation shows that the $T_{1,K}^{-1}$ values for nuclear spins in metallic

environments are proportional to both temperature, T, and the square of the Knight shift, K^2. Fluorine species in metallic environments may therefore be identified on the basis of analysis of the ^{19}F T_1^{-1} values as functions of both NMR frequency position and temperature.

Analyses of the 1D ^{19}F MAS NMR spectra and T_1^{-1} relaxation rates at temperatures of 276-395 K, shown in Fig. A2.5, reveal that the broad ^{19}F signal at 50 ppm in Fig. A2.3a corresponds to ^{19}F dopant atoms in metallic environments within the F:In_2O_3 NCs that exhibit Korringa-type relaxation behavior. By comparison, the ^{19}F signal at -50 ppm, which also manifests a broad distribution of ^{19}F environments, exhibits no Korringa-type temperature-dependencies in its spin-lattice relaxation behavior, consistent with its assignment to a distribution of isolated ^{19}F dopants in the In_2O_3 lattice that experience chemical and/or paramagnetic shifts, but not metallic Knight shifts. The ^{19}F frequency axis in Fig. A2.3a is renormalized in Fig. A2.5a such that the signal from isolated F^- dopant species (-50 ppm in Fig. A2.3a) is set to a Knight shift K of 0 ppm. As shown in Fig. A2.5a, the broad ^{19}F signal distribution at K = 100 ppm (50 ppm in Fig. A2.3a) from ^{19}F species in metallic environments does not change significantly in width or position over the temperature range 276-395 K, consistent with the expected temperature-invariance of Knight shifts for heavily-doped semiconductors.[46] The ^{19}F T_1^{-1} values were measured by ^{19}F saturation recovery experiments, and the $T_{1,K}$ values for each isochromat across the ^{19}F Knight-shifted signal distribution were extracted by subtraction of the temperature-independent contribution ($T_{1,0}^{-1}$) from the overall relaxation rate, T_1^{-1}:

$$T_{1,K}^{-1}(K,T) = T_1^{-1}(K,T) - T_{1,0}^{-1} \quad , \qquad \text{(A2.4)}$$

The temperature- and shift-independent term $T_{1,0}^{-1}$ depends on the MAS rate and was measured to be 6.9 ± 0.3 s^{-1} at 25 kHz MAS and 4.8 ± 0.5 s^{-1} at 35 kHz MAS. Due to the

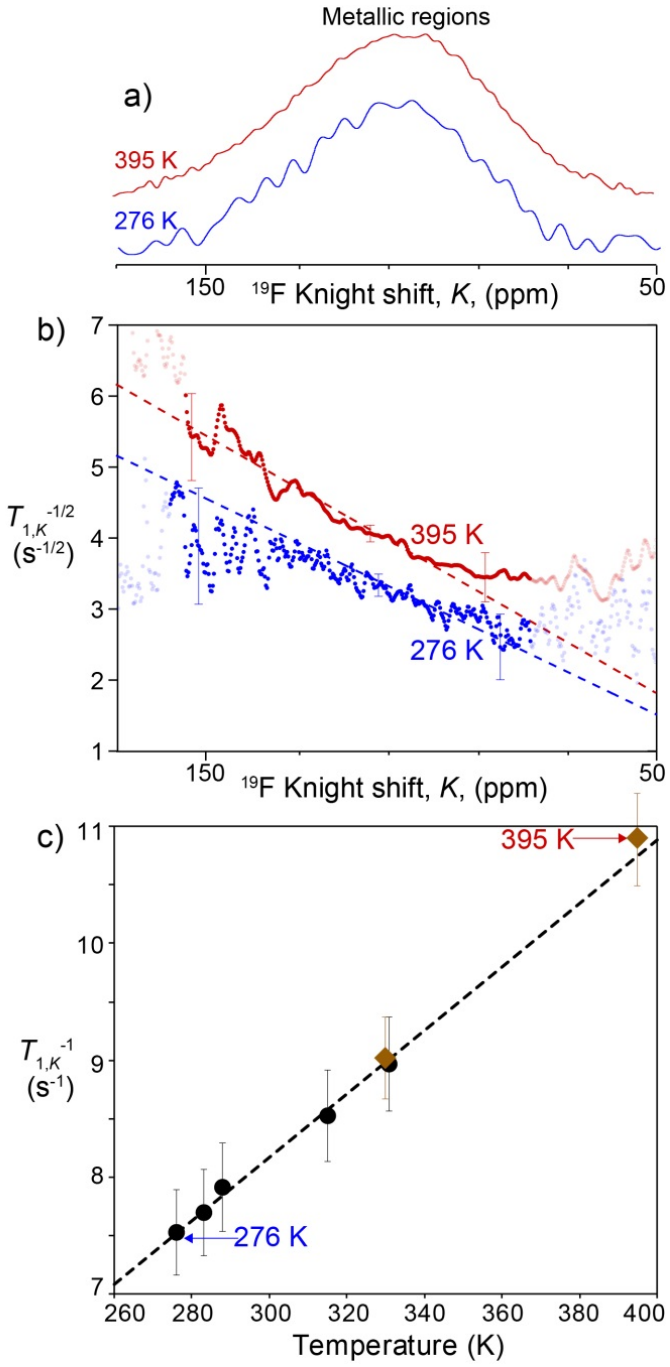

Figure A2.5. (a) Enlargement of the Knight-shifted ^{19}F spectral region (boxed region in Fig. A2.3a) showing a comparison of the 1D solid-state ^{19}F echo MAS NMR spectra of F:In_2O_3 NCs (3% InF_3) diluted in 1:1 ratio by mass with KBr. The frequency axis is renormalized with the zero Knight shift peak at -50 ppm, corresponding to the signal from isolated F^- dopants in the F:In_2O_3 NCs. The spectra were acquired at 9.4 T, 35 kHz MAS and 395 K (red) or 25 kHz MAS and 276 K (blue). (b) Plot of the square root of the ^{19}F spin-lattice relaxation rate due to Korringa relaxation, $T_{1,K}^{-1/2}$, for different ^{19}F Knight shifts K in F:In_2O_3 NCs (3% InF_3), measured at 9.4 T, 35 or 25 kHz MAS, and at 395 K (red) or 276 K (blue). Partially transparent data points correspond to spectral regions with little or no ^{19}F signal

intensity, resulting in large uncertainties that are not pertinent to the analyses. (c) Plot of the ^{19}F $T_{1,K}^{-1}$ at the peak maximum of the Knight shift distribution (K = 100 ppm) as a function of temperature. Black circles and brown diamonds indicate $T_{1,K}^{-1}$ values measured under MAS conditions of 25 kHz and 35 kHz, respectively. The dashed lines in (b) and (c) indicate theoretical values obtained from the Knight-Korringa equation (eq. 3).

MAS dependence of $T_{1,0}^{-1}$, this term likely reflects the contribution to the ^{19}F T_1^{-1} relaxation rate of strong ^{19}F-^{19}F and/or ^{19}F-electron dipole-dipole couplings, which are partially averaged under MAS conditions. The experimentally-measured T_1 values at the different MAS rates and temperatures are shown in Fig. A2.6, for comparison with the $T_{1,K}$ values obtained using Eqn. A2.4 and the theoretical $T_{1,K}$ values from Eqn. A2.4. The square root of the temperature-dependent relaxation term, $T_{1,K}^{-1/2}$, is plotted as a function of K for the K = 50 to 175 ppm region (boxed region in Fig. A2.3a) in Fig. A2.5b. At temperatures of 395 K (red) and 276 K (blue), the measured $T_{1,K}^{-1/2}$ values show excellent agreement across the entire ^{19}F Knight shift distribution with the theoretical values predicted by the Knight-Korringa expression at the different temperatures (dotted lines), which notably has no adjustable parameters and is derived from first principles.[45,46,48]

Additionally, the Knight-Korringa relation holds across the entire temperature range of 276-395 K. The Korringa-type plot in Fig. A2.5c shows a plot of the $T_{1,K}^{-1}$ values extracted at the maxima of the ^{19}F Knight shift distribution (K = 100 ppm), as a function of temperature, revealing excellent agreement with the Knight-Korringa relation over the entire temperature range. This corroborates the conclusion that the broad ^{19}F signal at 50 ppm in Fig. A2.3a and Fig. A2.4 arises from a distribution of Knight shifts that manifest a range of couplings of ^{19}F nuclei to conduction band electrons in regions of the F:In_2O_3 NCs with different extents of metallic character. The ^{19}F atoms, acting as anionic n-type dopants, therefore are sufficiently

dense that their associated unpaired electrons form a conductive network within the heavily-doped In_2O_3 lattice.

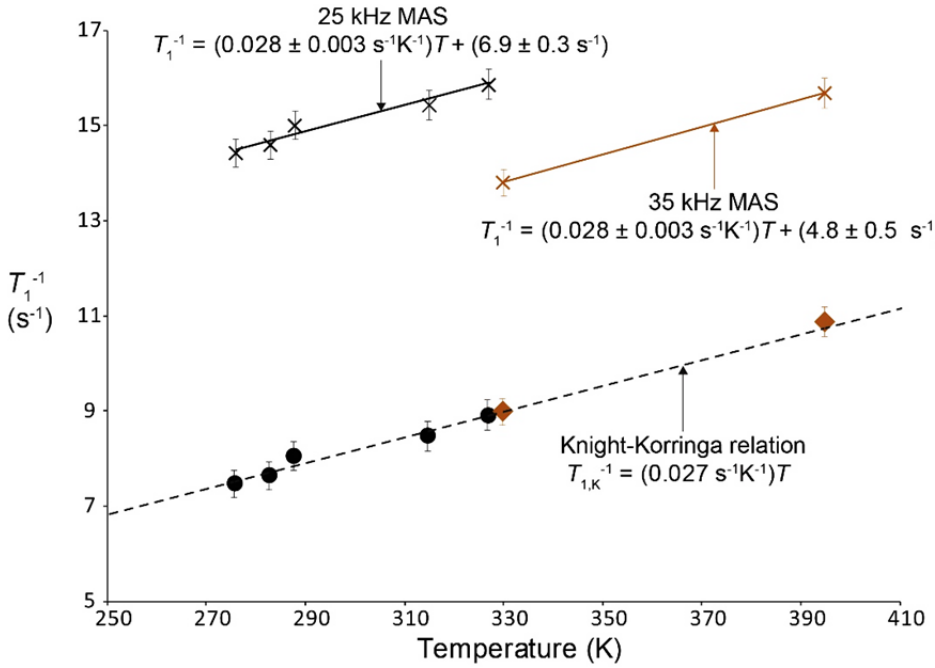

Figure A2.6. Plot of the experimental ^{19}F T_1^{-1} values (X symbols) measured at the peak maximum of the Knight shift distribution (K = 100 ppm) as a function of temperature. The black and brown data points were measured under MAS conditions of 25 and 35 kHz, respectively. The black and brown solid lines are linear fits to the data points, with the corresponding equations shown. The slopes of the linear fit equations are within experimental error of the slope predicted from the theoretical Knight-Korringa relation (black dashed line), and the intercept values are the temperature-independent $T_{1,0}^{-1}$ values for the different MAS conditions. The black circles and brown diamonds are the experimental data points corrected for the temperature-independent $T_{1,0}^{-1}$ terms (same points as in Fig. A2.5c), which show excellent agreement with the Knight-Korringa relation, as discussed in the text. Error bars were calculated using standard error propagation methods and indicate uncertainties associated with the signal-to-noise ratios of the ^{19}F MAS NMR spectra and the quality of the fits to the ^{19}F saturation-recovery measurements.

Furthermore, based on the quantitative single-pulse ^{19}F NMR spectrum of the F:In_2O_3 NCs (3% InF_3) in Fig. A2.4b, approximately 82 ± 1% of all of the ^{19}F species are in sub-surface metallic environments in the In_2O_3 lattice, 17 ± 1 % in residual InF_3, and <1% at isolated dopant sites in the In_2O_3 lattice. The combined solid-state 2D $^1H\{^{19}F\}$ NMR correlation and ^{19}F T_1 relaxation analyses establish that only a small percentage (1-2%) of ^{19}F

species are at the surfaces of the F:In_2O_3 NCs. The majority of ^{19}F species are incorporated into the F:In_2O_3 NCs in sub-surface metallic domains, consistent with F^- as an anionic dopant within the In_2O_3 lattice.

The metallic domains are also manifested by evidence of conduction band electron influences on local ^{115}In environments in the F:In_2O_3 crystal lattice. Specifically, analyses and comparison of the solid-state wideline ^{115}In NMR spectra in Fig. A2.7 of undoped bulk In_2O_3 and F:In_2O_3 NCs show differences that are characteristic of the coupling of ^{115}In nuclei to free electron carriers. Acquisition of solid-state ^{115}In NMR spectra has been exceedingly challenging in the past due to the highly quadrupolar character of ^{115}In nuclei ($I = 9/2$), which often exhibit very broad (several MHz) and poorly resolved ^{115}In NMR signals.[50] Very few solid-state ^{115}In NMR spectra of inorganic materials have been reported, with emphases primarily on materials with ^{115}In atoms in symmetric environments, such as cubic zincblende semiconductors like InP and InN,[51,52] which yield narrower and more tractable lineshapes. Recent wideline NMR techniques enable the detection and analysis of very broad NMR signals, even for quadrupolar nuclei in paramagnetic or conductive materials.[53–55]

Here, the frequency-stepped quadrupolar Carr-Purcell-Meiboom-Gill (QCPMG) technique[56] was used to measure the solid-state ^{115}In NMR spectra of bulk undoped polycrystalline In_2O_3 and F:In_2O_3 NCs (Fig. A2.7). The QCPMG pulse sequence yields manifolds of very narrow, evenly-spaced NMR signals (spikelets), though which cannot cover the entire ^{115}In spectral range of these materials, but can be systematically acquired as a series that can be overlain to map the full ~2 MHz broad central transition (CT) region of the ^{115}In NMR spectrum. For example, the ^{115}In NMR spectrum in Fig. A2.7a of bulk undoped In_2O_3 is presented as a mosaic overlay of 22 individual QCPMG sub-spectra (plotted in

different colors) that were acquired at evenly spaced frequency intervals. Though detailed analysis of the ^{115}In NMR lineshapes is complicated by overlap of the numerous ^{115}In satellite transitions (STs) of the quadrupolar ^{115}In nuclei, the sensitivity and resolution of the wideline ^{115}In QCPMG spectra is sufficient to simulate the ^{115}In CT regions and estimate the quadrupolar coupling constant (C_Q), asymmetry parameter (η), and isotropic shift (δ_{iso}) for the bulk In_2O_3 (Table A2.1). Such NMR parameters are highly sensitive to the chemical and electronic environments of ^{115}In species in In_2O_3 and to our knowledge have never previously been measured or reported.

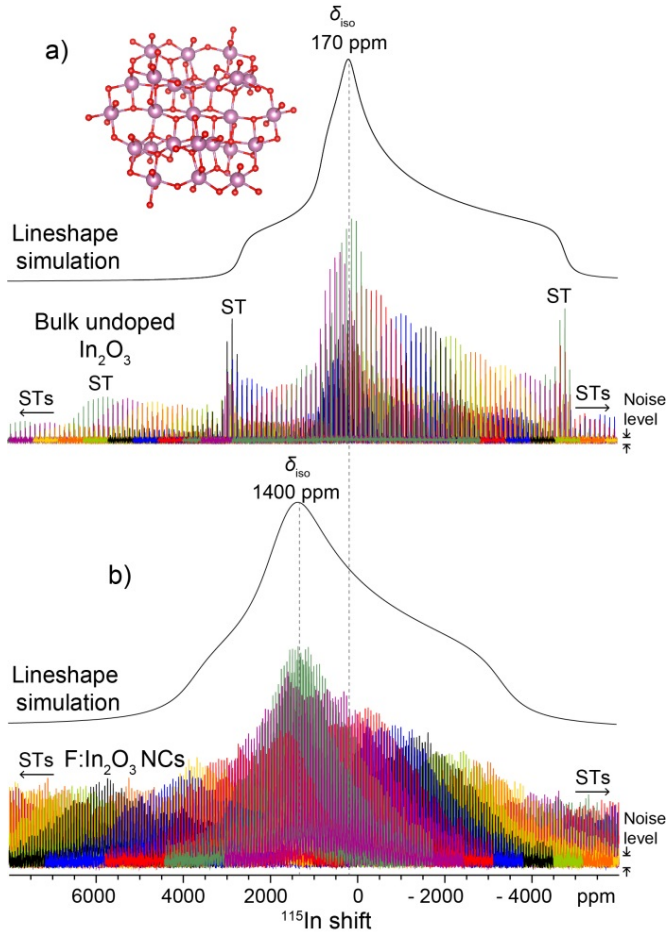

Figure A2.7. Solid-state 1D ^{115}In NMR spectra of (a) undoped microcrystalline In_2O_3 and (b) F:In_2O_3 NCs (3% InF) acquired at 295 K, under static conditions, and at magnetic field strengths of (a) 18.8 T and (b) 19.6 T. The spectra are an overlay of 22 different sub-spectra (shown as different colors) acquired at evenly-spaced frequency intervals. Simulated ^{115}In NMR lineshapes generated using the parameters in Table A2.1 are shown offset above the

experimental ^{115}In NMR spectra. Signal intensities arising from ^{115}In satellite transitions are indicated by "ST." The inset in (a) shows the crystal structure of cubic bixbyite In_2O_3 with In atoms as pink and oxygen atoms as red.

Table A2.1. Parameters for the ^{115}In simulated lineshapes in Figure A2.7

	η[a]	C_Q (MHz)[b]	δ_{iso} (ppm)[c]	Gaussian Line broadening[d] (ppm)
Bulk undoped In_2O_3	1	128	170	300
F:In_2O_3	1	139	1400	800

[a] Asymmetry parameter
[b] Quadrupolar coupling constant
[c] Isotropic shift (including chemical and Knight shifts)
[d] Gaussian line broadening apodization was applied to account for distributions of chemical shifts, Knight shifts, and/or quadrupolar parameters

Compared to bulk In_2O_3, the ^{115}In NMR spectrum of F:In_2O_3 NCs is displaced and broadened, consistent with the coupling of ^{115}In nuclei to unpaired conduction band electrons. Both undoped polycrystalline In_2O_3 (Fig. A2.7a) and F-doped In_2O_3 NCs (Fig. A2.7b) exhibit very broad spectral features in the -4000 to 4000 ppm range that arise from the CT of ^{115}In nuclei in the different materials. The ^{115}In CT regions for both materials are reproduced by a single simulated ^{115}In lineshape with $C_Q \approx 130$ MHz and $\eta = 1$, though with different isotropic shifts (Fig. A2.7, black spectra, see also Table A2.1). The bulk undoped In_2O_3 (cubic bixbyite phase by XRD) exhibits an isotropic ^{115}In shift of 170 ppm, consistent with diamagnetic ^{115}In environments in the In_2O_3 lattice. By comparison, the ^{115}In spectrum of F:In_2O_3 NCs (3% InF) exhibits an isotropic ^{115}In shift of 1400 ppm, displaced more than 1200 ppm from the position for diamagnetic In_2O_3. This displacement provides evidence that the majority of ^{115}In species in the F:In_2O_3 lattice experience substantial Knight shifts[45] arising from interactions with unpaired conduction band electrons associated with the F dopant species. The ^{115}In Knight shifts corroborate the ^{19}F NMR and T_1 spin-lattice relaxation time analyses discussed above. The ^{115}In NMR spectrum of the F:In_2O_3 NCs is also broadened compared to that of bulk undoped In_2O_3, indicating a larger distribution of

chemical shifts, Knight shifts, and/or quadrupolar parameters (Table A2.1). The continuous distributions of signal intensity extending to higher and lower frequencies in both of the ^{115}In NMR spectra in Fig. A2.7 arise from the very broad and overlapping ^{115}In satellite transitions, which are expected to span frequency regions of tens of MHz. To the best of our knowledge, the solid-state ^{115}In NMR spectra presented here are the first ^{115}In NMR analyses of In_2O_3, and evidence the sensitivity of ^{115}In NMR to different electronic environments in technologically-important In_2O_3 materials. The solid-state ^{115}In and ^{19}F NMR analyses together provide complementary and consistent evidence for metallic ^{115}In and ^{19}F environments in the heavily-doped F:In_2O_3 lattice.

A2.3.4 Optical Properties of F:In_2O_3 NCs

Considerations of charge compensation accompanying fluorine doping (Eqn. A2.2) as well as the NMR analyses of the ^{19}F and ^{115}In species show that the anionically doped F:In_2O_3 NCs contain substantial free-electron populations leading to LSPR response. Liquid-cell FTIR spectra confirm that the F:In_2O_3 NCs exhibit IR range LSPR, with an absorption tail towards the visible region that is responsible for their blue appearance. In the F:In_2O_3 cubes, the highly defined corners and edges can be expected to result in multimodal LSPR extinction peaks in the IR spectral range. F:In_2O_3 cubes (3% InF_3) have highly pronounced plasmon peaks at 3496 cm^{-1} (FWHM 1157 cm^{-1}) and 5469 cm^{-1} (Fig. A2.8a, green), respectively ascribed to corner- and edge-dominated LSPR modes, by comparison to analogous modes observed for silver cubes[57]. Lower fluorine-doped F:In_2O_3 concave cube NCs exhibit changes in LSPR peak shape due to NC shape effects. Sharp concave cubes (2% InF_3) show well-defined modes with LSPR peaks at 2974 cm^{-1} and 5378 cm^{-1} (Fig. A2.8a,

orange). Concave cubes (1% InF_3) with elongated <111> directional corners, exhibit a complex LSPR response centered at 3030 cm^{-1} (Fig. A2.8, red). Previous literature on plasmonic octopod Ag NCs has described the breakdown of simple cubic LSPR modes due to elongated corners.[58,59] By contrast, no multimode LSPR peaks are observed for rounded F:In_2O_3 NCs (1% InF_3) grown at 280 °C[28] due to their spherical shape.[9]

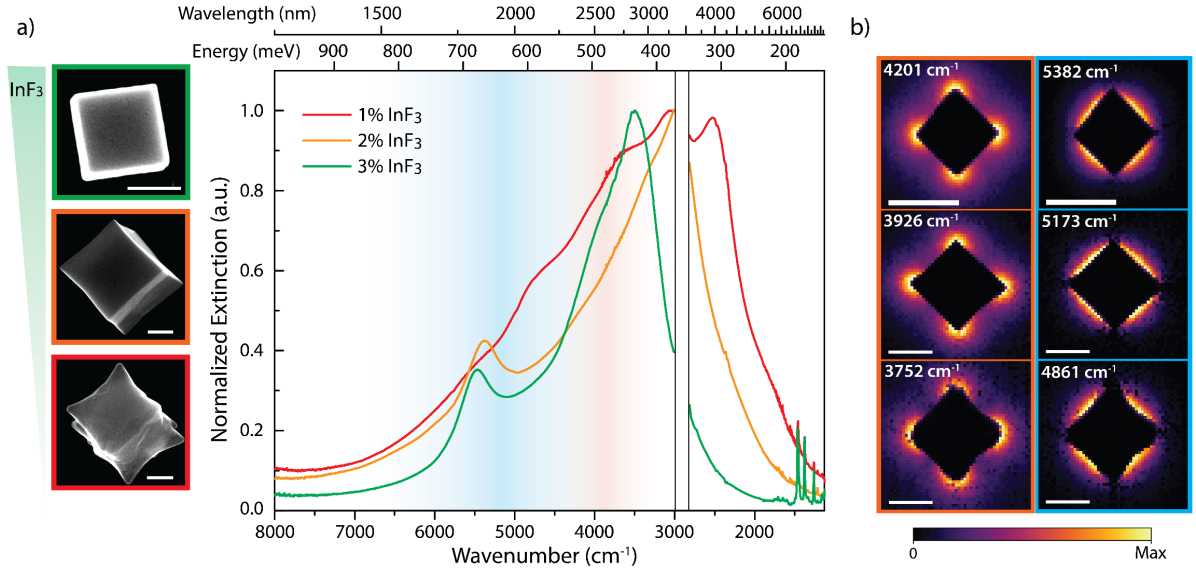

Figure A2.8. (a) Liquid cell FTIR spectra of F:In_2O_3 NCs with corresponding SEM images. F:In_2O_3 cube (green), F:In_2O_3 concave cube (orange), and F:In_2O_3 concave cube (red). Scale bars are 100 nm. Spectral bands saturated by ligand absorption are shown as blank regions. (b) F:In_2O_3 (3% InF_3) cube (top), F:In_2O_3 (2% InF_3) concave cube (middle), and F:In_2O_3 (1% InF_3) concave cube (bottom) EELS maps for corner mode frequencies (around 3900 cm^{-1}, left, orange) and edge mode frequencies (around 5100 cm^{-1}, right, blue) LSPR mode. Scale bars are 200 nm.

To definitively assign the contributions to the multimodal FTIR peaks observed in faceted F:In_2O_3 NCs, we performed STEM-EELS mapping of individual cubes. Optical LSPR excitation in the FTIR only allows ensemble far-field extinction measurements of cubes, where the incidence IR excitation wavelength (1250-10000 nm) is within the LSPR quasi-static limit range.[9] The sub-Ångstrom diameter probe available in the STEM can directly sample and map the near-field localization of LSPR modes, and thanks to recent advances in monochromation these mid-infrared frequencies are now straightforwardly

accessible using EELS.[60,61] The spatial maps are acquired through spectrum imaging (SI), where the beam is rastered across the region of interest and a spectrum is acquired at each probe position resulting in a three-dimensional dataset with two spatial-dimensions and one spectral dimension. From here, individual plasmon modes are deconvoluted through the non-negative matrix factorization (NMF) method to produce spatially resolved EELS maps of individual LSPR modes.[57] For each structure spatially- and spectrally-distinct corner and side modes can be observed and mapped through the deconvolved spectrum imaging, which are plotted in Fig. A2.8b. The corner modes of F:In_2O_3 cube (3% InF_3), sharp concave cube (2% InF_3), and concave cube (1% InF_3) NCs, are observed at 4201 cm^{-1}, 3926 cm^{-1}, and 3752 cm^{-1} respectively, with the side mode resonances centered at 5382 cm^{-1}, 5173 cm^{-1} and 4861 cm^{-1}. It is important to note that for the side modes, the NMF-deconvolution results in a spectral component with multiple peaks, likely corresponding to spatially overlapped edge and face modes. The reported peak center is the average of these face and edge modes. Details of the deconvolution and the EELS experiments are presented in greater detail in ref. 28.

While FTIR samples the ensemble behavior of the NCs and EELS samples the optical properties of individual crystallites, the match is strong enough to determine the modal nature of the FTIR peaks from the EEL-SI. The STEM analyses support that the high energy FTIR peaks correspond to the edge and face modes, while the lower energy peaks correspond to the corner modes. As in FTIR, in EELS the edge mode is observed at higher energy for the cube (3% InF_3) than for the sharp concave cube (2% InF_3) NCs. The frequencies of the corner modes do differ significantly between FTIR and EELS, likely originating from differences in the dielectric function in the liquid-cell FTIR experiments and the SiN/ultra-high-vacuum environment in the STEM.[62] The observed blueshift in the EELS mode relative to the FTIR

spectrum is attributed to the lower refractive index (n=1) of surrounding vacuum in STEM, as compared to the TCE solution medium (n=1.5) in the liquid-cell optical measurement.[63,64]

A2.4 Conclusions

Fluorine plays a dual role as a dopant, influencing preferential growth of certain crystal facets and the directing morphology of colloidally synthesized In_2O_3 NCs, as well as inducing IR range LSPR by aliovalent doping within the In_2O_3 NC lattice. In this study, we have demonstrated that introducing fluorine precursors in a typical heat-up method colloidal synthesis yields highly faceted F:In_2O_3 cube NCs with shape-dependent LSPR responses. Morphological control is demonstrated for the formation of concave cubes by adjusting the dopant concentration during F:In_2O_3 NC synthesis. Small percentages (1-2 at.%) of fluorine species are shown to be at the surfaces of the F:In_2O_3 NCs and hinder growth of {100} facets, as determined by combined solid-state 2D $^{1}H\{^{19}F\}$ NMR and DFT analyses. By comparison, the majority of fluorine species are incorporated into sub-surface metallic environments in the F:In_2O_3 lattice, consistent with F^- acting as an anionic dopant, as revealed by variable-temperature analyses of ^{19}F spin-lattice relaxation times and comparison to the Knight-Korringa relation. Complementary analyses of wideline ^{115}In NMR spectra show that the majority of ^{115}In species in the F:In_2O_3 species interact with unpaired conduction band electrons, providing corroboratory evidence that the F:In_2O_3 NC lattice is heavily doped beyond the metal-insulator transition. Arising from the combined effects of dopant-induced free-carriers and highly-faceted NC shapes, multimodal LSPR extinction features are observed in the IR. Single-particle LSPR near-field modes spatially localized around sharp morphological features are directly observed by STEM- EELS.

With this understanding of the role played by fluorine both on the NC surface and in the lattice, F:In_2O_3 NCs provide a valuable platform material for exploring properties and applications of LSPR-active NCs. Analogous to Ag nanocubes that exhibit visible LSPR,[57] well-defined In_2O_3 nanocubes are able to be colloidally synthesized, with shape-dependent LSPR in the IR spectral range. Near-field localization of IR light will make these highly faceted F:In_2O_3 NCs a platform material to evaluate near-field enhancement effects and explore applications unique to the infrared, including coupling LSPR to molecular vibrational modes[19] and IR emissive excitons.[65] To meet these demands, control of NC sizes and LSPR spectral tunability need be advanced. Further synthetic advances, such as the systematic incorporation of co-dopants,[18] may lead to additional LSPR tuning by increasing free electron compensation in In_2O_3 NCs. However, synthetic questions remain to fully understanding cationic co-dopant incorporation in metal oxides in the presence of anionic dopants.[19,66] The understanding of the dual role of fluorine as an anionic dopant in F:In_2O_3 NCs is expected to provide a foundation for addressing these questions and challenges, and further improving the properties of these versatile materials.

A2.5 Materials and methods

Materials

Indium (III) acetylacetonate ($In(acac)_3$, 99.99%), Indium (III) fluoride (InF_3, > 99.9%), Indium (III) chloride ($InCl_3$, 99.999%), Indium (III) bromide ($InBr_3$, 99.999%), Oleic acid (OA, 90%, technical grade), Octylamine (OcAm, 99%), Trioctylamine (TOA, 98%) and tetrachloroethylene (TCE, ≥ 99%) were purchased from Sigma-Aldrich. Toluene (99.5%) was purchased from Fisher Chemical. All chemicals were used as received without any further purification.

Fluorine-Doped Indium Oxide (F:In_2O_3) NC Synthesis

All synthesis procedures were carried out using standard Schlenk line techniques aided by a nitrogen-filled glovebox. For the growth of 3% doped F:In_2O_3 cubes, a mixture of $In(acac)_3$ (399.78 mg, 0.97mmol), InF_3 (5.15 mg, 0.03 mmol), OA (1 ml), OcAm (0.5 ml) and TOA (3.5 ml) was loaded in a three-neck round-bottom flask in the glovebox. This precursor mixture was then stirred with a magnetic bar at 600 rpm and degassed under vacuum at 120 °C for 15 min. The mixture turned transparent and colorless during this operation signifying the formation of indium oleate. Thereafter, the flask was filled with nitrogen and further heated at a ramp rate of 15 °C/min to 320 °C. The colorless reaction mixture turned cloudy and opaque which signified cube growth and was designated as the growth reaction start time. The growth reaction was allowed to run for 5 min at 320 °C or the desired set point temperature. Subsequently, growth was terminated by removing the heating mantle and the reaction mixture was cooled by blowing an air jet on the flask. The cubes were washed and dispersed in toluene and centrifuged at 4500 rpm for 5 mins. This wash process was repeated three times. The resultant cubes were re-dispersed in toluene for further analysis.

Varying concentrations of F doping in these NCs was achieved by controlling the molar ratio of InF_3 to $In(acac)_3$, while keeping other reaction parameters identical. Aliquots (0.1 ml), at various reaction times during growth, were extracted from the reaction mixture with a nitrogen purged syringe needle and quenched into TCE for further analysis.

Indium Oxide (In_2O_3) NC Synthesis

Undoped indium oxide (In_2O_3) NCs were synthesized by adding $In(acac)_3$ (1 mmol) in the reaction flask without InF_3 while keeping other reaction parameters identical to the procedure described above for the F-doped NCs.

Chlorine/Bromine Doped Indium Oxide ($Cl:In_2O_3$, $Br:In_2O_3$) NC Synthesis

$Cl:In_2O_3$ (3% $InCl_3$) NCs were synthesized by adding $In(acac)_3$ (0.97 mmol), substituting $InCl_3$ (0.03 mmol) precursor for InF_3 in the reaction flask, while keeping other reaction parameter identical. In a similar manner, $InBr_3$ (0.03 mmol) was used to synthesize $Br:In_2O_3$ (3% $InBr_3$) NCs keeping other reaction parameters identical.

FTIR Spectra

FTIR spectral measurements were conducted using a Bruker Vertex 70 FTIR at 4 cm^{-1} scan resolution. Aliquot solutions were diluted in TCE and loaded into a liquid cell with KBr windows for FTIR measurements. NCs dispersed in TCE were sonicated for 1 hour to prevent aggregation and then loaded into the liquid cell for recording the spectra.

Electron Microscopy

Samples were prepared by drop-casting NC solutions onto carbon-coated 400 mesh copper grids (Ted Pella) and the imaging was performed in a Hitachi S5500 scanning electron microscope (SEM) operating in the scanning transmission electron microscopy (STEM) mode at an accelerating voltage of 30 kV. NC size analysis was done with ImageJ software with 250 NC count. High resolution transmission electron microscopy (HRTEM) images and selected-area electron diffraction (SAED) patterns were acquired with JEOL 2010F transmission electron microscope (TEM) equipped with a CCD camera and a Schottky field emission gun operating at 200 kV.

X-ray photoelectron spectroscopy (XPS)

Samples were prepared by drop casting NC solutions on silicon substrates and the measurements were performed in a Kratos Axis Ultra DLD spectrometer with a monochromatic Al Kα source (1486.6 eV). Wide survey scans were acquired at analyzer pass energy of 80 eV and the high-resolution narrow region scans were performed at a pass energy of 20 eV with steps of 0.1 eV. Spectral acquisitions were performed with photoelectron take-off angle at 0° with respect to the surface normal and pressure in the analysis chamber was maintained at around 10^{-9} torr. Data analysis was performed in CasaXPS software using the Kratos relative sensitivity factor library. The binding energy (BE) scale was internally referenced to the C 1s peak (BE for C-C = 284.8 eV).

DFT Calculations

DFT calculations were performed using the Vienna Ab-initio Simulation Package (VASP)[67,68] with PAW pseudopotentials[69] in the package. The Perdew-Burke-Ernzerhosf (PBE) exchange-correlation functional[70] was used in all the DFT calculations. A 3×3×1 Monkhorst-Pack k point mesh for the Brillouin zone integration was used, with a vacuum layer of 15 Å to prevent interactions between periodic images of the slab. Further details are provided in Ref. 28.

Solid-State ^{19}F and ^{115}In NMR spectroscopy

Solid-state ^{1}H and ^{19}F magic angle spinning (MAS) nuclear magnetic resonance (NMR) spectra were acquired on a Bruker ASCEND 400 MHz (9.4 T) solid-state DNP NMR spectrometer operating at Larmor frequencies of 400.202 and 376.532 MHz for ^{1}H and ^{19}F, respectively. For the solid-state MAS NMR measurements, the F:In_2O_3 NCs were mixed with KBr powder in a 1:1 ratio by mass. The KBr served as an internal temperature probe for accurate determination of the sample temperature under the different measurement

conditions.[71,72] The 1D ^{19}F Hahn echo spectrum was acquired at 35 kHz MAS, at 395 K, and using a 90°-τ-180°-τ pulse sequence with rotor-synchronized τ delay times of one rotor period and 100 kHz rf pulses. The 2D $^{1}H\{^{29}F\}$ NMR correlation spectrum was acquired by using a 2D dipolar-mediated *H*eteronuclear *M*ultiple *Q*uantum *C*orrelation (HMQC) pulse sequence, where the ^{1}H-^{19}F nuclear dipole-dipole couplings were reintroduced by using $SR26_4^{11}$ recoupling[73] with 50 kHz rf power for recoupling. The ^{19}F spin-lattice (T_1) relaxation analyses relaxation times at different temperatures were measured by using a saturation-recovery pulse sequence with Hahn echo detection.

The solid-state ^{115}In NMR spectrum of undoped bulk polycrystalline In_2O_3 (99.9% purity, Aldrich) was acquired on Bruker AVANCE-III Ultrashield Plus 800 MHz (18.8 T) narrow-bore spectrometer operating at a Larmor frequency of 174.354 MHz for ^{115}In and using a Bruker 3.2 mm broadband double-resonance H-X probehead. The solid-state ^{115}In NMR spectrum of the F:In_2O_3 NCs was acquired on a 19.6 T Bruker DRX NMR spectrometer (National High Magnetic Field Laboratory) operating at a Larmor frequency of 182.266 MHz for ^{115}In and using a custom-built 3.2 mm double resonance H-X probehead. The ^{115}In NMR spectra were acquired using a quadrupolar Carr-Purcell-Meiboom-Gill (QCPMG) pulse sequence,[56] which yields manifolds of very narrow, evenly-spaced NMR signals (spikelets), which can be systematically acquired as a series that can be overlain to map the full central transition (CT) region of the ^{115}In NMR spectra. Each ^{115}In NMR spectrum is presented as a mosaic overlay of 22 individual QCPMG sub-spectra (plotted in different colors) acquired at evenly spaced frequency intervals. The ^{115}In spectra were referenced to a 1 M $In(NO_3)_3$ solution at 0 ppm. Further details on the ^{19}F and ^{115}In NMR analyses are provided in Ref 28.

Scanning Transmission Electron Microscope-Electron Energy Loss Spectroscopy

Plasmon mapping was performed in a Nion high-energy-resolution monochromated EELS STEM (HERMES) at Oak Ridge National Laboratory operated at 60 kV and a Nion prototype spectrometer.[74,75] Using the variable slit we chose an energy resolution of 186 cm^{-1} (23 meV) to optimize the resolution between the plasmon peaks and the signal in the monochromated beam. For the plasmon deconvolution we use the non-negative matrix factorization routine available in the Python HyperSpy library (http://hyperspy.org/). More details can be found in Ref 28.

A2.6 References

(1) Agrawal, A.; Cho, S. H.; Zandi, O.; Ghosh, S.; Johns, R. W.; Milliron, D. J. *Chem. Rev.* **2018**.
(2) Xia, Y.; Xia, X.; Peng, H.-C. *J. Am. Chem. Soc.* **2015**, *137* (25), 7947.
(3) Seo, D.; Park, J. C.; Song, H. *J. Am. Chem. Soc.* **2006**, *128* (46), 14863.
(4) Zhou, S.; Li, J.; Gilroy, K. D.; Tao, J.; Zhu, C.; Yang, X.; Sun, X.; Xia, Y. *ACS Nano* **2016**, *10* (11), 9861.
(5) DeSantis, C. J.; Skrabalak, S. E. *Langmuir* **2012**, *28* (24), 9055.
(6) Alvarez, M. M.; Khoury, J. T.; Schaaff, T. G.; Shafigullin, M. N.; Vezmar, I.; Whetten, R. L. *J. Phys. Chem. B* **1997**, *101* (19), 3706.
(7) Naik, G. V.; Shalaev, V. M.; Boltasseva, A. *Adv. Mater.* **2013**, *25* (24), 3264.
(8) Luther, J. M.; Jain, P. K.; Ewers, T.; Alivisatos, A. P. *Nat Mater* **2011**, *10*, 361.
(9) Agrawal, A.; Kriegel, I.; Milliron, D. J. *J. Phys. Chem. C* **2015**, *119* (11), 6227.
(10) Kanehara, M.; Koike, H.; Yoshinaga, T.; Teranishi, T. *J. Am. Chem. Soc.* **2009**, *131* (49), 17736.
(11) Buonsanti, R.; Llordes, A.; Aloni, S.; Helms, B. A.; Milliron, D. J. *Nano Lett* **2011**, *11*, 4706.
(12) Gordon, T. R.; Paik, T.; Klein, D. R.; Naik, G. V.; Caglayan, H.; Boltasseva, A.; Murray, C. B. *Nano Lett.* **2013**, *13* (6), 2857.
(13) Ghosh, S.; Manna, L. *Chem. Rev.* **2018**, *118* (16), 7804.
(14) Xia, X.; Xie, S.; Liu, M.; Peng, H.-C.; Lu, N.; Wang, J.; Kim, M. J.; Xia, Y. *Proc. Natl. Acad. Sci.* **2013**, *110* (17), 6669.
(15) Liu, G.; Yang, H. G.; Pan, J.; Yang, Y. Q.; Lu, G. Q. (Max); Cheng, H.-M. *Chem. Rev.* **2014**, *114* (19), 9559.
(16) Meyns, M.; Iacono, F.; Palencia, C.; Geweke, J.; Coderch, M. D.; Fittschen, U. E. A.; Gallego, J. M.; Otero, R.; Juárez, B. H.; Klinke, C. *Chem. Mater.* **2014**, *26* (5), 1813.
(17) Ghosh, S.; Gaspari, R.; Bertoni, G.; Spadaro, M. C.; Prato, M.; Turner, S.; Cavalli, A.; Manna, L.; Brescia, R. *ACS Nano* **2015**, *9* (8), 8537.
(18) Ye, X.; Fei, J.; Diroll, B. T.; Paik, T.; Murray, C. B. *J. Am. Chem. Soc.* **2014**, *136* (33), 11680.
(19) Agrawal, A.; Singh, A.; Yazdi, S.; Singh, A.; Ong, G. K.; Bustillo, K.; Johns, R. W.; Ringe, E.; Milliron, D. J. *Nano Lett.* **2017**, *17* (4), 2611.
(20) Gordon, T. R.; Cargnello, M.; Paik, T.; Mangolini, F.; Weber, R. T.; Fornasiero, P.; Murray, C. B. *J. Am. Chem. Soc.* **2012**, *134* (15), 6751.

(21) Avadhut, Y. S.; Weber, J.; Hammarberg, E.; Feldmann, C.; Schellenberg, I.; Poättgen, R.; Schmedt Auf Der Günne, J. *Chem. Mater.* **2011**, *23* (6), 1526.
(22) Sherry, L. J.; Chang, S.-H.; Schatz, G. C.; Van Duyne, R. P.; Wiley, B. J.; Xia, Y. *Nano Lett.* **2005**, *5* (10), 2034.
(23) Hoang, T. B.; Akselrod, G. M.; Argyropoulos, C.; Huang, J.; Smith, D. R.; Mikkelsen, M. H. *Nat. Commun.* **2015**, *6*, 7788.
(24) Hsu, S.-W.; Tao, A. R. *Chem. Mater.* **2018**, *30* (14), 4617.
(25) Hrelescu, C.; Sau, T. K.; Rogach, A. L.; Jäckel, F.; Feldmann, J. *Appl. Phys. Lett.* **2009**, *94* (15), 153113.
(26) Stiles, P. L.; Dieringer, J. A.; Shah, N. C.; Duyne, R. P. Van. *Annu. Rev. Anal. Chem.* **2008**, *1* (1), 601.
(27) Kim, J.; Agrawal, A.; Krieg, F.; Bergerud, A.; Milliron, D. J. *Nano Lett.* **2016**, *16* (6), 3879.
(28) Cho, S. H.; Ghosh, S.; Berkson, Z. J.; Hachtel, J. A.; Shi, J.; Zhao, X.; Reimnitz, L. C.; Dahlman, C. J.; Ho, Y.; Yang, A.; Liu, Y.; Idrobo, J.; Chmelka, B. F.; Milliron, D. J. *ChemRxiv,* **2018**, DOI: 10.26434/chemrxiv.7355042.v1.
(29) Dean, J. A. *Lange's handbook of chemistry*; McGraw-Hill, 1992.
(30) Yang, H. G.; Sun, C. H.; Qiao, S. Z.; Zou, J.; Liu, G.; Smith, S. C.; Cheng, H. M.; Lu, G. Q. *Nature* **2008**, *453* (7195), 638.
(31) Karsi, N.; Lang, P.; Chehimi, M.; Delamar, M.; Horowitz, G. *Langmuir* **2006**, *22* (7), 3118.
(32) Walsh, A.; A. Catlow, C. R. *J. Mater. Chem.* **2010**, *20* (46), 10438.
(33) Jansons, A. W.; Plummer, L. K.; Hutchison, J. E. *Chem. Mater.* **2017**, *29* (13), 5415.
(34) Khurshid, H.; Li, W.; Chandra, S.; Phan, M.-H.; Hadjipanayis, G. C.; Mukherjee, P.; Srikanth, H. *Nanoscale* **2013**, *5* (17), 7942.
(35) Sadoc, A.; Biswal, M.; Body, M.; Legein, C.; Boucher, F.; Massiot, D.; Fayon, F. *Solid State Nucl. Magn. Reson.* **2014**, *59–60*, 1.
(36) Subba Ramaiah, K.; Sundara Raja, V. *Appl. Surf. Sci.* **2006**, *253* (3), 1451.
(37) Kröger, F. A.; Vink, H. J. In *Solid State Physics*; Seitz, F., Turnbull, D., Eds.; Academic Press, 1956; Vol. 3, pp 307–435.
(38) Walsh, A. *Appl. Phys. Lett.* **2011**, *98* (26), 261910.
(39) Runnerstrom, E. L.; Kelley, K. P.; Sachet, E.; Shelton, C. T.; Maria, J.-P. *ACS Photonics* **2017**, *4* (8), 1885.
(40) Seo, J.-S.; Jeon, J.-H.; Hwang, Y. H.; Park, H.; Ryu, M.; Park, S.-H. K.; Bae, B.-S. *Sci. Rep.* **2013**, *3*, srep02085.
(41) Shannon, R. D. *Acta Crystallogr. Sect. A Cryst. Physics, Diffraction, Theor. Gen. Crystallogr.* **1976**, *32* (5), 751.
(42) Yamakawa, N.; Jiang, M.; Key, B.; Grey, C. P. *J. Am. Chem. Soc.* **2009**, *131* (30), 10525.
(43) Kiczenski, T. J.; Stebbins, J. F. *J. Non. Cryst. Solids* **2002**, *306* (2), 160.
(44) Kiczenski, T. J.; Stebbins, J. F. *J. Am. Ceram. Soc. 89* (1), 57.
(45) Yesinowski, J. P. *Top. Curr. Chem.* **2011**.
(46) Yesinowski, J. P.; Berkson, Z. J.; Cadars, S.; Purdy, A. P.; Chmelka, B. F. *Phys. Rev. B* **2017**, *95* (23), 1.
(47) Knight, W. D. *Phys. Rev.* **1949**, *76* (8), 1259.
(48) Slichter, C. P. *Principles of Magnetic Resonance*, 3rd ed.; Springer Series in Solid-State Sciences; Springer-Verlag: Berlin Heidelberg, 1990.
(49) Korringa, J. *Physica* **1950**, *16* (7–8), 601.
(50) Zapart, W.; Zapart, M. B.; Zhukov, A. P.; Popolitov, V. I.; Shuvalov, L. A. *Phys. Lett. A* **1987**, *121* (5), 248.
(51) Han, O. H.; Timken, H. K. C.; Oldfield, E. *J. Chem. Phys.* **1988**, *89* (10), 6046.
(52) Jung, W. S.; Han, O. H.; Chae, S. A. *Mater. Lett.* **2007**, *61* (16), 3413.
(53) Schurko, R. W. *Acc. Chem. Res.* **2013**, *46* (9), 1985.
(54) Pell, A. J.; Pintacuda, G. *Prog. Nucl. Magn. Reson. Spectrosc.* **2015**, *84–85*, 33.

(55) Kim, J.; Ilott, A. J.; Middlemiss, D. S.; Chernova, N. A.; Pinney, N.; Morgan, D.; Grey, C. P. *Chem. Mater.* **2015**, *27* (11), 3966.
(56) Hung, I.; Rossini, A. J.; Schurko, R. W. *J. Phys. Chem. A* **2004**, *108* (34), 7112.
(57) Nicoletti, O.; Peña, F. de la; Leary, R. K.; Holland, D. J.; Ducati, C.; Midgley, P. A. *Nature* **2013**, *502* (7469), 80.
(58) Naumov, I. I.; Li, Z.; Bratkovsky, A. M. *Appl. Phys. Lett.* **2010**, *96* (3), 033105.
(59) Mulvihill, M. J.; Ling, X. Y.; Henzie, J.; Yang, P. *J. Am. Chem. Soc.* **2010**, *132* (1), 268.
(60) García de Abajo, F. J. *Rev. Mod. Phys.* **2010**, *82* (1), 209.
(61) Hachtel, J. A.; Lupini, A. R.; Idrobo, J. C. *Sci. Rep.* **2018**, *8* (1), 5637.
(62) Li, G.; Cherqui, C.; Bigelow, N. W.; Duscher, G.; Straney, P. J.; Millstone, J. E.; Masiello, D. J.; Camden, J. P. *Nano Lett.* **2015**, *15* (5), 3465.
(63) Ringe, E.; DeSantis, C. J.; Collins, S. M.; Duchamp, M.; Dunin-Borkowski, R. E.; Skrabalak, S. E.; Midgley, P. A. *Sci. Rep.* **2015**, *5*, 17431.
(64) Johns, R. W.; Bechtel, H. A.; Runnerstrom, E. L.; Agrawal, A.; Lounis, S. D.; Milliron, D. J. *Nat. Commun.* **2016**, *7*, ncomms11583.
(65) Akselrod, G. M.; Weidman, M. C.; Li, Y.; Argyropoulos, C.; Tisdale, W. A.; Mikkelsen, M. H. *ACS Photonics* **2016**, *3* (10), 1741.
(66) Cao, S.; Zhang, S.; Zhang, T.; Lee, J. Y. *Chem. Mater.* **2018**, *30* (14), 4838.
(67) Kresse, G.; Furthmüller, J. *Phys. Rev. B* **1996**, *54* (16), 11169.
(68) Kresse, G.; Joubert, D. *Phys. Rev. B* **1999**, *59* (3), 1758.
(69) Perdew, J. P.; Burke, K.; Ernzerhof, M. *Phys. Rev. Lett.* **1996**, *77* (18), 3865.
(70) Monkhorst, H. J.; Pack, J. D. *Phys. Rev. B* **1976**, *13* (12), 5188.
(71) Yesinowski, J. P.; Ladouceur, H. D.; Purdy, A. P.; Miller, J. B. *J. Chem. Phys.* **2010**, *133* (23), 234509.
(72) Thurber, K. R.; Tycko, R. *J. Magn. Reson.* **2009**, *196* (1), 84.
(73) Brouwer, D. H.; Kristiansen, P. E.; Fyfe, C. A.; Levitt, M. H. *J. Am. Chem. Soc.* **2005**, *127* (2), 542.
(74) Krivanek, O. L.; Lovejoy, T. C.; Dellby, N.; Carpenter, R. W. *Microscopy* **2013**, *62* (1), 3.
(75) Spiegelberg, J.; Idrobo, J. C.; Herklotz, A.; Ward, T. Z.; Zhou, W.; Rusz, J. *Ultramicroscopy* **2018**, *187*, 34.